Environmentally assisted creep crack growth in 316H stainless steel

Laurie Podesta

UM–20XX/XXX

THÈSE DE DOCTORAT
DE
L'UNIVERSITÉ DE MONTPELLIER

Présentée par

Laurie PODESTA

pour obtenir le grade de

DOCTEUR DE L'UNIVERSITÉ DE MONTPELLIER

Domaine

MÉCANIQUE – GÉNIE CIVIL

Sujet de la thèse

Etude expérimentale de la fissuration en fluage de l'acier 316H vieilli sous environnement CO_2
Environmentally assisted creep crack growth in 316H stainless steel

Soutenue à Moret-sur-Loing le 12 décembre 2016 devant le jury composé de :

Eric ANDRIEU	Enseignant-Chercheur, INP-ENSIACET Toulouse	Rapporteur
Pierre FEISSEL	Maître de Conférence, HDR, UTC Compiègne	Rapporteur
Félix LATOURTE	Ingénieur de Recherche, EDF R&D	Encadrant industriel
Jean-Michel MURACCIOLE	Maître de Conférence, Université de Montpellier	Co-encadrant
Jean-Loup STRUDEL	Chair Professor, University of Hyderabad	Examinateur
Evelyne TOUSSAINT	Professeure, Polytech Clermont Ferrand	Présidente
Laurent WALTZ	Maître de Conférence, Université de Montpellier	Co-encadrant
Bertrand WATTRISSE	Professeur, Université de Montpellier	Directeur

LMGC-Montpellier
Université de Montpellier / CNRS / LMGC
163, rue Auguste Broussonnet, F-34090 Montpellier, France

ACKNOWLEDGEMENT

Dans un premier temps, je souhaiterais remercier les membres de mon jury. Messieurs Andrieu et Feissel qui ont eu la lourde tâche (240 pages...) de rapporter mon travail de thèse. Madame Evelyne Toussaint pour avoir accepté de présider mon jury et Monsieur Strudel pour s'être intéréssé au domaine de la Mécanique de la Rupture des matériaux métalliques et d'avoir partagé, lors de la soutenance, son expérience. Je vous remercie pour les échanges nombreux qui ont suivi.

Je souhaiterais remercier EDF R&D, EDF Energy et le Laboratoire de Mécanique et Génie Civil de Montpellier. Une éternelle reconnaissance à mon équipe d'encadrement, mon équipe de choc pour m'avoir accompagnée depuis mon cursus d'ingénieur jusque dans les derniers instants de la thèse. Merci pour les années à Polytech et merci plus encore de m'avoir fait confiance pour mener à bien ces travaux. Votre pédagogie, votre écoute et votre capacité à vous rendre disponible m'ont permis de conduire ces recherches avec l'encadrement nécessaire tout en ayant la sensation d'être complètement libre et autonome. Je crois que cet équilibre n'est pas commun. Merci Bertrand, Félix, Jean-Michel et Laurent.

Je souhaiterais remercier le Groupe T24 du Département MMC pour m'avoir accueillie il y a presque 4 années maintenant. Merci en particulier à Sébastien, Géraud, Rémi et Malik. Je me suis toujours sentie chez moi parmi vous tous.

La qualité et la richesse des travaux expérimentaux présentés dans cette thèse ont été rendues possible grâce à la participation et l'implication de nombreux personnels d'EDF R&D (Expertise Métallurgique, Fluage, labo M, Microscopie du MAI) et de l'atelier. Merci en particulier à Didier et Jérôme ainsi que Nicolas, Laurent, Dominique, Julien et surtout Michel. Merci d'avoir toujours accepté avec envie et curiosité de relever avec moi tous les défis expérimentaux rencontrés durant cette thèse.

Cette thèse étant réalisée sur deux sites géographiquement séparés, un soutien administratif important a été nécessaire. Merci à Lydie et Chantal pour votre aide et l'affection que vous m'avez témoignée.

Je souhaiterais également remercier les doctorants qui m'ont convaincue de faire une thèse : Adrien, Elodie et Mickaël ainsi que ceux qui m'ont aidée durant cette thèse : Qiwei, Emeric, Wen, Julien, Li et Tarik. Merci pour tous les bons moments partagés et votre soutien dans les derniers moments de la thèse où c'est particulièrement difficile. Merci infiniment !

Je voudrais également remercier mes amis pour avoir été là dans les moments névralgiques : Marion, Guillaume et Val. Merci d'avoir compris mes absences souvent et mes silences parfois.

Enfin, je souhaiterais remercier du fond du coeur ma famille. Mes grands-parents pour m'avoir transmis le goût de l'effort. Mon parrain et ma marraine qui m'accompagnent sur le chemin de la vie. Mes cousins et mon oncle Alain pour ma passion de la mécanique auto/moto. Si je défends

une thèse en mécanique, vous y êtes pour beaucoup. Merci à ma tante et mes cousines pour nos moments privilégiés à Montpellier. Merci à ma soeur Marine pour son amour et à Loki pour sa douceur et ses papouilles.

Je réserve ces quelques lignes pour remercier la personne qui me guide, me conseille et m'encourage avec amour depuis toujours. Maman, cette thèse est aussi la tienne. Tu as mis tant d'efforts à me tirer vers le haut que j'ai fini par côtoyer les étoiles. Je t'aime.

"Si un jour vous veniez à aimer un objet, un lieu, une personne ou un concept, soyez certain que cela vous changerait. Peut-être pas d'une façon significative ou bien consciente mais là, quelque part au fond de vous, s'opèrerait une transformation. Ces modifications sont l'essence de notre personnalité. Elles nous permettent d'évoluer, de grandir et nous donnent la capacité d'aborder la vie avec d'autres perspectives. Je n'ai alors qu'un conseil à donner si la situation se présente : laissez-vous posséder car les plus belles choses dans la vie ne sont pas celles que l'on possède mais celles qui nous possèdent."

N. Laval

A ma Famille, celle que la vie nous donne et surtout celle que l'on se crée.

Contents

Introduction

The industrial challenges

EDF Energy is one of the largest energy companies in the United Kingdom (UK), supplying around 5 million residential and business accounts with electricity or gas (20% of the UK) (see Figure 1). EDF Energy is part of EDF Group and employs over 13,500 people across the country. The headquarters of EDF Energy in UK are located in London and the branch dedicated to the nuclear safety, EDF Nuclear Generation, is based at Gloucester.

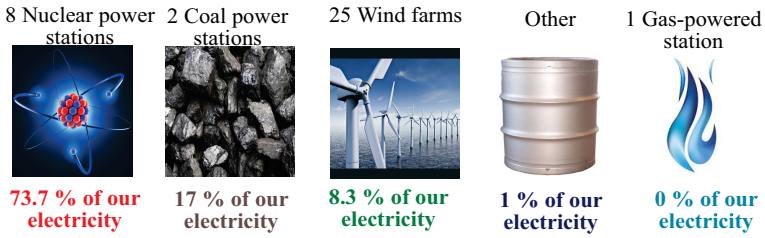

Figure 1: EDF Energy Fuel Mix between the period April 2012 - March 2013 (EDF Energy).

In the coming years, the life of existing nuclear plants in the UK has to be extended in order to achieve the company's vision of generating 65 TWh over 9 years (see Figure 2).

The long term operation of Advanced Gas cooled Reactors (AGR) is a current research area at the core of EDF Energy industrial strategy, due to the number of installed AGR plants (see Figure 2), due to the power demand in UK and due to the planned end of operation of these reactors. Some generalities on AGR design and operation are provided hereafter.

Description of Adanced Gas cooled Reactor

The AGR was a natural evolution from the MAGNOX (MAGnesium Non OXidising) technology and is unique to the UK. The MAGNOX drawbacks were the limited thermal efficiency of the plant and the reaction of austenitic stainless steels with water, limiting the lifespan of the reactor. A greater thermal efficiency requires a higher temperature reactor: the reactor gas and fuel cans temperatures can reach 650 °C and 800 °C respectively in normal operation of AGR reactor. The secondary circuit is operated with a steam pressure of 165 bar and a temperature close to 540 °C. In the AGR technology, carbon dioxide gas is used to transfer the heat produced in the reactor to the boilers. The gas is pumped through the channels of the reactor at high pressure by gas circulators (see Figure 3).

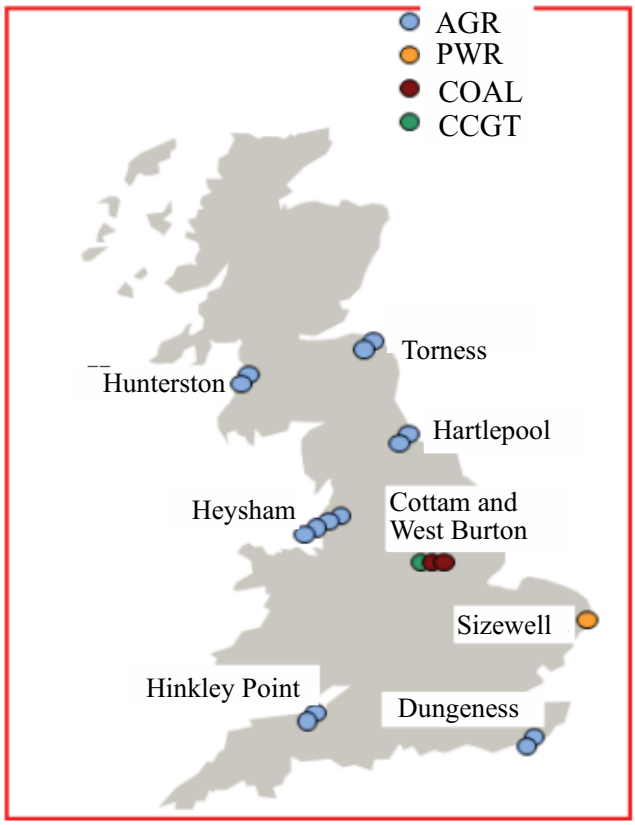

Figure 2: EDF Energy exploits 8 nuclear plants of AGR design (blue circles), 2 coal-fired power plants (COAL), 1 pressurized water reactor (PWR) and 1 gas power plant (CCGT) (EDF Energy)

The operating conditions of these reactors are very different from that of pressurized water reactors operating in France:

- the temperature of operation in the primary circuit is more elevated and ranges from 500°C to 550°C, which changes the damage modes of austenitic stainless steels (ASS) used in several high temperature components such as boilers, steam headers, manifolds like bifurcations and tailpipes (see Figure 4). While ASS are prone to stress corrosion cracking in pressurized water reactors, they will develop creep deformation in AGR operating conditions.

- the environmental effects are different. Oxydation in PWR is strongly related with the water chemistry, while in AGR it is driven by the carbon dioxyde, carbon monoxide and other gases and elements present in the primary coolant.

- higher temperature in AGR also increases the diffusion rate in metals, promoting migration of intersticials and dislocation climb, nucleation and growth of cavities, and increasing oxydation kinetics as well.

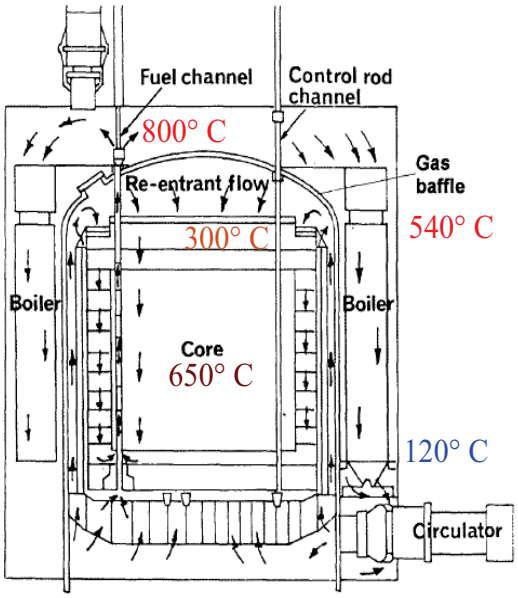

Figure 3: Description of gas flow in AGR [1].

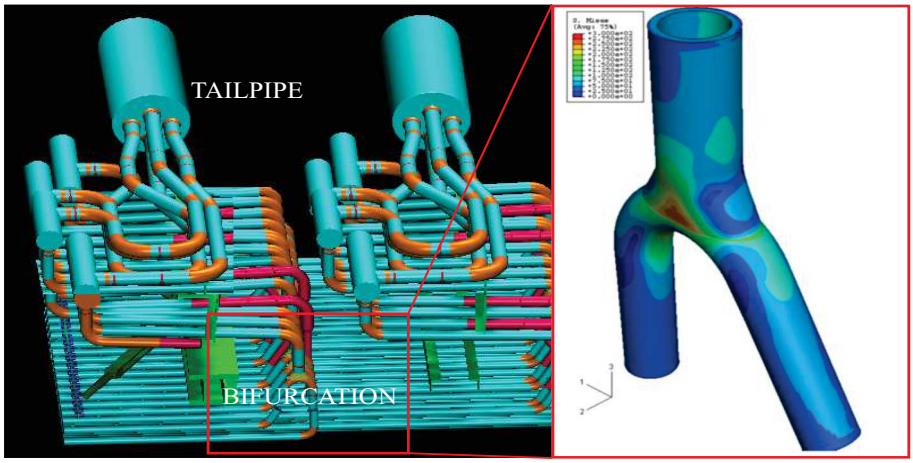

Figure 4: Boiler modelling and description of stresses in tailpipe [2].

Due to the elevated pressures and temperatures in AGR, some areas of the boilers operate in creep regime. As shown in Figure 4, the bifurcations and tailpipes in the steam header are complicated components that require welding operations during their manufacturing. The probability of crack initiation and propagation in the weld subjected to creep loading conditions due to the presence of surface defects, residual stresses and other heterogeneities needs to be considered and assessed in view of long term safe operation of the power plant.

The R5 rule procedure (Volume 4/5), used in UK, provides assessment methods for defects in structures operating at high temperatures and under creep-fatigue loading conditions [3]. The information needed to perform analysis are operating conditions, defect nature, material data and structural calculations to correlate materials data with the behaviour of complex structures [4].

These rules rely on experimental validations that must be the most representative of operating conditions and are statedly reviewed [5]. The creep cracking mechanisms are usually studied at the macroscopical scale. Example of experimental assessments include creep tests on compact tension specimens [6, 7, 8].

It is proposed in this work to study the creep cracking phenomenon at the microstructural scale. This scale reduction is motivated by two main aspects. First, a microstructural study should allow a much more accurate creep crack initiation and growth measurement. Second, a microstructural study is more appropriate to study the correlations between environmental effects and material performance. Improvements are expected from merging metallurgy-chemistry-corrosion and mechanical engineering disciplines.

This work is part of the environmental project lead by EDF Energy and known as the Environmental Impact on the Structural Integrity of Nuclear Components (ENVISINC). It is itself part of the High Temperature Behaviour of Austenitic Stainless Steels (HiTBASS) work program. This project is based on the collaboration between universities (Manchester, Bristol, Imperial College of London) and industrials (EDF Energy, EDF R&D, AMEC and Frazer-Nash).

Research objectives

The industrial issues of creep cracking in oxidizing environment require performing specific experiments. During a conventional creep test, the post-processings consist in observing the macroscopic strain response and the evolution of the creep strain rate to identify the creep law parameters and describe the material creep response.

Creep crack initiation and growth are phenomenon occuring at the microscopic scale, resulting in detrimental instabilities. The choice of a specimen design with small dimensions allows a surface preparation in view of imaging the specimen with different electronic microscopy techniques, with the objective of understanding material changes, and monitoring the crack morphology and extent and its evolution at the grain scale. To quantify the effects of AGR environment on material mechanical properties, a specific ageing treatment has been set-up to reproduce the embrittlement of components in service.

Some innovative developments are required to capture and measure relevant quantities from the microscopical observations, making a mechanical assessment possible. The Digital Image Correlation (DIC) has been chosen to derive kinematic fields associated with the creep crack situation. This technique is indeed well suited to situations where heterogeneities develop, such as fracture, plasticity, localization, etc... The use of DIC has been already validated and demonstrated in the literature for such situations, but its application to small scale creep remains experimentally challenging. The PhD work adressing this objective is presented in this manuscript, structured as follows:

1. The first part is focused on the material and mechanical properties of 316 stainless steels at high temperature and provides a review of several works related with creep understanding, creep cracking models and assessment procedures for this material.

2. The second chapter introduces microstructural and chemical caracterizations that were conducted on 316H stainless steel cast provided by EDF Energy for this PhD thesis. After a characterization of the as-received state, the effects of dry oxidation at high temperature in CO_2 environment for 316 stainless steels are presented.

3. In the Chapter 3, the experimental strategy for creep is presented. A comparison of creep responses for different specimen geometries is proposed, as well as a comparison between carburized and as-received material.

4. The Chapter 4 introduces a specific digital image correlation technique proposed in this work in view of monitoring creep cracks. This method requires the use of surface markers that have been deposited using e-beam microlithography. Fracture mechanics theories are introduced and used in a kinematic projection allowing to extract crack parameters.

5. Finally, several experimental assessments are presented in Chapter 5. Full field measurements are conducted on *in-situ* 316H and 316L single end notched tensile specimens loaded at room temperature or at 500 °C.

Chapter 1

Material and mechanical properties of 316 stainless steels at high temperature

The austenitic stainless steel AISI 316H has been commonly used in the AGR boilers. Its good corrosion resistance and its creep properties make this material suitable to manufacture the components operating in the conditions of the reactor (550 °C, CO_2). A literature review of the Grade 316 material properties and of its creep properties is proposed.

Contents

1.1 Presentation of 316H stainless steel

1.1.1 Use of Grade 316 in Nuclear Power Plants

The AISI 316L is one of the most popular austenitic stainless steel grades. The increased molybdenum content provides a better overall corrosion resistance, particularly a higher resistance to pitting and crevice corrosion in chloride environments. The austenitic structure gives excellent toughness, even down to cryogenic temperatures. This steel exhibits a combination of high yield stress, high strain hardening and high ductility. It is often used in various high temperature applications such as defense or nuclear domains [9]. In 1977, the first Pressurized Water Reactor (PWR) was built in France (see Figure 5). Several PWR in-core components such as baffle bolts are made from cold worked 316L. The "L" in Grade 316L stands for the low carbon content. This grade is highly resistant to sensitization associated to grain boundary carbide precipitation.

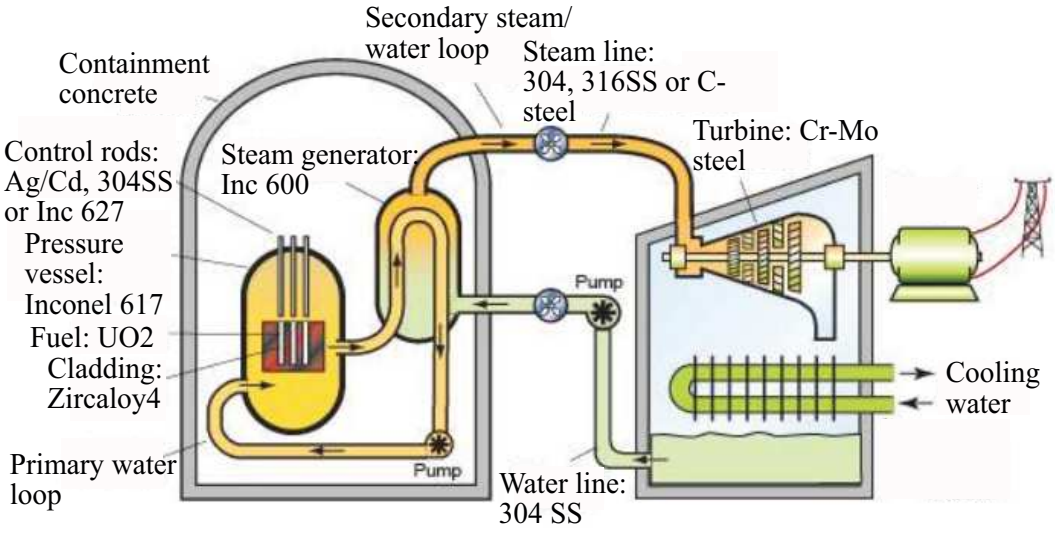

Figure 5: Pressurized Water Reactor (PWR) design [10]

In 1986, the French sodium-cooled fast breeder reactor named Superphoenix started to produce electricity. 316L material was chosen to manufacture Superphoenix intermediate heat exchangers operating between 525 °C and 550 °C (see Figure 6). The pressure vessel was made of 316LN, a nitrogen controlled specification of 316L. In the next years, the 316LN became a candidate material for several components of the fourth generation reactor, named GEN IV, based on advanced sodium-fast reactor design.

In UK, EDF Energy Nuclear Generation mainly operates plants of Advanced Gas cooled Reactor (AGR) design (see Figure 7). The temperature in the boiler is ranging between 500 °C and 550 °C. The boiler components operating at the higher pressure and temperature conditions are made from 316H. Grade 316H is comparable to 316L but the carbon content is about three times higher than that of 316 L from 0.04 %wt to 0.10 %wt (see Table 1). Grade 316H has higher strength at high temperatures (above 500 °C) compared to the Grade 316 and is therefore a good candidate to manufacture structural components subjected to high pressure and high temperature. The chemical compositions of various 316 grades are provided in Table 1.

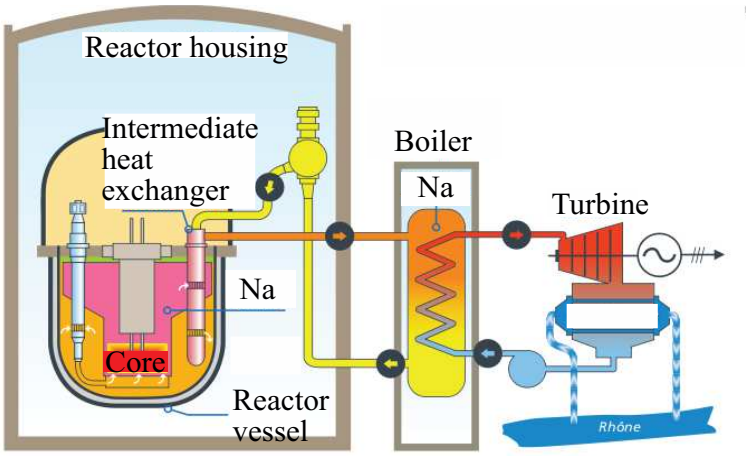

Figure 6: Sodium-cooled fast breeder reactor. Source: EDF

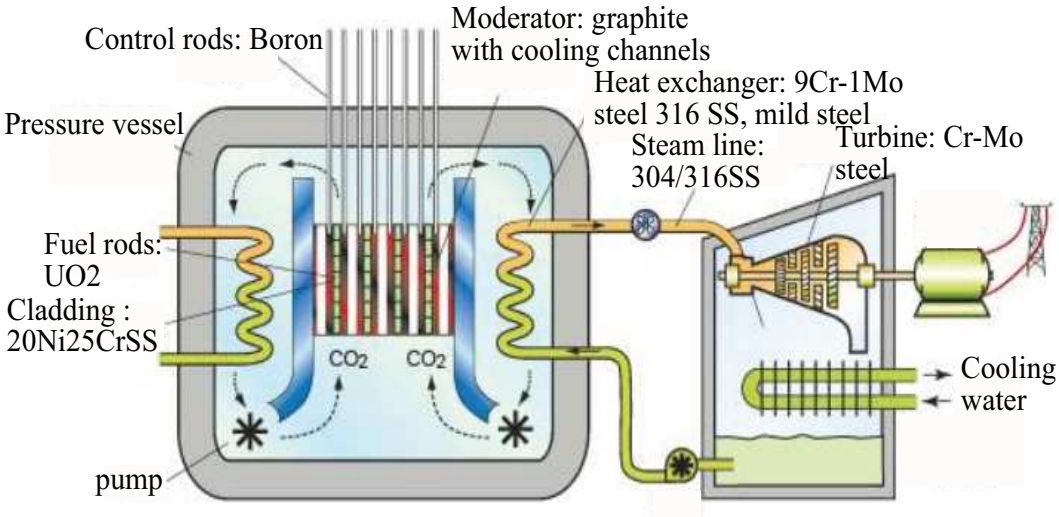

Figure 7: Advanced Gas cooled Reactor (AGR) design [10].

Grade		C	Mn	Si	P	S	Cr	Mo	Ni	N
316	Min	-	-	-	-	-	16.0	2.00	10.0	-
	Max	0.08	2.0	0.75	0.045	0.03	18.0	3.00	14.0	0.10
316L	Min	-	-	-	-	-	16.0	2.00	10.0	-
	Max	0.03	2.0	0.75	0.045	0.03	18.0	3.00	14.0	0.10
316H	Min	0.04	-	-	-	-	16.0	2.00	10.0	-
	Max	0.10	2.0	0.75	0.045	0.03	18.0	3.00	14.0	-

Table 1: Composition specification (in %wt) for the Grade 316 [11].

The mechanical properties (see Table 2) are specified for flat rolled products (plate, sheet, coil) in ASTM A240/A240M at room temperature. It is admitted that similar but not necessarily identical properties are specific to other products like pipes and bars.

Grade	Minimal tensile strength (MPa)	Minimal yield strength 0.2% proof (GPa)	Minimal elongation (% in 50 mm)	Maximum Rockwell B hardness	Maximum hardness Brinell B	Young's elastic modulus (MPa)
316	515	205	40	95	217	193
316L	485	170	40	95	217	193
316H	515	205	40	95	217	193

Table 2: Mechanical properties at room temperature for Grade 316 [11].

Between room temperature and 550 °C, the mechanical properties evolve. At 550 °C, the Young's modulus E equals to 140 GPa and the yield stength 0.2% proof equals to 170 MPa [12].

Now that some general properties have been discussed for Grade 316 stainless steel, we propose to introduce the evolution of the mechanical properties and the environmental performance of Grade 316 in the AGR's operating conditions.

1.1.2 Environmental performance of Grade 316 stainless steel

At high temperature (up to 500 °C), austenitic stainless steels are prone to the sensitization phenomenon, that leads to $Cr_{23}C_6$ chromium carbide precipitation in the material. These carbides are responsible for material embrittlement. Another important phenonemon that must be taken into account at this temperature is the material oxidation. In the following sections, we will describe the effects of sensitization and oxidation in nuclear power plant operating conditions.

1.1.2.1 The sensitization in nuclear power plant

Since the 1980's, the sensitization phenomenon has been identified as a concern regarding the safe operation of industrial components. Several research works aimed at characterizing the influence

of the chemical content of the material used in nuclear power plant as well as the effects of the operating conditions. In 1989, Beneke has studied the influence of nitrogen and molybdenum on sensitization properties of low-carbon austenitic stainless steel [13]. The influence of neutron on sensitization in neutron-irradiated austenitic stainless steel has been quantified by Kenik [14]. Further complementary studies dealing with material microstructure effects have been conducted [15, 16, 17, 18, 19]. A study of intercrystalline corrosion of components made of stainless steel was also conducted later for EDF [20]. Some main conclusions of this work are summarized hereafter. The intercrystalline corrosion can be classified as a generalized corrosion phenomenon that affects the grain boundaries (GB) of alloys, and is detrimental for the mechanical strength or the structural integrity of the components. Intercrystalline corrosion is mainly induced by the local chromium depletion in the matrix. In stainless steel, the chromium depletion is due to carbide precipitation such as $Cr_{23}C_6$ at grain boundaries (see Figure 8).

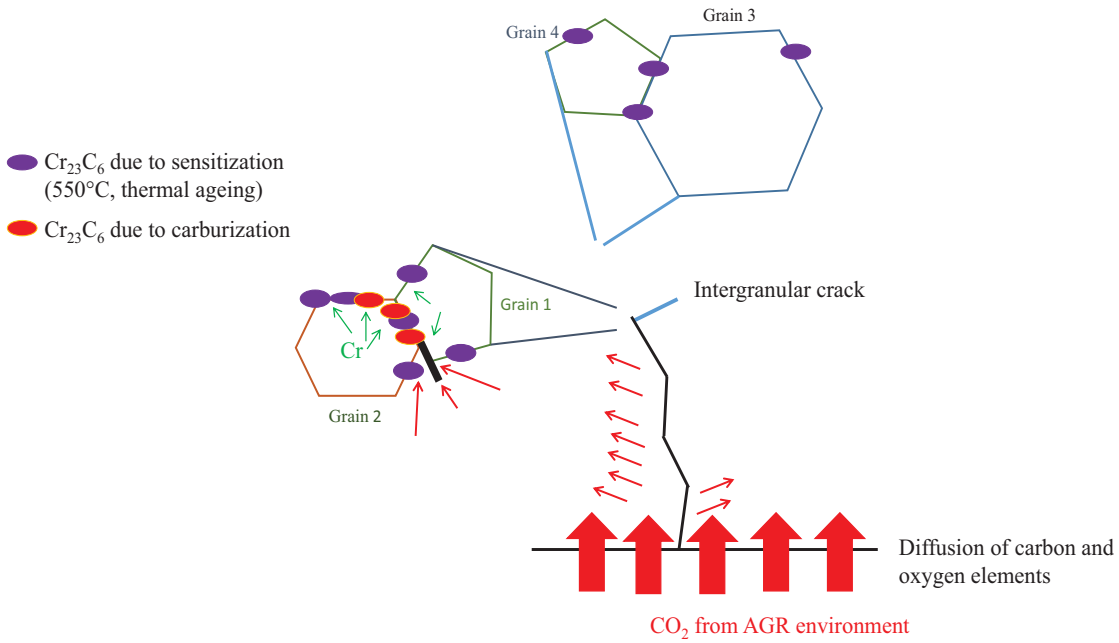

Figure 8: Description of combined carbide precipitation $Cr_{23}C_6$ from sensitization and carburization at grain boundaries.

A temperature ranging from 500 to 750 °C, and a chromium content inferior to 12% is needed to sensitize 316 steel. The growth of carbide results from the combined diffusion of carbon and chromium atoms in the vicinity of grain boundaries. The diffusion rate of chromium in the matrix is smaller than that of carbon, resulting in a local depletion of chromium in solid solution together with carbide precipitation up to reaching a thermodynamic equilibrium (see Table 3).

Element	Q_D (kcal/mole)
Fe	68
Cr	58.8
Mo	56
C	41
B	20

Table 3: Diffusion activation energies for some 316 SS elements [21].

Time-Temperature-Sensitization diagramms known as TTS diagramms are used to describe the domain of intercristalline corrosion. The sensitization domains appear as delimited by parabolas of horizontal axes (see Figure 9). T_s is the upper temperature above which precipitates are not existing and T_m is the temperature below which sensitization can occur. On the right side of the sensitization domain, desensitization can occur: precipitates dissolve back in solid solution.

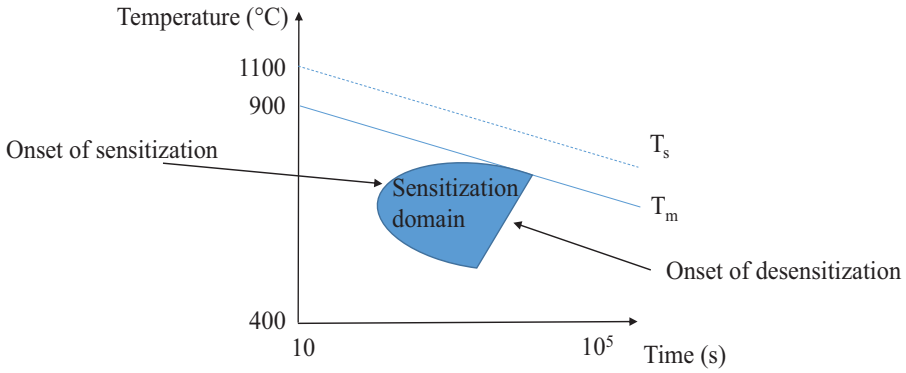

Figure 9: Illustration of a sensitization domain typically associated with a parabollic shaped boundary.

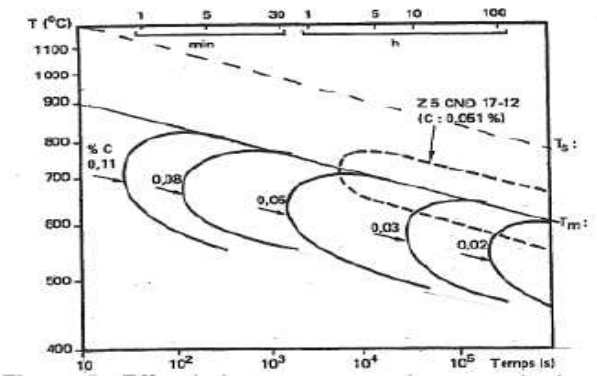

Figure 10: Effect of carbon content on sensibilization behavior of a 18Cr10Ni steel (AISI 304). T_m is the maximal temperature for carbide existence and T_s is the maximal temperature for the onset of sensitization [20].

The TTS diagram provided in Figure 10 reports different sensitization domains in a 18Cr10Ni steel (AISI 304) with different carbon contents [20]. Increasing the carbon content induces a shift of the sensitization domains towards shorter times. Noel has shown that chromium and molybdenum are involved in the carbide equilibrium in the matrix and the diffusion flow during the carburization. Increasing chromium and molybdenum content have a limiting effect on sensitization.

Several studies have also demonstrated that welds have higher susceptibility to sensitization [22, 23]. The microstructural heterogeneities generated by high temperature environment have also been highlighted in the recent work of Warren on 316H [24] (see Figure 11). Recently, Warren *et al.* has shown that ferrite can play a role on the susceptibility to creep cavitation by preferential diffusion of vacancies at austenite-ferrite boundary jonctions [24]. Their material has been removed from an attachment weldment of a boiler header component which has been subjected to 65,015 h operation at temperature ranging between 490 and 530 °C and subsequently aged during 22,000 h at 500 °C. It exhibits approximately 2 % mixed ferrite, of δ and α phase.

In the 316H material provided by EDF Energy, no ferrite has been found during the optical observations.

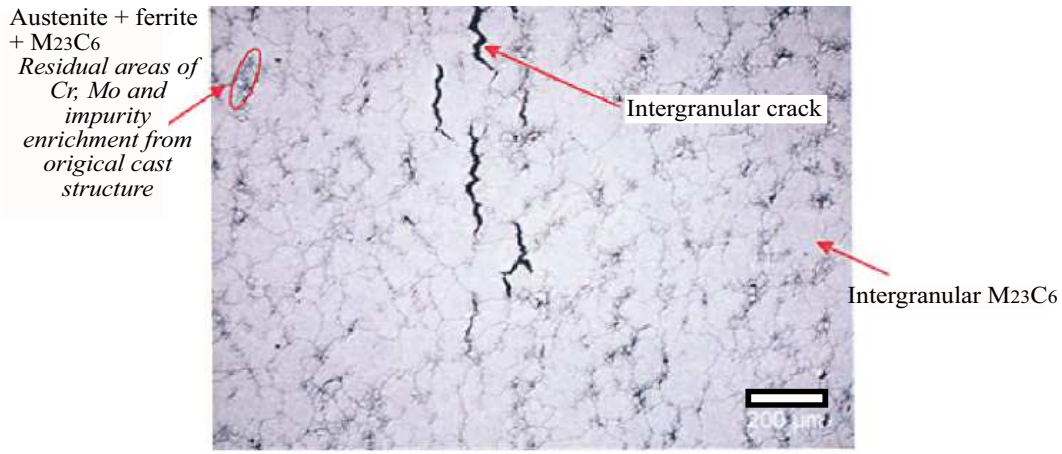

Figure 11: Optical micrograph of the ex-service Type 316H aged, showing the heterogeneities in the material structure: intergranular cracks, carbide [24]. The scale bar is 200 µm.

1.1.2.2 Dry oxidation of metals containing iron at elevated temperature

At elevated temperature in AGR environment, oxidation phenomenon occurs. This oxidation leads to the growth of an oxide layer at the metal surface (see Figure 12 a), the formation of passivated film at the metal interface [25], diffusion of oxygen and other elements in the bulk [26, 27]. The different oxidation studies have been motivated by several industrial issues such as the reduction of mechanical properties, material embrittlement, undesired surface effects [28, 29, 30, 18, 31]. In fact, the oxidation leads to surface and grain boundary modifications that affect in turn fatigue behaviour, tensile resistance [32, 33, 34, 35] and fracture toughness [36]. Moreover, the diffusion of elements in the material is responsible for increased material hardness [37] and weaker fretting fatigue limit [38, 39, 40, 41]

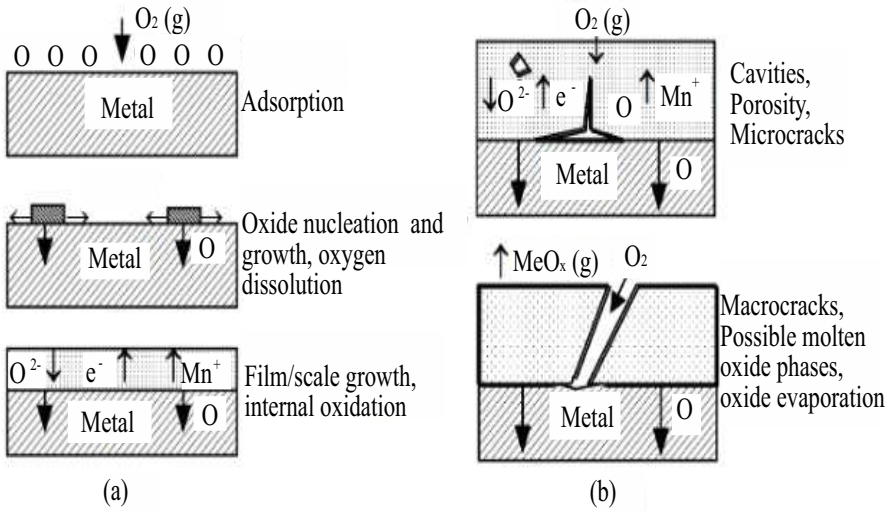

Figure 12: Schematic illustrations of oxide layer formation: (a) oxide layer growth, (b) development of discontinuities at the interface of oxide layer and material base metal [28, 31].

The oxide growth results from the underlying microstructure and metal properties. Several oxide morphologies can be observed. A multilayer structure is generally obtained, with compact (see Figure 12 a) or porous layers (see Figure 12 b) with similar or different compositions between two successive layers (see Figure 12, Figure 13).

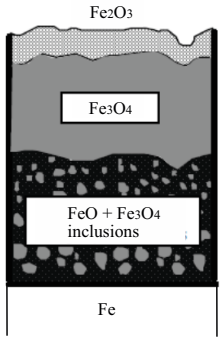

Figure 13: Schematic cross section of the scale obtained after oxidation of an iron sheet in air, at 850°C for 4 hours. The observed magnetite (Fe_3O_4) inclusions precipitated during cooling [42].

The oxidation of iron in air or pure oxygen environment, at high temperature (up to 600°C) at atmospheric pressure or equivalent, may lead to three types of oxide growth : FeO (wustite), Fe_3O_4 (magnetite) and Fe_2O_3 (hematite). The oxide layer growth rate depends on the partial pressure of oxygen and on the temperature.

During the growth of the initial oxide layer, compressional stresses arise. When their level exceeds a given threshold, or bond strength, the oxide layer accomodates with buckling behavior and scaling/spalliation (see Figure 14). The spalliation is followed by a renewal of the oxidation process or eventually by a crack initiation in the metal layer as it can be seen during carburization.

In Figure 15, the work of Evans is summarized. This figure depicts the spalliation sequence in relationship with the oxiodation-induced stresses [43]. Two cases appear and depend on the mechanical properties of the oxide and the interface formed with the underlying metal. If the oxide has a weak strength compared to that of the interface, oxide cracking happens before the spalliation. If the adhesion between the metal and the oxide is strong compared to the oxide, spalliation happens prior to the cracking.

When the external oxide layer cracks (see Figure 15), the base metal is in contact with the gaseous environment again. Then, two cases are generally considered:

1. The chemical contents, the microstructure and the mechanical state of the freshly exposed surface are the same as during the initial exposure and an oxidation sequence can restart as initially;
2. The external surface is oxidised. The mechanical properties of this layer are different from that of the base metal. The oxidising process is either stopped or has a modified kinetic.

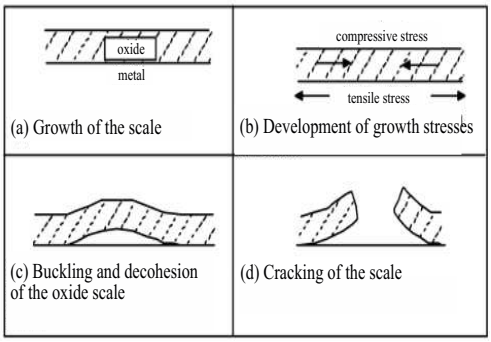

Figure 14: Schematic description of the oxide scale buckling and cracking due to compressive stress [42].

Different possible reactions betwen gases and metals are illustrated in Table 4 obtained from [29]. In AGR, the primary circuit gas contains carbon monoxide, carbon dioxide and moisture so oxidation and carburization are prone to develop at the surface of austenitic stainless steels. Protective atmospheres play a key role in avoiding the oxidation and/or the decarburization or the carburization in the superficial layers of steel during heat treatment.

The AGR's boilers operate at high temperature in CO_2 environment. The oxidation reactions between iron and CO_2 gas are given as:

$$Fe + CO_2 \rightleftharpoons FeO + CO \tag{1.1}$$

$$3FeO + CO_2 \rightleftharpoons Fe_3O_4 + CO \tag{1.2}$$

The existence domains of FeO and Fe_3O_4 are given by the diagram in Figure 16. At 550°C, it is expected to form Fe_3O_4 layer.

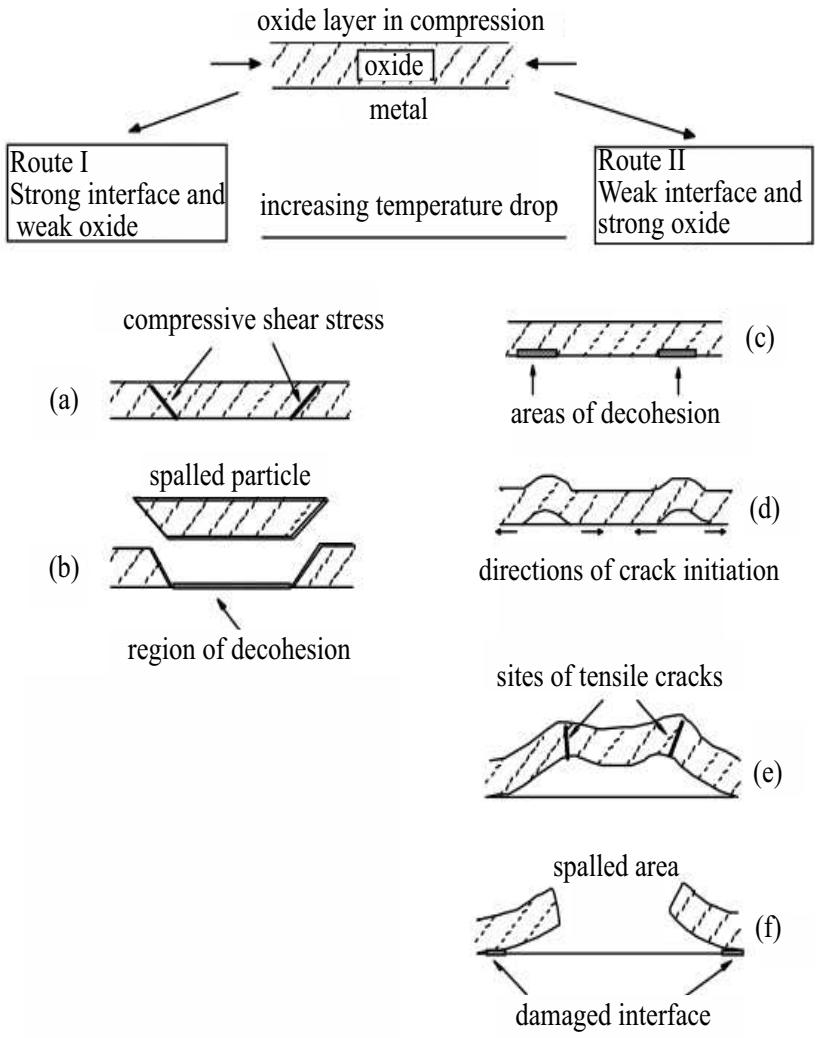

Figure 15: Illustration of different possible spalliation sequences [43].

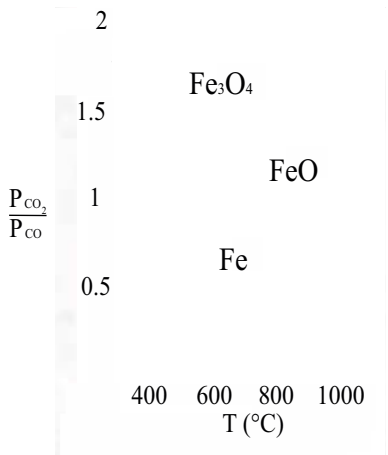

Figure 16: Equilibrium diagramm between Fe-FeO-Fe_3O_4 in CO/CO_2 atmosphere. The temperature is given in °C, P_{CO_2}, P_{CO} are the partial pressures of CO_2 and CO respectively [29].

Metals	O_2	CO	CO_2	H_2	[H_20]
Steel with carbon	Oxidation and decarburization	Reduction and carburization	Oxidation and decarburization	Reduction	Oxidation and decarburization
Stainless steels	Oxidation	Reduction and carburization	Oxidation and decarburization	Reduction	Oxidation
Cast irons	Oxidation and decarburization	Reduction	Oxidation and decarburization	Reduction	Oxidation and decarburization
Al and alloys	Oxidation	Neutral	Oxidation	Cripping	Oxidation
Cu and alloys	Oxidation	Reduction	Oxidation	Reduction	Neutral
Ti and alloys	Oxidation	Cripping	Oxidation	Cripping	Oxidation

Table 4: Main chemical reactions between gases and metals [29].

1.1.2.3 Microstructural evolutions under creep loading at high temperature

Creep is also often combined with thermal ageing of the material. In 1980, Deleury studied the influence of microstructure, temperature and stresses on creep response of Type 316L and Type 316H [21, 44]. Thermal ageing at 550 °C during 3×10^4 hours leads to $Fe_{23}C_6$ precipitation preferentially at grain boundaries then in incoherent twin boundaries and finally within the grains on dislocations. At this temperature, the precipitation is heterogeneous. Moreover, the capability of 316H to deform prior to fracture under creep loading is called creep ductility and this property decreases due to this precipitation.

Several components of interest aim at transporting water or steam from boilers to turbine in order to produce electricity. The steam pressure combined with the elevated temperature lead to creep loading. Creep assisted by environment has been identified as one of the mechanisms potentially leading to boiler components failure. In the next section, we propose to introduce the creep theories and the characteristics of creep cracking in Grade 316 austenitic stainless steels.

1.2 Presentation of creep behaviour and mechanisms and of some assesment methods

1.2.1 Introduction to creep

Creep is an irreversible deformation process which generally appears when the temperature exceeds one third of the melting temperature (T_f). The plastic strain can increase at constant temperature with time and sometimes leads to failure even if the applied stress is smaller than the ultimate tensile stress. The creep regime is thermally activated and it is widely considered that the strain rate follows an Arrhenius law. Creep is often associated with other loadings such as creep-fatigue, creep-relaxation or creep-oxidation [45]. A creep test consists in applying a constant load at one

extremity of a tensile specimen whereas the other one is clamped. The crosshead displacement is recorded as a function of time and an extensometer is sometimes used to monitor more precisely the specimen gauge deformation. The macroscopic evolution of creep strain involves a continuous variation of creep strain rate. A classical conventional creep curve is given in Figure 17.

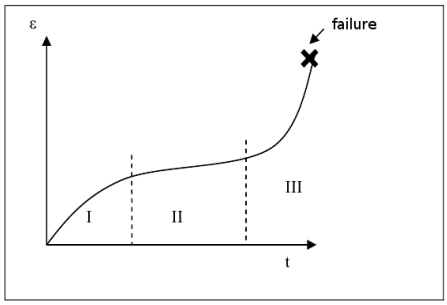

Figure 17: Typical conventional creep curve.

- During the primary step (I) or transient step, the creep strain rate strongly decreases due to the numerous modifications in the dislocation network introduced during the loading step, resulting in strain hardening. The relative elongation under load is generally inferior to 1%. For some material and some creep conditions, primary creep is not observed.
- During the second step (II), the strain-rate reaches its minimum and is nearly constant. The minimal strain rate is often a useful creep information to derive and identify creep models. This step is named the secondary creep.
- In the last part of the response (tertiary creep , denoted step III), the creep strain-rate strongly increases and some specific damage phenomenons such as creep cavitation develops. Moreover, geometrical instabilities such as necking can occur. The combination of damage, necking or both lead to the creep rupture of the specimen. The transition from secondary to tertiary creep regime is associated with an increase of the creep strain-rate compared to its minimal value.

During creep, strains can be measured at the microscopic and macroscopic levels. The measurements of plastic strain or slip transfer in grains at the microstructural scale have been widely studied [46, 47, 48, 49]. These authors have found that these deformations are mostly intragranular at room temperature. At higher temperatures in case of creep, the strain is accumulated at the grain boundaries. The intergranular aspect of creep may responsible for crack initiation and growth at grain interfaces.

Two creep theories can be separated with respect to matter diffusion in the grain structure: the diffusion creep and the dislocation creep. The microstructure and the applied stresses affect the dominant creep mechanisms (see Figure 18).

The diffusion creep:

In the case of the diffusion creep model developped by Coble, it is generally admitted that the strain is not related to a displacement of dislocations but is mainly due to the migration of atoms

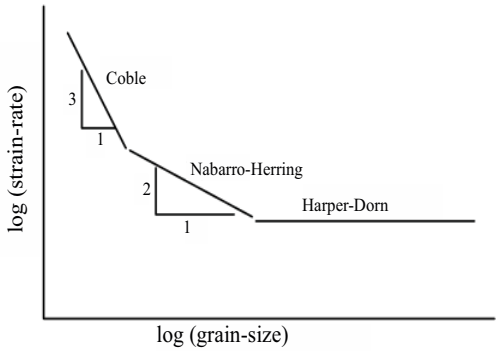

Figure 18: Creep models in function of loading and material grain size [50].

along the grain boundaries [51]. Coble described the strain-rate as a diffusion phenomenon along the grain boundaries:

$$\dot{\varepsilon} = k_C \frac{\sigma}{d^3} \left(D_{GB} \exp\left(\frac{-Q_{GB}}{RT} \right) \right) \tag{1.3}$$

with D_{GB}, the coefficient of diffusion at the grain boundary in [$m^2 s^{-1}$], k_C an empirical constant in [m^3 N^{-1}], d the mean diameter of the grain in [m], Q_{GB} an activation energy in [kJ mol^{-1}] and R the gas constant in [kJ mol^{-1} K^{-1}] and the applied stress σ in [N m^{-2}]. Temperature T is expressed in Kelvin. In this work, the relationship between the strain rate and the stress has been derived with the assumption of a uniform distribution of grain dimension. It is known that the austenitic stainless steels have a polycrystalline structure with a distribution of grain size that may be due to manufacturing or thermal ageing. In 1977, Crossland has studied the possibility of diffusion creep in austenitic stainless steels [52]. Few years later, Schneibel and Coble have studied the influence of grain size distribution [53]. As well as Hazzledine [54], they have shown that Coble's theory is influenced by the size, the shape and the arrangement of the grains. Their assessment work was pursued by Henderson on the effect of impurities [55]. Soula confirmed that creep strain rate is proportional to the stress in the diffusion creep regime [56] .

The dislocation creep:

The dislocation creep appears when the temperature is superior to 0.7 T_f. This theory is known as the Nabarro-Herring creep [57, 58]. This model is convenient for larger grain sizes and higher temperatures than the Coble creep. It results from a combined movement of dislocations: climbing and sliding. The strain rate is constrained by the climbing step and the diffusion mechanism. It can be expressed as:

$$\dot{\varepsilon} = k_{NH} \frac{\sigma}{d^2} \left(D_L \exp\left(\frac{-Q_L}{RT} \right) \right) \tag{1.4}$$

with D_L the diffusion coefficient in the lattice in [$m^2 s^{-1}$], Q_L the activation energy of the lattice in [kJ mol^{-1}] and k_{NH} represents an empirical constant in [m^2 N^{-1}].

For very large grains, there is a competition between Nabarro-Herring creep and Harper-

Dorn creep which happens at low stresses [59]. This transition has been studied since the 1970's [60, 61, 62] when creep data on copper was not suitable for the Nabarro-Herring creep. Recently, Wong and Breton have summarized the creep and the creep fatigue models available [63, 64]. For small grain sizes, Grain Boundary Sliding (GBS) dominates at intermediate stresses and temperatures but won't be discussed here.

1.2.2 Phenomenological creep models

In this section, we introduce classical macroscopic creep models developped to account for the mechanical response at constant temperature. The impact of parameters such as temperature, time or loading mode on creep mechanisms has been first studied by Larson and Miller [65]. Their work was focused in particular on the effect of temperature on creep response and was pursued in details by Hayhurst [66, 67], Murry [45], Soula [56] and more recently by Touboul [68]. For low levels of stresses, the strain-rate follows a creep power law commonly named Norton law:

$$\dot{\varepsilon} = A_{PL}\left(\frac{\sigma}{\sigma_0}\right)^n \tag{1.5}$$

in which σ_0 is the reference creep stress, n the power coefficient and A_{PL} [s^{-1}] a power law coefficicent. The power law coefficient, A_{PL} can account for the dependancy of strain rate to temperature via an Arrhenius relation:

$$A_{PL} = C_t \exp\frac{-Q_{PL}}{RT} \tag{1.6}$$

with C_t [s^{-1}] material constant parameter, Q_{PL} the activation energy for the given deformation process (diffusion or dislocation) ([kJ mol^{-1}]). It is usually known that for metallic alloys the value of n ranges between 3 and 5. For very low stresses at high temperature, it can reach $n = 1$. In this case, the main mechanism to consider is diffusion creep. At high stresses, the strain rate can be expressed with an exponential formulation:

$$\dot{\varepsilon} = A_e \exp\left(\frac{\sigma}{\sigma_0^e}\right) \tag{1.7}$$

with A_e and σ_0^e adjustable parameters.

For intermediate stress levels, an hyperbolic sinus expression can be used:

$$\dot{\varepsilon} = A_{HS} \sinh\left(\frac{\sigma}{\sigma_0^{HS}}\right)^{n_{HS}} \tag{1.8}$$

with A_{HS}, σ_0^{HS}, n_{HS} adjustable parameters.

The double creep Norton's law is a phenomenological model able to capture the transition between the low level (*i.e.* creep dislocation) and the high level of stresses (*i.e.* diffusion creep) (see Equation (1.9)). Gaffard has studied the influence of the stress level on the steady strain rate of 9Cr1MoNbV material using smooth round tensile bars [69, 70]. As initially proposed by Contesti *et al.* [71] and Pugh [72], Gaffard has written the strain rate tensor $\underline{\dot{\varepsilon}}$ considering three viscoplastic

deformation mechanisms:

$$\underline{\dot{\varepsilon}} = \underline{\dot{\varepsilon}}_e + \underline{\dot{\varepsilon}}_{qp} + \underline{\dot{\varepsilon}}_{vp} + \underline{\dot{\varepsilon}}_d \tag{1.9}$$

where $\underline{\dot{\varepsilon}}_e$ is the elastic strain rate tensor, $\underline{\dot{\varepsilon}}_{qp}$ refers to the quasi plastic flow regime, $\underline{\dot{\varepsilon}}_{vp}$ refers to the viscoplastic creep regime (given by a Norton law) and $\underline{\dot{\varepsilon}}_d$ refers to the diffusional creep regime.

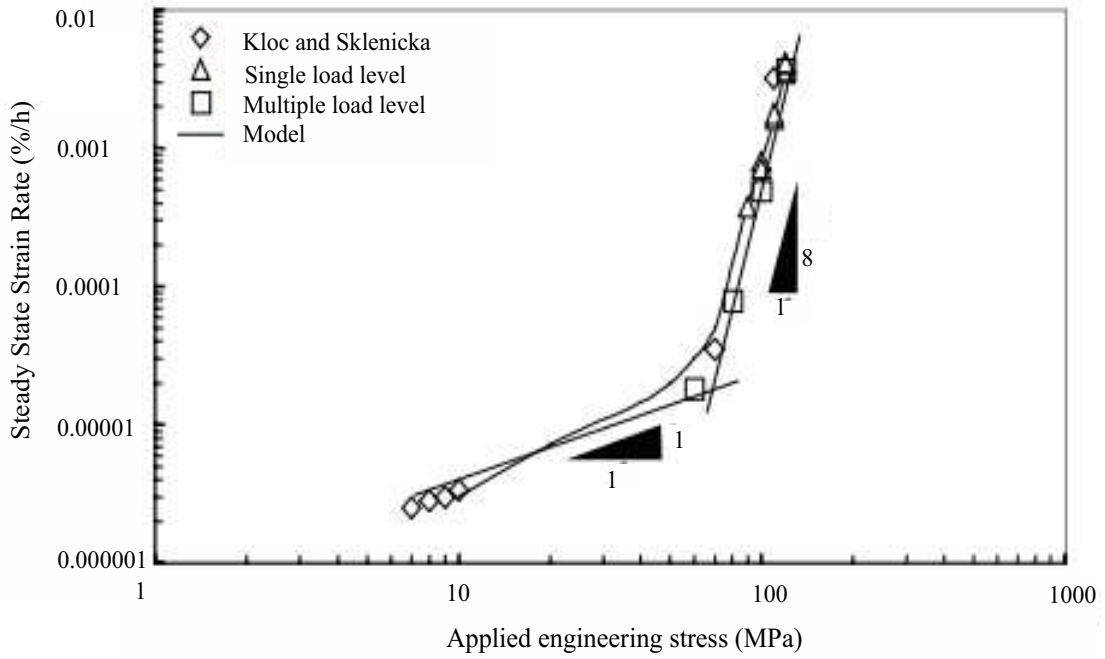

Figure 19: Example of evolution of steady strain rate with respect of level stress for 9Cr1MoNbV at 625 °C [69].

In Figure 19, Gaffard has studied the influence of level stress on the steady strain rate evolution for 9Cr1MoNbV at 625 °C. By distinguishing the low level of stresses (< 70 MPa) and the high ones (> 70 MPa) which corresponds to the transition between two regimes, he has identified that for the diffusion creep, the creep power law exponent equals to 1 and for the diffusion creep, the exponent equals to 8. Kloc and Sckenicka have obtained data on P91 helicoidal spring systems [73]. An other example of the double Norton law use can be found in [74].

1.2.3 Creep strength in Grade 316

In order to estimate the remaining life span, the accumulated damage must be known. Creep damage consist in microstructural evolutions associated with the creation of free surfaces, for instance through the nucleation and growth of cavities and microcracks at grain boundaries. Creep damage ultimately results in component failure. The deterministic evaluation of creep remaining life is challenging due to common scatter in creep data or to the often needed data extrapolation for long creep times.

The Remaining Life Assessment (RLA) of a component is often predicted from creep rupture data using a temperature-time parametric method such as the Larson-Miller Parameter (P_{LM})

method or the Monkman-Grant Relationship (MG).

In the context of sodium-cooled fast breeder reactor development in the eighties, a consortium of French actors (CEA/EDF/AREVA) has studied the creep behaviour of 316L(N). The NIMS institute in Japan has focused on 316 FR material behaviour which is a low carbon version of 316, specially designed for fast reactors (FR). Several test data are pooled in Figure 20. The loading chosen by NIMS is ranging between 250 and 400 MPa. The tests performed by the EDF/CEA/AREVA have been carried out also at lower stress (down to 100 MPa). The material from NIMS institute seems to exhibit better creep strength than the 316L(N).

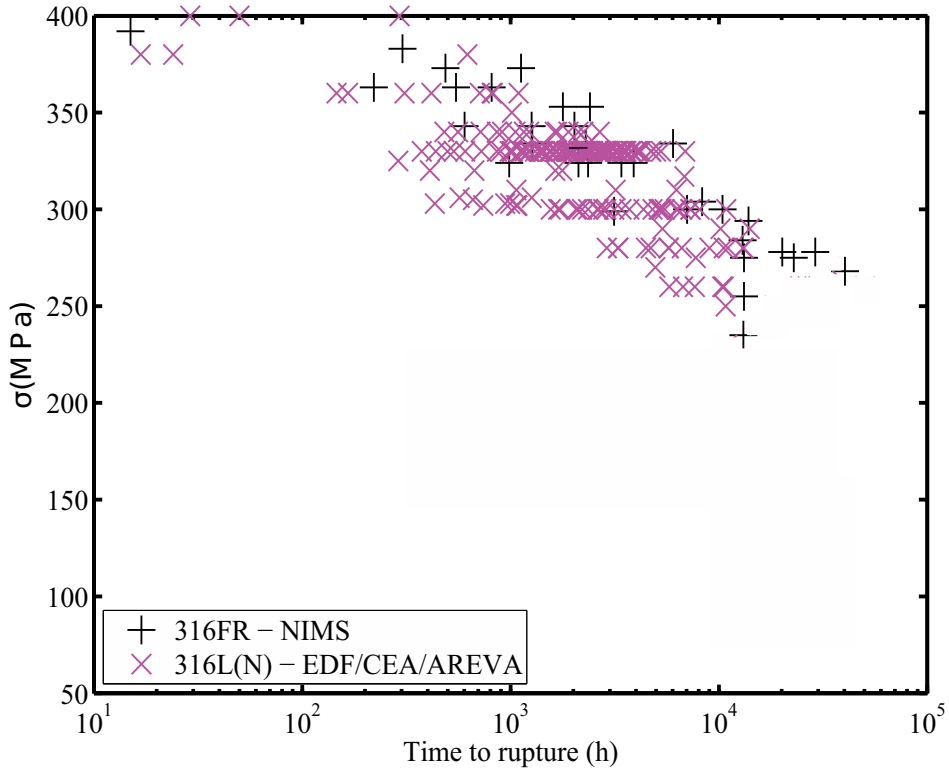

Figure 20: Creep tests on Grade 316. Database from NIMS institute and CEA/EDF/AREVA.

1.2.4 Creep strength assessments: the simplified models

1.2.4.1 The Larson-Miller method

The Larson-Miller method is a simplified method predicting creep rupture time in steady-state creep, considering a given temperature and stress [65]. It was first used by General Electric in the 1950's to perform research on turbine blades. The Larson-Miller parameter P_{LM} describes the equivalence of time and temperature for a steel under the thermally activated creep process. This relationship allows to define the equivalent time to rupture at different temperatures. This model

is based on Arrhenius' rate equation:

$$P_{LM} = T \cdot \left(C_{LM} + \log\left(\frac{t_f}{t_0}\right)\right) \tag{1.10}$$

with P_{LM} the Larson-Miller parameter, t_f is the time to failure [h], t_0 the reference time [h], T is the temperature [K] and C_{LM} is a material constant.
If C_{LM} is known, to determine the rupture time under constant stress at a given temperature, an accelerated test at the same stress at a higher temperature is performed, leading to P_{LM} identification. The desired rupture time at the smaller temperature can then be readily determined. Usually, C_{LM} equals 20 for C-Mn and low alloy steels and 30 for higher alloy steels as 9% Cr steels.

An example of Larson-Miller curve for AISI 310SS [75] is presented in Figure 21.

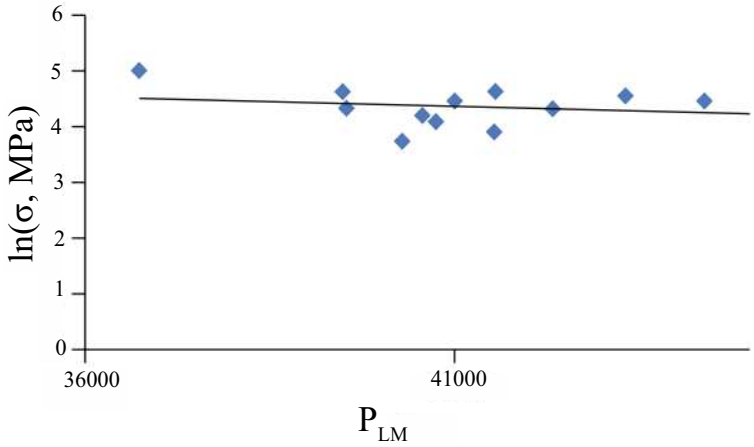

Figure 21: Master curve for temperatures between 973 and 1073 K and stresses 66.6-94.6 MPa for AISI 310SS [75]

1.2.4.2 The Monkman-Grant relationship:

The Monkman-Grant relationship relies on a near constant fracture ductility of the material and a power law relationship between time and strain rate [76]. In this model, the time to reach the failure (t_f) and $\dot{\varepsilon}_{min}^{m}$ the minimum creep rate are related as:

$$(\dot{\varepsilon}_{min})^{m} t_f = C_{MG} \tag{1.11}$$

where m and C_{MG} are constants. For metallic materials, m is usually ranging between 0.8 and 0.95 while the C_{MG} constant varied between 3 and 20. If the minimum strain rate is related to the stress through an exponential law, the Larson-Miller parameter P_{LM} can be obtained using the Monkman-Grant relationship with m = 1. An example of Monkman-Grant relationship for copper is given in Figure 22.

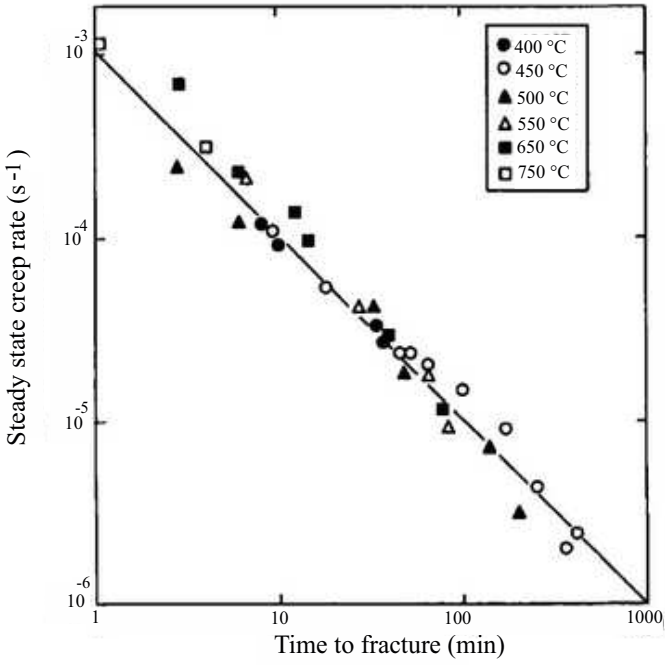

Figure 22: Relation between minimum creep rate $\dot{\varepsilon}_{min}$ and time to fracture t_f for copper [77].

1.2.4.3 The ECCC data sheet about the rupture of 316 stainless steel

The European Creep Collaborative Committee (ECCC) is a voluntary group involving over 35 European organisations. ECCC was formed in 1991 to co-ordinate Europe-wide development of creep data for materials involved in high temperature nuclear reactors. The ECCC is involved in the European data coordination on creep and in the ensuing activities of assessment and comparison. The purpose being to gather the ressources available in each single member state, build up an optimal assessment based on creep values and ultimately set up high production and design standards.

The available data : average rupture time (T, σ)

In Table 5 and Table 6, we introduce the data available for tests at 550 °C. In 2014, 131 tests points were available and 7 tests were still ongoing.

Test duration	< 10000 h	10000 to 20000	20000 to 30000	30000 to 50000	50000 to 70000	70000 to 100000	> 100000
	93	19	9	3	1 (2)	3 (1)	3 (4)

Table 5: Quantity and duration of data used in assessment of 316 stainless steel behaviour at 550 °C. Ongoing test numbers are reported between parentheses [78].

t_f (h)	10^4	3×10^4	10^5	2×10^5
Stress (MPa)	247	218	188	172

Table 6: Average rupture time at 550 °C [78].

The Larson Miller curve

Subsequently to the analysis of the data (see Figure 23), a master equation linking the temperature, the stress and the time to rupture has been identified (Equation 1.12).

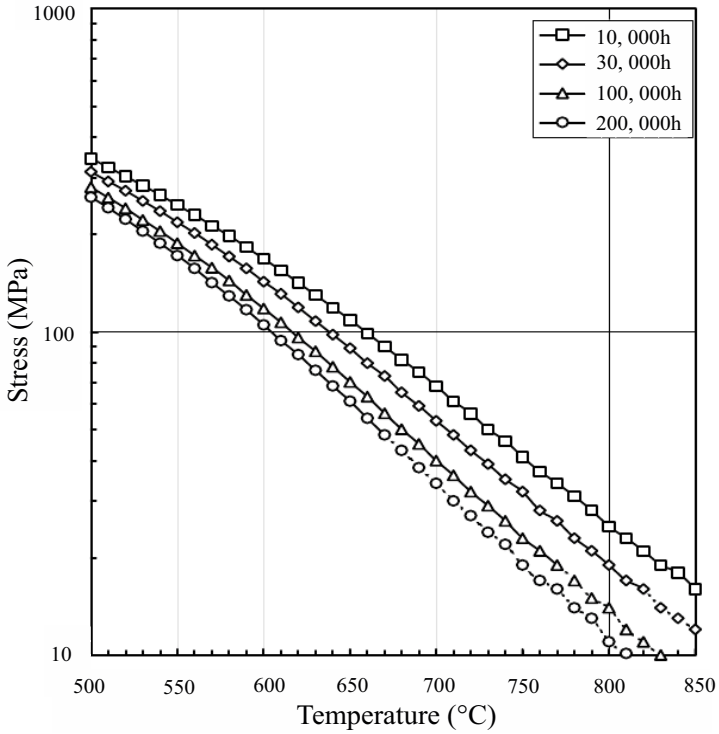

Figure 23: Master equation resulting from analysis of data about the 316 stainless steel [78].

$$log_e(t_f^*) = A + B\, log_{10}(T) - C\, log_{10}\sigma_0 + \left(\frac{D}{T}\right) - E\frac{\sigma_0}{T} \tag{1.12}$$

with A = -234.18, B = 62.14, C = 7.78, D = 71314.4609, E = 19.32 and where t_f^* is the predicted failure time [h], T is the absolute temperature [°C] and σ_0 is the applied stress [MPa]. Considering this equation with temperature and loading as input parameters, a time to failure can be estimated.

1.3 Creep crack models

Creep crack can initiate and grow in austenitic stainless steels in their creep regime. Creep cracking of components is a severe industrial issue that has to be addressed in view of safe and long

term operation. Creep cracking is a complex scientific problem combining environmental effects such as in stress corrosion cracking, diffusion effects leading to the void formation ahead of the crack tip, interactions between the crack and plasticity.

In term of long time operating conditions and safety assessment, several european actors active in nuclear industry have funded between 1996 and 2000 the HIDA European project whose objective was to harmonize the assessment procedure of high temperature cracking [79]. The aim of this project was to be able to predict the behaviour of features type specimens or components containing manufacturing, in-service or process related defects submitted to creep and/or high temperature fatigue sollicitations under standard laboratory testing conditions.

Several codifications or standards are currently used to predict creep cracking in nuclear power plants, such as the R5 procedure in UK, RCC-MR in France, PNAE in Russia, KTA in Germany or JSME/JIS in Japan.

The knowledge of the creep crack growth (CCG) in components containing defects is essential to predict their lifetime in service. To characterize creep crack growth rate denoted $\dot{a}_{CCG}$, experimental tests are usually performed on CT specimen. From these experiments, the C* parameter is determined and gives access to $\dot{a}_{CCG}$ through a linear relationship. The standard relative to this specific test and the creep crack theories allowing to determine C* parameter will be discussed in the following section.

1.3.1 Creep crack growth prediction using C* methods

Considering an industrial approach, this CCG must rely on simple concepts and on measures easy to implement, as the knowledge of the loading applied to the component. Riedel and Rice have shown that for ductile material at high temperature a unique parameter C^* may be used to describe the mechanical fields surrounding the crack tip [80, 81]. C^* is always considered as similar to J, the Rice's integral [82].

The objective was to describe the cracking kinematics using a parameter representative of loading C^* and material constants A and q:

$$\dot{a}_{CCG} = A\,(C^*)^q \tag{1.13}$$

where A and q are material constants.

The standard specimen used for creep crack growth measurements is the Compact Tension (CT) specimen. The general geometry and its dimensions are presented in Figure 24 and Figure 25.

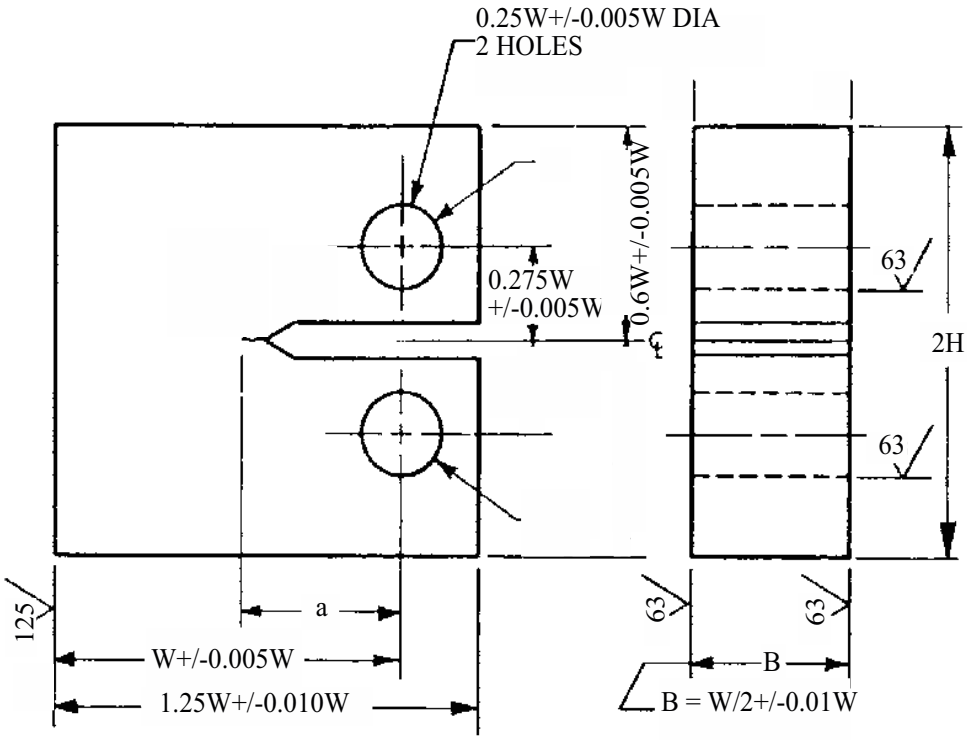

Figure 24: Compact Tension specimen design. Source: ASTM E1921-13

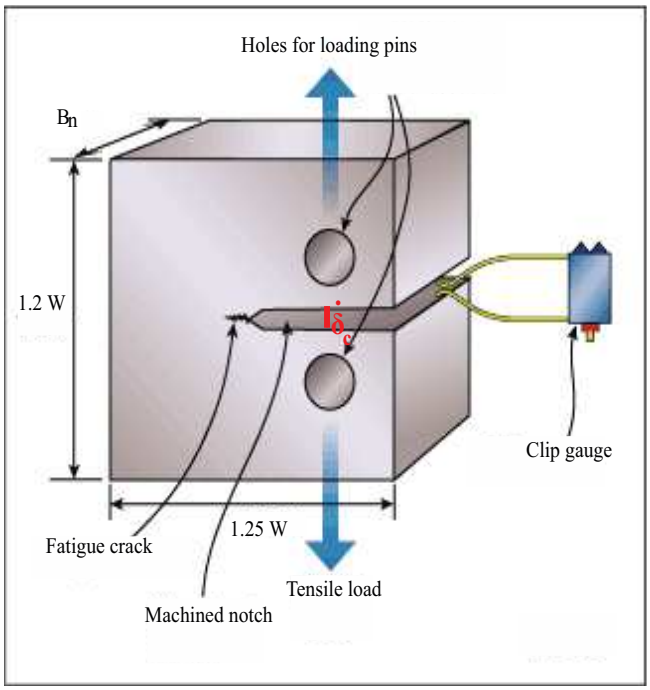

Figure 25: Schematic representation of Compact Tension specimen design.

The creep crack sequence can be separated in three different steps described in Figure 26:

- Incubation: At t < t_i with t_i the time to reach the initiation of crack, the initial crack is blunting and damage develop ahead of crack tip (see Figure 26 a). Data obtained prior to a crack extension δ_a of 0.2 mm are considered to be part of the incubation period and should be excluded for the C^* estimation;
- Initiation: when the Crack Opening Displacement (COD) reaches a critical value δ_i, a short crack of length δ_a resulting from the coalescence of the previous damages appears (see Figure 26 b). At this time, t = t_i;
- Propagation: the crack has formed during the initiation step and its length increases $\delta_a^t > \delta_a^{t_i}$ (see Figure 26 c).

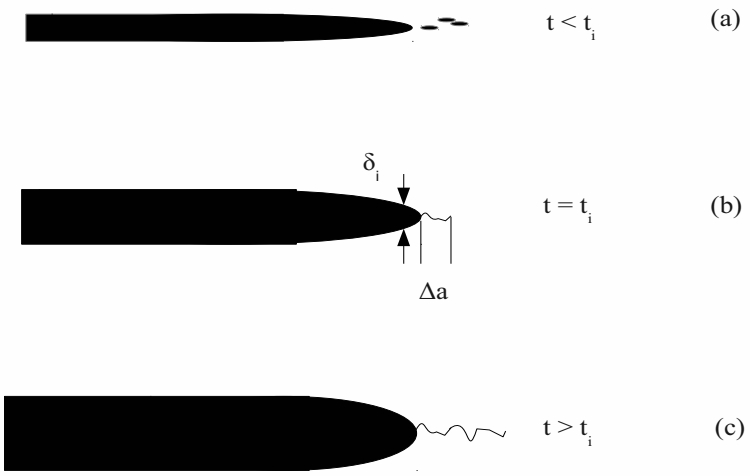

Figure 26: Description of the three steps of creep crack development [3, 4, 83]

Creep crack initiation occurs when reaching a critical local crack tip strain. Prior to the onset of creep cracking, there is an incubation period in which sufficient creep damage develops ahead of the crack starter (in the CT for example) to initiate creep crack extension. Dean *et al.* expressed the incubation time t_i in terms of a critical crack tip opening displacement δ_i or for widespread creep conditions by a relationship of the form [7]:

$$t_i (C^*)^{\beta} = \gamma \tag{1.14}$$

where β and γ are material constants.

The parameter C^* is defined by the standard ASTM-1457-00/01 as:

$$C^* = \int_{\Gamma} \dot{W}(t) \mathrm{d}y - T_i \frac{\partial \dot{U}_i}{\partial x} \mathrm{d}s \tag{1.15}$$

where Γ is a contour around the crack tip, $\dot{W}(t)$ the strain energy density rate, T_i the components of the traction vector and $\dot{U}_i$ are the components of the velocity vector [84, 85].

To achieve the application of a deterministic C^* based approach to a nuclear power plant safety assessment, the CCG behaviour of Type 316H steels has been widely studied [8, 86, 87, 88, 2]. Several tests have been performed on compact tension specimens at 550 °C considering the ASTM E1457-00 (the standard test method for CT testing). The creep crack growth rates have been caracterised using C^* parameter (see Figure 25). C^* can be expressed as [8]:

$$C^* = \frac{n}{n+1} \frac{(P.\dot{\Delta}_C)}{(B_n.(W-a))} \eta \tag{1.16}$$

where n is the exponent in Norton's law, P the applied load, B_n the net specimen thickness (distance between the side grooves), W the specimen width, a the current crack length and $\dot{\Delta}_C$ the creep component of load-line displacement rate (monitored using an extensometer inserted in the machined front face notch of the CT) (see Figure 24). η is given by:

$$\eta = 2 + 0.552(1 - (a/W)) \tag{1.17}$$

$\dot{\Delta}_C$ is given by:

$$\dot{\Delta}_C = \dot{\Delta}_T - (\dot{\Delta}_e + \dot{\Delta}_p) \tag{1.18}$$

with $\dot{\Delta}_T$, $\dot{\Delta}_e$, $\dot{\Delta}_p$ are the total, elastic and plastic load-line displacement rates. The elastic load-line displacement can be expressed with respect of the crack growth rate:

$$\dot{\Delta_e} = \frac{2\dot{a}B_n}{P}\frac{K^2}{E'} \tag{1.19}$$

$$E' = \frac{E}{1-\nu} \text{ for plane strain} \tag{1.20}$$

$$E' = E \text{ for plane stress} \tag{1.21}$$

E is the Young modulus and ν the Poission ratio. An expression of $\dot{\Delta_p}$ is given in [89].

These values can be obtained by considering the load-displacement curve (see Figure 27).

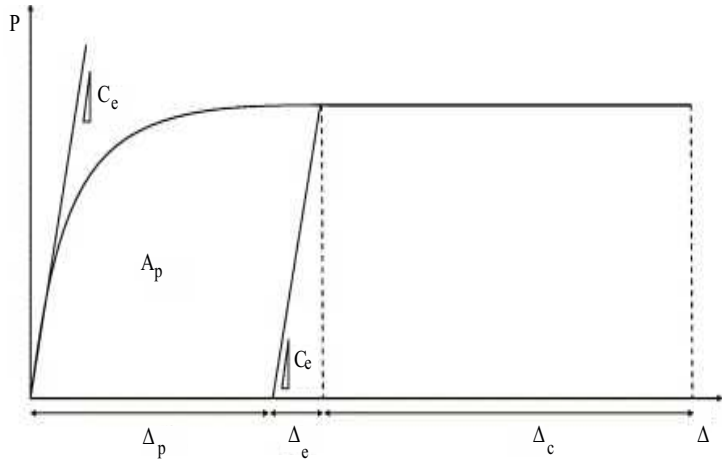

Figure 27: Definition of plastic, elastic and creep displacement respectively denoted Δ_p, Δ_e and Δ_c. A_p is the plastic area under the load-line displacement curve, generated during a constant load creep crack growth test and C_e is the linear elastic compliance function, which is a function of the crack length a [90].

The plastic displacement Δ_p is obtained using the following equations:

$$A_p = \int_0^{\Delta_p} P \, d\Delta_p \tag{1.22}$$

$$\Delta_p = \Delta_T - \Delta_e = \Delta_T - C_e(a)P \tag{1.23}$$

with C_e is the linear elastic compliance function, which is a function of crack length a.

For SENT specimen, C^* can be expressed using the same equation (Equation 1.16) with η = 5.0 ($\frac{a}{W}$) - 0.06 for:

$$0.1 < (\frac{a}{W}) < 0.5 \tag{1.24}$$

$$1 < (\frac{L}{W}) < 3 \tag{1.25}$$

The validity criteria for C^* are regulated by the ASTM E1457-07 [89]. A criterion is that the material must be identified as 'creep-ductile' (true when $\dot{\Delta_C}/\dot{\Delta_T} > 0.5$). The time for 0.2 mm crack extension, $t_{0.2}$ must also be exceeded as it is considered to encompass the transient crack growth region, during which creep damage is building up to a steady state distribution.

A review of the different methods leading to an accurate estimation of C^* has been proposed by Molinie in [91]. Chronologically, Landes and Begley have described C^* with an energetic approach [92]:

$$C^* = -\frac{1}{B}.\frac{\delta \dot{U}}{\delta a} \tag{1.26}$$

with B the specimen thickness and $\dot{U}$ the potential energy rate.

$$\dot{U} = \int_0^{\dot{\Delta}} P d\dot{\Delta} \tag{1.27}$$

where P is the applied load or with if $\dot{\Delta}$ (displacement) constant,

$$\dot{U} = -\int_0^{P} \dot{\Delta} dP \tag{1.28}$$

To calculate C^*, several tests have to be performed to get an accurate estimate.

Then, Harper and Ellison [93, 94] have developed a methodology based on Landes and Begley's work and considering inputs from Nikbin's researches [95]. The analytic expressions depend on the sample geometry and for a CT specimen, the following relationship is derived:

$$C^*_{HE} \cong \frac{(2P\dot{\Delta})}{(B(W-a))} \tag{1.29}$$

with W for width and a for crack length.

Finally, Molinie propose to explore the Kumar and Shih numeric method [91] . It is based on an analogy between C^* and J-integral and on calculations performed by Kumar considering the non-linear elastic case and introduced an hypothesis of crack stationarity. For a CT sample, the expression is:

$$C^*_{KS} = B_2(W-a)\, h_1(\frac{a}{w}, n_2) \left[\frac{P}{(\alpha B(W-a)\alpha_1(\frac{a}{W}))}\right]^{n_2+1} \tag{1.30}$$

$$\alpha = 1.455 \text{ in the plane strain case} \tag{1.31}$$

$$\alpha = 1.072 \text{ in the plane stress case} \tag{1.32}$$

Molinie specifies that $h_1((a/W), n_2)$ is a tabulated fonction and $\alpha_1(a/W)$ is given as [91]:

$$\alpha_1(a/W) = \left[(2(\frac{a}{w}) - a)^2 + 2(2(\frac{a}{w}) - a) + 2\right]^{1/2} - \left[(2(\frac{a}{w}) - a) + 1\right] \tag{1.33}$$

The advantage underlined by Molinie is that the results of C^* don't depend on the scatter in values of $\dot{U}$.

1.3.2 NSW and modified NSW models

Virtual methods for the prediction of creep crack growth (CCG), using finite element analysis (FE), have been implemented. Since finite element CCG rate predictions can be compared to experimental data and to the Nikbin Smith Webster model [95] (NSW) and its modified version (NSW-MOD) which are based on ductility exhaustion argument. These models will be presented in the following sections.

1.3.2.1 The NSW model

This model proposed in the 1980's assumes that a creep process zone r_c exists ahead of the crack tip where creep damage accumulates and that creep damage could be measured in terms of creep ductility exhaustion. The material experiencing creep damage for the first time meets the fracture process zone and the material failure occurs when the creep ductility is exhausted at the crack tip. The steady state creep crack growth rate in the NSW's model is given as [95]:

$$\dot{a}_{CCG} = \frac{(n+1)}{\varepsilon_f^*}\left(\frac{C^*}{I_n}\right)^{(n/n+1)} (Ar_c)^{1/(n+1)} \tag{1.34}$$

where $\varepsilon_f{}^*$ is the critical multiaxial failure strain obtained for a given crack tip stress state and I_n is a parameter only depending on the creep exponent n.

$$\varepsilon_f^* = \varepsilon_f \text{ in plane stress condition} \tag{1.35}$$

$$\varepsilon_f^* = \varepsilon_f/30 \text{ in plane strain condition [96]} \tag{1.36}$$

Yatomi has corroborated the good agreement of this model with CCG rates measured for a wide range of materials [86].

1.3.2.2 The modified NSW model

This new model, named NSW-MOD, is presented in [86]. It takes into account the dependence of creep strain with the crack tip angle θ, the material creep exponent n and the stress state. A Multiaxial Strain Factor (MSF) estimated by a Cocks and Ashby model is added to achieve this new relationship. This parameter takes into account the void growth and coalescence model. The crack growth rate equation is:

$$\dot{a}_{CCG}^{NSW-MOD} = \frac{(n+1)}{\varepsilon_f^*}\left(\frac{C^*}{I_n}\right)^{(n/n+1)} (Ar_c)^{1/(n+1)} \max(\tilde{\sigma}_e^n(\theta,n)/MSF(\theta,n)) \tag{1.37}$$

with σ_m, σ_e which are respectively the mean (hydrostatic) stress and the equivalent (Mises) stress. This two stresses and MSF are dependant of θ and n.

1.3.3 The creep crack growth behavior of type 316H steels

316H material creep crack growth (CCG) at high temperature has been widely studied by researchers to improve the understanding of its cracking behaviour. Mehmanparast, Nikbin, Dean and Davies have contributed to the most recent CCG data at 550 °C available on CT specimens

[90, 86, 12, 87, 97, 88, 98, 99]. The following results have been extracted from their respective work.

In Table 7, we introduce some results from 316H tests from EDF Energy partners. The thermal ageing, the presence of residual stresses and the microstructure influence the CCG.

Material	Upper bound	Mean bound	Lower bound
Weld metal	A = 0.021, q = 0.811	A = 0.005, q = 0.811	A = 0.001, q = 0.811
Heat affected zone metal	A = 0.221, q = 0.891	A = 0.088, q = 0.891	A = 0.035, q = 0.891

Table 7: Comparisons between A and q parameters for weld 316H material and 316H Heat Affected Zone metal (from EDF Energy partners)

By performing comparisons between 316H stainless steel parent and weldment, they have found that creep crack growth rates for the cracks located within the Heat Affected Zone are higher and the initiation times lower than the parent values [90], probably due to the grain size difference. Davies [90] has recorded the creep load line displacement for several CT specimens machined in 316H weldment (see Figure 28). In this work, they have noticed that little crack growth is observed for the first 80 % of the test time. CT1 and CT2 results are indicated with square symbols because the dimensions of these specimens are larger than the standard ones. t_{CCG} refers to the creep crack growth test duration.

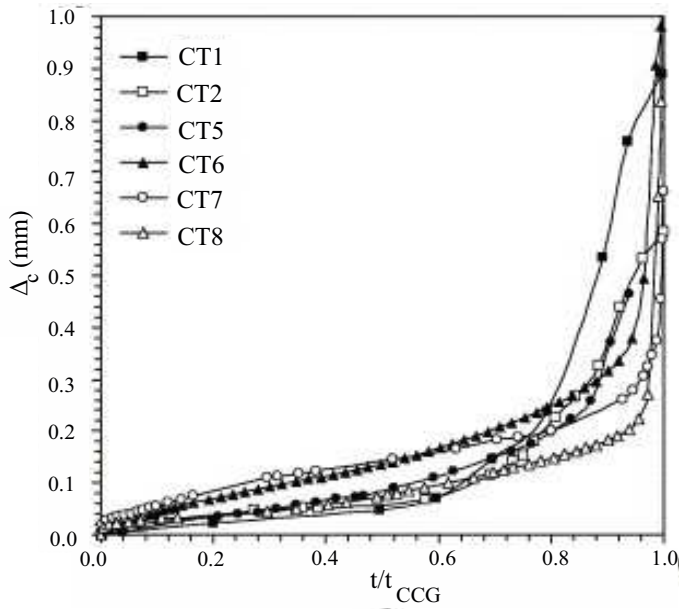

Figure 28: Creep load line displacement (Δ_C) with respect of the normalised time [90].

Dean has summarized all the results obtained from creep crack growth tests performed on 316H from four ex-service components [8]. Creep crack growth tests are often performed during short term period to obtain results within a practicale time scale (< 4,000 h, *i.e.* six months). It means that the load applied to the specimen is much higher than the yield stress leading to

plasticity development. Davies *et al.* has studied long-term tests (> 16,000 h) performed onto 316H CT specimens (denoted C(T)) at 550 °C and have made some comparisons with the previous model NSW-MOD for various specimen geometries (see Figure 29) [12].

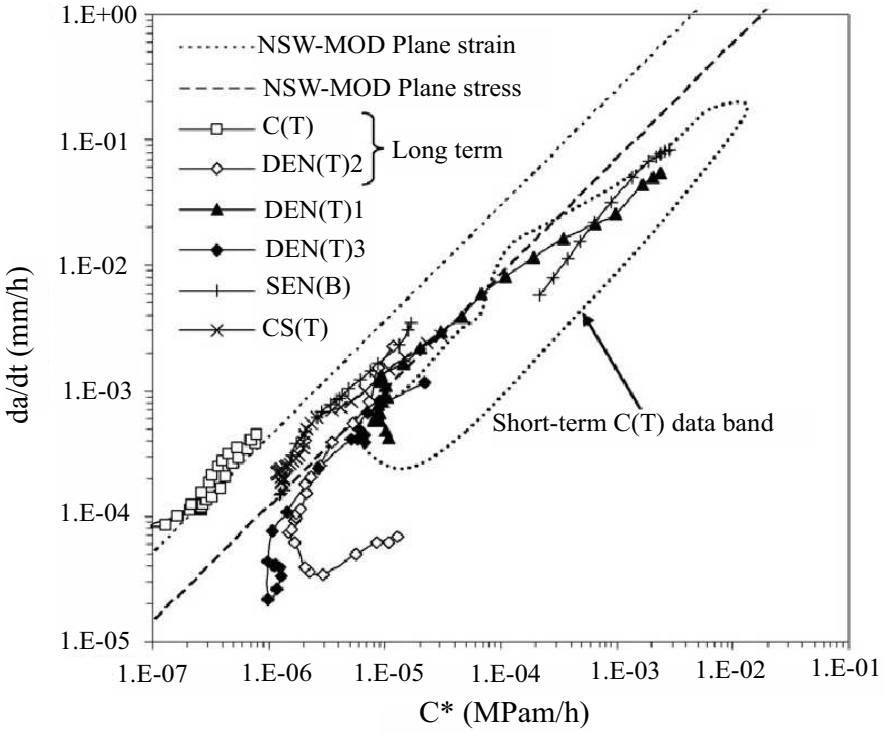

Figure 29: Comparison of creep crack growth rates from short and long-term tests of various specimen geometries with the NSW-MOD model's predictions [12].

The long-term C(T) test data follow the plane strain prediction lines and the CCG is higher compared to the long and short-term tests for a given value of C^*. The creep parameters for the model prediction and the power law are given in Table 8. The creep failure strain ε_f has been obtained by measuring the reduction of area during an uniaxial creep test.

A (stress in MPa, time in h)	n	r_c (μm)	ε_f (%)
$1.56\ 10^{-35}$	11.95	50	21

Table 8: Creep parameters for material 316H steel at 550 °C [12].

Moreover, Dean has observed a change in cracking mode from ductile to brittle intergranular fracture when increasing test duration. At the microscopic scale, the changes can be observed at the grains. In the ductile case, the grains are deformed contrary to the results found studying the brittle fracture surface.

In [90], they have shown that a disctinction can be done with respect of plane stress conditions or plane strain conditions for parameters $\max(\tilde{\sigma}_e^n(\theta,n)/MSF(\theta,n))$ and I_n (see Table 9).

	Plane stress	Plane strain
$\max(\tilde{\sigma}_e^n(\theta,n)/MSF(\theta,n))$	2	10
I_n	3.1	4.4

Table 9: NSW-MOD model values used for 316H parent material at 550 °C [90].

Considering the NSW-MOD model, failure occurs when $(\tilde{\sigma}_e^n(\theta,n)/MSF(\theta,n))$ reaches its maximum value. By performing comparison of the two models with experimental data (type 316H at 550 °C), Yatomi shown that the NSW-MOD solution provides the best estimate of CCG rates over a wide range of C^* parameters examined (see Figure 30).

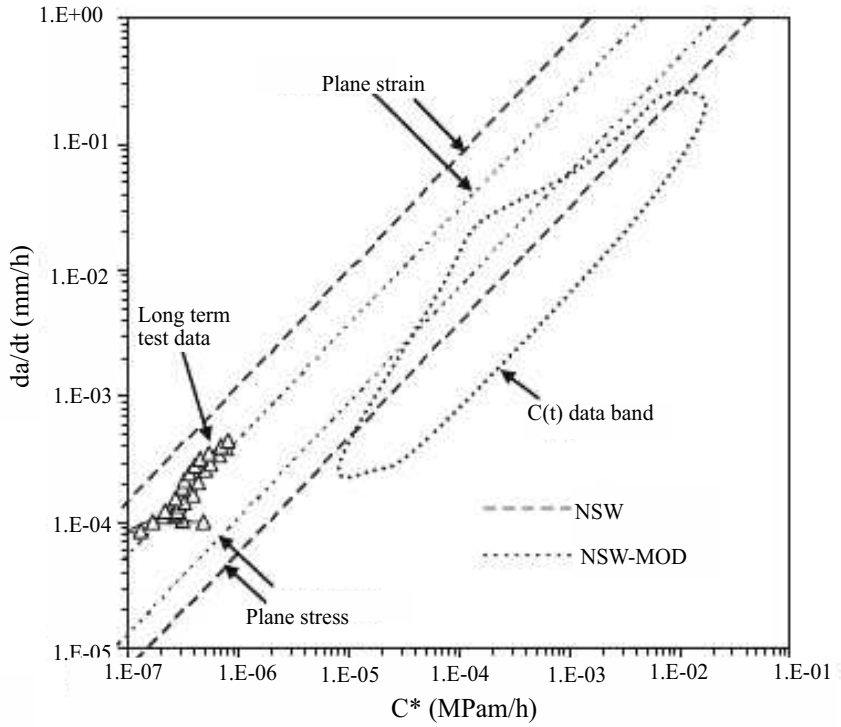

Figure 30: Comparison of NSW and NSW-MOD predictions with experimental data [86].

1.4 Industrial needs and conclusion

The austenitic stainless steel AISI 316H has been commonly used in AGR boilers. Its good corrosion resistance and its particular creep properties make this material suitable to manufacture the components operating in the conditions of the reactor. In view of safe operation engineering, the creep crack initiation and growth needs to be well predicted for 316H components in CO_2 environment. This objective is challenging since the creep fracture is potentially affected by a number of parameters:

- material heterogeneities such as carbide-induced stress heterogeneities,
- microstructure and grain boundary properties,
- effect of carbides at grain boundaries on the grain boundary toughness,
- environment effect and diffusion of elements from the surrounding environment in the material,
- temperature effect,
- stress effect:
  - normal stress to the grain boundaries,
  - stress triaxiality,

To improve the knowledge of creep crack mechanisms in this context, it is proposed to conduct experiments allowing to collect data on crack initiation and growth, with the objective of identifying a creep crack law for an environmentally aged material. Environmental effects on the 316H microstructure have been characterized during this PhD and will be presented in the next chapter.

Chapter 2

Environmental effects on 316H microstructure evolution

In the context of environmentally assisted creep crack growth, the impact of environment on the material behaviour must be studied to better describe the interaction between chemistry and mechanics at the microstructural scale. The as-received material has been aged without being exposed to AGR environment. A preconditioning treatment has been set-up to reproduce a carburized and oxidized condition similar to that observed during operation. The aim of this chapter is to highlight the effects of both carburisation and oxidation on 316H at the microscopical scale and to present the specimen preparation methods, developped to study the carburization effects on creep response.

Contents

2.1 Introduction

This chapter aims at precising the carburized and oxidized condition of the specimens subjected to creep loading during this PhD work. A reference 316H material was provided by EDF Energy. Test specimens from this material have also been subjected to a carburization treatment, mimicking the exposure to an AGR environment. The as-received and carburized materials have been thoroughly characterized to highlight the microstructural effects of both oxidation and carburization.

2.2 Presentation of as-received 316H stainless steel

The material was provided by EDF Energy Generation Ltd. It has been obtained from an ex-service AGR superheater header of about 65 mm wall thickness from Hartlepool power plant (see Figure 31). Hartlepool is located on the North-East coast of England (EDF Energy, Hartlepool power station, Tees Road, Hartlepool TS25 2BZ (see Figure 2)). This site regroups two AGR reactors built between 1969 and 1984.

This component has been in service for 98,704 hours at a typical temperature ranging between 490 and 530 °C. Despite this long service time, the material was not exposed to the AGR gas environment; therefore the service has only led to thermal ageing since stresses were too low for any significant creep deformation or damage [2]. Two different sections of header 1C2/3 from Hartlepool A (HRA) named MT0920/13 and MT0920/14 have been cut (see Figure 31).

The reference given to the material is Cast 55915. The chemical results in Table 10 have been reported by EDF Energy [100, 101]. The mean grain size of this material is 76 $\pm$ 11 µm. These authors have explained the grain size variation by the different thermomechanical histories used during the part manufacturing.

Grade	B	C	Cr	Co	Mn	Mo	Ni	P	Si	S
316H 55915	0.003	0.05	16.9	0.09	1.56	2.26	11.4	0.021	0.49	0.009

Table 10: Chemical contents of 316H Cast 55915 (%wt) [100, 101].

A specimen and material sampling was performed by AMEC to study creep crack initiation and growth in the Cast 55915. A preliminary study has consisted in characterizing the microstructural state of the as-received Grade 316H. This study needed some specific machining at different places to highlight possible material changes with respect to the sampling location in the thickness. The designation of the locations is:

- ES, for External Skin,
- IS, for Internal Skin,
- AC, for At Core;

Combining X-ray fluorescence analysis using AXIOS device (FE Gene) and combustion tests using HORIBA EMIA-920, the chemical compositions in AC, in IS and ES of the header 1C2/3 have been obtained. The results are summarized in Table 11.

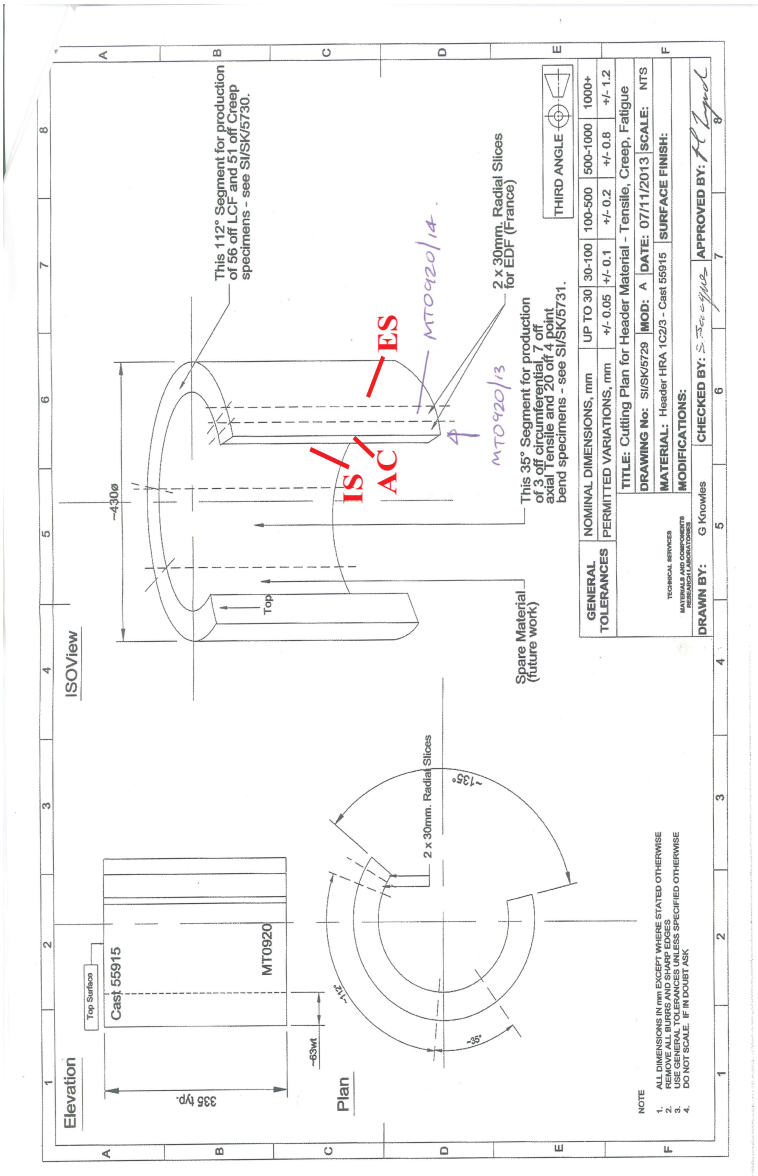

Figure 31: Drawing illustrating the machining of the two slices sent by AMEC.

Element	ES (External Skin)(%wt)	IS (Internal Skin) (%wt)	AC (At Core) (%wt)	AISI 316H (%wt)
C	0.051	0.050	0.051	0.04-0.10
N	0.082	0.080	-	-
O	0.011	0.016	-	-
Si	0.49	0.49	-	<1.0
P	0.019	0.019	-	<0.04
S	0.013	0.013	0.013	<0.03
Ti	0.01	0.01	-	-
Cr	16.8	16.8	-	16.0-18.0
Mn	1.6	1.6	-	<2.0
Fe	Bal.	Bal.	-	Bal.
Co	0.069	0.069	0.051	-
Ni	11.5	11.5	-	10.0-14.0
Mo	2.3	2.3	-	2.0-3.0

Table 11: Chemical contents of 316H as-received in the Header 1C2/3 (%wt).

Before characterizing the mechanical properties of carburized 316H material, it is essential to accurately describe the material microstructure. Several metallographic observations of the 316H material subjected to environmental ageing have been done. Three rombohedral specimens (5 mm x 6 mm x 8 mm) have been machined to study separately the different areas of the AMEC's slices. Specimens were mechanically grounded using abrasive sheets from 9 µm to 1 µm in a Struers' TenuPol-5 instrument. A final treatment relying on chemical attack using oxalic acid (10 %) has been performed to reveal the microstructure.

The microstructure appears as rather heterogeneous (see Figure 32): the smallest grain diameter is of a few microns and the largest one is around a hundred microns. Nevertheless, a similar microstructure morphology is observed in the three different areas. The scatter in the grain size could be due to chemical segregation or to heterogeneous cooling during the manufacturing process of Cast 55915. In the vicinity of the smallest grains, numerous carbides have been found and could be partly responsible for the microstructure heterogeneity. A reasonnable assumption is that these carbides pin the grain boundaries during the initial quench of the material.

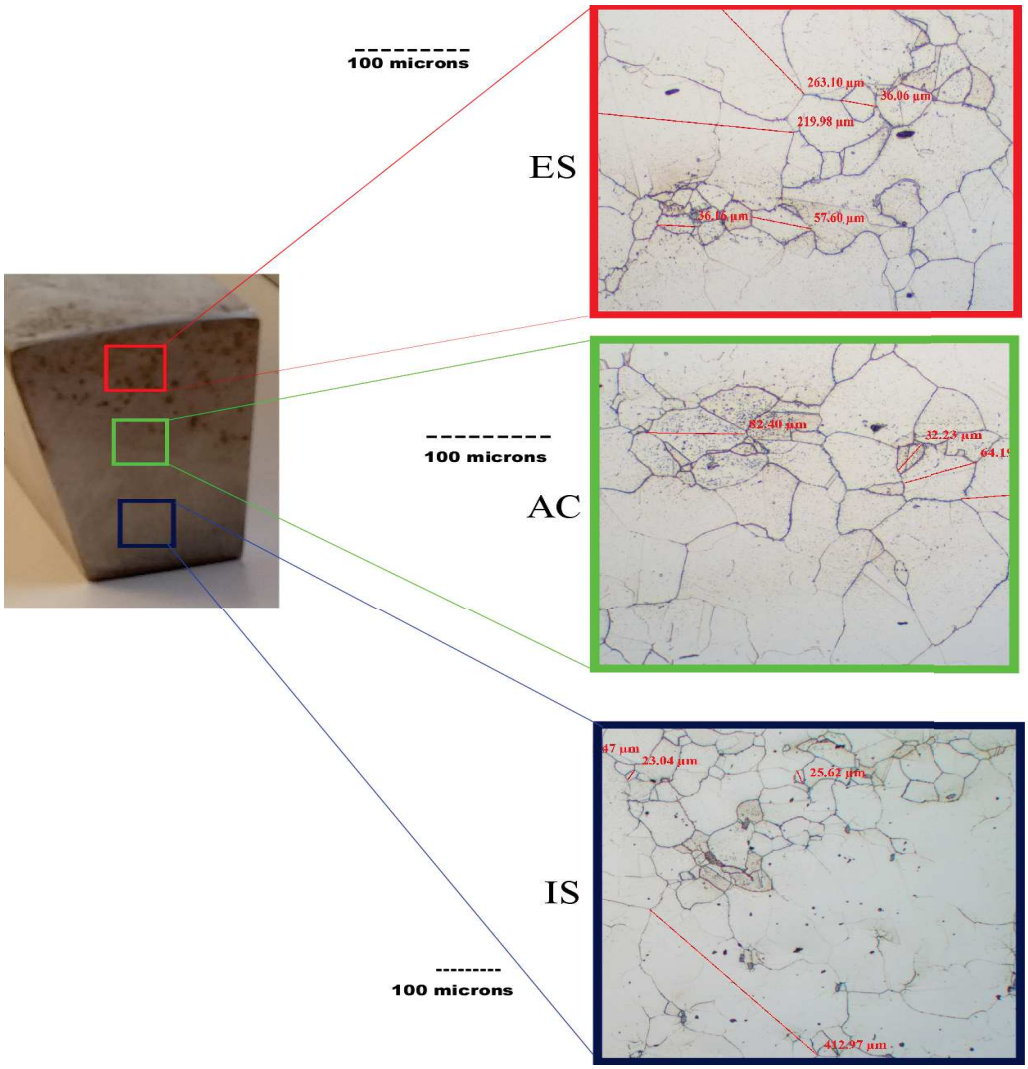

Figure 32: Microstruture in the three areas of the sample (AC/ES/IS).

Due to intergranular aspect of the creep cracking issues, a fine characterization of the as-received 316 H microstructure and its evolution surrounded by oxidizing atmosphere at high temperature is necessary. Several microscopic systems have been used to finely characterize the 316H material received from EDF Energy.

Scanning Electron Microscopy (SEM) was used to evaluate the mean grain size and the crystal misorientations using Electron Back Scattered Diffraction technique (EBSD). This technique requires a fine polishing preparation allowing to remove the hardened layer due to the machining or mechanical polish step. The final step of this preparation relies on an Oxide Polishing Solution (OPS) finish that produces a scratch-free and deformation-free surface. The EBSD maps have been obtained using OIM TSL software.

Comparing the grain size histogram presented in Figure 33 for the external skin (ES) in the three directions, we observe that the grains are larger in the LS direction. It can be attributed to the manufacturing process. The identified mean diameter for this as-received material is around 65 µm, which is consistent with the value found by EDF Energy. The mean grain sizes along the LS direction in the external skin (ES) and in the internal skin (IS) are close but as mentioned above, numerous large grains are found in the external skin. The microstructure reveals numerous Σ_3 twin boundaries (see Figure 32, Figure 33, Figure 34, Figure 35) with a characteristic misorientation angle of 60 °.

After characterizing the microstructure and the chemical content of the as-received Grade 316H, a specific procedure is developped to obtain test specimens allowing to study the creep crack growth in this material. The methodology to get these specimens and the preparation procedure to obtain a material representative of the embrittled carburized 316H in service are presented in the following section 2.3.

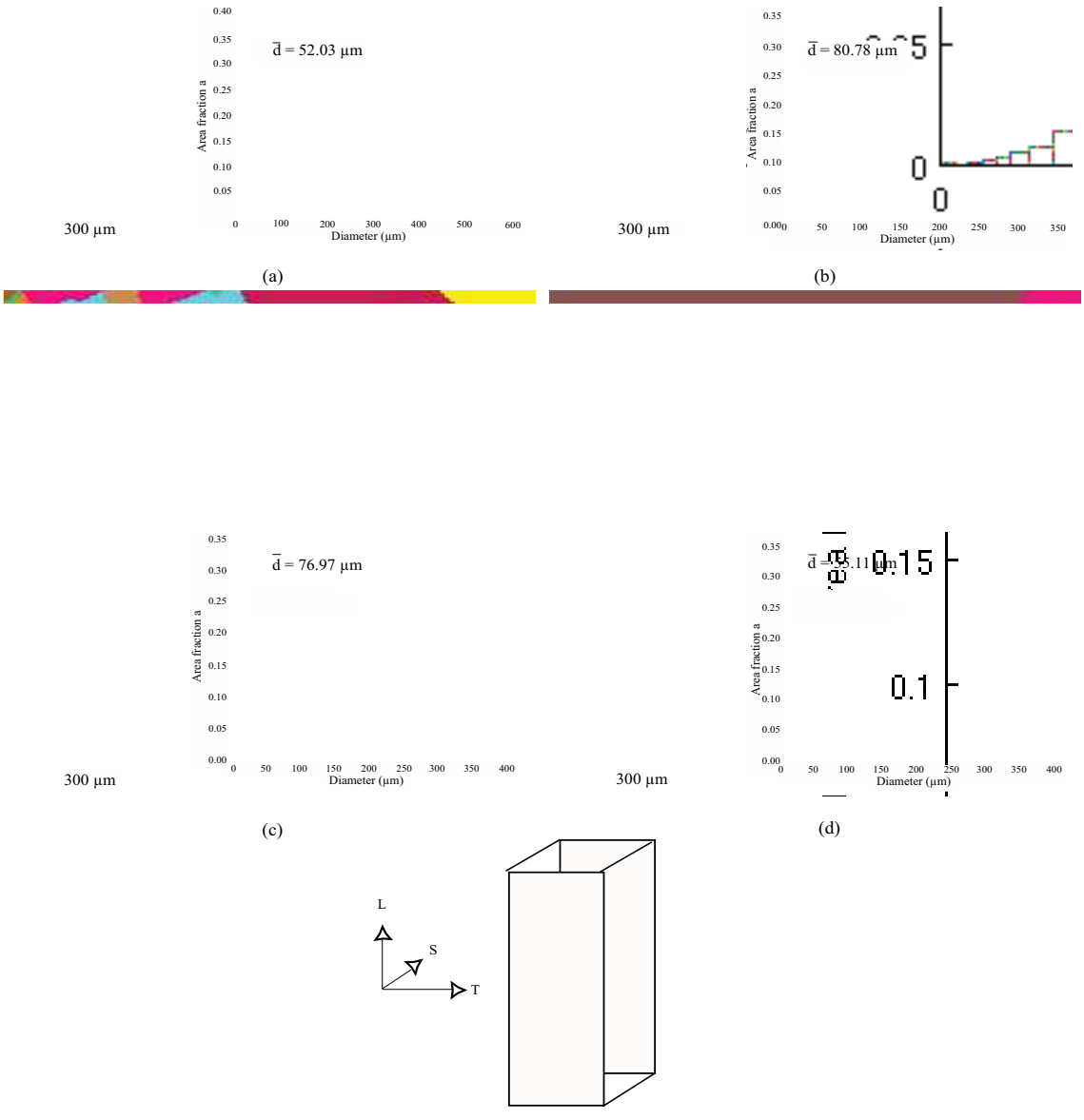

Figure 33: Comparison of microstructure in External Skin (ES) along LS direction (a), TS direction (b), TL direction (c) and in Internal Skin (IS) along TS direction (d).

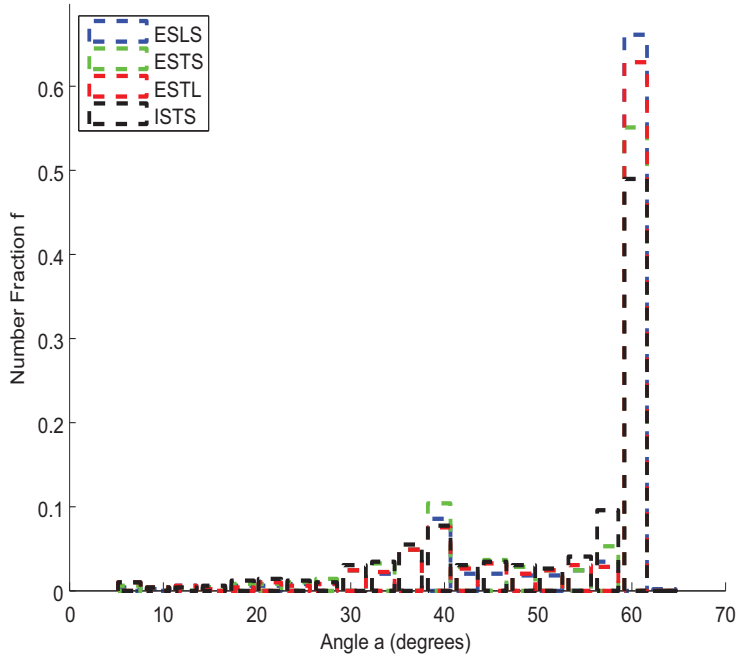

Figure 34: Comparison of misorientations in the external skin and in the internal skin.

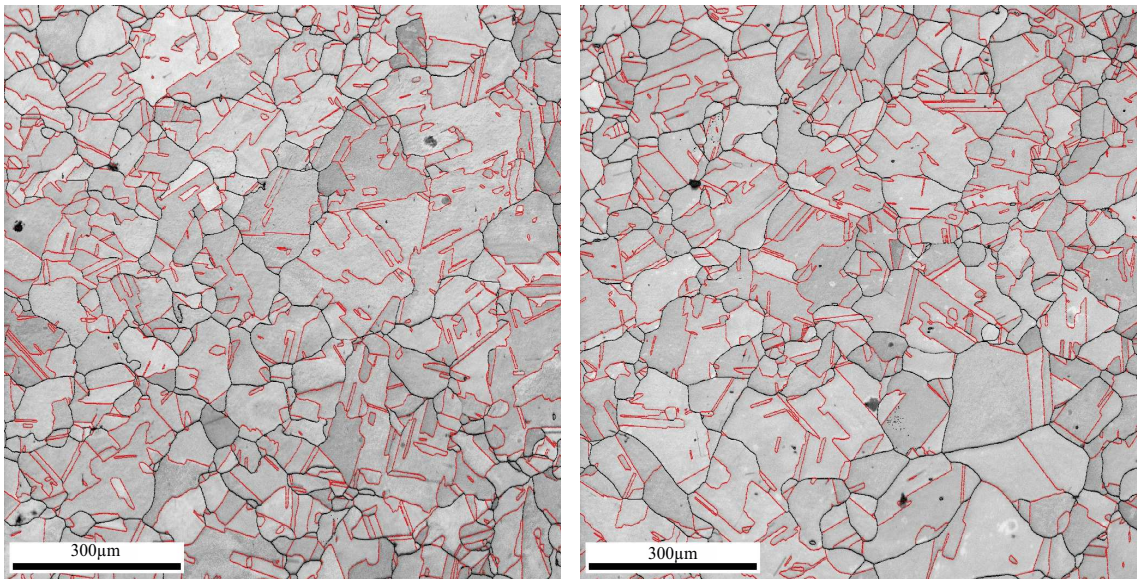

(a) (b)

Figure 35: Representation of twin grain boundaries (red segments) on Index Quality maps for (a) ES along LS direction and (b) ES along TL direction.

2.3 Specimen preparation

2.3.1 Microsized creep specimen preparation

To study crack initiation and propagation at the microscopical scale, we propose to follow the propagation resulting from the stress field induced by a sharp defect. The propagation will be monitored at the scale of few grains using SEM technique coupled with DIC methods on millimetric fields of view. To experimentally obtain a sharp defect, fatique cycles are applied to a CT specimen. These specimens are then cut in a stack of thin slices and the crack location is determined for each slice. Single Edge Notched Tensile (SENT) specimen are then machined in order to precisely locate the crack in the middle of the specimen. The creep loadings are then applied to SENT samples using two microcreep rigs available at EDF Lab Les Renardières. This methodology for obtaining microsized samples and for performing microcreep tests is described in Figure 36.

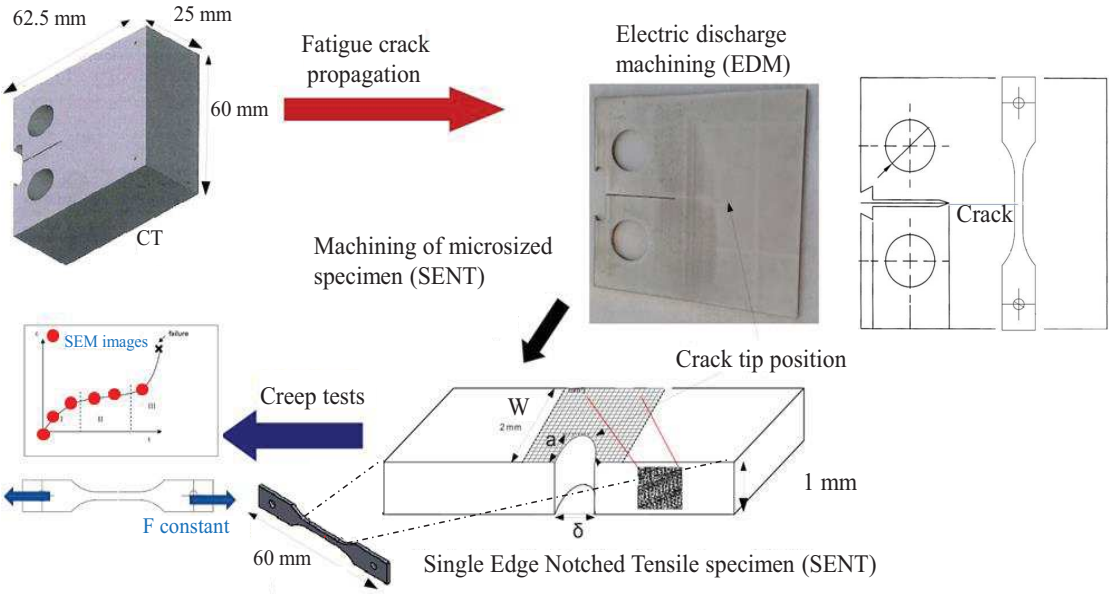

Figure 36: Methodology description for performing creep tests on microsized sample (SENT).

As mentioned above, the preparation starts by CT25 compact tension specimen machining from as-received material. Loading cycles are then applied to the CT25 to propagate a sharp crack from the notch, representative of defects that can potentially nucleate in service. Then, the CT is cut into 1 mm thick slices using Electric Discharge Machining (EDM) and polished up to 4000 SiC paper to allow the crack tip detection from SEM imaging. The SENT are machined so as to locate the crack in the middle of the gauge part with a desired ratio of $a/W = 0.15$, a being the crack length and W being the width of the specimen. The obtained fatigue crack path seems to be mainly intergranular with a few transgranular segments (see Figure 38). In some samples, some bifurcations are visible.

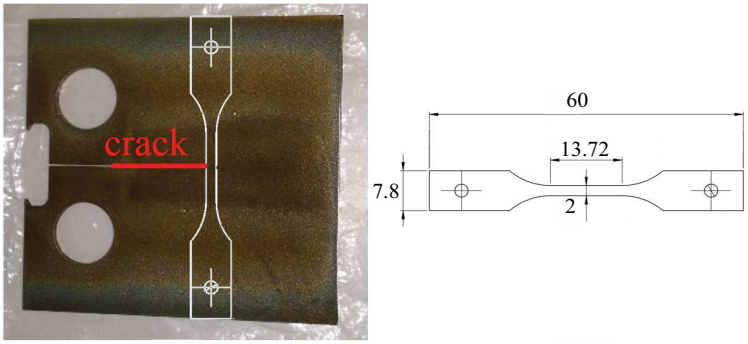

Figure 37: Preliminary machining of pre-cracked CT sample (a) before performing the final EDM of the SENT (b).

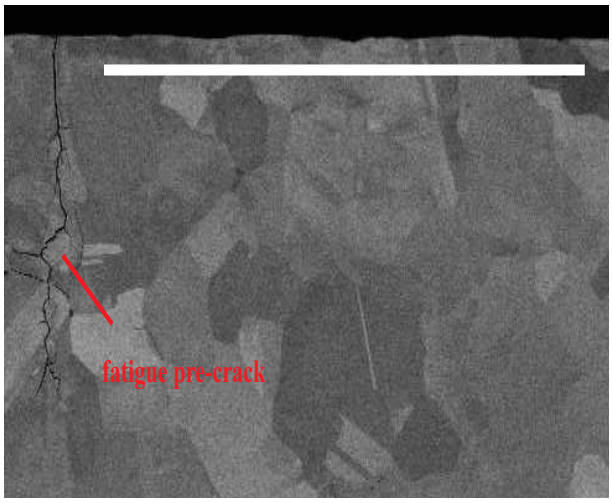

Figure 38: Inter/trans-granular fatigue crack path appears at SENT surface after fine polishing. The scale bar is 500 μm.

2.3.2 The in-service sensitization

Preliminary studies conducted by EDF Energy have led to the conclusion that carburization results in grain boundary embrittlement. This has motivated several research works, as for instance the Oxide Monitoring Scheme (OMS) conducted by Bristol and Manchester Universities [2]. This work is devoted to understanding how carburization develops during service in an AGR environment, for 316H stainless steel exposed to CO_2 gas whose composition is given in Table 12. The gas pressure is constant at 41.3 ± 1 bar.

Element	CH_4	CO	CO_2	H_2	H_20
Content	230 ± 50 vpm	$1 \pm 0.01\%$	Balance	260 ± 50 vpm	400 ± 50 vpm

Table 12: Chemical contents of AGR's gaseous environment (vpm = volume per million) [2].

At room temperature, the oxidation of 316H is very limited (see Figure 39 a) but at high temperature in CO_2 environment, the surface starts to oxidise into Fe_3O_4 and into duplex oxide made of chromium-rich spinel. As soon as the magnetite grows, a chromia-rich layer is formed (Cr_2O_3). It acts as a barrier to diffusion from the gas environment containing carbon and oxygen (see Figure 39 b). When the chromia layer fails, the carbon and oxygen can diffuse from the surface to the bulk material. Duplex oxide layer grows as well as carbide precipitation (see Figure 39 d). When the integrity of chromia layer is guaranteed, the carbon and oxygen use the grain boundary as preferential diffusion path. A faster diffusion along the grain boundaries is expected due to the local disorder. Carbide can be found deeper than the Cr_2O_3 layer (see Figure 39 c). If the chromia spalls from a surface intersecting grain boundaries, the two last phenomena can be combined (see Figure 39 e).

The combined diffusion of carbon and oxygen elements has been highlighted by metallographic studies. Duplex oxide forms in the early stages of carburisation and carbon diffuses from the surface to the bulk material using grain boundaries as preferential path (see Figure 40).

The aged 316H received from EDF Energy, referenced to as "as received material", has not been exposed to carbon containing gas environment. To get a representative material of the embrittled component, an industrial preconditioning treatment has been set-up by EDF Energy with the collaboration of Manchester University. The procedure is described in the following section.

2.3.3 The preconditioning treatment in autoclave

The industrial preconditioning of 316H lab specimens has been performed by AMEC following specifications provided by EDF Energy. Chevalier proposes in [2] to reproduce the carburization process using the following protocol:

1. Increase the surface reactivity (ultra fine polishing leading to deformation-free surface) [102, 103],

2. Control the corrosion environment by confining the specimen in an autoclave,

3. Accelerate the corrosion kinetics by increasing temperature (and pressure).

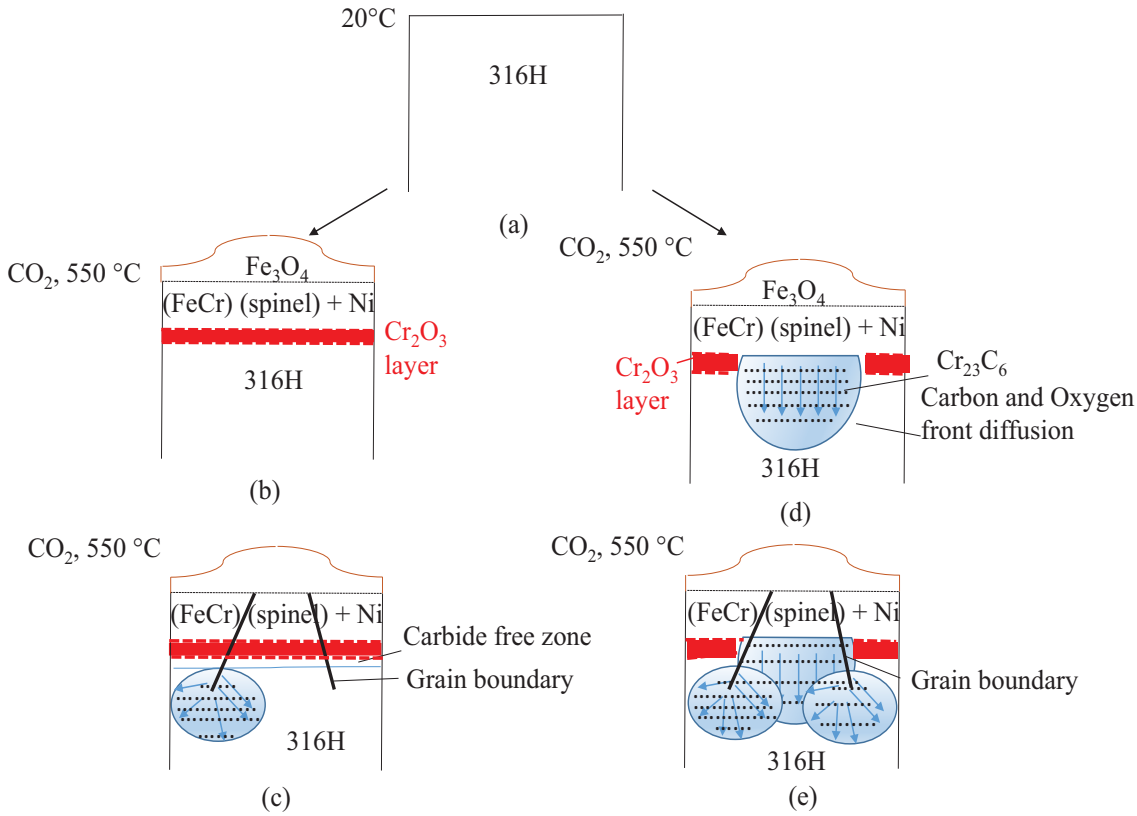

Figure 39: Representation of both oxidation and carburization at 550 °C in CO_2 environment: at room temperature (a), combined diffusion of oxygen and carbon due to Cr_2O_3 layer failure (d) the phenomenon presented in (d) can be coupled with preferential diffusion at grain boundaries (e). If the Cr_2O_3 is formed, no oxidation and carburization generally occur (b) but the grain boundary presence can generate carburization or oxidation deeper as the grain boundaries act as preferential path for oxygan and carbon elements (c).

The depth of carburized layer is related to chemical interactions between surface and gas environment and thus mainly depends on the gas composition and the surface preparation. The University of Manchester focused on determining how modification of gas composition and of material conditions at the surface play a role in the rate and extent of carburisation. For instance, elevating H_2O and/or CO contents may accelerate the carburisation process. A review of gas chemistry effects on oxidation and carburisation was proposed by Lloyd [104].

In order to be as representative as possible and to obtain a reasonable carburization time, OPS polishing has been performed followed by an exposure at 600 °C using the gas composition of AGR reactor (see Table 12). In these conditions, 2,000 hours treatment were required to get about 100 µm of "carburized material" at the surface of creep and fatigue specimens (see Figure 41).

For the specimen used in this study, the sample surface preparation was performed on Rotopol-31/RotoForce 4 from Struers with abbrasive SiC paper and sheet from 6 µm to OPS finish (see Table 13). The polishing of the specimens may introduce bending or twisting due to their small

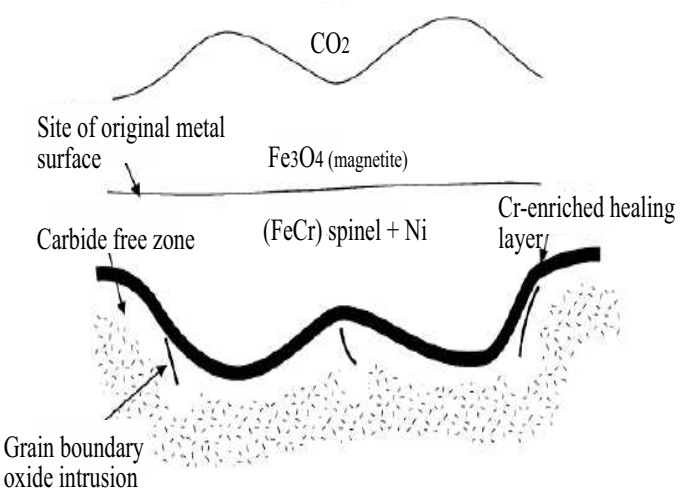

Figure 40: Both oxidation and carburisation develop at high temperature in CO_2 environment [2].

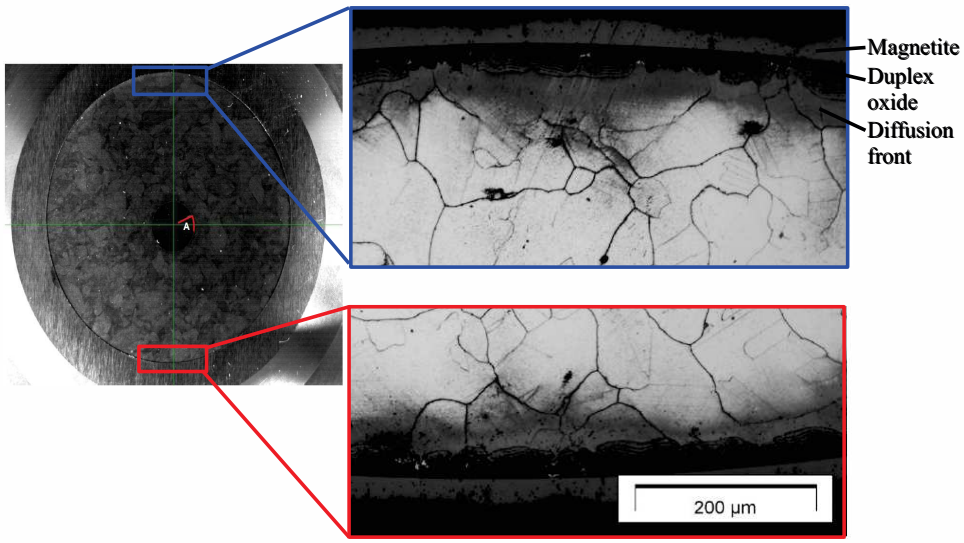

Figure 41: Influence of the preconditioning treatment on the microstructure of a round bar 316H specimen [100].

width and thickness. In order to limit these risks, it has been decided to polish only one face of the specimen. Consequently, a slight bending is generated during the preconditioning process due to the development of residual stresses induced by the oxide growth on the activated surface. It has been shown that unnotched flat dogbone samples polished on both faces do not exhibit this

bending (see Figure 42).

N °	Paper type	Lubricant	Time (minutes)	Load (N)	Rpm
1	SiC-paper 320	Water	3	15	150
2	SiC-paper 500	Water	2	15	150
3	SiC-paper 800	Water	2	15	150
4	SiC-paper 1000	Water	2,5	15	150
5	SiC-paper 1200	Water	2	15	150
6	SiC-paper 2400	Water	4	15	150
7	SiC-paper 4000	Water	4	15	150
8	MD-FLOC 6 µm	DP-Lubricant	3	10	100
9	MD-MOL 3 µm	DP-Lubricant	8	10	100
10	MD-NAP 1 µm	DP-Lubricant	10	10	100
11	MD-NAP 1/4 µm	DP-Lubricant	3	15	100
12	MD-CHEM 0.02 µm	OPS	30	5-7.5	20-30

Table 13: Polishing programm for SENT design.

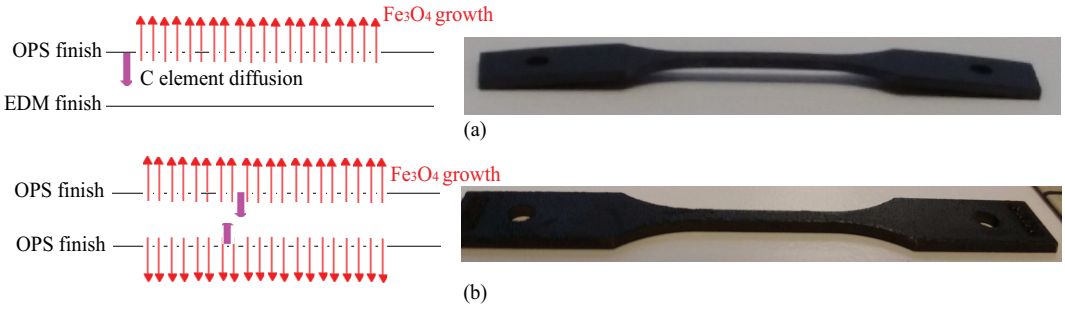

Figure 42: Asymmetrical surface preparation has led to asymmetrical oxide growth and residual stresses apparition (a). Conversely, a symmetrical preparation allows a homogeneous oxide growth on both sides (b).

2.3.4 Validation of the preconditioning treatment

The precise determination of the carburized zone thickness is not easy to achieve because of the carbide small dimensions. Consequently, the validation of the carburization treatment was performed by comparing the hardness profiles on ex-service components (submitted to the real carburization process) and the preconditioned samples. Considering that hardness variations are only attributed to material carburization is a rather rough approximation since surface effects like machining or grinding can also increase hardness. Chevalier reports that in the uncracked carburized sections, hardness typically reached values up to 300Hv whereas the bulk hardness was around 180Hv [100]. He defined the carburized zone as the region of increased hardness, typically 300-500 µm from the surface. In the cracked regions, hardness can reach 600Hv and he associated

this hardness increase to the carburization process. After the carburization treatment, our preconditioned samples showed a 200 µm penetration and a 600Hv peak hardness. These values are consistent with the ones obtained for ex-service samples (300-500 µm depth with a 300-600Hv after 50,000 hours of service).

The microhardness indents were post-processed using the commercial software of the microindenter and a manual monitoring performed on SEM observations (see Figure 43). In Figure 44, the peak hardness reaches 600Hv in the preconditioned sample.

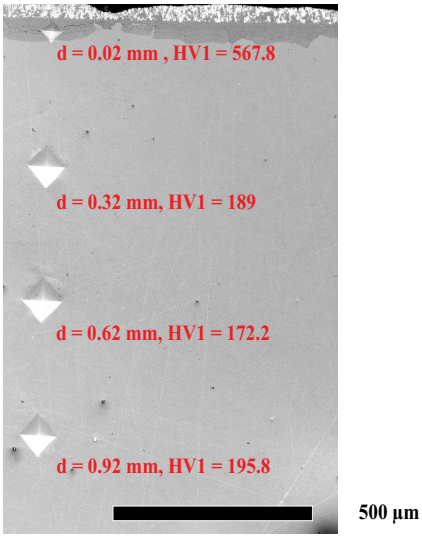

Figure 43: SEM image in BSE mode (Z contrast) of sample after 2,000 h of preconditioning exposure time. The scale bar is 500 µm.

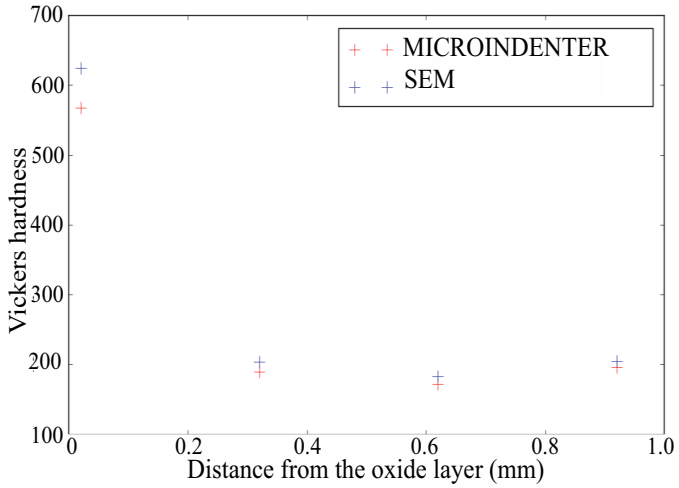

Figure 44: Vickers hardness profile through a cross section in preconditioned sample after 2,000 h exposure time at 600 °C.

2.4 Chemical study of carburisation on 316H aged

2.4.1 Chemical characterization

The chemical study has been performed on the as-received material using the microscopy facilities available at EDF Lab Les Renardières. An Electron Probe MicroAnalyser (EPMA), an Energy-Dispersive Spectrum (EDS) technique using SEM and Transmission Electron Microscopy (TEM) have been used to obtain chemical cartographies of preconditioned samples. The resolution of SEM techniques was about 1 μm^3.

After a polishing preparation up to paper SiC 400 µm and alumina polishing solution, the different layers resulting from oxidising treatment have been identified. In agreement with Chevalier (see Figure 40, Figure 41), two distinct areas corresponding to magnetite (Fe_3O_4) and duplex oxide layers have been observed. Imagings with a low current and a very small beam interaction zone have highlighted the carbon and oxygen diffusion fronts (see Figure 45). Hereafter, the duplex oxide layer will be named "Layer I" and the underlying area embedding the diffusion front will be denominated "Layer II". The thickness of the magnetite layer ("Layer 0") is about 50 µm and the layer I thickness is ranging between 50 and 60 µm. The diffusion front thickness is not uniform and can reach 200 µm in thickness.

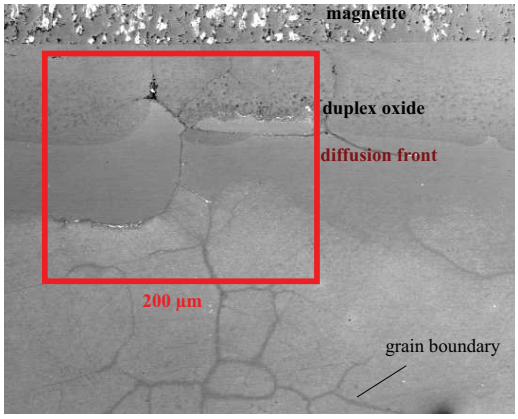

Figure 45: SEM image in SE mode using a very small beam current (5.5 nA) highlights the formation of several areas resulting from the simulated carburisation.

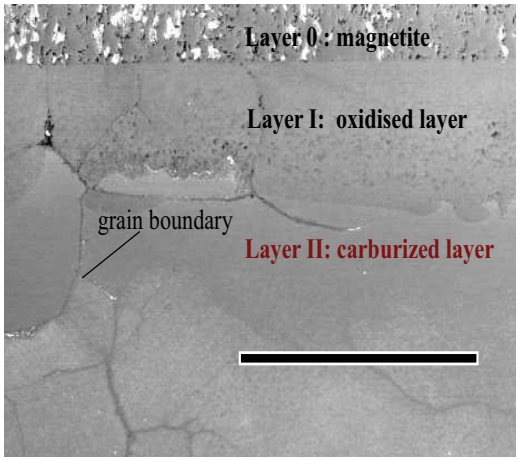

Figure 46: SEM image in SE mode using a very small beam current (5.5 nA) highlights the formation of several areas resulting from the simulated carburisation: layer 0, layer I and layer II. The scale is 100 µm.

Chemical analyses have been carried out in each layer to characterize the chemical content and to highlight the diffusion of chemical species responsible for intergranular cracking. The results will be presented layer by layer. Figure 46 illustrates the different layers resulting from the carburization process. Layer 0 refers to the magnetite. This layer is well characterized [105, 106, 107, 108, 109]. Its structure doesn't contain any carbide and thus, was not investigated further. Layer I corresponds to oxidised layer. Layer II refers to the carburized zone.

2.4.2 The oxidised layer: layer I

In order to get an overall estimation of the chemical composition of the material in the oxidised layer, EPMA analyses are made by coupling a SEM with an Wavelength-Dispersive X-Ray Spectroscopy (WDS). A wavelength-dispersive spectrometer uses the characteristic X-rays generated by individual elements to enable quantitative analyses and to create element composition maps. The spatial resolution of these techniques gives access to 50 µm width observation fields. As a consequence, the observed fields show the oxidised layer and a small part of the carburized zone (see Figure 47). A match between chromium (see Figure 48 b) and oxygen (see Figure 48 c) chemical maps can be found, that is an indication of chromium oxide presence. The lack of agreement between carbon and chromium suggests a less significant chromium carbide presence.

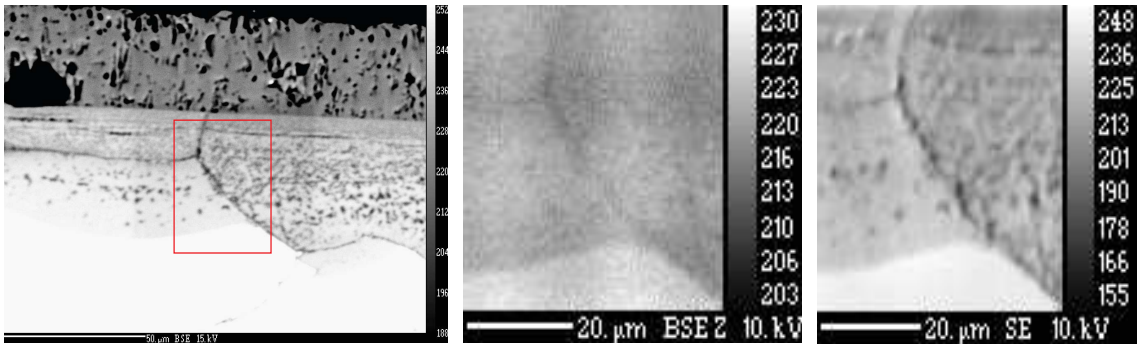

(a) (b) (c)

Figure 47: Zone Of Interest at the interface between the layer I and the layer II (a) in SE mode, (b) in BSE mode and (c) using EPMA.

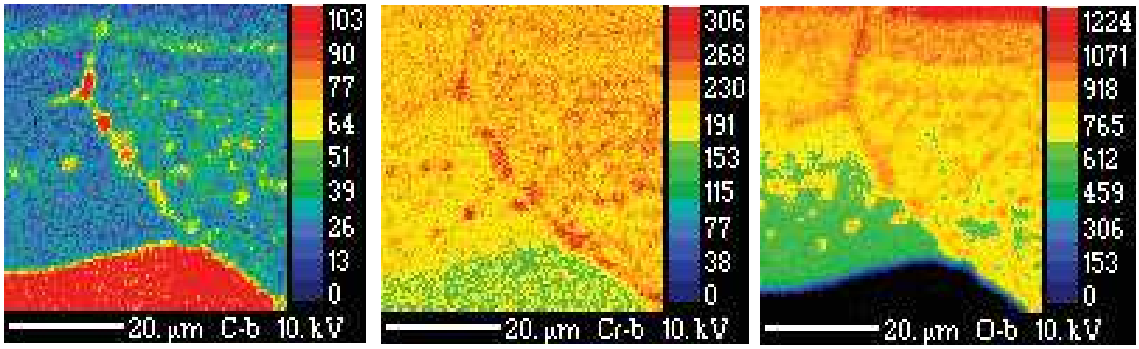

(a) (b) (c)

Figure 48: Chemical maps for the same ZOI as in Figure 47 b, Figure 47 c: Carbon elements (a), Chromium elements (b) Oxygen elements (c) using EPMA.

These results were confirmed using EDS mode from the SEM FEI Quanta 600. The EDS detector is used to separate the characteristic X-rays of different elements into an energy spectrum and to find the chemical composition of materials down to a spot size of a few microns and to create element composition maps. The preconditioned 316H material exhibits a slight increase of chromium and nickel contents in the layer I. These chemical contents are given in Table 14.

	C	O	Si	Cr	Fe	Ni	Mo
Layer I close to Layer 0	1.93	18.18	0.63	23.05	37.64	15.34	3.24
Layer I close to Layer II	2.2	17.68	0.68	22.32	36.05	17.72	3.34
Layer II	-	0	0.53	17.74	65.54	11.91	2.51

Table 14: Chemical compositions obtained by EDS in the layer I and the layer II regions (% wt).

The layer I is also extremely rich in oxygen elements. Some manganese sulfide (MnS) precipitates are also present and have been detected using EDS technique. With this technique, the confidence in results for carbon content is also limited by the possible contamination of the sample surface. Nevertheless, the oxidised region contains less carbon elements than the carburized layer.

The EDS/EPMA chemical resolution is not sufficient to highlight chromium carbide presence in the material. So we used Transmission Element microscopy (TEM) to investigate the precipitation of $Cr_{23}C_6$. The resolution of this technique using available TEM (about 1×0.1 µm) is higher than the one of EDS/EPMA technique. As an example, this technique has already been used in the field of stress corrosion cracking to study the influence of oxidation in the alloy 182 and 82 [110] and more recently in alloy 600 for PWR issues [111]. To produce a sample thin enough to allow electronic transmission, a Focused Ion Beam (FIB) Helios SEM has been used (see Figure 49). The ion beam is used to locally remove material: the sample has been prepared using a multi-pass scanning in order to get the required precision on its dimensions. A platinium deposition was performed on the sample before cutting to protect the surface from the ion beam detrimental effects (grain deformation) (see Figure 49 b). The chosen area is located at the grain boundary interface in the layer I (see Figure 49 a) to highlight possible chemical gradients in the vicinity of the grain boundary that would suggest the role of the interface in the carbon and oxygen diffusion.

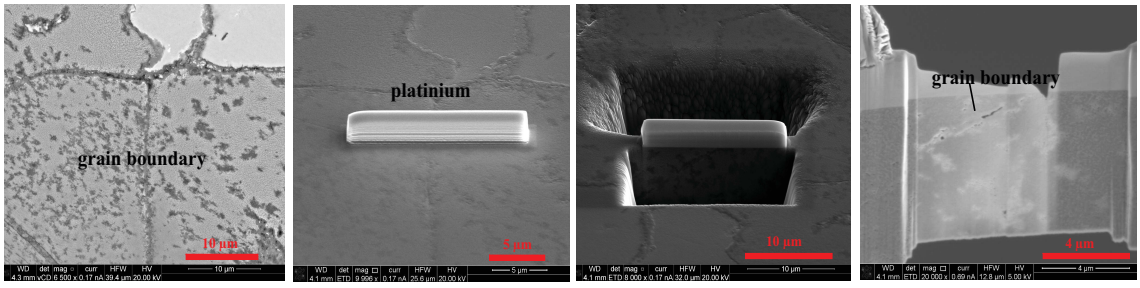

(a) (b) (c) (d)

Figure 49: An area containing a grain boundary in the layer I is chosen (a). A platinium layer is deposited to protect the surface for ion beam (b). Then, successive cuts are performed using the ion beam of FIB (c) to extract a thin sample convenient for TEM imaging (d).

At the end of the thin slice preparation, the specimen is about one hundred nanometers thick. Due to the grain boundary presence as well as the porosity, the sample cracked during the preparation (see Figure 50). Nevertheless, one of the specimen remaining sections has been observed using TEM TECNAI Osiris in Scanning Transmission Electron Microscopy (STEM) mode providing elementary composition and crystal information at atomic scale. The STEM works on the same principle as a normal SEM by focusing an electron beam into a very small spot which is scanned over the sample. This electron beam interacts with the sample and the transmitted beam

is collected by a detector. In Figure 50, the Region Of Interest (ROI) is observed with an High Angle Annular Dark Field (HAADF) detector which provides a dark rendering of dense areas.

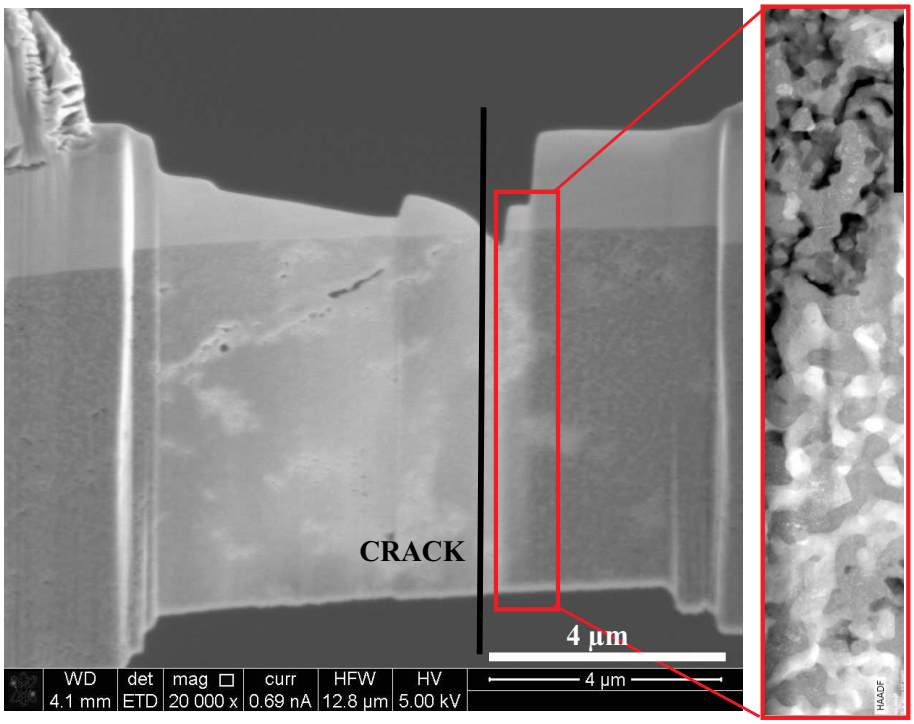

Figure 50: SEM image of the thin sample in SE mode before its failure and TEM observations of a 1 µm x 4 µm zone. The black scale bar of the TEM image is 1 µm.

The chemical maps provided in Figure 51 highlight the enrichment in oxygen elements and the FeCr spinel duplex oxide with nickel presence which are characteristic of oxidation at high temperature. Here again, only traces of carbon have been found and they were attributed to contamination arising during specimen preparation and microscopy.

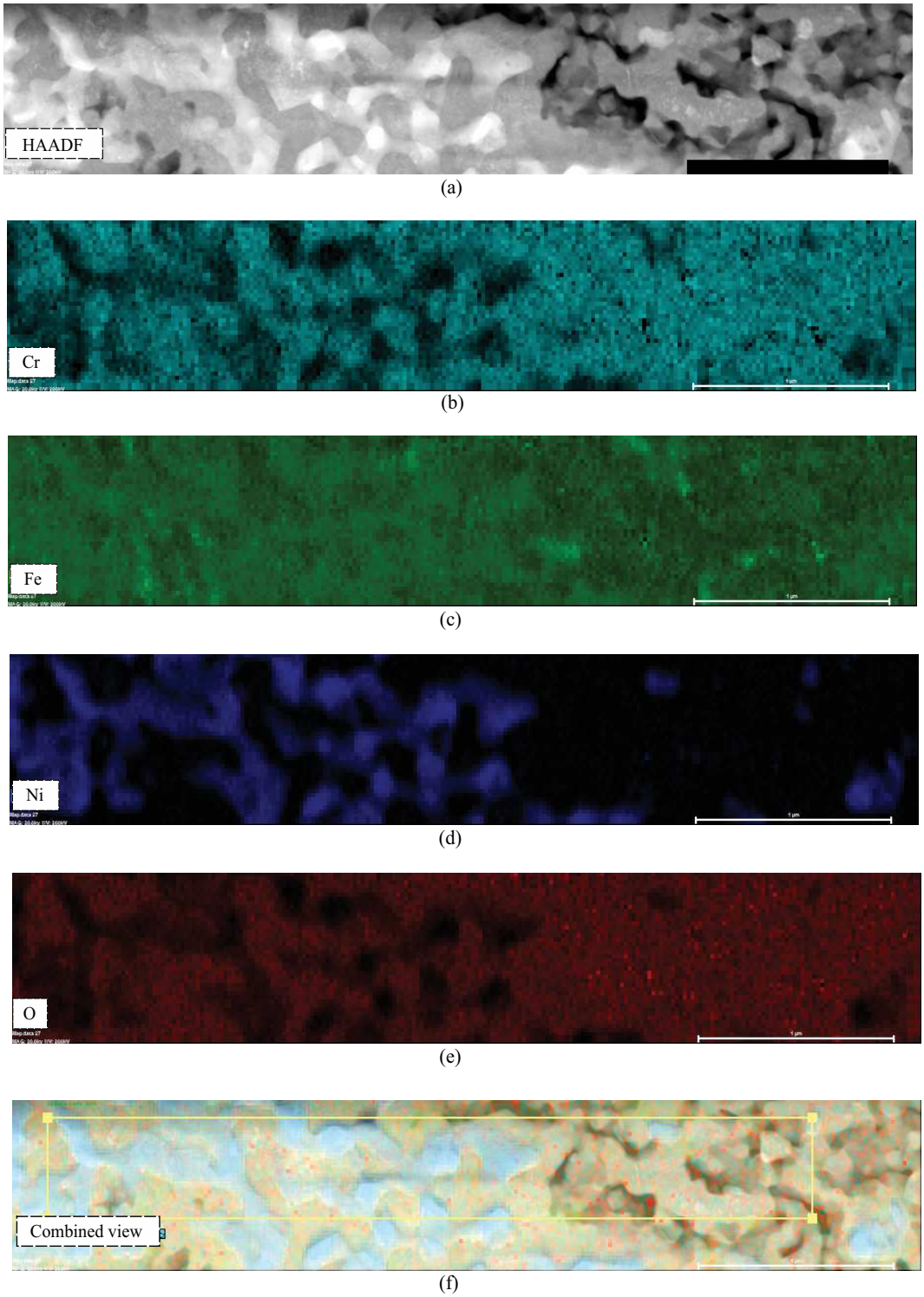

Figure 51: Image in HAADF mode of the ROI (a) and the chemical maps of Chromium (b), Iron (c), Nickel (d), Oxygen (e). A combined representation of the above maps is proposed in (f).

2.4.3 The carburized layer: layer II

No carbide precipitation has been found in layer I. Both carbon and oxygen elements may have diffused deeper in the material using the grain boundaries as preferential paths. A new thin sample embedding a grain boundary has been machined in the layer II at the interface of layer II and 316H base material (see Figure 52). The grain boundary appears as a thick layer (>1 µm) in which a high amount of porosities/cavities is observed. Nevertheless, the structure in the grain boundary vicinity seems to be stronger than in layer I and the sample hasn't failed during the FIB preparation.

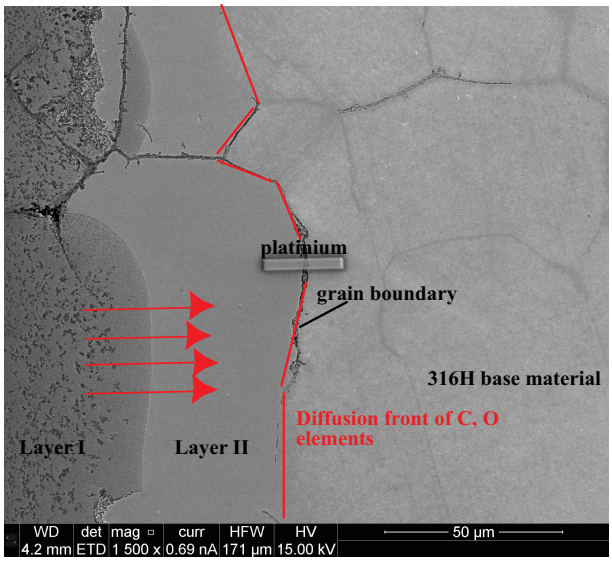

(a)

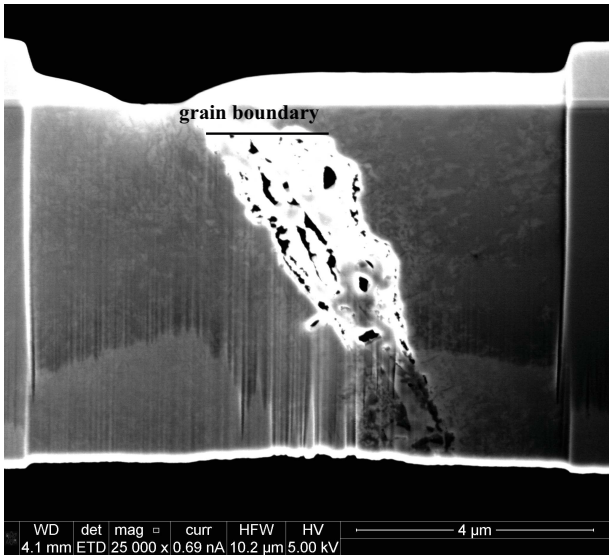

(b)

Figure 52: SEM image of the chosen Region of Interest (a) for thin sample extraction using FIB (b). The grain boundary is located close to the identified diffusion front of carbon and oxygen elements. The grain boundary is thick (> 1 µm) and contains porosity/cavities.

The TEM observations using the HAADF mode have revealed the presence of elongated structures of about 200 nm in length and a few nanometers in width (see Figure 53).

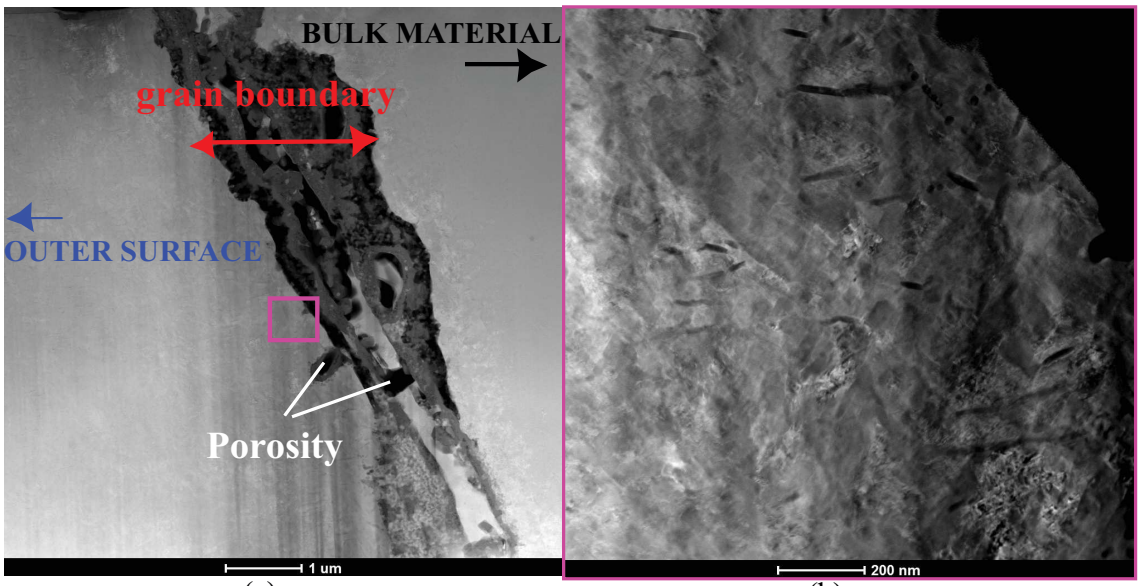

Figure 53: SEM image in HAADF mode of the thin sample extracted at the interface between the layer II and the 316H substrat (a). Expanded view shows the grain boundary vicinity and numerous long and thin structures (b).

Chemical analyses have been performed in the vicinity of the grain boundary in order to better understand the path diffusion of additional elements in the material resulting from oxidizing environment at high temperature. The grain boundary acts as a preferential path for the carbon and oxygen elements, which have been coroborated by the correponding cartographies presented in Figure 54 and Figure 55. A correspondance between chromium and carbon maps has highlighted that these elongated structures should be carbide precipitates (see Figure 54 and Figure 55). Several of them have been found on the left side of the grain boundary towards the environmentally exposed side. Fewer of them have been found on the right side of the grain boundary in the bulk material direction. This observation highlights the key role played by the grain boundary in the carbon and oxygen diffusion process, as well as the precipitation heterogeneity resulting from oxidizing environment at high temperature.

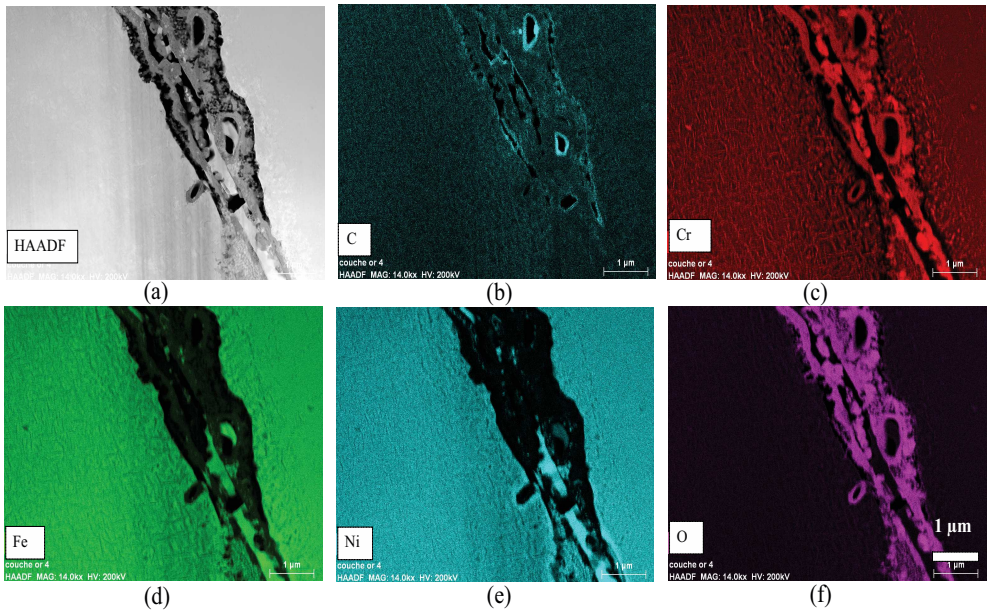

Figure 54: SEM image in HAADF mode of the Region of Interest close to the grain boundary (a). The chemical maps of Carbon (b), Chromium (c), Oxygen (f) are in good agreement with a combined diffusion of oxygen and carbon along the grain boundary path. A correlation between iron and nickel can be observed between subplots (d) and (e).

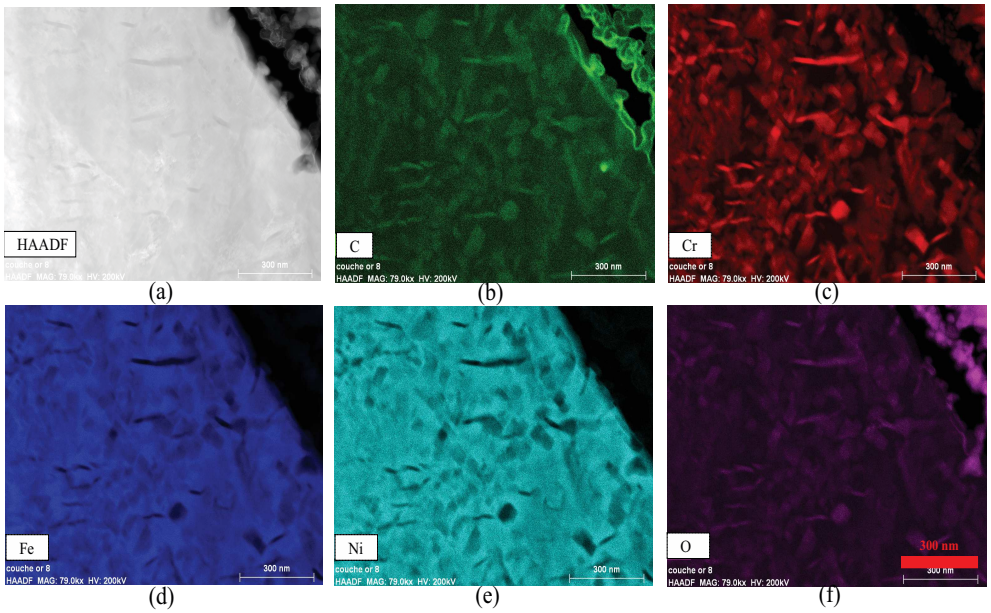

Figure 55: The chemical maps performed in the area shown in Figure 53 b show Carbon (b) and Chromium (c) concentration, as an evidence that the thin structures are carbide precipitates. The red scale bar is 300 nm.

2.4.4 Conclusion about chemical effects generated by carburization

The 2,000 hours preconditiong treatment has led to the formation of three successive layers (0, I, II respectively from the outside to the bulk material).

Layer 0: magnetite Fe_3O_4

During the treatment, a superficial layer made of magnetite (Fe_3O_4) has grown from the initial surface. The thickness of this layer is about 50 µm and is non uniform due to crystallographic orientation dependance (see Figure 41 and Figure 45). Its structure is rather porous suggesting weak mechanical properties.

Layer I: (FeCr) spinel and Nickel

Preconditioning led to carbon and oxygen diffusion from the surface to the bulk material. Only oxygen atoms reacted with the metallic elements to create FeCr spinel and enriched nickel zones corresponding to the duplex oxide layer formation. The chemical analyses have not shown the presence of carbon element or carbide precipitation in this zone.

Layer II: enriched with $Cr_{23}C_6$

Using low beam current SEM imagings, the diffusion front of carbon and oxygen has been identified. In this region, a thin sample has been machined using FIB technique. Numerous carbides of ellipsoidal morphologies have been found. The chemical maps suggest a dispersed carbide precipitation from grain boundary to the grain center.

2.5 Surface modifications due to oxidation in Type 316 in air at 550 °C

The preconditioned SENT samples are prepared in view of being submitted to high temperature (550 °C) creep loading in oxidising gas environment (air). It is expected in these conditions that sample surface will react with the surrounding gas. Oxygen and carbon elements continue to diffuse in the material and the oxide layer will grow at the surface.

DIC has been chosen to perform fine measurements of kinematic fields around the crack tip during the mechanical loading. The oxidation may generate significative surface modifications that would be detrimental to kinematic measurements. As an example, Touboul has shown that at 625 °C even in vacuum, oxide could be responsible for pattern deterioration (see Figure 56 a) [68].

He showed that after 500 h of creep test under a loading of 60 MPa, some cracks appeared perpendicularly to the loading axis disturbing the kinematic fields measurements for a few level of deformation (see Figure 56 c). After three months in high vacuum (10^{-7} bar), the tungsten pattern was completely covered up by an oxide (see Figure 56 b) (50 µm) preventing any measurement from the reference state.

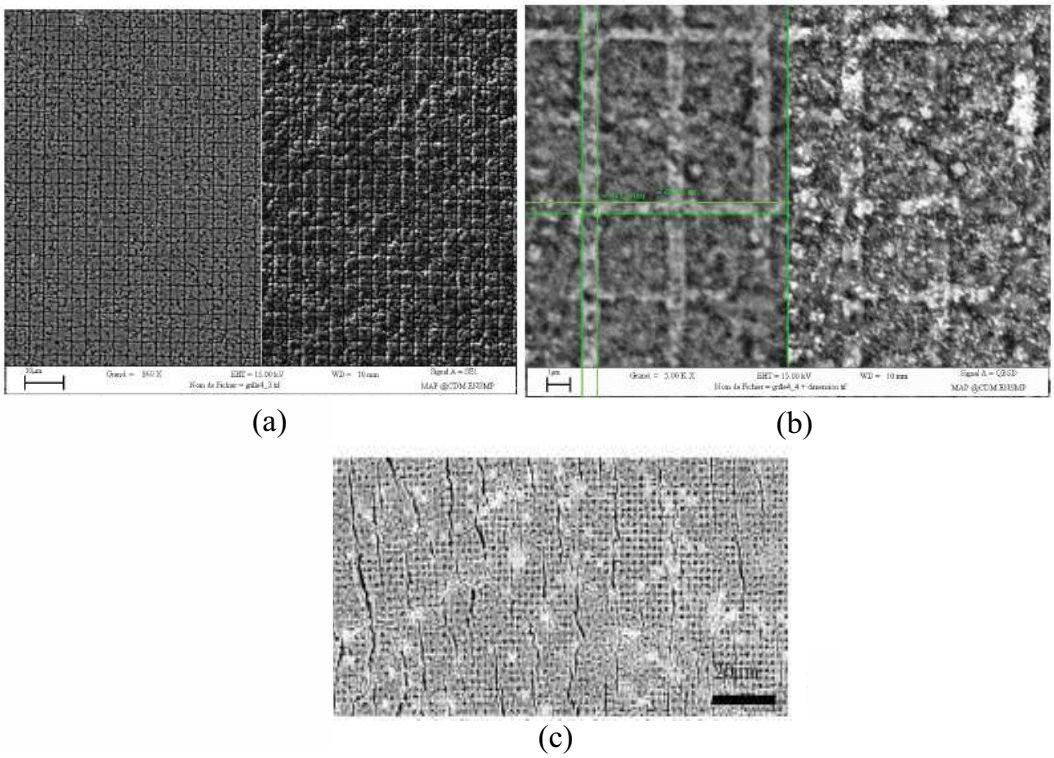

Figure 56: (a) SEM imaging of tungsten grid onto P91 after 3 months at 625 °C in SE mode (left) and BSED Z contrast (right) vacuum 10^{-4} bar. The scale bar is 20 µm. (b) Optical imaging of tungsten grid onto P91 after 500 hours at 625 °C vacuum 10^{-9} bar. The left scale bar is 40 µm and the right one is 20 µm. (c) SEM imaging of tungsten grid onto P91 after 3 months at 625 °C in SE mode (left) and BSED Z contrast (right) vacuum 10^{-7} bar. The scale bar is 1 µm [68].

Soula has also observed the effects of temperature on grid pattern in WSi_2 at high temperature (see Figure 57). Submitted to thermal ageing at 750 °C during 460h in high vacuum environment, grid patterns have been damaged. Even if oxygen trappers have been used, the kinematic fields cannot be measured (see Figure 57 b).

As it has been shown that Type 316 stainless steel is prone to oxidise at 550 °C in air, a preliminary study was performed to study the oxide development (chemistry, kinetics) in the creep experimental conditions to avoid DIC pattern damage during creep tests. To improve the accuracy of the kinematic measurements, the observed surface has to be patterned. This pattern must be stable during the loading involving high temperature creep in an oxidising atmosphere. The proposed strategy relied on the deposition of a mixed pattern made of regular grids and speckle using microlithography technique. This pattern choice represents a good compromise between spatial resolution and accuracy (small scale speckle pattern) and robustness with respect to surface modi-

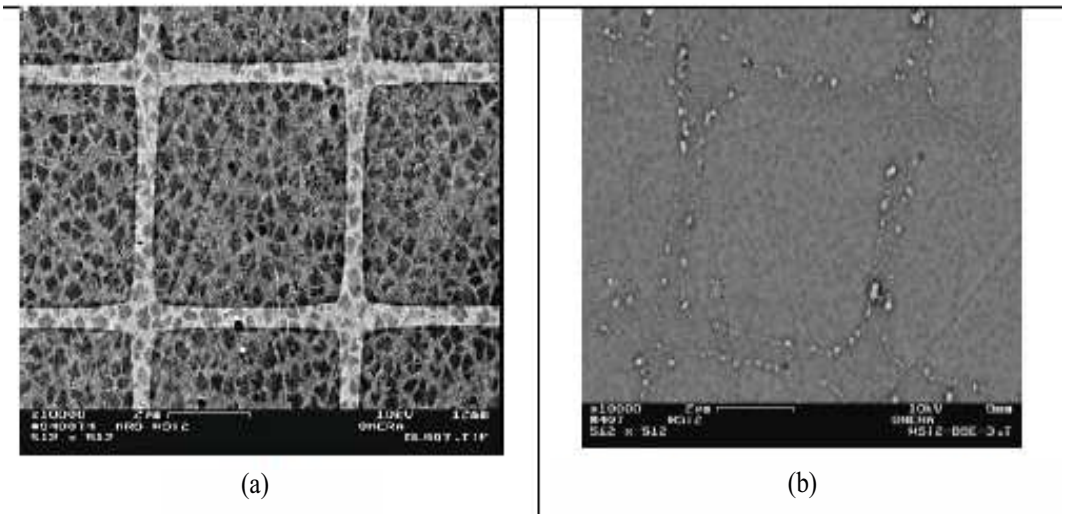

Figure 57: Grid pattern made of WSi_2 (a) after 460h at 750 °C in high vaccum environment with oxygen trappers [56].

fication (regular grid). In order to modify the surface reactivity, the patterning was performed after two different surface preparations:

1. OPS finish surface, of high reactivity,

2. OPS finish surface covered by a protective metal layer of Chromium, Nickel, Hafnium or Niobium reducing the reactivity.

Before introducing these aspects, we will start by describing the development of oxidation in Type 316 at 550 °C in air.

The surface modifications associated with the oxidation were monitored on OPS surface finish. The pattern was deposited directly on the finely etched surface without protective metallic coating. A sample, named B3-3, made of 316LN has been covered with a tungsten pattern of 20-nm thickness and placed in the furnace at 550 °C under air flow during five weeks. After the thermal ageing, the contrast has changed and an oxide has grown at the surface leading to pattern damages (see Figure 58). This figure demonstrates that DIC will not be possible in the current situation where the preconditioned sample is solely etched and patterned.

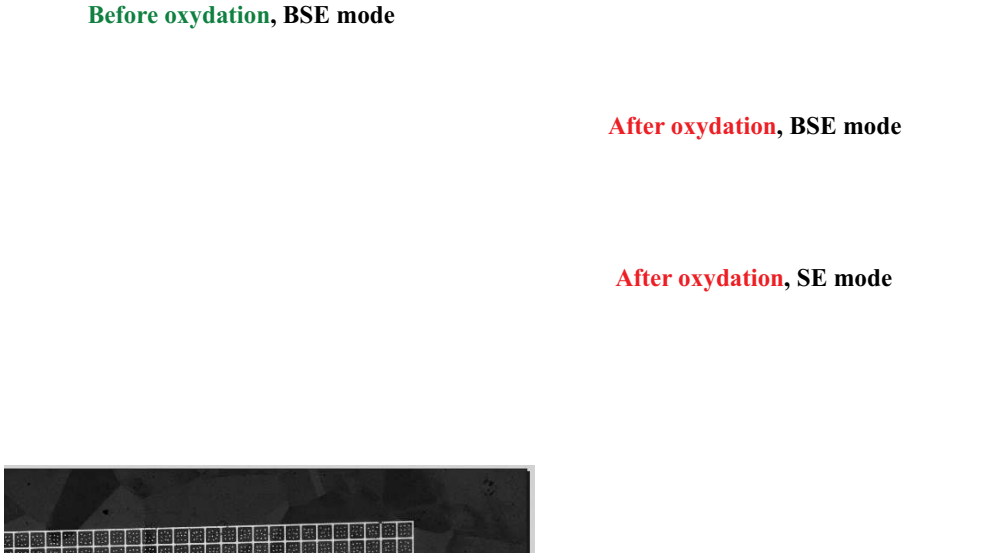

Figure 58: SEM imagings in SE/BSE mode of B3-3 sample **before** and **after** oxidation during five weeks at 550 °C in air.

Then, the oxide layer seems to be very brittle. A simple handling leads to oxide damage. As a consequence, it is unlikely that the strains measured at the specimen surface will be a good indicator of the underlying material deformation.

And finally, the oxidation induces changes between images that are detrimental for DIC. The oxide grows from the metal and covers the pattern preventing the correlation between successive SEM images. Between two creep interruptions, it is really important that the pattern stays unmodified to insure the crack monitoring. Touboul has already raised this issue in high vacuum [68]. He has tried to strictly control the environment of the creep test using a high vacuum of 10^{-9} bar without fully preventing the oxide growth. Some cracks appeared perpendicularly to the loading axis (see Figure 56). Afterward, he tried to cover the pattern with a chromium layer to protect

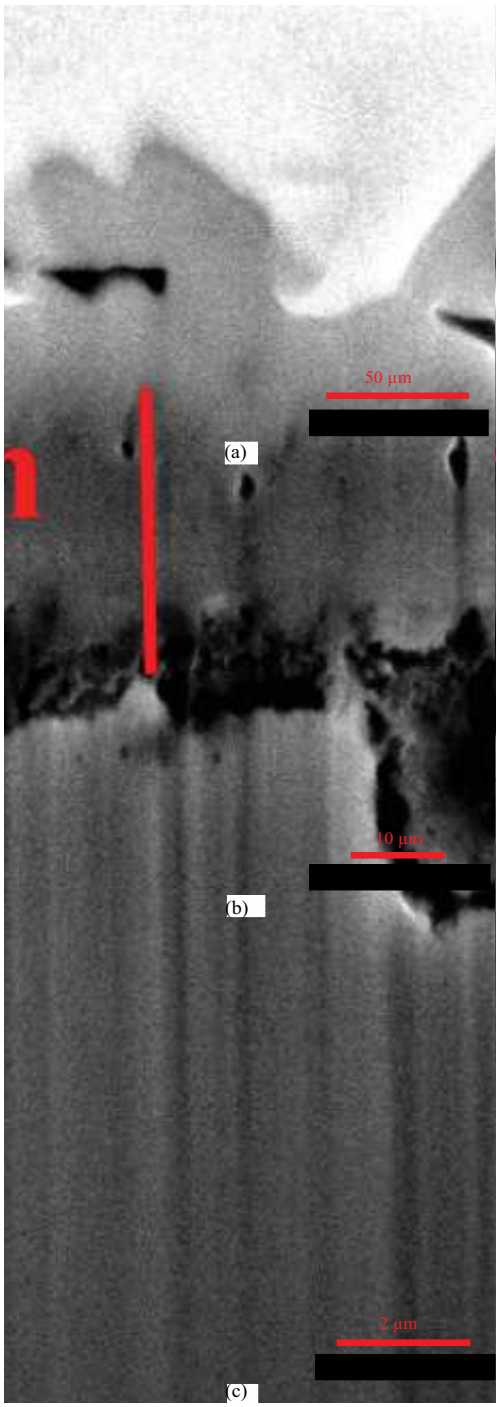

Figure 59: SEM imaging of studied area for the oxide thickness identification (a) magnification: x1500, (b) magnification: x5000, (c) magnification: x35000.

the sample surface from oxidation. In this work, we will introduce the two strategies chosen to insure the pattern integrity during creep test at high temperature in air. The detailed results of these strategies are presented in Appendix A.

2.6 Conclusions

The 316H stainless steel has been used to manufacture boiler components operated at high temperature in CO_2 environment under creep loadings. These specific conditions potentially lead to creep crack initiation and growth at the component surface. To better predict the 316H cracking behaviour, an aged but uncarburized and non-oxidised 316H material was provided by EDF Energy for this PhD work and is referred to as "as-received" material. The as-received 316H stainless steel has been submitted to several investigations in order to characterize its microstructure and to highlight the effects of both oxidation and carburization on its behaviour.

The microstructure of the 316H as-received material is heterogeneous and contains numerous twin boundaries. The deposited component wasn't exposed to AGR's environment and to creep loading during its lifetime in operation. As the occurrence of the intergranular crack is due to spread precipitation of chromium carbide $Cr_{23}C_6$, a preconditioning treatment has been set-up by EDF Energy to reproduce the in-reactor environmental exposure. This oxidising treatment requested a fine polish state of the sample to maximize the diffusion of oxygen and carbon elements from the surface to the bulk material. After 2,000 hours at 600 °C, the depth of carburization can be monitored using microhardness or Vickers hardness cartography. The Vickers' hardness increase at the surface compared to the bulk material is due to the crystal lattice deformation. The diffusion of the addition elements (oxygen and carbon) has been highlighted by combining several microscopy techniques as the Electron Probe MicroAnalyser (EPMA) or the TEM microscope. Fine measurements of the chemical content have highligthed a match between the chromium and carbon cartographies as a proof of chromium carbide presence deep in the specimen (200 µm deep from the initial surface).

To monitor the crack growth and the kinematic fields, Digital Image Correlation technique will be used. This technique relies on gray level conservation and the surface marker have thus to remain stable in SEM images. One of the preliminary studies has been devoted to the surface protection from oxidation. At elevated temperature in air, an oxide layer thicker than one micron is expected to form at the surface. Two strategies have been explored: the chemical solution to remove the oxide layer without damaging the protective chromium-rich layer and the metal coating to avoid the interaction between the austenitic stainless steel and the oxygen elements. Despite these efforts, no conclusive results have been obtained and monitoring the crack in the foreseen experimental conditions will be extremely challenging.

As a consequence, an alternative solution to the crack monitoring in air is proposed. An *in-situ* tensile device has been used to apply loading to SENT specimen. Two SEM suitable for high temperature mechanical testing are available at EDF R&D Lab Les Renardières: the FEI Quanta 600 and the Tescan Mira. The FEI Quanta 600 can be used up to 500 °C. The vacuum environment in the SEM chamber will reduce the oxidation that was observed in this chapter, and images can be acquired continuously that will also improve the correlation between successive images. The results of these tests are presented in the Chapter 5.

Before adressing the micromechanical creep crack test issues, standard creep tests are needed to characterize the creep behaviour of several 316H specimens in absence of cracks. This experimental work is presented in the next chapter.

Chapter 3

High temperature mechanical testing of Grade 316H stainless steel

In operating conditions, the components are subjected to steam pressure at high temperature leading to creep deformation. During creep, creep cracks can potentially nucleate and grow. To better understand the creep cracking mechanisms, we propose to conduct creep tests at 550 °C in air. The creep tests are conducted on previously carburized material. Since environmental creep would require specific experimental facilities, creep is only conducted in air. This methodology allows to study the effect of carburization on the crack initiation and initial growth. Three types of specimens are considered: round bar samples, microcracked specimens and flat dogbone tensile specimens. The first type of specimen allows obtaining the effective behaviour of the material and the others allow fine measurements with the objective to characterize initiation and growth of crack from a single notch.

Contents

3.1 Introduction

The final objective of the PhD thesis is to monitor creep cracks using microscopy techniques. The objective of this experimental work is to obtain mechanical quantities of interest: the discontinuities associated with the crack, plasticity field in the process zone and intergranular and intragranular mechanisms.

Since creep cracks are strongly interacting with the creep deformation of the surrounding material, it is also important to characterize the creep behaviour of the material. For this reason, it was chosen to also conduct conventional creep tests and not only microcracking tests. An overview of the full experimental program is provided in the following.

Our experimental program is integrated in a larger project involving several universities and research labs in UK. No description of this project will be provided since it is beyond the scope of this PhD, however some results will be provided for comparison when needed. A list of proposed experiments is given in Table 15. Three different specimen designs are considered: the conventional round bar tensile sample (RBT), the Single Edge Notched Tensile specimen (SENT) and the flat dogbone tensile specimen (FT) (see Figure 60). In this table, the last column provides the conventional nominal creep stress for RBT and FT experiments and the remote far field stress for SENT experiments. The specimen designs are given in Figure 60 c and Figure 60 d. The SENT and the FT have the same outer dimensions. Two different creep rigs are used to conduct these experiments.

Specimen design	Carburized	σ_∞ (MPa)
RBT	No	270
RBT	No	290
SENT	Yes	64
SENT	Yes	96
SENT	Yes	128
FT	No	270
FT	Yes	270

Table 15: Experimental creep program at 550 °C in air.

A convention for the test designation is proposed as:

Institute	Material	σ	Shape	Test label
EDF or UM or ICL	C or N		RBT or SENT or FT	

with *Institute* referring to EDF, University of Manchester (UM) or Imperial College of London (ICL), with *Material* refering to carburized (C) or non-carburized (N) 316H, σ providing the applied stress in MPa and *Shape* being substituted by the specimen designation and *Test label* referring to the number attributed to the test (see Table 15).

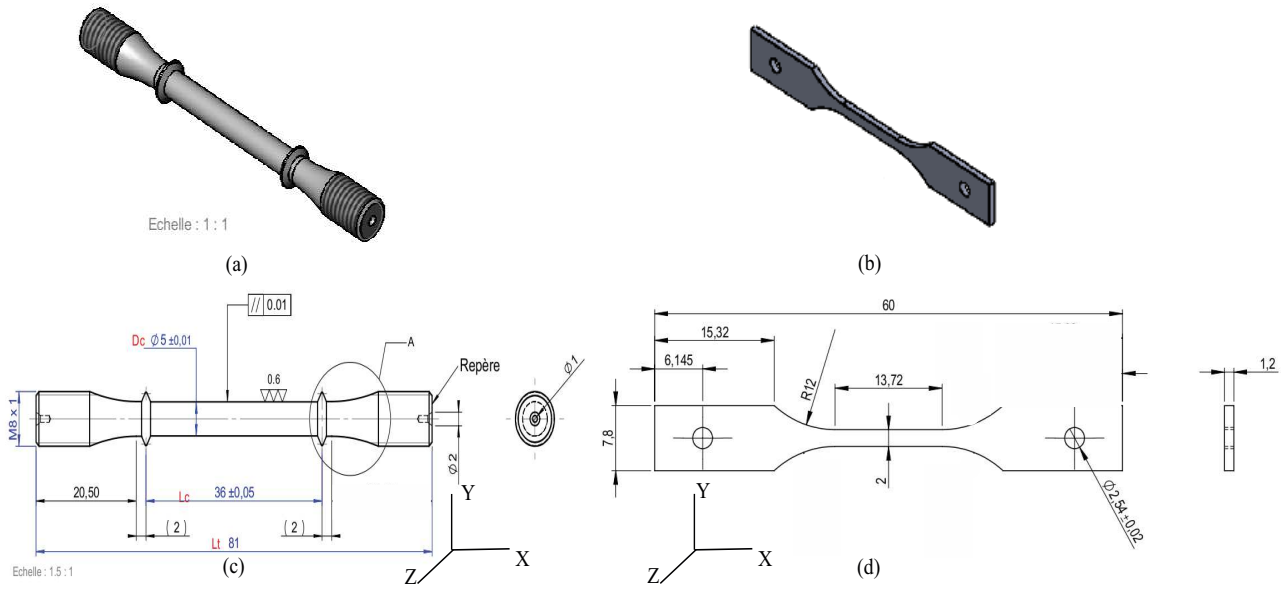

Figure 60: The round bar sample geometry (a, c) and the microsized specimen geometry (b, d).

In the following sections, we will introduce the results of creep tests and we will mainly focus on two aspects: the comparison of different specimen geometries and the comparison of carburized and non carburized material.

3.2 The effects of carburization on creep response

3.2.1 At different loading levels: comparison with other laboratories

In this section, we only consider the response of large specimens: RBT and conventional creep specimen tested in UK labs. Creep responses will also be compared for the microsized specimen design in a subsequent part.

Two tests at 270 MPa and two tests at 290 MPa have been performed in air at 550 °C using conventional creep rigs. The specimens are made from non carburized material. As a consequence, the specimen designation is EDF-N-270-RBT and EDF-N-290-RBT. The creep strain response of each specimen is presented in Figure 61. The areal reduction at failure was measured using a binocular lens and ranges between 9 % and 17 %. From these test results, it is possible to extract the minimum creep strain rate (see Table 16). These values are useful to identify the parameters of a Norton's law.

Test denomination	min($\dot{\varepsilon}$) (h^{-1})	Time to rupture t_f (h)
EDF-N-270-RBT-1	1.148×10^{-6}	13488
EDF-N-270-RBT-2	1.15×10^{-6}	12279
EDF-N-290-RBT-3	2.19×10^{-6}	5348
EDF-N-290-RBT-4	1.72×10^{-6}	7496

Table 16: Minimum creep strain-rate and time at failure t_f for EDF-N-270-RBT and EDF-N-290-RBT tests at 550 °C in air.

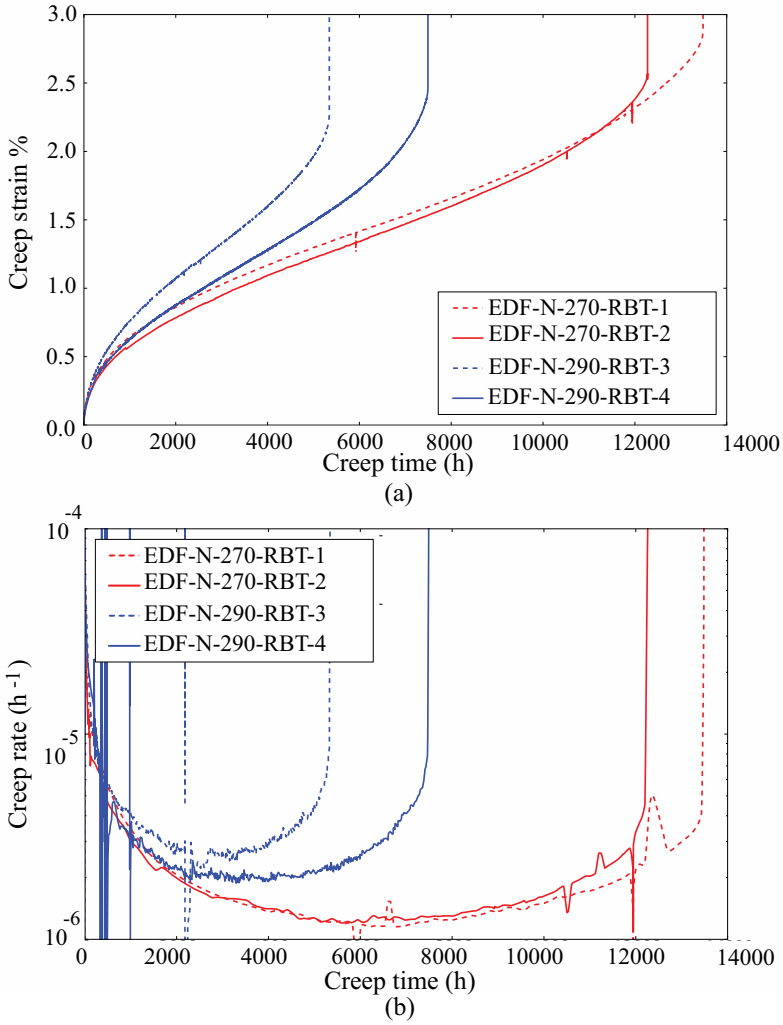

Figure 61: Creep strain as a function of time (T = 550 °C in air) for EDF-N-270-RBT and EDF-N-290-RBT (a) and corresponding creep strain-rates (b).

For each stress level, the creep responses are in good agreement one with each other. The relative deviation between the two tests on the time to rupture is 8.9 % for EDF-N-270-RBT

and 28.6 % for EDF-N-290-RBT, corresponding to an absolute deviation of 604.5h and 1074h, respectively.

Although the stress values are close and the number of experiments is limited, it is still possible to identify a simple Norton creep model (Equation 3.1).

$$min(\dot{\varepsilon}) = A.\sigma^n \tag{3.1}$$

A linear regression is performed between $log(\dot{\varepsilon})$ and $log(\sigma)$ leading to identify A and n parameters. These values are compared to available literature data in Table 17.

A	n	Experimental conditions
$(1.24\ 10^{-24})^{-7.38}$ MPa$^{-7.38}$.h^{-1}	7.38	316H at 550 °C in air
$(4.4\ 10^{-31})^{-7.9}$ MPa$^{-7.9}$.h^{-1}	7.9	316 at 650 °C [80, 81]
$(1.56\ 10^{-35})^{-11.95}$ MPa$^{-11.95}$.h^{-1}	11.95	HAZ from 316H at 550 °C [90]

Table 17: Creep Norton law parameters for Type 316 at high temperature.

The macroscopic tests performed on large specimens at high stress levels on the carburized material could lead to several percents of deformation during the initial creep load application step (temperature ramp from 20 °C to 550 °C and load ramp). For example in EDF-N-270-RBT and EDF-N-290-RBT, the deformation has reached 3.5 % and 5 %, respectively during the creep pre-loading (see Figure 62 and Table 18).

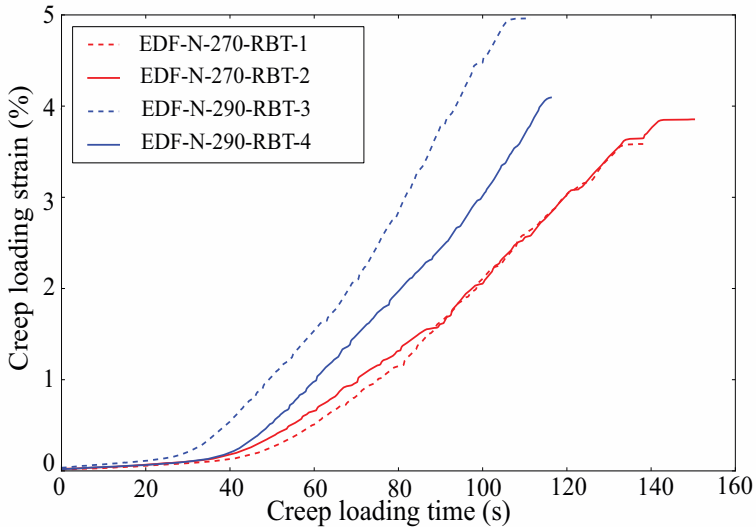

Figure 62: Creep loading strain (%) during the initial creep loading step for EDF-N-290-RBT and EDF-N-270-RBT specimens.

Test designation	$\varepsilon_{max}^{loading}$ (%)
EDF-N-270-RBT-1	3.58
EDF-N-270-RBT-2	3.85
EDF-N-290-RBT-3	4.96
EDF-N-290-RBT-4	4.09

Table 18: Maximum value of the creep loading strain (%) during the creep loading for EDF-N-270-RBT and EDF-N-290-RBT.

Several creep tests on conventional round bar sample have been performed by the University of Manchester (*UM*) and the Imperial College of London (*ICL*). Specimens have been machined both in carburized and as-received 316H coming from the same header component (see Section 2.2). A comparison between the results of the tests conducted in the different labs is shown in Figure 63.

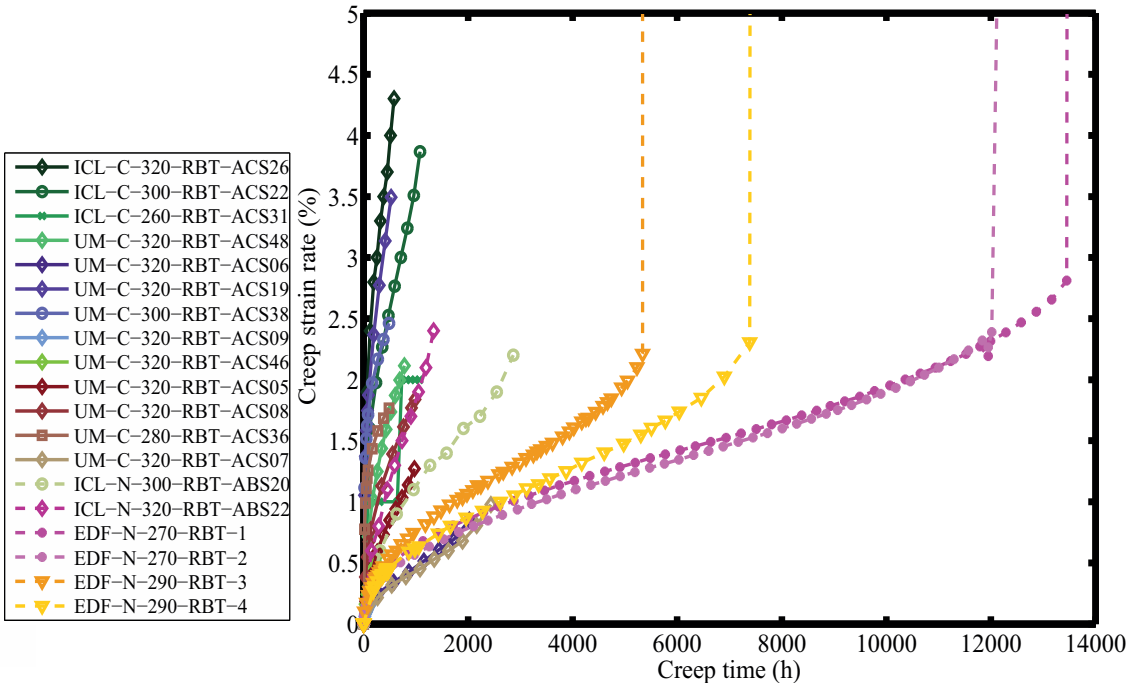

Figure 63: Comparisons between creep curves from ICL, UM and EDF on carburized and as-received RBT samples.

The minimum creep rate and the time to reach the failure for the tests of different labs are summarized in Table 19. These data can be collected to build a Monkman-Grant diagram (see Figure 64). A linear trend is generally observed but it is not the case when considering the results from the Imperial College London and the University of Manchester. The results may be influenced by the carburization and by the diameters of the round bar samples which are different for the RBT from UM (6.996 mm) and from EDF (5 mm).

Test denomination	Minimum creep rate (h^{-1})	Time to failure t_f (h)
ICL-N-300-RBT-ABS20	3.428×10^{-5}	3183
ICL-N-320-RBT-ABS22	3.429×10^{-5}	1480
ICL-C-320-RBT-ACS26	3.429×10^{-5}	649
ICL-C-300-RBT-ACS22	1.875×10^{-5}	1199
ICL-C-300-RBT-ACS31	4.0×10^{-4}	1153
UM-C-320-RBT-ACS48	7.774×10^{-6}	2565
UM-C-320-RBT-ACS06	2.759×10^{-4}	2310
UM-C-320-RBT-ACS19	3.189×10^{-5}	637
UM-C-300-RBT-ACS38	1.3×10^{-3}	592
UM-C-320-RBT-ACS38	6.899×10^{-4}	169
UM-C-320-RBT-ACS46	1.283×10^{-3}	330
UM-C-320-RBT-ACS05	9.096×10^{-4}	1094
UM-C-320-RBT-ACS08	1.3399×10^{-3}	1056
UM-C-280-RBT-ACS36	1.2×10^{-3}	592
UM-C-320-RBT-ACS07	2.515×10^{-4}	2704

Table 19: Minimum creep rate and time to failure t_f for the different tests: University of Manchester and the Imperial College of London. Source: University of Manchester and Imperial College of London

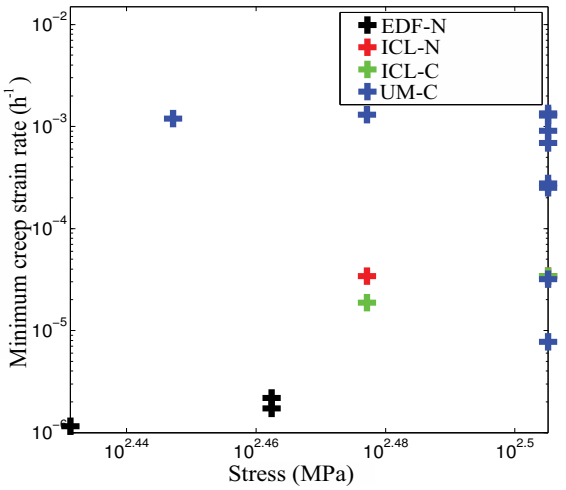

Figure 64: Monkman-Grant diagram for ICL, UM and EDF on carburized and as-received RBT samples.

3.2.2 Effect of carburization on the creep response for small specimens

A flat dogbone has been machined in a carburized plate received from EDF Energy in order to perform a comparison with the same specimen geometry made of as-received 316H. The two

samples have been submitted to a loading of 270 MPa in air at 550 °C. After 4,000 h, the non carburized EDF-N-270-FT sample hasn't reached the tertiary creep (see Table 20 and Figure 65).

Test designation	min($\dot{\varepsilon}$) (h^{-1})	Time to rupture t_f (h)
EDF-C-270-FT-9	4.79×10^{-5}	297
EDF-N-270-FT-1	9.01×10^{-7}	> 4,000

Table 20: Minimum creep rate and time to reach the failure t_f for EDF-N-270-FT-9 and EDF-C-270-FT-1- tests at 550 °C in air.

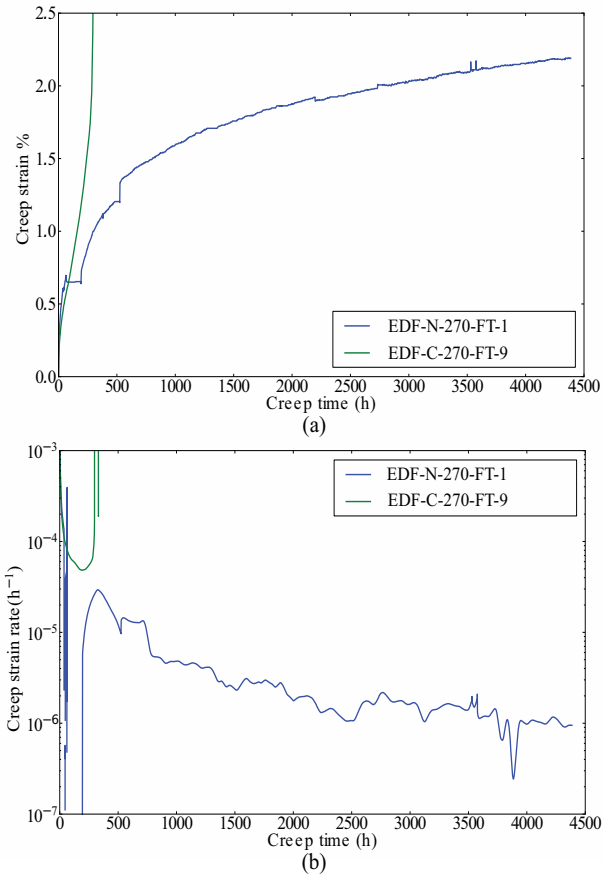

Figure 65: Creep strain response for the EDF-N-270-FT-1 and EDF-C-270-FT-9 (a) and creep strain rate curve (b).

We have seen that carburized material has different mechanical properties than that of the base metal. To explain the change in the minimum creep rate of preconditioned sample compared to the as-received material (see Table 20), we propose to consider that carburized layer of thickness t_{carb} was not supporting the load during the creep test. Thus, the material section is decreased to take into account this assumption leading to the expression of an "effective" specimen cross section (supporting the creep loading).

$$\begin{aligned} S_{carb} &= 2(W\, t_{carb}) \\ S_{tot} &= W\, t \end{aligned}$$

Then, the creep loading (σ_∞ = 270 MPa corresponding to $\frac{F}{S_{tot}}$) is modified to take into account the presence of carburized material:

$$\sigma_{eff} = \sigma_\infty \left(1 - \left(\frac{S_{carb}}{S_{tot} - S_{carb}}\right)\right)$$

Several thickness values of carburized material have been considered. Thus, an effective stress has been identified. From the Norton law presented above, a minimum creep strain rate can be obtained. The results are presented in Table 21.

t_{carb} (mm)	σ_{eff} (MPa)	min($\dot{\varepsilon}$) (h^{-1})
0.05	300	2.50×10^{-6}
0.1	337.5	5.98×10^{-6}
0.2	450	5.01×10^{-5}

Table 21: Minimum creep strain rate identified from a Norton law (see (Equation 3.1)) considering that creep loading is only supported by uncarburized material.

The experimental minimum creep strain rate is close to 5.0×10^{-5} h^{-1}. From Table 21, it corresponds to 200 µm of carburized material thickness from each face which is consistent with the SEM observations presented in Chapter 2. This study has shown that carburized material did not support the loading during the creep test, explaining the decrease of the minimum creep rate compared to the as-received material.

3.3 Effect of geometry on the creep response

Flat dogbone specimens have been machined in the as-received 316H. It is proposed to study the effects of the specimen geometry on the creep response by performing a comparison between the creep responses of the round bar tensile specimens of 5mm diameter (EDF-N-270-RBT-1, EDF-N-270-RBT-2) and the flat tensile specimen of 1mm thickness (EDF-N-270-FT) tests (see Figure 66).

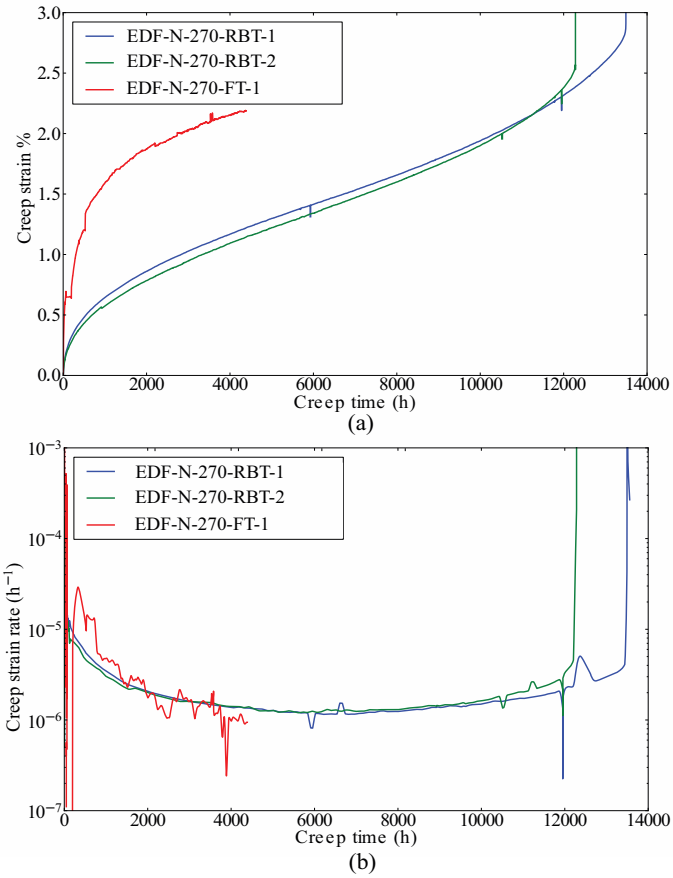

Figure 66: Comparisons between EDF-N-270-RBT-1, EDF-N-270-RBT-2 and EDF-N-270-FT-1: creep strain response (a) and creep strain rates (b).

The creep response of the round bar samples and the flat dogbone seem to be similar for a 270 MPa creep but a strain difference of 1.2 % in the 500h following the load application is observed. After this stage, the creep strains and strain rates are similar between small and large specimens, even if the process of manufacturing of the sample used was slightly different. In fact, the FT specimens have been obtained from a CT sample (L = 62.5 mm and h = 60 mm) whereas the RBT have been machined directly in the MT092/13 and MT092/14 cuts (see Section 2.2). Moreover, the machine finish of round bar sample is rougher leading to very small surface defects. An other important point is that the gripping system and the deformation measurement are different for conventional creep rigs and microfluameter. For the small specimen, the deformation is measured by monitoring the crosshead displacement.

3.4 The effects of carburization on the deformation mechanisms

In this section, we propose to study the effects of carburization at miscropical scale by performing SEM observations such as fractography.

- A general view obtained by stitching for the EDF-N-290-RBT spcimen is proposed in Fig-

ure 67. From this image, the fracture mechanisms are assumed to be a combination of creep cavities and inter/transgranular crack propagation or cleavage (see Figure 68);

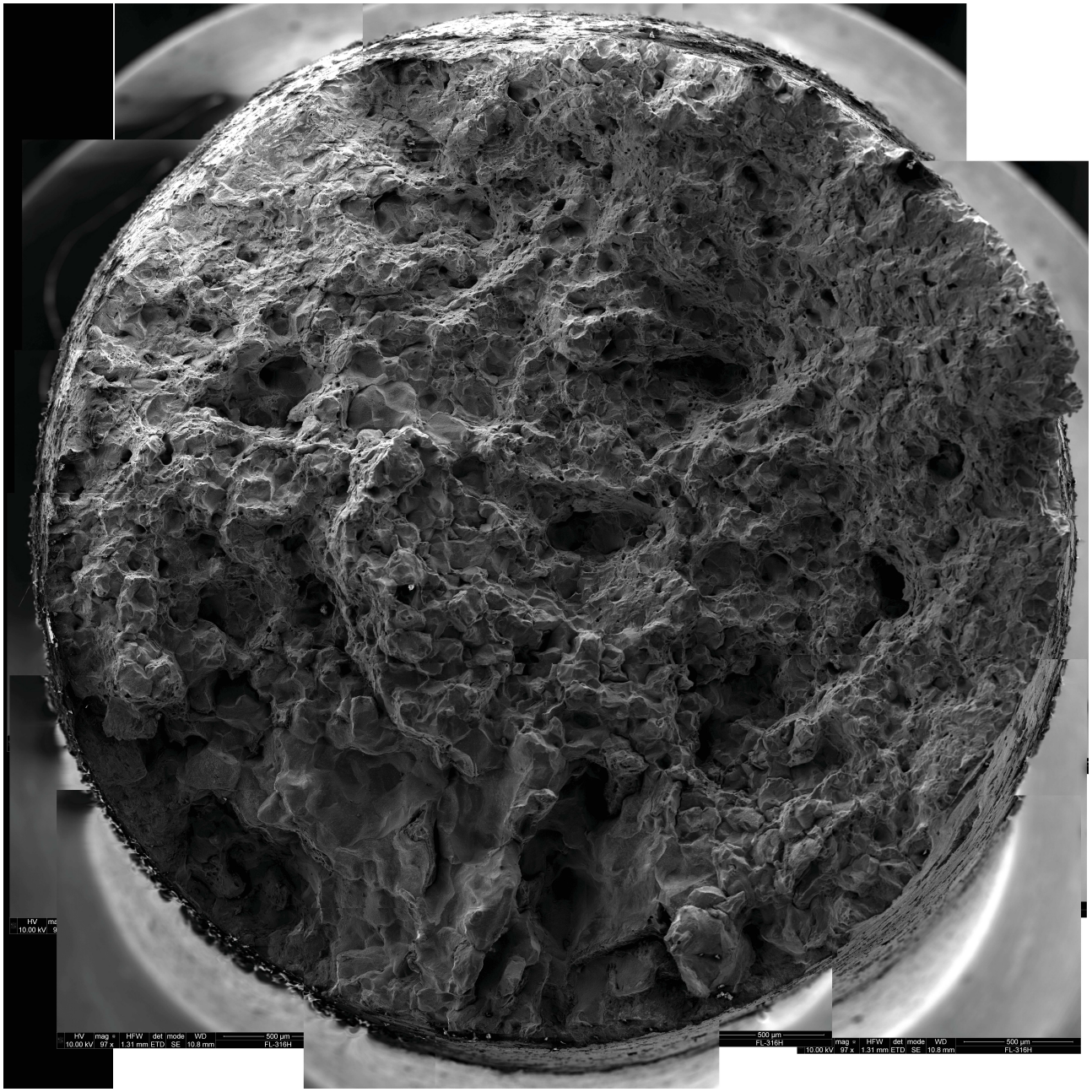

Figure 67: Global view of fracture surface for EDF-N-290-RBT test.

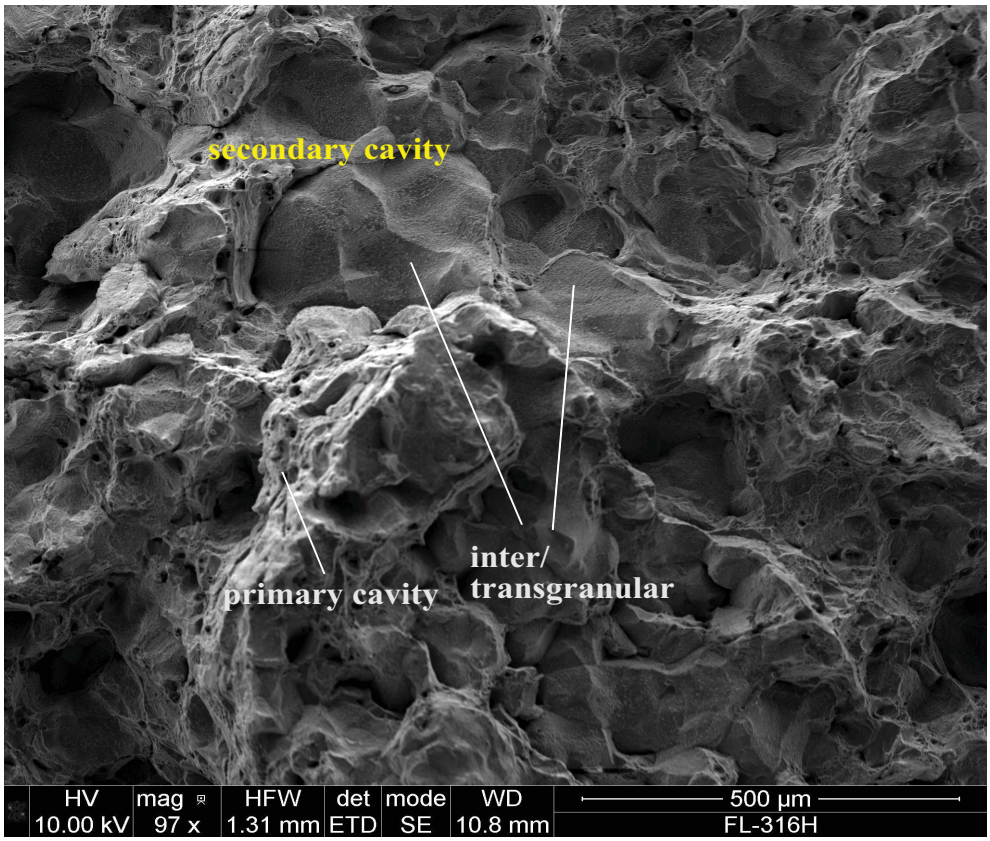

Figure 68: Magnified area of Figure 67: observations of primary and secondary creep cavities and intergranular fracture.

- Several tests have been performed on SENT specimens at 550 °C in air. All the samples have been submitted to preconditioning treatment in order to study the influence of both carburization and oxidation on creep crack growth.

The first test, C-128-SENT, was used as a reference to find a time convenient for the creep crack monitoring. For this specimen, the initial crack length is 300 µm. When conducting SEM observations, the crack was hidden by an oxide layer. The specimen has been submitted to a creep load of 128 MPa which corresponds to a stress intensity factor of 5 MPa.$\sqrt{m}$ [112]. After three weeks (see Table 22), the specimen was unloaded and removed from the creep rig to conduct SEM observations. During the cooling down period, the sample has failed (see Figure 69).

Test denomination	min($\dot{\varepsilon}$) (h^{-1})	Time to rupture t_f (h)
EDF-C-128-SENT-12	1.56×10^{-6}	530

Table 22: Minimum creep rate and time to reach the failure t_f for EDF-C-128-SENT-12 test at 550 °C in air.

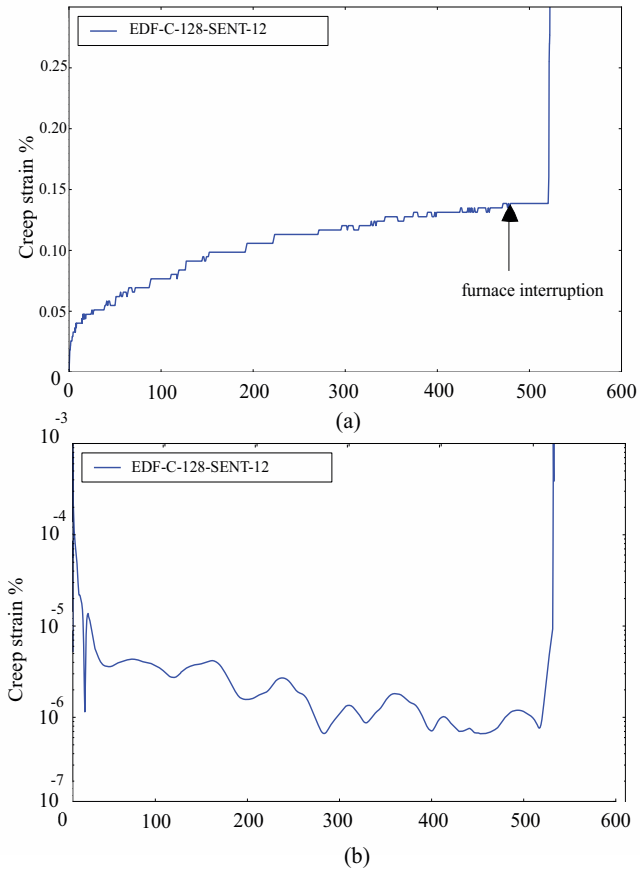

Figure 69: Creep strain response for the EDF-C-128-SENT-12 (a) and creep strain rate curve (b).

As discussed in the literature review, three different creep mechanisms can be active depending on the temperature and stress conditions (see Chapter 1 paragraph 1.2). A comparison between the C-270-FT and the C-128-SENT is proposed. Failure seems mainly inter/transgranular for the specimen C-270-FT (see Figure 70 a). At lower stress, cavity initiation and growth can develop corresponding to a creep-diffusion mecanism in pre-cracked sample (see Figure 70 b). On the right side of the C-128-SENT specimen, the fatigue pre-crack has propagated following an inter/transgranular path which is consistent with the SEM observations conducted at the specimen surface before carburization.

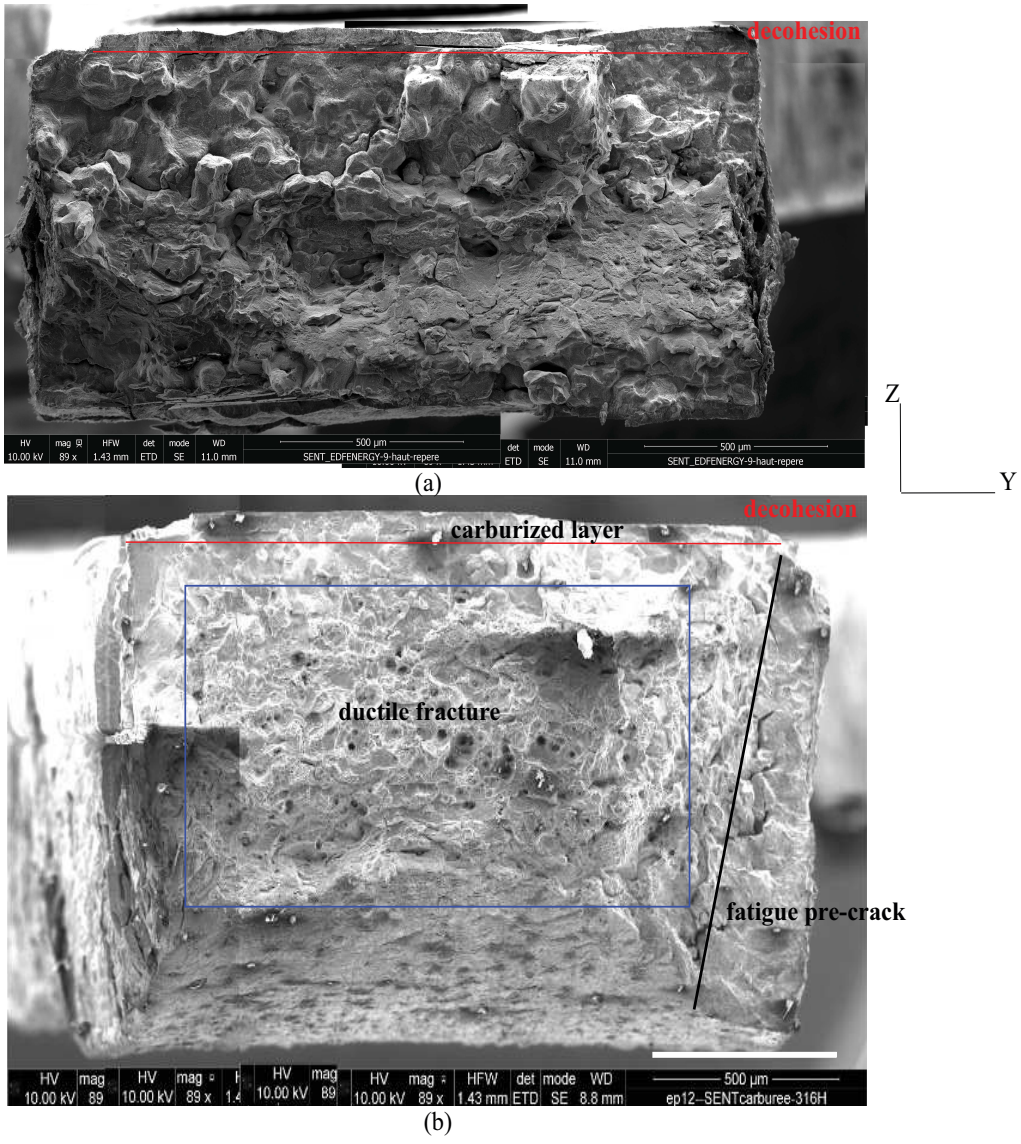

Figure 70: Comparisons between C-270-FT (a) and C-128-SENT (b). The specimen width is 2 mm.

SEM observations of the SENT specimen after failure have been conducted (see Figure 70). The fatigue pre-crack with an inter/transgranular path is visible on the right side of the specimen C-

128-SENT. At the top surface, a partial spalliation of the oxidised/carburized layer is observable. The embrittlement of these layers can be explained by their complex structures (see Figure 51 and Figure 52 in Chapter 2). In the specimen center, primary creep cavities and secondary creep cavities are present and characteristic of a ductile fracture (see Figure 70 b).

In Figure 71 a, the superficial layer has cracked and had been shredded. The cracks are perpendicular to the loading direction and seem to be deep. For these cracks, a depth of 250 µm has been quantified by performing SEM observations of sample edges (see Figure 72). Contrary to the pre-conditioned surface, no crack has been observed on the uncarburized face. This result suggests the fact that the reactivity of the surface to oxidation is increased by the preliminary surface polishing. Then, the oxide cracked under creep loading leading to crack initiation and growth on the sample pre-conditioned surface.

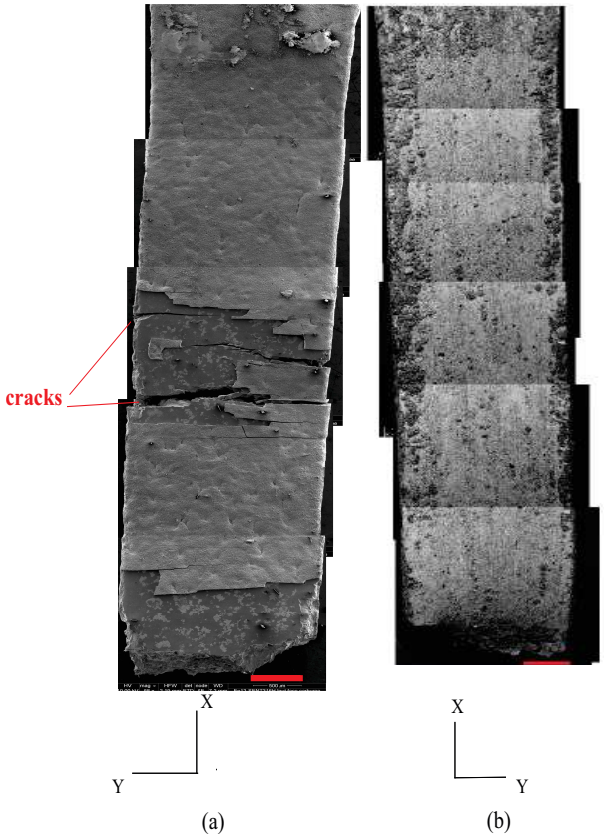

Figure 71: General view of the specimen after failure in SE mode of carburized surface (a) and uncarburized face (b). The red scale bar is 500 µm.

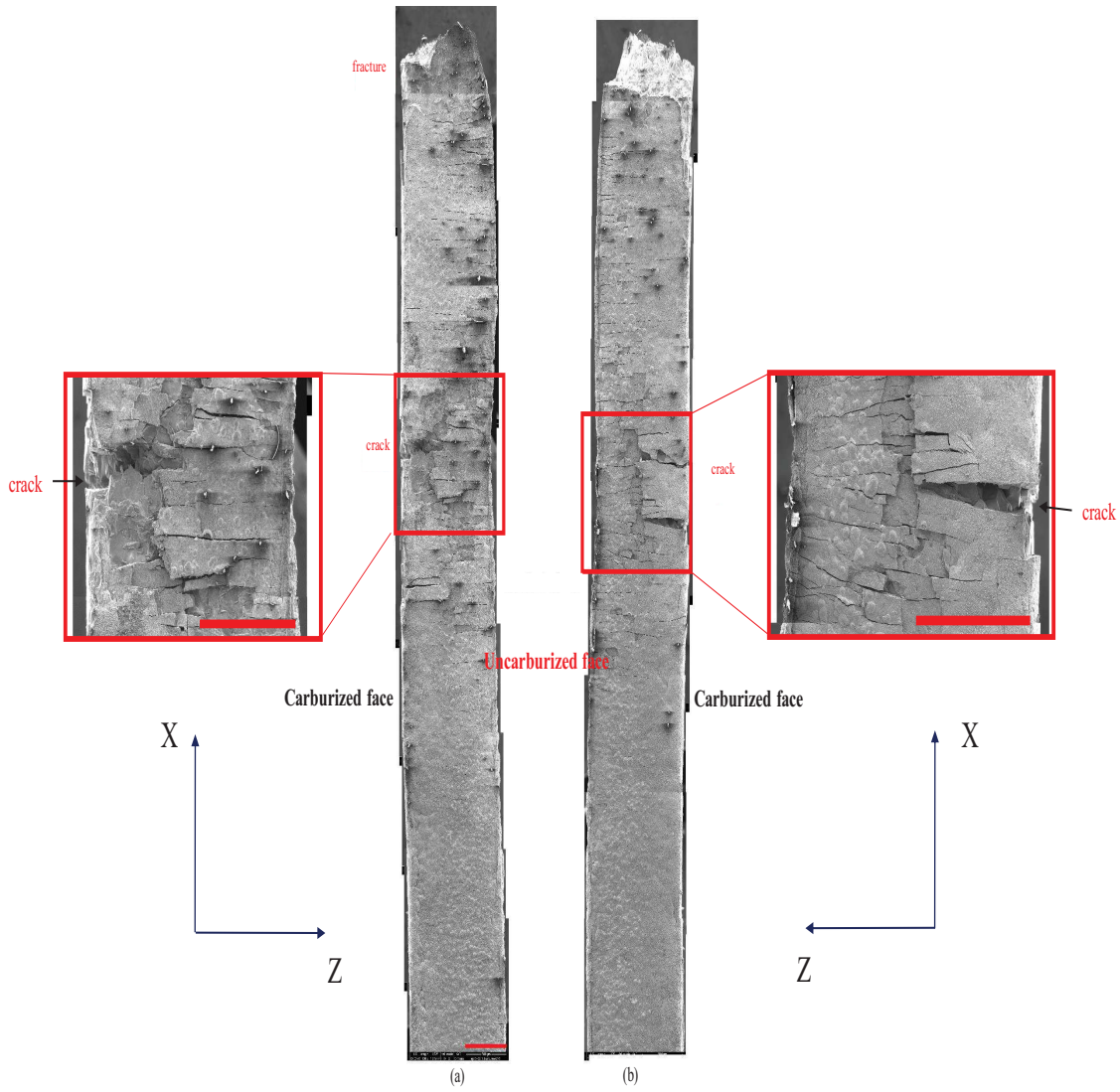

Figure 72: General view of the specimen after failure in SE mode of carburized surface (a) and uncarburized face (b). The red scale bar is 500 µm.

For C-128-SENT, the creep loading strain, $\varepsilon_{max}^{loading}$, equals to 0.0984 % (see Figure 73) and the global creep strain developped during this test is close to 0.25 %.

Several academic partners of EDF Energy have identified a deformation thresholdof 0.5% associated with crack initiation in the carburized layer. We have shown that the deformation generated by the loading can be greater or equal to this threshold value (see Table 18 and Figure 73). This deformation limit is confirmed by SEM observations of failed specimens. Numerous cracks perpendicular to the loading directions have been observed. The cracks formed during the initial loading may also be detrimental for the creep response of carburized specimen subjected to more than 0.5 % of loading strain, as opened cracks may lead to stress concentrations in the underlying uncarburized material.

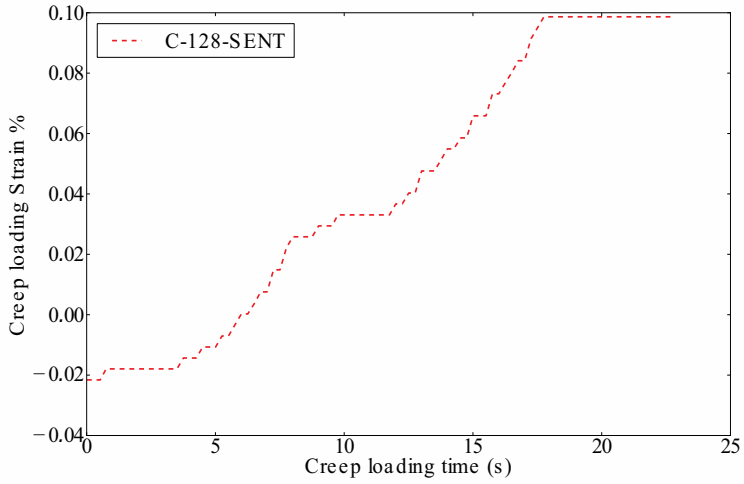

Figure 73: Creep loading strain (%) during the loading of C-128-SENT specimen. $\varepsilon_{max}^{loading}$ (%) equals to 0.0984 %.

Conclusions from microscopy:

By comparing SEM images of flat specimen containing a fatigure pre-crack (EDF-C-128-SENT-12) and uncracked flat dogbone specimen (EDF-C-270-FT-9), we have observed that:

- the load level triggers several failure modes. These stresses could lead to a change in the fracture mechanisms. Considering low stresses, creep cavity initiation and growth has been observed and is attributed to ductile fracture. At high stresses, the creep time is not sufficient to allow the creep cavities to nucleate and grow;
- the preconditioning treatment has led to the growth of oxidised and carburized layers. These layers are less ductile and numerous cracks perpendicular to the loading direction appeared. This multiple cracking phenomenon generate stress concentration and multiple discontinuities in the kinematic fields. In Chapter 5, we will introduce an example of *in-situ* multiple crack monitoring using DIC and the method specifically developped to identify each crack tip position.

3.5 Conclusion

In operating conditions, the components are subjected to steam pressure at high temperature leading to creep loading. To better understand the creep crack mechanisms, we have proposed to conduct creep tests at 550 °C in air. Three types of specimens were considered: round bar sample, microcracked specimen and flat dogbone.

The conventional specimens, RBT, have been submitted to two loadings: 270 and 290 MPa. The creep responses of the as-received 316 H have allowed to identify the Norton's law coefficients A and n. The results are consistent with the literature [81]. A comparison with some tests performed at the Imperial College of London is proposed. The preconditioning treatment has a negligible effect on the conventional round bar tensile specimen creep response. At microscopical scale, both preconditioned and uncarburized samples have been tested. The oxidising treatment has reduced the ductility of the material.

The effect of geometry has been quantified using the as-received material. The microsized specimen deformation happened faster than with the Round Bar Tensile specimen (RBT). To reach 2% of creep strain, it took about 3,000h to the flat tensile specimen N-270-FT and more than 10,000h to N-270-RBT for a same load. Nevertheless, the slope of the three curves seem similar. The minimum creep rate has not been reached yet. The difference between the creep response of the two geometries can be explained by the manufacturing of the sample: the location in the cuts and by the Electric Discharge Machining (EDM) finish. The microsized specimens have been obtained from Compact Tension (CT) sample. These dimensions requested a particular positioning in the MT092/13 and MT092/14 cuts.

By comparing the fracture surface of two microsized specimens (C-128-SENT and C-270-FT), a variation in the failure mechanism is highlighted. At low stresses, numerous primary and secondary cavities are observed that are characteristic of diffusion creep. At higher stresses, the microstructure is revealed by the inter/transgranular path of the crack.

An interrupted creep test on a preconditioned Single Edge Notched Tensile specimen (SENT) has been performed in order to get a crack monitoring at the microscopical scale. Between each creep period, some SEM images of the ROI have been taken. These images has been used to obtain the kinematic fields. A DIC method handling discontinuities has been developped. The crack propagation is measured by comparing the position of the crack tip identified by this procedure. The theory, the principles and the numerical validation of the proposed DIC method are presented on reference tests in Chapter 4. These tests will be part of the experimental validation program adressed in the Chapter 5.

Chapter 4

Development of a crack tip identification procedure using DIC

By using advanced experimental techniques providing full field measurements, it is expected to detect mechanical fields singularities induced by cracks and other material discontinuities. In the context of creep crack growth, image analyses and Digital Image Correlation (DIC) are relevant techniques to monitor the crack advance and the plasticity and strain fields surrounding a propagating crack. Moreover, by performing acquisitions well sequenced in time, it is also possible to measure kinematic fields before and after crack initiation, and to precisely determine initiation time under a given load. The aim of this chapter is to introduce the numerical strategy developped to monitor kinematic fields in the presence of a crack, and to identify the crack tip position from SEM images using DIC.

Contents

4.1 Introduction

Advanced experimental techniques such as Digital Image Correlation (DIC) provide spatially dense kinematic fields that are usefull to characterize material behaviour when mechanical heterogeneities develop. This technique is therefore interesting in the context of predicting the lifetime of industrial components operating in specific conditions, when mechanical heterogeneities are involved. Coupling between DIC measurements and mechanical models (analytical or numerically-based such as FEM) has already been introduced with the objective of better characterizing the material behaviour. Several works have been devoted to the study of plasticity [113, 114], damage mechanics [115], fracture mechanics [116, 117, 118, 119] and plasticity at the microscale [120, 121, 122, 123, 124]. It is now possible to determine mechanical fields induced by cracks and other material discontinuities [125, 126, 127, 128, 129, 130]. Fracture mechanics problems have been adressed by introducing the linear elastic fracture mechanics (LEFM) displacement shape functions in the digital image correlation criterions [131, 132]. In specific cases of brittle failure, a single field expressed only using LEFM expressions is sufficient to properly describe the kinematic field surrounding a crack, allowing in turn to derive stress intensity factors [133, 127]. Extension of this approach to an X-FEM description of the kinematic has also been proposed, increasing the flexibility of the method [132]. Another way of characterizing a crack has been proposed in [134], and consists in obtaining first a kinematic field using conventional subset-based (or local) DIC, and then projecting the field using LEFM-based expressions. This second technique is of great interest when plasticity develops in the crack process zone, and the plastic zone can be depicted when plastic yield criterion is known.

The aforementionned methods developped to study fracture mechanics can potentially be applied to study a creep crack problem. By performing acquisitions well sequenced in time, it is also possible to measure kinematic fields before and after crack initiation, and to precisely determine initiation time under a known loading. Better determining initiation time leads to expected industrial method improvements, since conventional approaches are often conservative due to the lack of precise data and to their scatter. Being able to predict crack initiation between inspection times would also lead to improve safety.

While so-called global approaches have already been proposed in the literature to identify stress intensity factors in brittle failure [131], the focus is here to better locate crack tips from SEM images where the crack tip is not always easy to detect due to an oxide layer formed at high temperature. Possible plastic strains need to be captured as well. To achieve these objectives, an identification procedure of crack parameters relying on kinematic fields projection on a specific base is proposed. The choice of this method has also been motivated by the lack of knowledge on the material behaviour at the microscopic scale, for this creep crack problem.

This section is structured as follows: first, some generalities and literature review of digital image correlation will be provided. Then, some fundamentals of fracture mechanics will be discussed, and they will be used as a limestone to build the crack identification procedure described after. Finally, an assessment of the procedure will be proposed, considering two cases. The simplest assesment is conducted on virtual experiments obtained using Code_Aster finite element software, and directly providing the displacement fields. A second assesment is proposed by considering virtually deformed images using dispacement fields obtained during the first assessment. The application of this method to real experimental data will be discussed later in Chapter 5.

4.2 Kinematic fields measurement using Digital Image Correlation (DIC)

4.2.1 Principle

Digital Image Correlation (DIC) has been introduced in the early 80's in a mechanical context [135], and then became extremely popular due to its capability to measure heterogeneous strain fields. The method aims at comparing images of solids subjected to mechanical loads in order to derive kinematic fields of observable surfaces (and now volumes by using 3D images [136, 137, 138, 139]). To follow the displacement by image comparison, some markers have to be present on the surface, whose displacements are assumed to be equal to that of the underlying material.

The surface markers constitute one fundamental aspect of the DIC process impacting the measurement accuracy and performance. In this work, a microlithography technique has been chosen to pattern the specimen surface.

4.2.2 E-beam microlithography technique

4.2.2.1 Literature overview

The microlithography technique has been first used for mechanical properties measurements in the 1990's. Then, it has been widely applied in the domain of microelectronic device manufacturing due to its good resolution at the micrometric and nanometric scales. The patterns that can be obtained with this technique are particularly convenient for DIC when it is desired to conduct measurements at the micron scale for materials not exhibiting natural random surface pattern and therefore sufficient imaging contrast.

In general, to improve imaging contrast at a material surface, some markers can be deposited at the surface using different techniques such as:

- paint coating: two different paint colors can be used to create pattern with a convenient contrast (see Figure 74);
- microlithography coating: the pattern is obtained using interactions between polymer resins and SEM beam. This technique will be detailed in the following Section 4.2.2 [140, 110, 121, 141, 123] and in Appendix B;
- chemical etchant: the surface is etched using a chemical solution to reveal material microstructure. It is performed here with Nital 3 etchant which is a solution of 3 % in weight of nitric acid in ethanol. The sample is placed in the solution during a few tens of second. The acid etches preferentially grain boundaries revealing the microstructure. This technique can be used in addition to e-beam microlithography;

The microlithography relies on combined use of photosensitive polymer resins and the electron beam of a Scanning Electron Microscopy (SEM). This technique is divided into five steps described in Figure 75. Prior to the e-beam microlithography, the sample is subjected to a fine polishing treatment until Oxide Polishing Suspension (OPS) finish to provide a surface with good flatness and low roughness. Then, the principle consists in depositing a thin photosensitive film and expositing it with the electron beam of the SEM.

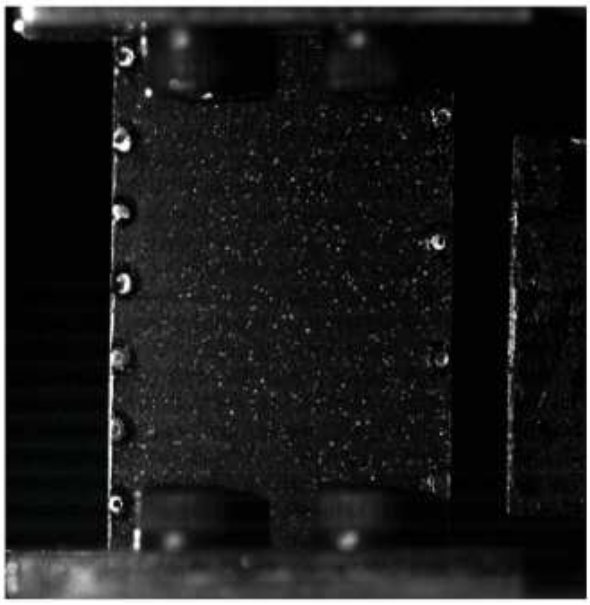

Figure 74: Sample with a pattern performed using black and white paints [122].

The obtained patterns are particularly convenient for DIC at the micron scale (the finest scale corresponding to around 100 nm) on material without natural random surface markers.

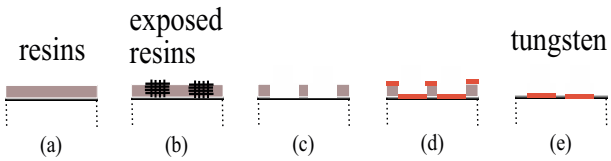

Figure 75: Surface tungsten patterning using e-beam lithography : (a) resin film deposition, (b) electron beam exposure, (c) exposed resin film development, (d) tungsten deposition and (e) residual resin film dissolution

- First of all, a polymer resin is deposited onto the sample surface (see Figure 75 a);
- Then, the sample is placed in the SEM chamber using a specific stage holder to avoid undesired movements during the process of e-beam exposition. Following a pattern design, the sample is exposed only at specific positions (see Figure 75 b) using the e-beam.
- After the e-beam exposition, the specimen is subjected to a chemical treatment using a "developper" solution. This chemical product interacts with the polymer and permits to remove the exposed area (see Figure 75 c);
- Then, a metal layer is sputtered over the specimen surface (see Figure 75 d);
- Finally, the unexposed resin is removed using a "remover" solution. At the end of the process, a pattern made of chosen metal following a given design is obtained (see Figure 75 e).

A detailed description of material required and chemical solutions used for e-beam microlithography is given in Appendix B.

Particularly efficient for gold deposited metal, the removing step is less adapted when using tungsten. In fact, the ultrasound cleaning convenient to remove resin from the sample surface may lead to pattern damage without completely achieving this process. The metal-metal bounds created during the coating step are stronger for tungsten than for gold due to its higher atomic number. An enhancement of this "classical" e-beam microlithography has been used. A thin layer of polymethylmethacrylate (PMMA) was initially used for the first method but the improved one relies on the use of two polymer resins with different sensitivities to e-beam (see Table 23 and Figure 76 a). First, a MMA copolymer resin is spin coated, then a PMMA layer is spin coated on the top of the cured MMA layer.

Polymer	Time (s)	Temperature (°C)	Photosensitivity
MMA(8.5)MAA EL 6	120	150	+
950 K PMMA 4	120	180	++++

Table 23: Curing conditions for the two polymer resins from Microchem.

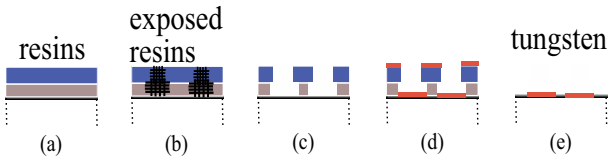

Figure 76: Surface tungsten patterning using e-beam lithography : (a) resin film deposition, (b) electron beam exposure, (c) exposed resin film development, (d) tungsten deposition and (e) residual resin film dissolution. Gray color is used for the copolymer resin and the blue color is used for the PMMA.

This difference in the resin photosensitivities leads to a specific shape of exposed holes in "cap" (see Figure 76 c). During the coating process, the cap limits the creation of bounds between tungsten and resins (see Figure 76 d). These metal free areas allow an easier removal step. The last microlithography step is also less time consuming (see Figure 76 e).

4.2.2.2 The choice of the convenient pattern design

Various geometries could be chosen for the pattern (grid, dot, circle, cross). Doumalin studied and compared the quality of each pattern morphology to conclude that the cross was the elementary pattern that could allow to get the best subpixel informations (in x and y directions) [142]. The pattern showing the best accuracy is constituted of an array of circles.

The chosen pattern for our intergranular crack problem is a combination of dots and microgrids (see Figure 77 and Table 24). It has been obtained using SEM Quanta 600 coupled with the RAITH system which controls the electron beam position (see Appendix B). The microgrids are particularly convenient to detect grain boundary sliding and shear. In the forseen experimental conditions of air environment at 550 °C, it is expected that patterns will interact with the atmosphere leading to potential damage detrimental for DIC. The dimensions and the periodic properties of the microgrids make them easier to monitor. Moreover, they remain visible after some surface damage

compared to a random speckle pattern. The dots are used to confer random characteristics to the pattern and to get kinematic information with a better spatial resolution compared to a periodic grid alone (see Figure 77).

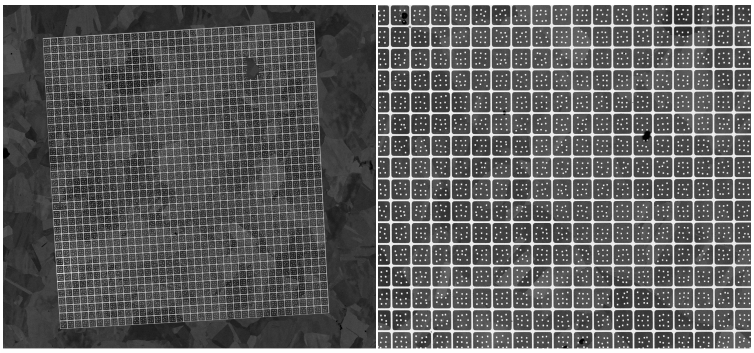

(a) (b)

Figure 77: SEM images of tungsten pattern. The pattern size is 400 µm and the grid step is 10 µm.

Dot size (µm)	Grid size (µm)	Space between microgrids (µm)
0.7-0.8	0.8-1.0	10

Table 24: Parameters of the microgrids/dots pattern.

Figure 78: Index quality and inversed pole figure maps from EBSD of a crack tip region of a 316L SENT specimen after loading (see Chapter 5). The pattern appears in black (due to the poor indexation on the deposited tungsten).

After testing, the evolution of the microstructure can be studied using EBSD technique. The Quality Indice of the method can be used to reveal the tungsten pattern at the sample surface and a correspondance between kinematic fields and polycrystalline structure can be done (see Figure 78). In the performed experiments, we used a pattern similar to that shown in Figure 77 which is particularly convenient for DIC at the micron scale (the finest scale corresponding to some 100 nm) but a methodology to get a DIC analysis at several material scales using a double-scale pattern has also been set-up. The results are introduced in Appendix C.

4.2.3 Imaging distortion quantification

4.2.3.1 Literature results on image distortion quantification

The acquisition of SEM images leads to distorsions due to the imaging technique. These distorsions are specific to each optical system and must be quantified. In fact, if the level of distorsion is too high, it could generate errors or biases in the kinematic fields and reduce the DIC accuracy and performance. Using SEM, the distorsions are more important at large scales. The influence of distorsions on displacement measurements is higher for large displacements.

In 2001, Garcia described in the context of kinematic field measurements the different optical distorsions due to the use of a standard camera in the visible spectrum [143]. Few years later, the distorsions of electronic imaging systems (such as SEM) have been widely studied by Sutton [144, 145, 146] (see Figure 79) or in Grediac [147]. The metrology Guery performed relied both on DIC measurements and rigid body motion to decorrelate the distorsions due to the patterning errors and due to the imaging technique. This quantification of errors can be extended to other measurements performed with SEM such as EBSD [148].

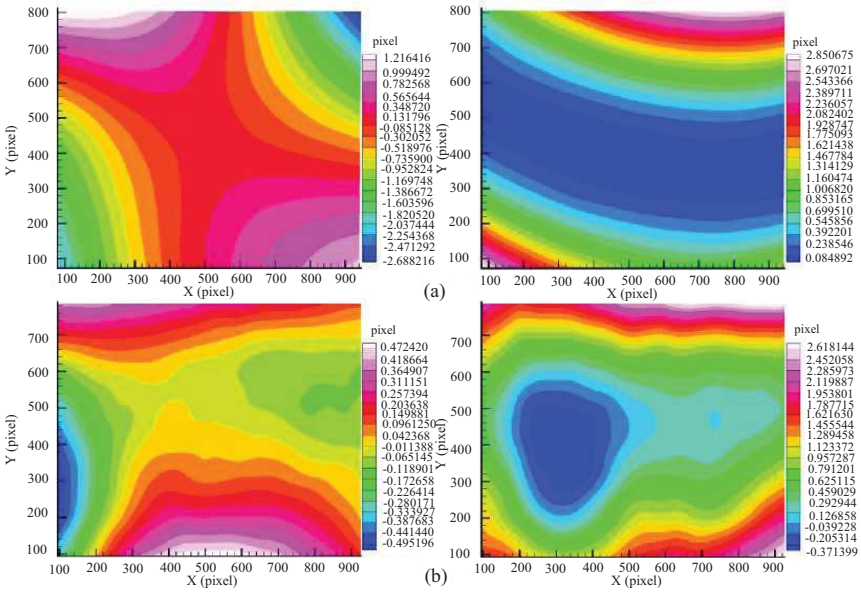

Figure 79: Measured horizontal and vertical distorsion fields in FEI Quanta 200 SEM at magnifications of (a) x200 and (b) x10000 for translations less than 50 pixels [145].

In Figure 80, we present the classical distorsions (barrel and pincushion shape). An example of distorsion effects on displacement fields after a vertical translation are presented in Figure 81 [149]. In this example, the standard deviation of the errors on displacements due to distorsion equals to 2.30.

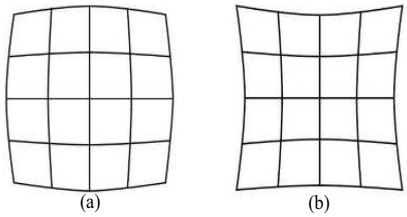

Figure 80: Classical distorsions observed on SEM images (a) a barrel shape and (b) a pincushion shape [147].

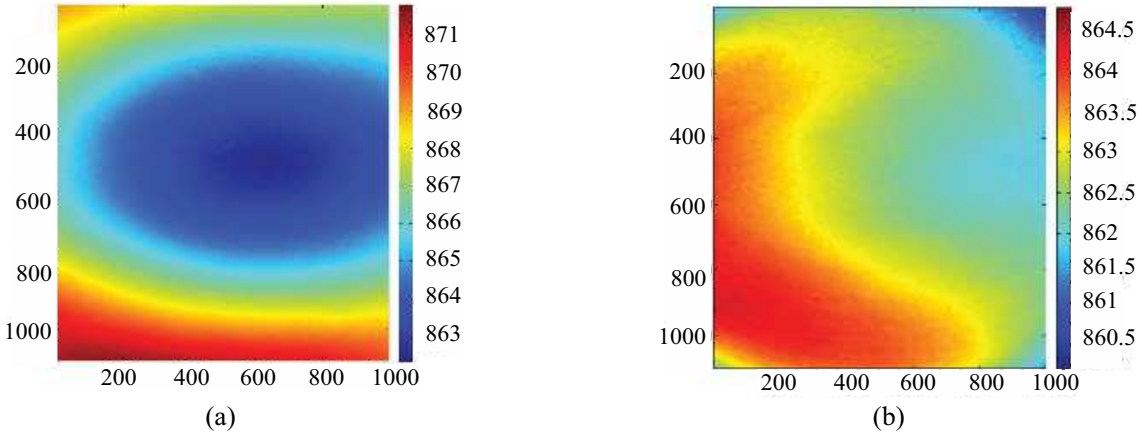

Figure 81: Displacement fields with distorsions (pixel) (a) and (b) with distorsion corrections [149].

In this PhD thesis work, the FEI Quanta 600 SEM has been used to perform most of the SEM imagings as well as e-beam microlithography (see Section 4.2.2) and *in-situ* experiments (see Chapter 5). The quantification of distorsions for this apparatus has already been performed by Guery in his work on the identification of cristal plasticity law parameters for 316L(N) stainless steel using DIC [150]. Guery has shown that the distorsions were negligible (see Figure 82). He used a method based on the acquisition of an a priori known calibration target, which led him to distinguish the errors due to the imaging system (see Figure 82 a,b) and the ones from the patterning errors (see Figure 82 c,d). The images have been taken at a working distance of 14 mm, with an acceleration voltage of 10kV. Images were acquired with a physical size of 240 nm per pixel and stored in 16 bit format.

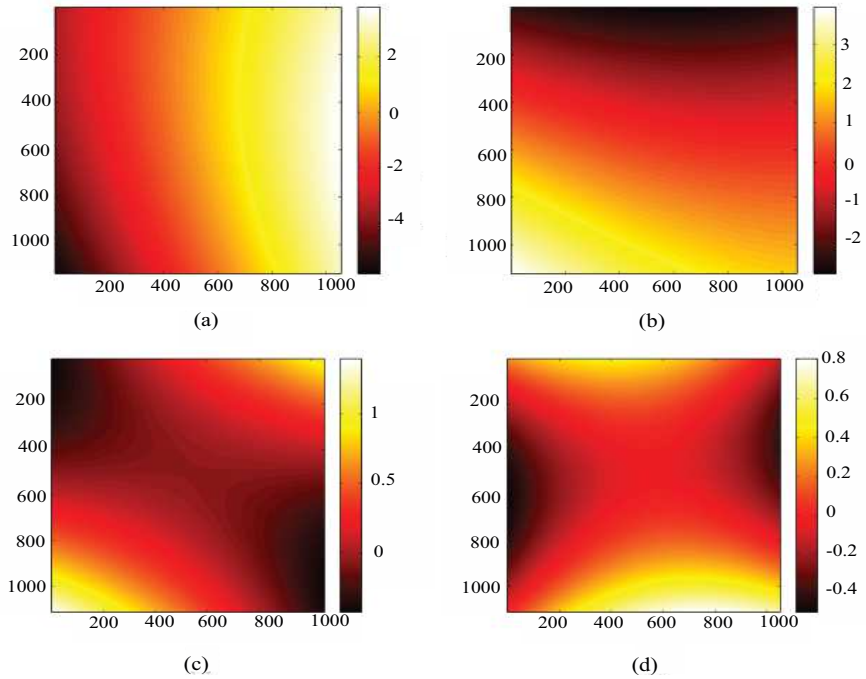

Figure 82: Imaging distorsions of a SEM along the horizontal (a) and the vertical (b) directions, and patterning errors along the horizontal (c) and the vertical (d) directions. The fields are expressed in pixels, whose physical size is 240 nm [121].

Another method to quantify the distorsions of SEM Quanta 600 is proposed in the following. Contrary to what has been used by Guery, this distorsion quantification method does not require the knowledge of the calibration targer pattern in advance and thus anihilates the "patterning errors". The characterization of the distorsions is performed by determining the transfer function of the "imperfect" imaging system. Several translations are imposed to the target. The displacement measured by DIC accounts for the actual translation and the distorsion. The optical distorsions are modeled through a displacement field expressed with a radial distorsion model constructed with polynomial laws as presented in [143, 149]:

$$\mathbf{u}_{dis}(M(x,y),P_d) = \sum_{j=1}^{n_d} b_j.\phi_j(x,y) \tag{4.1}$$

where $(\phi_j)_{j=1:n_d}$ represents the basis functions used to describe the distorsions, P_d is the vector regrouping the distorsion parameters, typically the optical center (x_{oc},y_{oc}) and the distorsion coefficients $(b_j)_{j=1:n_d}$. Classically, radial polynomial distorsion models are used [143], and they are limited to the first order terms:

$$\phi_j(r) = r^j$$

with $j = 1 : n_d$ and $r = \sqrt{(x-x_{oc})^2 + (y-y_{oc})^2}$ representing the distance to the optical center.

The principle of the method used in this PhD thesis work and the main results are presented in the following section.

4.2.3.2 Imaging distortion quantification methodology

It is important to characterize the effects of distorsions on the kinematic measurements and we proposed to quantify SEM distorsions considering translations consistent with the expected displacement during the real experiments. The calibration target consists in a sample similar to that illustrated in Figure 77.

Two sets of displacements have been applied using the SEM translational stage, with an increment of 50 pixels (*i.e* 4.85 µm) between each image. In the following, a reduced set of two cases have been considered for DIC analysis:

- **Case 1**: set of two images, with a dispacement increment of 250 pixels in the horizontal direction.

- **Case 2**: set of two images, with a dispacement increment of 250 pixels in the vertical direction.

The global idea is to characterize the distorsions due to the ”imperfect“ imaging system by performing imposed translation along the directions x and y. The total displacement considered is consistant with the expected displacement reached during an *in-situ* tensile test. Then, the displacement field is decomposed to study the mismatch between the DIC measurements and the imposed displacement using the stage. This procedure will allow to identify the presence of optical distorsions.

The sample used for this study has been machined in the mid-thickness of a plate made of an Inconel alloy 600. After the EDM, it has been polished until OPS finish for microlithographic purposes (see Figure 77). A tungsten pattern made of grids/dots (20 nm) has been deposited and covers a Region of Interest of 400 µm. The acceleration voltage was 10 keV at a working distance of 12.4 mm. The chosen magnification was 635 corresponding to a ZOI of 200 µm. The BSE detector in Z contrast mode is well adapted to increase the contrast between the alloy (nickel base) and the tungsten. The images are encoded using 2048 x 1780 pixels on 16 bits. The physical size of a pixel is 0.097 µm. Between each image acquisition, an incremental displacement of 50 pixels is performed using the SEM stage (*i.e.* 4.85 µm). As suggested above, displacements have been successively carried out in the two directions x and y. Then, DIC analysis have been performed with a local approach using Kelkins routine. Firstly developped by Wattrisse in VisualC++ [151], Kelkins is a component integrated in MAP platform developped by EDF R&D [152]. It has already been used to highlight the strain localisation in single grain of a 304L aggregate [153] or on Zircalloy-4 cladding material.

The displacement operated by the SEM stage is a rigid body translation motion and the measured displacement should correspond to pure translation. In Figure 83, we introduce the kinematic fields resulting from a vertical translation of 250 pixels. The displacement field is not strictly constant.

The distorsions generate heterogeneities resulting from magnification variations or induced by slight variations in the sample tilt with respect to the focal plane. To quantify the transformation homogeneity, we propose to calculate the transformation gradient $\mathbf{F}$ then to perform a polar decomposition of $\mathbf{F}$ as $\mathbf{F} = \mathbf{R}\,\mathbf{U}$. This polar decomposition can be interpreted as the transformation

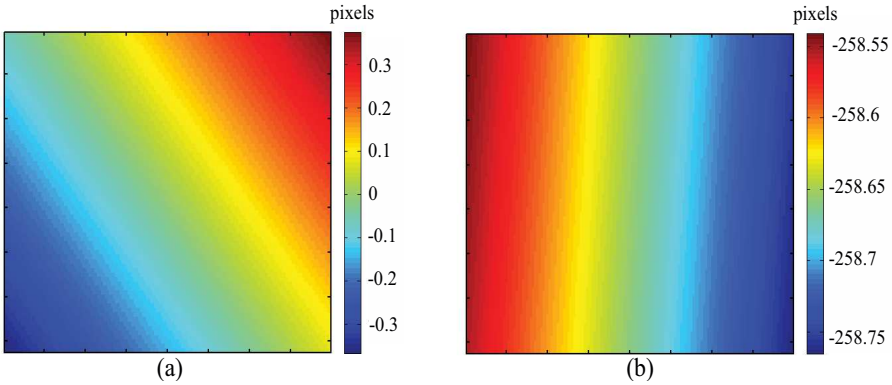

Figure 83: Kinematics fields after a vertical translation of 250 pixels: u_x (a) and u_y (b).

from the initial point to the current point separated by a "deforming transformation" **U** and **R**, an orthogonal rotation matrix.

$$\mathbf{F}(\underline{\mathbf{X}},t) = \frac{\partial \underline{\mathbf{x}}}{\partial \underline{\mathbf{X}}} = \mathbf{I} + \frac{\partial \underline{\mathbf{u}}(\underline{\mathbf{X}})}{\partial \underline{\mathbf{X}}} \tag{4.2}$$

In practice, a dense field $\underline{\mathbf{u}}(\underline{\mathbf{X}})$ is obtained using square subsets of 20 pixels dimension. This displacement is then projected on a polynomial field of the form:

$$u_x = ax + by + c \tag{4.3}$$
$$u_y = dx + ey + f \tag{4.4}$$

with x and y the components of the position $\underline{\mathbf{X}}$, and $a - f$ polynomial coefficients.

Once the fields are projected using the polynomial expressions of Equation (4.3), the transformation gradient simply writes:

$$\mathbf{F} = \begin{pmatrix} \frac{\partial u_x}{\partial x} & \frac{\partial u_x}{\partial y} \\ \frac{\partial u_y}{\partial x} & \frac{\partial u_y}{\partial y} \end{pmatrix} = \begin{pmatrix} a & b \\ d & e \end{pmatrix} \tag{4.5}$$

The rotation angle θ is obtained by applying arccos to $R(1,1)$: $\theta = \arccos(R(1,1))$.

	Case 1	Case 2
Polynomial fit Ux	$\begin{pmatrix} -566.0413 & 0.0008 \\ -0.005 & 0 \end{pmatrix}$	$\begin{pmatrix} 0.0295 & -0.0004 \\ 0.0003 & 0 \end{pmatrix}$
Polynomial fit Uy	$\begin{pmatrix} -3.2133 & -0.0005 \\ 0.004 & 0 \end{pmatrix}$	$\begin{pmatrix} -258.5009 & 0 \\ -0.0001 & 0 \end{pmatrix}$
F	$\begin{pmatrix} 1.0008 & -0.0005 \\ -0.0005 & 1.0004 \end{pmatrix}$	$\begin{pmatrix} 0.9996 & 0.0003 \\ 0 & 0.9999 \end{pmatrix}$
R	$\begin{pmatrix} 1 & 0 \\ 0 & 1 \end{pmatrix}$	$\begin{pmatrix} 1 & 0.0001 \\ -0.0001 & 1 \end{pmatrix}$
U	$\begin{pmatrix} 1.0008 & -0.0005 \\ -0.0005 & 1.0004 \end{pmatrix}$	$\begin{pmatrix} 0.9996 & 0.0001 \\ 0.0001 & 0.9999 \end{pmatrix}$
θ	4.1558×10^{-4}	0.0085

Table 25: Polar analysis of transformation gradient **F**. The horizontal et vertical translation cases are respectively denoted Case 1 and Case 2.

The distorsion fields are obtained by substracting homogeneous fields resulting from a homogeneous deformation (due to misalignments) and a pure translation to the kinematic fields obtained with Kelkins routine. The effects of SEM distorsions are an order of magnitude smaller than the displacement measured by DIC (see Figure 84). The horizontal periodic artefacts (see Figure 84 a) and the vertical periodic artefacts ((see Figure 84 b) are due to the grid pattern. The amplitude of these residual displacements are the same order than the classical displacement noise ranging between 0.01 and 0.1 pixel. It is thus assumed that there is no need to correct distorsions.

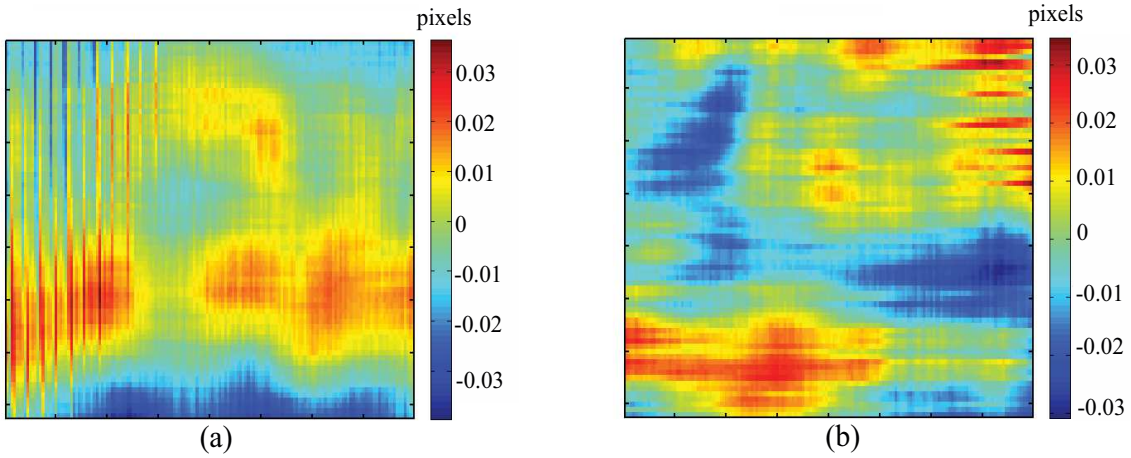

Figure 84: Distorsions u_x field in pixels after a translation of 250 pixels in the vertical direction (a) and distorsions u_y field in pixels after a translation of 250 pixels in the vertical direction (b).

4.3 Linear Elastic Fracture Mechanics

Fracture Mechanics is the science that focuses on the mechanical state associated with cracks, as well as crack initiation and growth. In the 1920's, Griffith initiated researches on brittle fracture [154]. His work was pursued by Irwin [155, 156, 157, 158, 159, 160] and Rice [82]. The researches of George R. Irwin on fracture of steel armor plating during penetration by ammunition has led to the theoretical formulation of fracture. Loadings applied to cracked structures generate discontinuities in the material stress fields or in the kinematic fields. Fracture Mechanics makes use of continuum mechanics laws (equilibrium equations, constitutive equations, etc ...) and of boundary conditions due to the geometrical discontinuity to determine stress, strain or displacement fields. Considering the case of a linear elastic medium, closed form solutions of displacement and stress fields have been derived by Westergaard [161]. In the other cases, it is difficult to identify the relationship between the continuum mechanics expressions and the boundary conditions generated by the crack. For example, Bassani and Qu have obtained complex solutions of stationary cracks in elastic bi-crystals, and they cannot be easily and directly applied due to the non unicity of solutions often given as complex polynomial roots [162, 163, 164, 165, 166, 167].

In case of non-linear behaviour such as plasticity, Hutchinson [168] and Rice-Rosengren [169] have studied the crack-tip stress field shape for a power-law hardening material. Their work is well known as HRR (Hutchinson-Rice-Rosengren) theory (semi-infinite crack in a power-law hardening material). Hutchinson began by defining a stress function Φ expressed for mode I crack problem as an asymptotic expansion:

$$\Phi = C_1(\theta) r^s + C_2(\theta) r^t + \ldots \tag{4.6}$$

where C_1 and C_2 are constants that depend on θ, the angle from the crack plane. This equation is analogous to the Williams' series for the linear elastic case. Restricting the ROI in a region near the crack tip, Hutchinson has expressed the stresses and the displacements in polar coordinates for both plane stress and plane strain conditions. The HRR theory stipulates that the J-integral can be used to characterize the singular stress and strain fields in the crack tip region. Nevertheless, close to the crack tip, the theory is not valid because it neglects finite geometry changes at the crack tip. Their work has been used to study crack growth in aluminium alloy [170, 171] or to adress creep problems [81].

Cracks in solids provide one of the strongest mechanical heterogeneity. Contrary to the circular hole studied by Inglis, the stress is infinite close to the crack tip in a linear elastic medium [172]. To overcome numerical or computational issues associated with the absence of finite limit, two approaches have been developped: the energetical approach [154] and the local approach [173, 161]. In this work, we will only focus on the local approach without performing energetical considerations.

Three elementary crack loadings can be defined. Each of them leads to analytical expressions of stress (σ) or displacement (u) fields. These different modes can be superposed to obtain mixed mode loading.

- The mode I, known as opening mode, is generated by applying a symmetric plane loading compared to the crack plane.
- The mode II named plane sliding is obtained by applying opposite loads parallel to the crack front.

- The mode *III* leads to out-of-plane sliding of the crack lips and is called antiplane shear mode.

The analytical expressions describing the mechanical fields in the vicinity of a crack are generally obtained on simple (infinite or semi-infinite) geometries. For example, a representation of a crack with a length of 2c in a infinite plate is given in Figure 85.

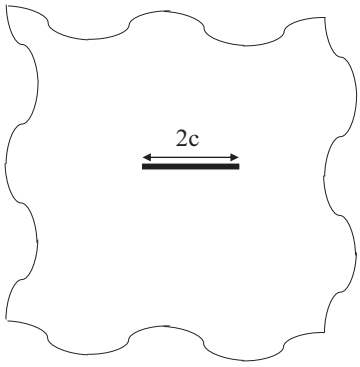

Figure 85: Representation of a crack with a length equals to 2c in a infinite domain.

The closed-form solutions generally express the mechanical fields in the polar coordinate system centered on the crack tip (see Figure 86).

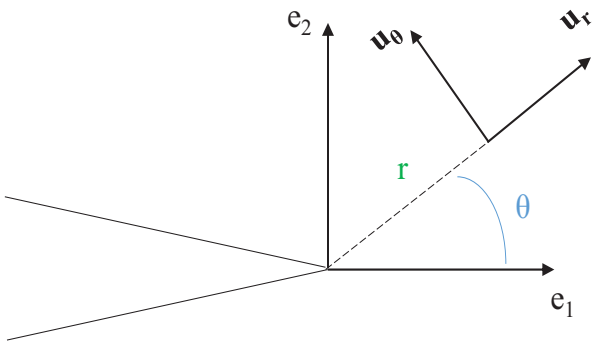

Figure 86: Local coordinate system around the crack tip.

When dealing with a finite geometry, it is necessary to locate the crack frame R_c in the global frame R_0 (see Figure 87).

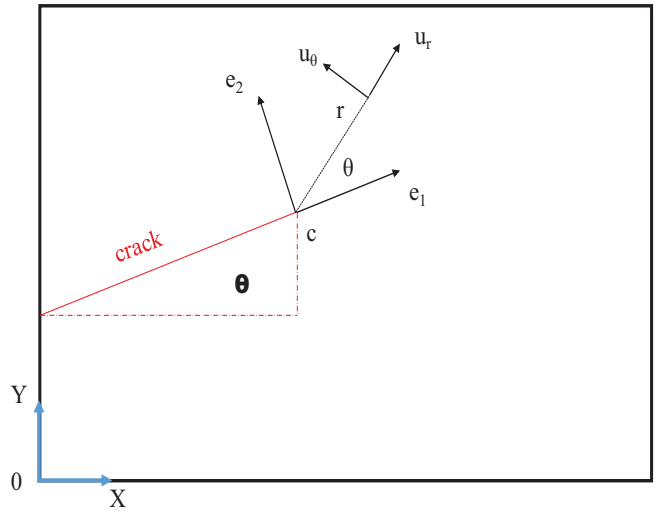

Figure 87: Local coordinate system around the crack tip R_c (c, e_1, e_2) expressed in the global coordinate system (here chosen as the initial image coordinate system R_0 (0, X, Y)).

In the particular case of a crack in 2D infinite domain, Westergaard has identified the analytic solutions of displacement fields as [161]:

$$u_r(r,\theta) = \frac{K_I}{\sqrt{2\mu}}\sqrt{\frac{r}{2\pi}}\cos\frac{\theta}{2}(\kappa-\cos\theta)+\frac{K_{II}}{\sqrt{2\mu}}\sqrt{\frac{r}{2\pi}}\sin\frac{\theta}{2}(\kappa+\cos\theta+2) \tag{4.7}$$

$$u_\theta(r,\theta) = \frac{K_I}{\sqrt{2\mu}}\sqrt{\frac{r}{2\pi}}\sin\frac{\theta}{2}(\kappa-\cos\theta)-\frac{K_{II}}{\sqrt{2\mu}}\sqrt{\frac{r}{2\pi}}\cos\frac{\theta}{2}(\kappa+\cos\theta-2) \tag{4.8}$$

with κ the Kolossov's constant, κ = (3-ν)/(1+μ) for plane stress or κ = (3-4μ) for plane strain conditions.

The mechanical fields near a crack can also be described using the Williams series formalism. The Williams series are validated for a straight semi-infinite crack in a homogeneous isotropic and linear elastic 2D material. The expression of the displacement field relies on a double sum. It can be expressed in the polar coordinates or using complex fields. Introducing solely mode *I* and mode *II*, the displacement field **u** is expressed using the complex notation as [173]:

$$\mathbf{u}(r,\theta) = \sum_{i=I,II}\sum_{n} a_i^n \varphi_i^n(r,\theta) \tag{4.9}$$

where a_i^n are the coefficients of the displacement field on the reference fields φ_i^n that form the complete set of linear elastic fields satisfying a condition of zero traction along the crack path. The components of the decomposition are denoted by the modes $i \in \mathbb{S}_i$ and the orders $n \in \mathbb{S}_n$. The expressions of the basis functions φ_i^n are respectively for mode *I* and mode *II*:

$$\varphi_I^n(r,\theta) = r^{n/2}\left(\kappa e^{jn(\theta/2)}-\frac{n}{2}e^{j(4-n)(\theta/2)}+(\frac{n}{2}+(-1)^n).e^{-jn(\theta/2)}\right) \tag{4.10}$$

$$\varphi_{II}^n(r,\theta) = j.r^{n/2}\left(\kappa e^{jn(\theta/2)}+\frac{n}{2}e^{j(4-n)(\theta/2)}-((\frac{n}{2}-(-1)^n).e^{-jn(\theta/2)})\right) \tag{4.11}$$

Using the complex notation, the displacement vector in the polar coordinates reads:

$$\mathbf{u}(r,\theta) = u_r(r,\theta) + j u_\theta(r,\theta) \tag{4.12}$$

where j is the perfect imaginary number ($j = e^{\frac{j\pi}{2}}$).

The displacement components in the global coordinate system can then be written:

$$u_x(r,\theta) = \Re\left(\sum_{i=I,II}\sum_{n} a_i^n \varphi_i^n(r,\theta)\right) \tag{4.13}$$

$$u_y(r,\theta) = \Im\left(\sum_{i=I,II}\sum_{n} a_i^n \varphi_i^n(r,\theta)\right) \tag{4.14}$$

with $\Re(\mathbf{a})$ the real part and $\Im(\mathbf{a})$ the imaginary part of complex $\mathbf{a}$.

According to the value of order n of the decomposition, the fields have different meanings and can be separated into two categories:

- subsingular terms (for $n \geqslant 0$). These terms vanish when r tends to 0.
- supersingular terms (for $n < 0$). The displacement fields are singular when r tends to 0.

Let us remark that for $n = 1$, the fields are proportional to the analytic expressions given by Irwin and are defined hereafter as Westergaard's expressions. The amplitude is a linear function of stress intensity factors (K_I, K_{II}, K_{III}). The stress intensity factors for mode I and II (K_I and K_{II}) depend on the magnitude of the load, the crack length and further geometrical parameters of the considered configuration.

More recently, Barranger has studied the displacement fields in a cracked SENT specimen in mode I [174]. He compared theory with 3D experiments obtained with Digital Volume Correlation. He used the first and the second terms of the Williams's series.

$$u_r(r,\theta) = \left(\frac{K_I}{\mu}\right)\sqrt{r/2\pi}\,\cos\left(\frac{\theta}{2}\right)\left(\frac{(1-\nu)}{(1+\nu)} + \sin^2\left(\frac{\theta}{2}\right)\right) - \left(\frac{\nu\,\sigma_{yy}\,\cos(\theta)}{E}\right) \tag{4.15}$$

$$u_\theta(r,\theta) = \left(\frac{K_I}{\mu}\right)\sqrt{r/2\pi}\,\sin\left(\frac{\theta}{2}\right)\left(\frac{2}{(1+\nu)} - \cos^2\left(\frac{\theta}{2}\right)\right) + \left(\frac{\sigma_{yy}\,\sin(\theta)}{E}\right) \tag{4.16}$$

with ν the Poisson coefficient.

These analytic expressions of displacement can be used as shape functions for the DIC [133, 175, 176]. In this case, the DIC procedure aims at identifying the coefficients a_i^n of the shape function considering the crack tip position as known. These approaches rely on the linearisation of the correlation criterion provided by the linear shape functions. The expressions in this section can be used as a basis of shape functions and combined with a classical DIC procedure with local approach. A functional between the displacement measured by DIC and from the LEFM expressions can be used. By minimizing this functional, the a_i^n can be identified as well as the crack tip position (x_c,y_c). This method is presented in the following section.

4.4 Crack parameters identification procedure

Using Williams' series displacement field provided in Equation (4.9), kinematic fields (u_r, u_θ) are provided in the local coordinate system R_c.

The displacement has to be expressed in the image coordinate system R_0 using the following relationships [1]:

$$r = \sqrt{(x-x_c)^2+(y-y_c)^2} \tag{4.17}$$

$$\theta = \arctan\left(\frac{x-x_c}{y-y_c}\right) \tag{4.18}$$

$$u_r = u_x\cos(\theta)+u_y\sin(\theta) \tag{4.19}$$

$$u_\theta = -u_x\sin(\theta)+u_y\cos(\theta) \tag{4.20}$$

Let us call $\mathbf{u}_k^W$ the displacement field expressed by Williams' series (Equation (4.9)), and $\mathbf{u}_k^{exp}$ a displacement field obtained experimentally on a set of control points $\mathbb{S}_{cp} = (x_k,\ y_k,\ k = 1\ldots N)$. Let us introduce a set of coefficients $\mathbf{p}$ allowing to parameterize the crack displacement field on the same control points $\mathbf{u}_k^W(\mathbf{p})$. The crack parameter identification consists in minimizing the gap between the modelled and the experimental field as follows:

$$\mathbf{p}^{opt} = \underset{p}{\text{Arg min}} \sum_{k=1}^{N} \left(\mathbf{u}_k^W(p) - \mathbf{u}_k^{exp}\right)^2 \tag{4.21}$$

The set of identified parameters $\mathbf{p}^{opt}$ can include several unknowns to be determined, among which:

- the crack tip coordinates (x_c, y_c),
- the crack orientation Θ,
- a reduced set of Williams' coefficient a_i^n, for a choice of orders $i \in \mathbb{S}_i$ and of modes $n \in \mathbb{S}_n$.

In the numerical method developped here, the subset of orders $\mathbb{S}_i$ is included in $\{I, II\}$ and the subset of modes $\mathbb{S}_n$ is a set of natural integers (thus potentially including subsingular and supersingular terms). If the subsingular modes are neglected, $\mathbb{S}_n \subset \mathbb{N}^+$

The crack tip position identification needs displacement fields as input data. Let N represent the total number of measured displacements. A restriction on the $\mathbf{u}_k^{exp}$ values can be done using the parameter R_{max} (see Figure 88). This parameter defines a Region Of Interest (ROI) for the projection around the crack tip position estimation $(x_0^{est}, y_0^{est}, \Theta_0^{est})$. The cost function minimization (Equation (4.21)) is then performed on a restricted area of the kinematic fields:

$$\mathbb{S}_R = \{k = 1..N \text{ with } \sqrt{(x_k-x_0)^2+(y_k-y_0)^2} \leqslant R_{max}\}$$

$$\mathbf{p}^{opt} = \underset{p}{\text{Arg min}} \sum_{k\in\mathbb{S}_R} \left(\mathbf{u}_k^W(p) - \mathbf{u}_k^{exp}\right)^2$$

[1] $\theta = 0$ if $x_c = 0$ and $y_c = 0$

The linearity of $\mathbf{u}_k^W(p)$ is verified for the Williams series coefficients but not for the crack parameters (x_c, y_c, Θ). Thus, to identify the optimal values of the set of parameters (a_i^n, (x_c, y_c, Θ)), a three steps minimization is proposed:

1. Firstly, the estimated crack parameters are considered and a linear minimization is performed to identify the corresponding a_i^n.

2. Secondly, a non-linear minimization is used to identify the optimum crack parameters by considering all the crack parameters (x_c, y_c, a_i^n). The non-linear minimization is performed using an unconstrained gradient-based algorithm.

3. To validate the convergence and the stability of the procedure identification results, the non linear minimization is performed a second time using the optimized parameters as initial guess and the distance between the parameters identified at each procedure iteration $d_{it1-it2}$ is calculated.

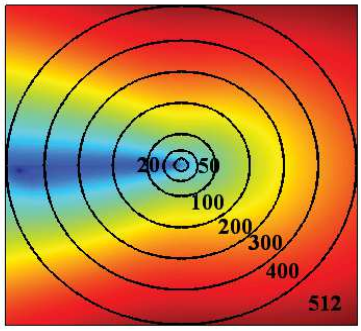

R_{max} (pixels)
512
400
300
200
100
50
20

Figure 88: Different sizes of Region Of Interest R_{max} for a crack position estimation in the center of a 1024 x 1024 image.

4.5 Assessment methodology and robustness of the crack parameters identification

Finite element (FE) simulations of intergranular cracks in bicrystals have been performed and used as reference fields to develop an identification procedure of the crack tip position. The virtual experimental fields are considered as $\mathbf{u}^{exp}$ in the minimisation problem of Equation (4.21).

Several constitutive behaviours will be considered: homogeneous elasticity, homogeneous isotropic plasticity (J_2) and crystal plasticity (anisotropic and heterogeneous). The crystal plasticity law proposed by Meric and Cailletaud has been chosen [177]. Then two kind of boundary conditions can be used to load the structure: the Westergaard's expressions in displacement prescribed for the global boundaries (Equation (4.9) with $n = 1$) or imposed uniform displacement on the upper and lower boundaries while the others are traction-free.

The different cases will be studied considering an increasing level of errors compared to the LEFM model (Figure 89). The comparison between $\mathbf{u}^{exp}$ from isotropic elasticity case and $\mathbf{u}^W$

projection should lead to the minimum errors. Then, it is expected that model errors will be significant as we consider imposed displacement as boundary conditions and heterogeneous, anisotropic and non- linear material behaviour.

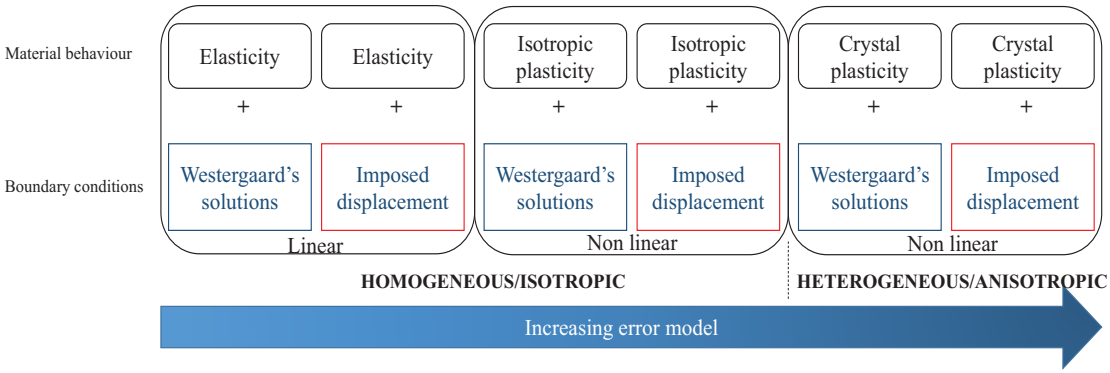

Figure 89: The assessment procedure is performed to quantify the modelling errors: from isotropic elasticity to anisotropic crystal plasticity.

Two strategies named Case I and Case II have been used to assess the procedure performance (Figure 90). In the Case I, the displacement fields from FEM have been used as the displacement from the experience $\mathbf{u}^{exp}$. These fields are considered as the reference fields. This approach will allow to quantify the errors resulting from an inadequate choice of model. The displacement fields are then projected onto the LEFM base and have been compared to the projected displacement fields $\mathbf{u}^{W}$. In the Case II, the considered experimental displacement fields are kinematic fields from DIC measurements performed on digital images deformed using the dispplacement field given by FE computation. This strategy will allow to quantify the coupled errors resulting from the DIC analysis as well as the errors from the choice of models not consistent with LEFM theories.

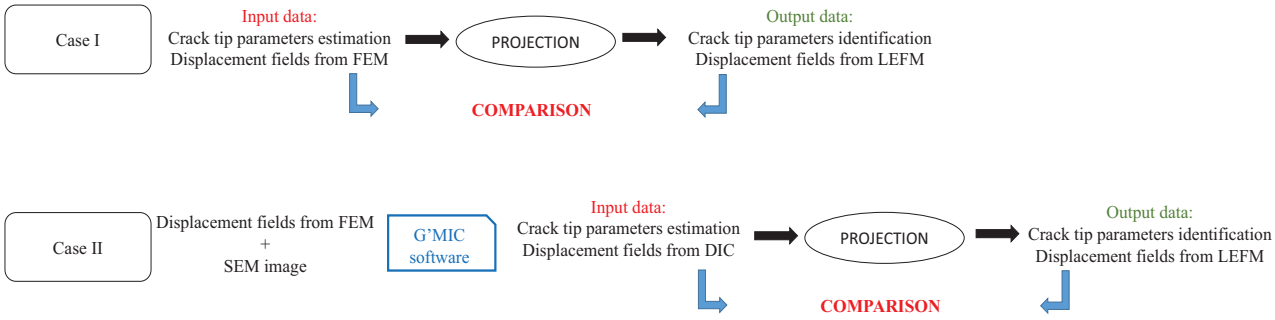

Figure 90: Strategies for the assessment of crack tip position identification procedure.

In the following sections, we will introduce the finite element modelling using Code_Aster software. Then, the procedure robustness is characterized considering cases without errors resulting from measurement technique (Case I). Finally, the procedure accuracy and performance will be assessed considering displacement fields containing errors from the DIC technique (Case II). The aim of this part is to propose a complete study of sensitivity to the crack parameter identification procedure. The influence of the initial guess of crack tip position, the sensitivity to the noise

and to the size of the Region Of Interest (ROI) surrounding the crack tip will be discussed.

4.5.1 The Finite Element Modelling (FEM) using Code_Aster

The simulation of the experimental tensile test is performed using the finite element software Code_Aster. An intergranular cracked bicrystal has been modelled and meshed with quadratic quadrangles (see Figure 91 a) using the Salome software (www.salome-platform.org). To improve numerical convergence, the crack is modelled as a notch of very small radius (r_{notch} = 0.005 µm). A mesh refinement in the notch tip region has been performed (see Figure 91 b). The mesh convergence has been assessed by performing simulations with different mesh refinements. The mesh presented in Figure 91 is considered as the best trade-off to obtain an accurate calculation at a reasonable calculation cost.

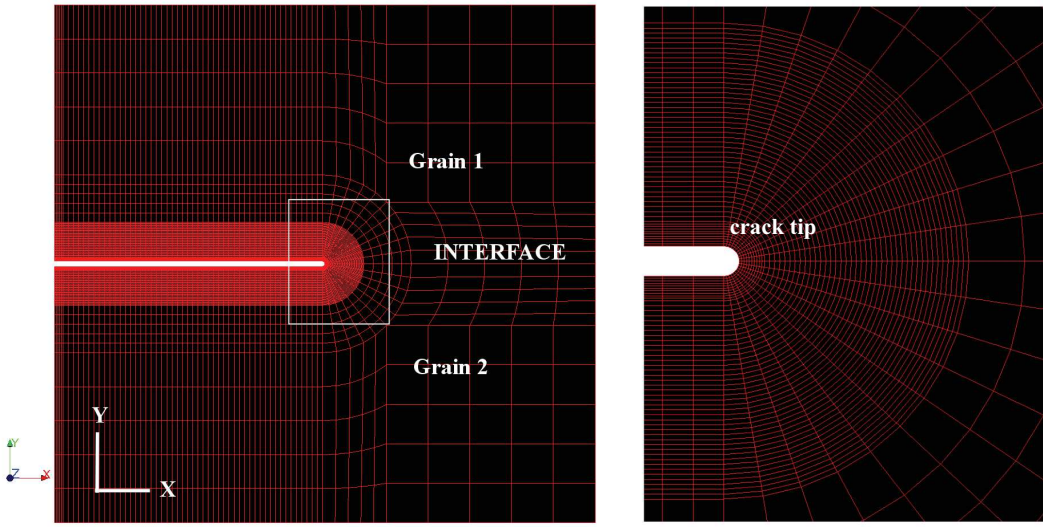

Figure 91: Cracked bicrystal mesh (7850 faces and 23951 nodes).

The crack position is perfectly known and its tip is placed in the image center with coordinates (x_c = 0.0, y_c = 0.0, Θ = 0.0 radian). Because of the non-dimensional nature of the problem, the width and height of the simulation box are taken equal to 1. This mesh will be used in the Case I and in the Case II .

As mentioned before, two boundary conditions can be used to load the structure: Westergaard's solutions in displacement prescribed for the global boundary (see Figure 92 a), or imposed displacement on the upper and lower boundaries while the lateral ones are traction-free (see Figure 92 b). This latter case (material properties and boundary conditions) is not consistent with the analytic solutions given by the Williams' series [173].

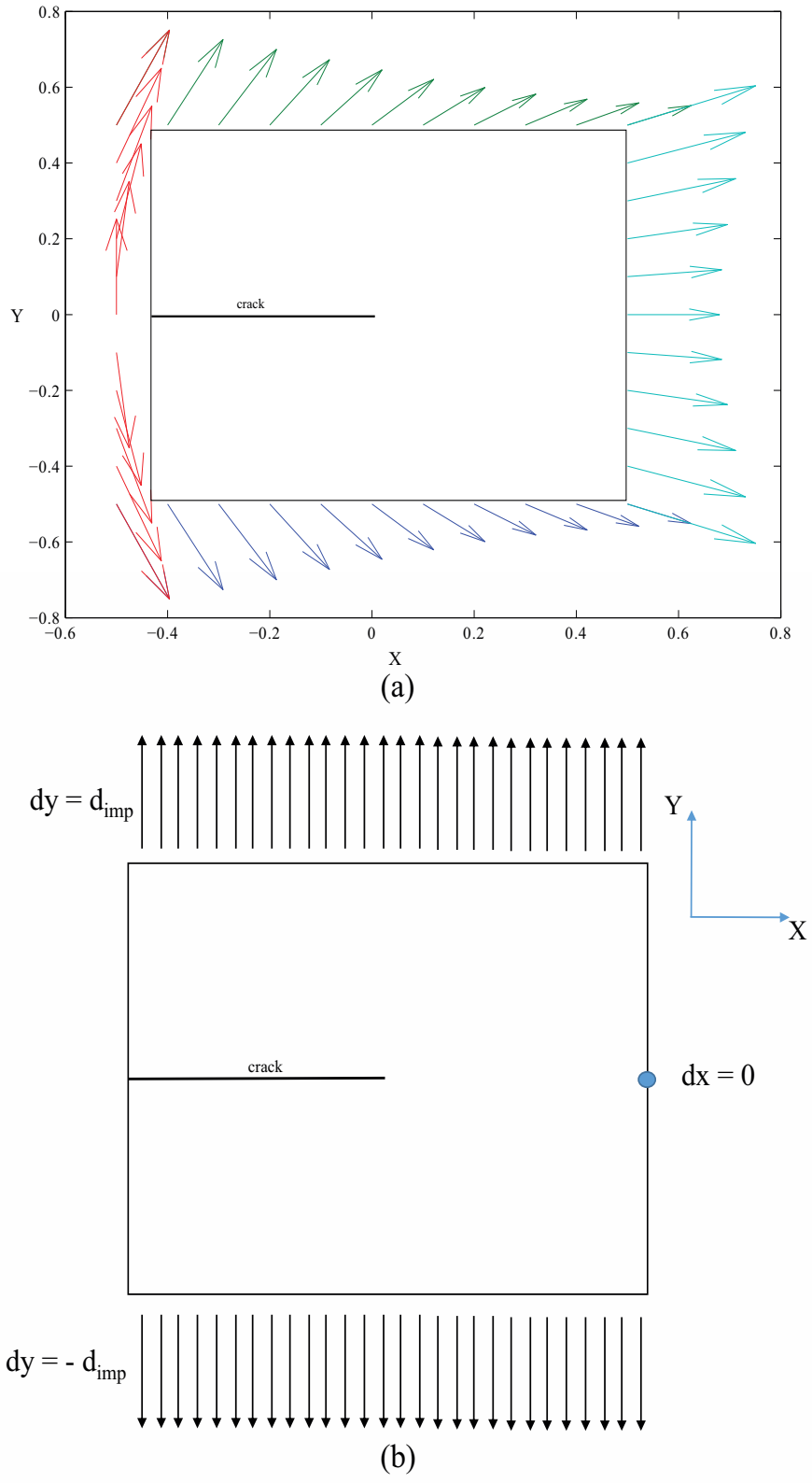

Figure 92: Representation of the boundary conditions used in the FE calculation: Westergaard's solutions (a) and "natural uniaxial tension" (b).

The Westergaard's expression used as boundary conditions ($\mathbf{u}^W$) is considering exclusively the mode I and the order $n = 1$:

$$\mathbf{u}^W(r,\theta) = a_I^1 \varphi_I^1(r,\theta) \tag{4.22}$$

$$\varphi_I^1(r,\theta) = \sqrt{r}\left(\kappa e^{j(\theta/2)} - (\frac{1}{2})\, e^{3j(\theta/2)} + (\frac{-1}{2})\, e^{-j(\theta/2)}\right) \tag{4.23}$$

whith κ is the Kolossov's constant ($\kappa = (3-\nu)/(1+\nu)$ in the stress plane conditions), with ν the Poisson coefficient.

In the following parts, the displacement fields are projected onto a LEFM base considering the mode I and the orders 0, 1 and 2.

As mentioned earlier, several mechanical behaviours have been considered for the FE calculation: elasticity, macroscopical isotropic plasticity (J_2) and crystal plasticity. The chosen material parameters in elasticity, macroscopic isotropic plasticity are given in Table 26. The parameter σ_y [MPa] represents the yield stress and H the slope of the isotropic hardening.

E (MPa)	ν	H (MPa)	σ_y (MPa)
193.10^3	0.29	2×10^3	300

Table 26: Material parameters in the elastic and J_2 cases.

The law chosen to describe the plastic response of single Face Centered Crystals (FCC) was initially proposed by Méric and Cailletaud [177] and is now commonly used to describe cyclic loadings in austenitic stainless steels [178]. Crystal plasticity is also relevant to model crystal creep deformation, for example on Ni-based single crystals [179] or in polycrystalline Ti-based alloys such as Ta_6V [180]. The cracked bicrystal has been separated in two areas each correponding to one grain. A chosen misorientation has been attributed to each zone (Figure 91).

The Meric-Cailletaud's law is a viscoplastic law and its flow equation writes :

$$\dot{p}_s = \left\langle \frac{|\tau_s - c\alpha_s| - r_s(p_s)}{k} \right\rangle_+^n \tag{4.24}$$

$$\dot{\gamma}_s = \dot{p}_s \frac{\tau_s - c\alpha_s}{|\tau_s - c\alpha_s|} \tag{4.25}$$

where $\langle\cdot\rangle_+$ refers to the positive part, $\dot{\gamma}_s$ the sliding velocity, τ_s the resolved shear stress and α_s the kinematic hardening. Parameters k and n are Norton's parameters and c represents the kinematic hardening modulus. Parameters p_s is the cumulated plastic deformation on the sliding system s:

$$p_s = \int_0^t |\dot{\gamma}_s| dt \tag{4.26}$$

The isotropic hardening r_s and the kinematic hardening α_s are defined as:

$$r_s = r_0 + q\left(\sum_{j=1}^{12} h_{sj}(1-\exp^{-bp_j})\right) \tag{4.27}$$

$$\dot{\alpha}_s = \dot{\gamma}_s - d\alpha_s \dot{p}_s \tag{4.28}$$

where r_0 is the initial critical resolved shear stress and h_{sj} stand for the terms of the interaction matrix between slip systems. Parameters q and b characterize the hardening and its saturation. d is a drag coefficient for the non linear kinematic hardening.

The Meric-Cailletaud's law depends on several material parameters whose values are given in Table 27 and Table 28 for a 316L polycristalline aggregate [178, 181].

E (MPa)	ν
193×10^3	0.29

Table 27: Parameters for the elasticity in case of Meric Cailletaud law for 316 SS [178, 181].

n	k (MPa.s$^{1/n}$)	c (MPa)	r_0 (MPa)	q (MPa)	b	h	d
11	12	40×10^3	120	237.1934	10	$\forall i,j,\ h_{ij} = 1.0$	1500.0

Table 28: Parameters for the Meric Cailletaud's law for 316 SS [178, 181].

A convention for the test designation is given below:

Mechanical behaviour	Boundary conditions
IE or IP or CP	WS (a_I^1) or ID (d_{imp})

with *Mechanical behaviour* referring to Isotropic Elasticity (IE), Isotropic Plasticity (IP) or Crystal Plasticity (CP), with *Boundary conditions* referring to the boundary conditions chosen to load the structure: Westergaard's Solutions (WS) associated with the loading coefficient a_I^1 or imposed displacement (ID) associated with the loading coefficient d_{imp}.

By choice, the position variables are expressed in the following using as referential a 1024 x 1024 image. And the x and y coordinates are ranging between 0 and 1023 pixels. The known crack tip coordinates are (x_c, y_c) = (512.0,512.0).

A convention is chosen for the estimation of the crack tip parameters and for the optimized values coming from the projection:

$$\begin{cases} x_{est} = \text{x coordinate of the estimated crack tip position} \\ y_{est} = \text{y coordinate of the estimated crack tip position} \\ \Theta_{est} = \text{angle of the estimated crack position} \\ x_{opt} = \text{x coordinate of the optimized crack tip position} \\ y_{opt} = \text{y coordinate of the optimized crack tip position} \\ \Theta_{opt} = \text{angle coordinate of the optimized crack position} \end{cases}$$

In the next section, the case of elasticity using displacement fields from FE with the two different boundary conditions is presented.

4.5.2 Test Case I considering an elastic behaviour

In Section 4.5.1, the parameters for the elastic behaviour have been given: the Young modulus is equal to 193 GPa and the Poisson's ratio $\nu = 0.29$. After the FE calculation, the displacement fields have been used as input data for the crack tip position identification. A comparison between the input displacement fields and the reconstructed displacement fields from LEFM considering the optimized parameters is proposed. In what follows, the Kolossov constant introduced in the Williams series is chosen in accordance with the FE computation 2D mechanical assumption (plane stress) and with the imposed elatic constants.

4.5.2.1 Test case IE-WS(0.001): isotropic elasticity and Westergaard boundary conditions

The crack parameter identification relies on the minimization of a cost function (see Equation (4.21)). In order to avoid convergence problems (multiple local minimas), the convexity of the cost function has to be verified. We propose to study the influence of the R_{max} parameter on the minimization of the cost function for the most adapted case : IE-WS(0.001). In Figure 93, the cost function has been plotted considering a fixed Θ^{est} of zero. Different initial estimates of crack tip are considered with the following bounds: $x^{est} \in [205,818]$, $y^{est} \in [0,1024]$. Different values of R_{max} are also considered.

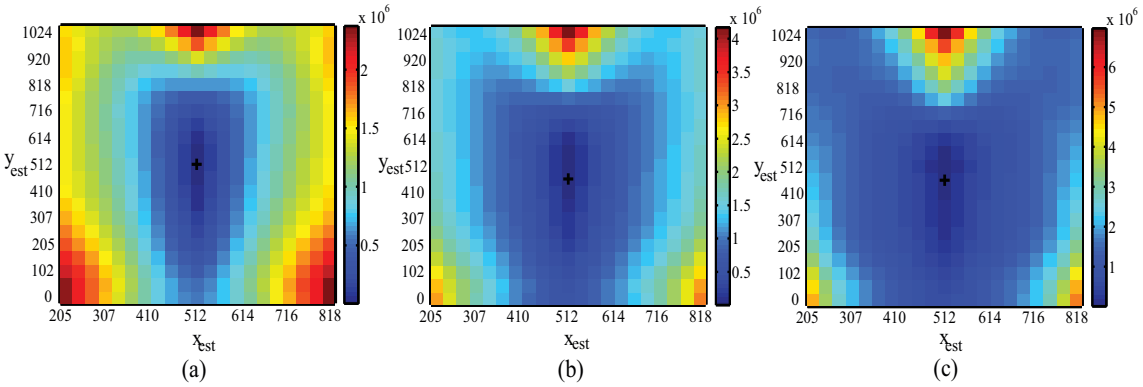

Figure 93: Cost function representations for IE-WS: (a) R_{max} = 512 pixels, (b) R_{max} = 400 pixels and (c) R_{max} = 300 pixels.

Figure 93 shows that the cost function is not convex on the studied domain. Nevertheless, we observe that the minimum is close to the known position of the crack tip.

An example of comparison between the displacement fields from FE computation and LEFM reconstruction is proposed in Figure 94. Due to interpolation issue, an erroneous displacement is observed in the kinematic fields from FE calculation at the intersection between left FE global boundary and the crack (see Figure 94 a).

In the results from crack parameter identification procedure, the cross symbol is used for the estimated value whereas the circle symbol is used for the optimized values. Notations u_x^{RBM} and u_y^{RBM} stand for the displacement field associated to the rigid body motion (translation and rotation).

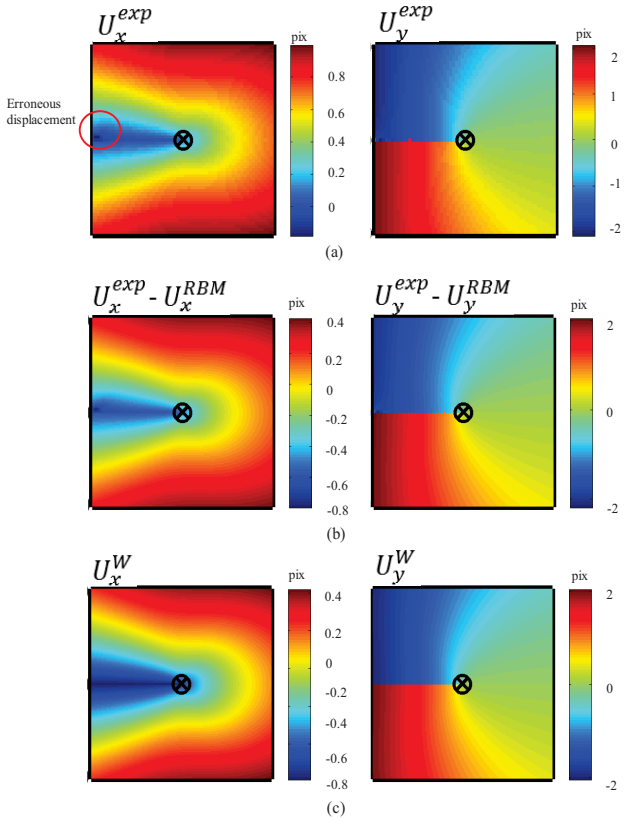

Figure 94: Comparison between the displacement fields for IE-WS R_{max} = 512 pixels: u_x^{exp}, u_y^{exp} (a) , $u_x^{exp} - u_x^{RBM}$, $u_y^{exp} - u_y^{RBM}$ (b) u_x^W, u_y^W (c). Notations u_x^{RBM} and u_y^{RBM} stand for the displacement field associated to the rigid body motion (translation and rotation). The cross symbol is used for the estimated values whereas the circle symbol is used for the optimized values.

When the estimated values correspond to the known crack tip position, the procedure is able to robustly identify the optimized crack parameters at the known crack parameters (x^{opt}, y^{opt}, Θ_{opt}) = (511.76,512.0, -5.66 $\times$ 10^{-15} radian) and the Williams parameter $a_I^{1\,opt}$ = 0.0286 with R_{max} = 512 pixels. The parameter $a_I^{1\,opt}$ is similar to one in the direct FE computation: a_I^1 = 0.0226.

The sensitivity to the ROI, the initial guessed values and to the noise is presented in the following paragraphs.

Sensitivity to the ROI dimension parameter R_{max}:

The considered ROI for the identification procedure has been decreased, with R_{max} = 128 pixels. The same strategy has been applied to assess the efficiency of the procedure to identify the correct

crack tip position, with a restricted set of points around the estimated coordinates of the crack tip. The crack parameters identified by the procedure correspond to the known crack tip position (x^{opt}, y^{opt}, Θ^{opt}) = (512.24, 512.0, 7.17×10^{-16} radian) and the Williams coefficient $a_I^{1\,opt} = 0.0226$ is similar to that provided to the direct FE calculation.

The optimized crack parameters considering R_{max} equals to 128 pixels, are in good agreement with the known crack tip position and the kinematic fields are well reproduced by the Williams series. The procedure is particularly efficient because there is no mismatch between the applied boundary condition and the choice of the shape function basis to describe the linear elastic response of the material.

Sensitivity to the initial crack parameters:

In the study of the sensitivity of the procedure to the initial guess values of the parameters to be optimized, R_{max} has been chosen equal to R_{max} = 512 pixels. One hundred draws of x_0^{est} and y_0^{est} with a standard deviation error of 10% ($\sigma_{x_0^{est}}$, $\sigma_{y_0^{est}}$ = 50 pixels) relative to the image size have been performed (see Figure 95).

The results of x_{opt} and y_{opt} represented in Figure 96 a together with the draws of x_0^{est} and y_0^{est}. Globally, the optimized positions are close to the known crack tip position (x_c, y_c) = (512, 512) (see Figure 96 b).

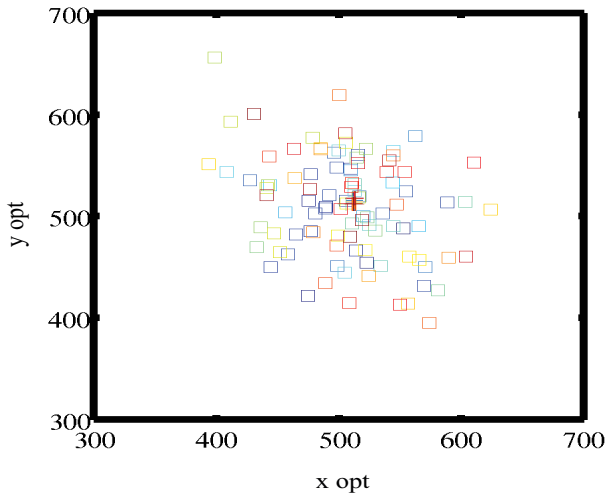

Figure 96: Results from optimization for one hundred draws with $\sigma_{x_0^{est}}$, $\sigma_{y_0^{est}}$ = 50 pixels considering IE-WS (R_{max} = 512 pixels). The square symbol is used for the optimized values and the cross symbol is used for the optimized values.

The estimated mean and standard deviation for x, y and Θ have been compared to the optimized ones (see Table 29). The parameter $\sigma_{a_I^{1\,est}}$ is identified by the procedure before non-linear minimization.

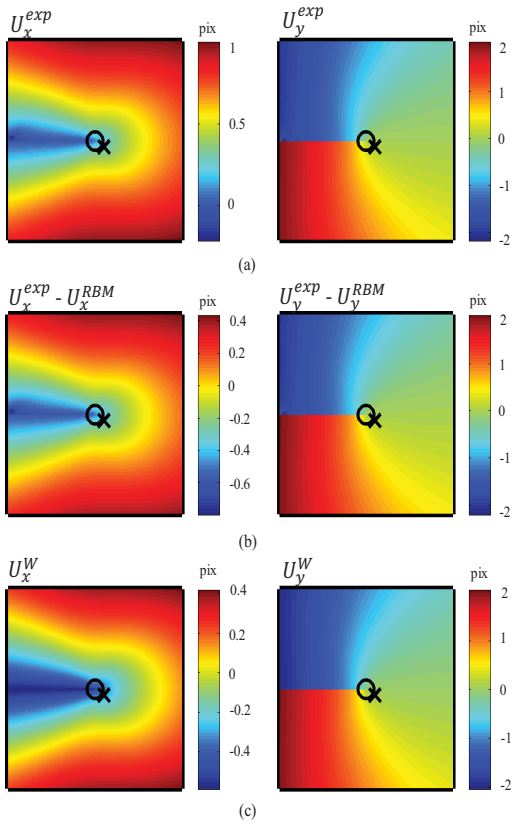

Figure 95: Comparison between the displacement fields for IE-WS (R_{max} = 512 pixels) and $\sigma_{x_0^{est}}$, $\sigma_{y_0^{est}}$ = 50 pixels: u_x^{exp}, u_y^{exp} (a), $u_x^{exp} - u_x^{RBM}$, $u_y^{exp} - u_y^{RBM}$ (b) u_x^W, u_y^W (c). Notations u_x^{RBM} and u_y^{RBM} stand for the displacement field associated to the rigid body motion (translation and rotation). The cross symbol is used for the estimated values whereas the circle symbol is used for the optimized values.

x_c	512	$\bar{x}^{est}$	512	$\bar{x}^{opt}$	512.29
y_c	512	$\bar{y}^{est}$	512	$\bar{y}^{opt}$	512.86
Θ	0.0	$\bar{\Theta}^{est}$	0	$\bar{\Theta}^{opt}$	-3.1×10^{-14}
a_I^1	2.26×10^{-2}	$\bar{a}_I^{1\,est}$		$\bar{a}_I^{1\,opt}$	2.85×10^{-2}
		$\sigma_{x_0^{est}}$	50	$\sigma_{x_0^{opt}}$	0.94
		$\sigma_{y_0^{est}}$	50	$\sigma_{y_0^{opt}}$	2.7425
		$\sigma_{\Theta_0^{est}}$	0	$\sigma_{\Theta_0^{opt}}$	4.36×10^{-13}
		$\sigma_{a_I^{1\,est}}$		$\sigma_{a_I^{1\,opt}}$	4.50×10^{-5}

Table 29: Comparisons of statistics for estimated and optimized crack parameters in pixels and radian for IE-WS with $\sigma_{x_0^{est}} = \sigma_{y_0^{est}}$ = 50 pixels and R_{max} = 512 pixels.

Table 29 shows that the identification is robust with respect to the initial guess on the crack

position. The average of the optimized parameters are very close to to the theoretical values and the standard deviation of the optimized parameter is very small with respect to these theoretical values. The standard deviation on the optimized positions $\sigma_{x_0^{opt}}$ and $\sigma_{y_0^{opt}}$ is 20 times smaller than the imposed perturbation on $x^{est\,2}$ and $y^{est\,2}$. In Table 29, the cells corresponding to ($\bar{a}_I^{1\,est}$ and $\sigma_{a_I^{1\,est}}$) are empty because these values are computed by the algorithm, they are not chosen by the user.

To confirm the stability of the procedure, the distance between the optimized values from the first optimization ($x^{opt\,1}$, $y^{opt\,1}$) and the second one ($x^{opt\,2}$, $y^{opt\,2}$) is studied:

$$d_{it1-it2} = \sqrt{(x^{opt\,2} - x^{opt\,1})^2 + (y^{opt\,2} - y^{opt\,1})^2} \tag{4.29}$$

Globally, the optimization procedure is stable: the distance between the two minimizations $d_{it1-it2}$ (see Section 4.4) is inferior to 10 pixels for 50% of the draws and inferior to 20 pixels for 70% of draws (see Figure 97).

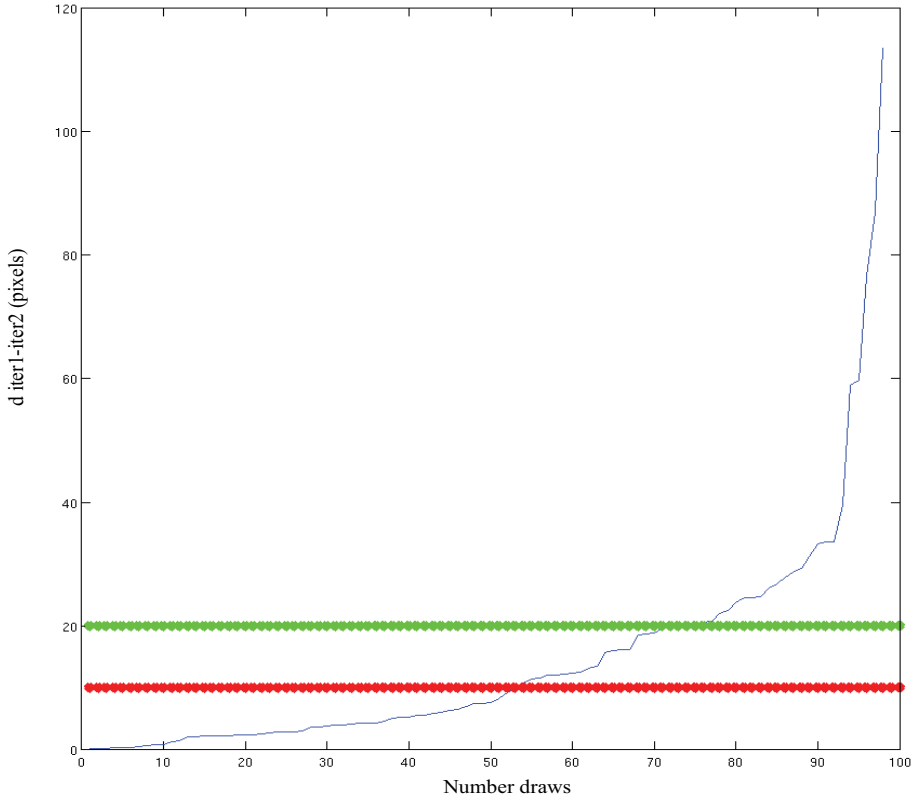

Figure 97: Distance between the optimized solutions from the two minimizations. The red line is used for $d_{it1-it2}$ equals to 10 pixels and the green line is used for $d_{it1-it2}$ equals to 20 pixels.

A complementary study with a standard deviation error of 0.1 radian for Θ_0^{est} ($\sigma_{\Theta^{est}}$ = 0.1 radian) has been performed (see Figure 98). The identification procedure is able to identify accurately the crack orientation even if the initial guess value is far from $\Theta_0 = 0$ radian (see Figure 98 a). The maximal error after optimization is inferior to 0.02 radian (*i.e.* 1.5 °) for the angle and 10 pixels for the crack tip coordinates.

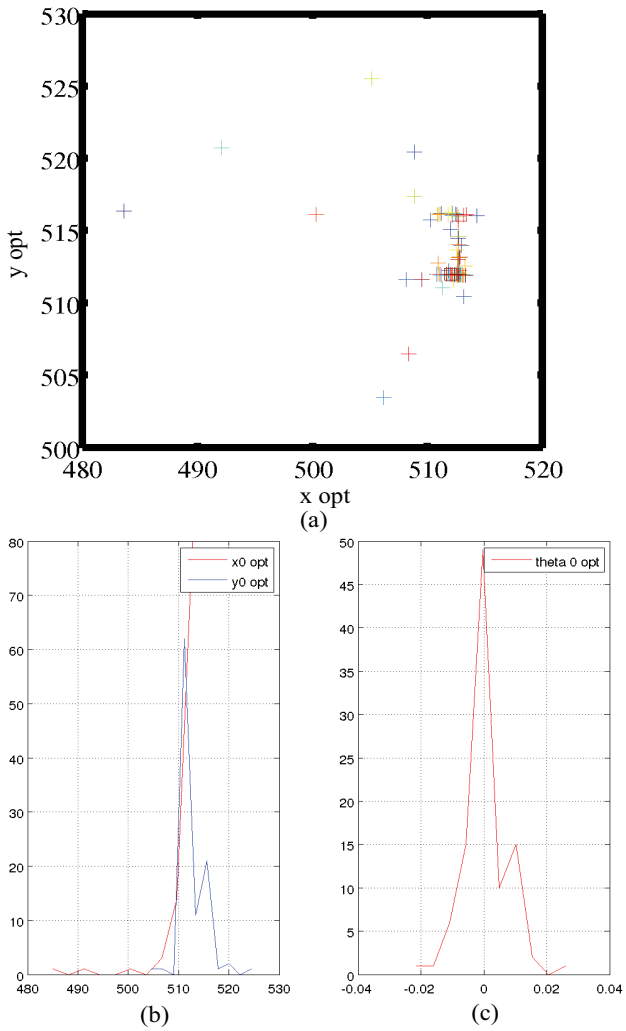

Figure 98: Results from optimization for hundred draws with $\sigma_{\Theta^{est}} = 0.1$ radian considering IE-WS ($R_{max} = 512$ pixels) (a). Probability density functions for x^{opt} and y^{opt} (b) and for Θ_{opt} (c).

The errors on crack parameters generated by an error of the crack angle estimation are presented in Table 30 : 4 pixels for the x coordinate and 3 pixels for the y coordinate. The procedure is able to robustly identify the crack angle despite a large misestimation of its value. These results are considered satisfactory in terms of both crack tip position identification and crack angle identification. The parameter $a_I^{1\,est}$ is identified by the procedure before non-linear minimization.

$\bar{x}^{est}$	512	$\bar{x}^{opt}$	511.48
$\bar{y}^{est}$	512	$\bar{y}^{opt}$	513.17
$\bar{\Theta}^{est}$	0	$\bar{\Theta}^{opt}$	4.59×10^{-4}
$\bar{a}_I^{1\,est}$		$\bar{a}_{I\,opt}^{1}$	2.86×10^{-2}
$\sigma_{x_0^{est}}$	0	$\sigma_{x_0^{opt}}$	3.90
$\sigma_{y_0^{est}}$	0	$\sigma_{y_0^{opt}}$	2.64
$\sigma_{\Theta_0^{est}}$	0.1	$\sigma_{\Theta_0^{opt}}$	7.0×10^{-3}
$\sigma_{a_I^{1\,est}}$		$\sigma_{a_I^{1\,opt}}$	2.55×10^{-4}

Table 30: Comparisons of statistics for estimated and optimized crack parameters in pixels for IE-WS with $\sigma_{\Theta^{est}} = 0.1$ radian and $R_{max} = 512$ pixels.

Sensitivity to the noise:

When SEM images are considered, the noise due to the imaging system must be taken into account. The noise may disturb the DIC quality and the results from the crack parameters identification. The first sensitivity analysis we propose here is to focus on the influence of image noise by perturbing directly the FE displacement fields. The superimposed noise is supposed to be white, centered and Gaussian. Several amplitudes (b) have been tested: $b = [0, 0.001, 0.01, 0.1]$ in percent of the overall displacement amplitude which is here around 2 pixels.

As we have shown that R_{max} has no influence on the identification procedure, we have chosen $R_{max} = 128$ pixels to perform the sensitivity to the noise study.

The results of crack tip position identification for $b = [0.001, 0.01, 0.1]$ are shown in Figure 99. A complete identification of crack parameters (crack position and angle and Williams' series coefficients) has been conducted for the different noise amplitude b. The results of the hundred draws are provided in Figure 99. The crack angle optimization results are clustered on a centered domain of 1×10^{-13} radian amplitude.

The $d_{it1-it2}$ for each noise amplitude is inferior to 1 pixel. The procedure optimization is stable.

A statistic approach of the noise influence is proposed in Table 31. The mean values of crack tip coordinates are very close to the imposed crack tip position. The standard deviation of crack tip coordinates is inferior to 0.5 pixels whatever the chosen noise amplitude.

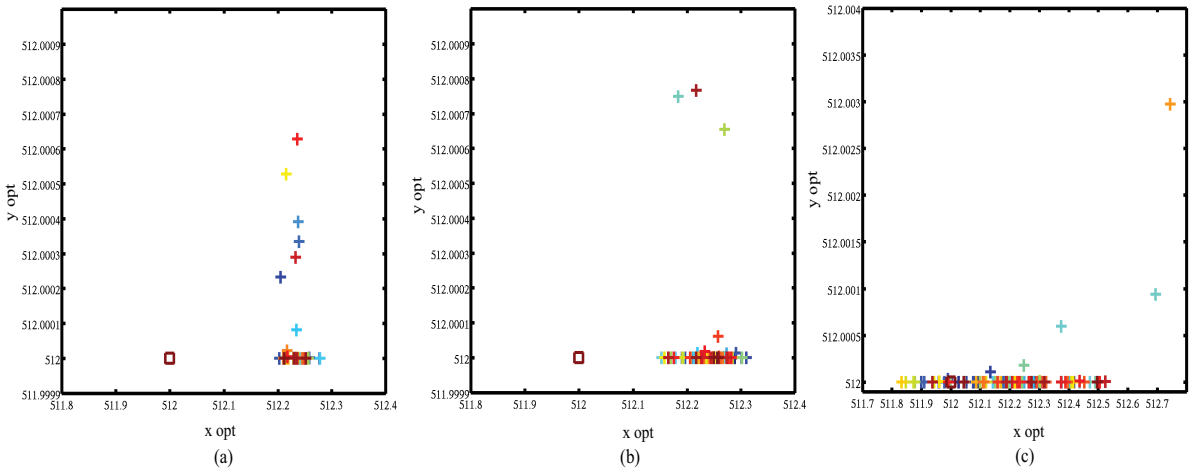

Figure 99: Representation of x^{opt}, y^{opt} with R_{max} = 128 pixels for the different values of noise: b = 0.001 (a), b = 0.01 (b) and b = 0.1 (c). The square symbol is used for the estimated values and the cross is used for the optimized values.

b = 0.001, displacement amplitude [-2,2]	$\bar{x}^{est}$	512	$\bar{x}^{opt}$	512.23
	$\bar{y}^{est}$	512	$\bar{y}^{opt}$	512.00
	$\bar{\Theta}^{est}$	0	$\bar{\Theta}^{opt}$	4.03×10^{-15}
	$\bar{a_I^1}^{est}$		$\bar{a_I^1}^{opt}$	2.86×10^{-2}
	$\sigma_{x_0^{est}}$	0	$\sigma_{x_0^{opt}}$	0.0135
	$\sigma_{y_0^{est}}$	0	$\sigma_{y_0^{opt}}$	1.01×10^{-4}
	$\sigma_{\Theta_0^{est}}$	0	$\sigma_{\Theta_0^{opt}}$	3.21×10^{-4}
	$\sigma_{a_I^{1\,est}}$		$\sigma_{a_I^{1\,opt}}$	2.79×10^{-6}
b = 0.01, displacement amplitude [-2,2]	$\bar{x}^{est}$	512	$\bar{x}^{opt}$	512.24
	$\bar{y}^{est}$	512	$\bar{y}^{opt}$	512.00
	$\bar{\Theta}^{est}$	0	$\bar{\Theta}^{opt}$	2.63×10^{-15}
	$\bar{a_I^1}^{est}$		$\bar{a_I^1}^{opt}$	2.86×10^{-2}
	$\sigma_{x_0^{est}}$	0	$\sigma_{x_0^{opt}}$	0.0332
	$\sigma_{y_0^{est}}$	0	$\sigma_{y_0^{opt}}$	1.24×10^{-4}
	$\sigma_{\Theta_0^{est}}$	0	$\sigma_{\Theta_0^{opt}}$	3.67×10^{-4}
	$\sigma_{a_I^{1\,est}}$		$\sigma_{a_I^{1\,opt}}$	7.0763×10^{-6}
b = 0.1, displacement amplitude [-2,2]	$\bar{x}^{est}$	512	$\bar{x}^{opt}$	512.21
	$\bar{y}^{est}$	512	$\bar{y}^{opt}$	512.00
	$\bar{\Theta}_0^{est}$	0	$\bar{\Theta}_0^{opt}$	2.63×10^{-15}
	$\bar{a}_{I\,est}^1$		$\bar{a}_{I\,opt}^1$	2.86×10^{-2}
	$\sigma_{x_0^{est}}$	0	$\sigma_{x_0^{opt}}$	0.1791
	$\sigma_{y_0^{est}}$	0	$\sigma_{y_0^{opt}}$	3.16×10^{-4}
	$\sigma_{\Theta_0^{est}}$	0	$\sigma_{\Theta_0^{opt}}$	8.87×10^{-14}
	$\sigma_{a_I^{1\,est}}$		$\sigma_{a_I^{1\,opt}}$	4.63×10^{-5}

Table 31: Statistics for identification of the influence of noise with R_{max} = 128 pixels (b = 0.001, 0.01, 0.1) on procedure.

As already mentioned, the configuration tested here (elastic material submitted to loading with WS boundary conditions) is the most consistent case with the LEFM analytic expressions. Consequently, the identification is very efficient and the noise doesn't seem to affect the results of the optimization procedure for the mean crack parameter identification, with the chosen amplitudes.

Multiple errors case:

For this case, we have combined the sources of errors presented above: errors on estimated crack tip coordinates ($\sigma_{x_0^{est}}$, $\sigma_{y_0^{est}}$), errors on crack angle ($\sigma_{\Theta^{est}}$) and noise (b). The maximal amplitude errors have been chosen equal to $\sigma_{x_0^{est}} = \sigma_{y_0^{est}} = 50$ pixels and $\sigma_{\Theta^{est}} = 0.1$ radian and $b = 0.1$. The ROI equals to $R_{max} = 512$ pixels. One hundred draws have been performed.

In Figure 100, a comparison between the displacement fields from experience and from LEFM procedure is proposed.

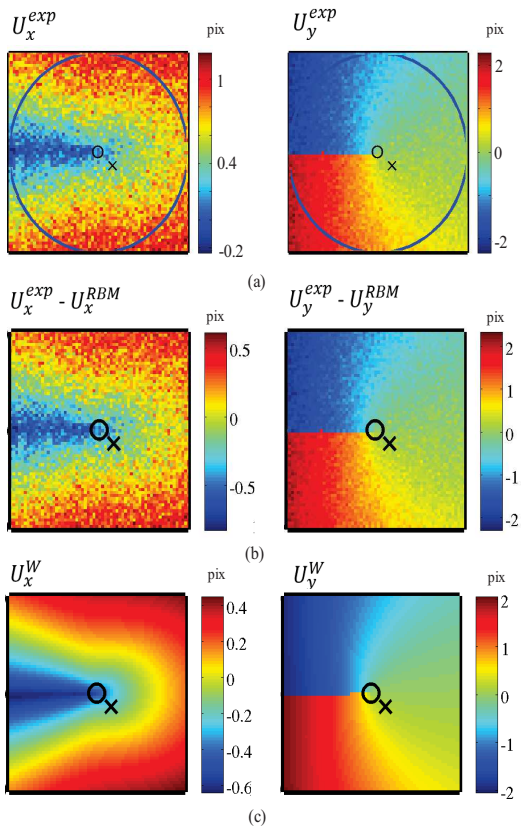

Figure 100: Comparison between the displacement fields for IE-WS ($R_{max} = 512$ pixels) and multiple sources of error: u_x^{exp}, u_y^{exp} (a), $u_x^{exp} - u_x^{RBM}$, $u_y^{exp} - u_y^{RBM}$ (b) u_x^W, u_y^W (c). Notations u_x^{RBM} and u_y^{RBM} stand for the displacement field associated to the rigid body motion (translation and rotation). The cross symbol is used for the estimated values whereas the circle symbol is used for the optimized values.

The results of optimization procedure for one hundred draws are presented in Figure 101. The optimized values are clustered around the imposed crack tip position, underlying the robustness of the method.

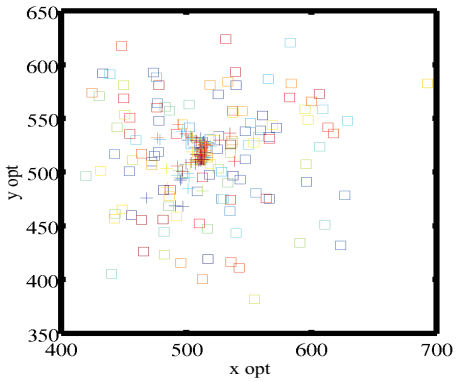

Figure 101: Representation of x^{opt}, y^{opt} for multiple source of errors on the estimated crack parameters for IE-WS R_{max} = 512 pixels. The square symbol is used for the estimated values and the cross symbol is used for the optimized values.

A summary of the identification statistics is proposed in Table 32. The standard deviation for both coordinates $\sigma_{x_0^{est}}$ and $\sigma_{y_0^{est}}$ is inferior to 15 pixels. The crack angle identification is also accurately determined: $\sigma_{\Theta_0^{opt}} = 3.99 \times 10^{-2}$ radian.

$\bar{x}^{est}$	512	$\bar{x}^{opt}$	506.92
$\bar{y}^{est}$	512	$\bar{y}^{opt}$	514.95
$\bar{\Theta}^{est}$	0	$\bar{\Theta}^{opt}$	-5.0 $\times 10^{-3}$
$\bar{a_I^1}^{est}$		$\bar{a_I^1}^{opt}$	2.87 $\times 10^{-2}$
$\sigma_{x_0^{est}}$	50	$\sigma_{x_0^{opt}}$	13.11
$\sigma_{y_0^{est}}$	50	$\sigma_{y_0^{opt}}$	13.73
$\sigma_{\Theta_0^{est}}$	0.1	$\sigma_{\Theta_0^{opt}}$	3.99 $\times 10^{-2}$
$\sigma_{a_I^{1\,est}}$		$\sigma_{a_I^{1\,opt}}$	7.13$\times 10^{-4}$

Table 32: Comparisons of statistics for estimated and optimized crack parameters in pixels for IE-WS with multiple source of errors and R_{max} = 512 pixels.

Conclusions:

In the case of homogeneous elastic material with Westergaard's solutions used as loading conditions:

- It is consistent with the use of analytic expressions from Williams' series;
- The efficiency of the procedure, even if we consider noisy displacement fields has been proved;

- The procedure is able to accurately identify crack parameters even in situations when the initial values are far from the actual crack tip position.

4.5.2.2 Test case IE-ID(0.2): isotropic elasticity with uniform boundary conditions

Imposed displacement on the upper and lower boundaries of the simulation domains while the lateral ones are traction-free has been chosen as boundary conditions with a given value of imposed displacement. A graph illustrating the applied displacement is proposed in Figure 92. In this work, we have chosen to project the displacement fields computed by FE analysis on a specific set of Williams'series restricted to mode I crack using order 0, 1 and 2. In this case, a bias is expected due to the mismatch between the FE fields and the projection basis.

The same strategy that has been used for test case IE-WS is used. We propose to firstly study the influence of R_{max} then to quantify the effects of the initial guessed values and finally the errors generated by a white noise.

Sensitivity to the Region Of Interest R_{max}:

In this case, the estimated crack parameters are chosen equal to the known crack parameters $(x_c, y_c, \Theta) = (512.0, 512.0, 0.0)$. A comparison between the optimized crack parameters for R_{max} = 512 pixels and R_{max} = 128 pixels is proposed in Table 33.

Due to the mismatch between the LEFM projection base and the imposed displacement as boundary conditions, the optimization is slightly more efficient with R_{max} = 128 pixels. In this case, the considered set of points are farther from the global boundaries for small R_{max}. This identification is less accurate in the direction of the crack.

R_{max} = 512 pixels	x^{est}	512	x^{opt}	518.88
	y^{est}	512	y^{opt}	512.00
	Θ^{est}	0	Θ^{opt}	-6.86×10^{-15}
R_{max} = 128 pixels	x^{est}	512	$\bar{x}^{opt}$	517.74
	y^{est}	512	y^{opt}	512.00
	Θ^{est}	0	Θ^{opt}	3.42×10^{-14}

Table 33: Comparison of estimated and optimized crack parameters for IE-ID with R_{max} = 512 pixels and R_{max} = 128 pixels.

Sensitivity to the initial guessed values:

Using the same strategy than the one introduced in Paragraph 4.5.2.1, the sensitivity with respect to the initial guess values of the identification procedure performance has been studied with $\sigma_{x_0^{est}}$, $\sigma_{y_0^{est}}$ = 50 pixels. As R_{max} = 128 pixels gives the best optimized crack parameters, we have chosen to study the influence of errors on crack tip coordinates with the same set of points. To obtain a statistic vision, a hundred draws have been performed.

The optimized crack tip coordinates are presented in Figure 102.

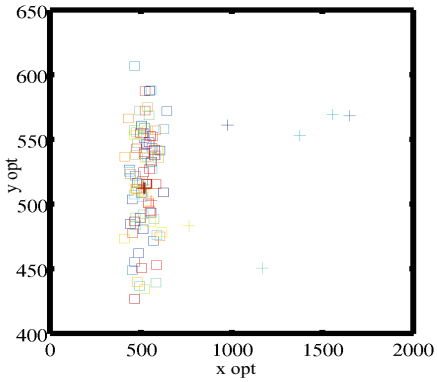

Figure 102: Results from optimization for hundred draws with $\sigma_{x_0^{est}}$, $\sigma_{y_0^{est}}$ = 50 pixels considering IE-ID (R_{max} = 128 pixels). The square is used for the estimated values and the cross symbol is used for the optimized values.

Globally, the optimized parameters are close to the imposed crack parameters (x_c, y_c, Θ). In Figure 102, we observe that some draws have estimated coordinates located outside the domain containing the crack tip ($(x^{opt} - x^{est})^2 + (y^{opt} - y^{est})^2$)). The distance between the results from optimization #1 and #2 is inferior to 20 pixels for 50 % of the draws. Table 34 gives the mean values and thes standard deviations on the optimized parameters determined on the set of a hundred draws. By eliminating points out of the region containing the crack, the efficiency of the procedure is largely increased.

			$R < R_{max}$	$R < R_{max}$ and $\sqrt{(x^{opt} - x^{est})^2 + (y^{opt} - y^{est})^2} \leqslant R_{max}$
$\bar{x}^{est}$	512	$\bar{x}^{opt}$	563.20	517.05
$\bar{y}^{est}$	512	$\bar{y}^{opt}$	513.54	512.36
$\bar{\Theta}^{est}$	0	$\bar{\Theta}^{opt}$	-3.08×10^{-13}	-3.27×10^{-13}
$\sigma_{x_0^{est}}$	50	$\sigma_{x_0^{opt}}$	195.30	4.90
$\sigma_{y_0^{est}}$	50	$\sigma_{y_0^{opt}}$	12.65	1.13
$\sigma_{\Theta_0^{est}}$	0	$\sigma_{\Theta_0^{opt}}$	1.43×10^{-12}	1.51×10^{-12}

Table 34: Comparisons of statistics for estimated and optimized crack parameters in pixels for IE-ID with $\sigma_{x_0^{est}}$, $\sigma_{y_0^{est}}$ = 50 pixels and R_{max} = 128 pixels.

An additional post-processing could consist in eliminating the optimized values outside the region around the crack tip but it won't be used here.

The efficiency of the procedure decreases compared to the previous case due to the mismatch between the boundary conditions and the projection basis. Moreover, by comparing the results with *Rmax* = 512 pixels and R_{max} = 128 pixels, we have shown that the effects of non-consistent boundary conditions can be reduced by diminishing. R_{max} has to be decreased to increase the accuracy of crack tip identification. The crack coordinate is determined with a better accuracy in the

direction y ($\bar{y}^{opt}$ = 512.35 pixels, $\sigma_{y_0^{opt}}$ = 1.13 pixels) than in the x direction ($\bar{x}^{opt}$ = 517.05 pixels, $\sigma_{x_0^{opt}}$ = 4.90 pixels).

Sensitivity to the noise:

Using the strategy introduced above, a numerical noise b is added to the displacement fields b = [0, 0.001, 0.01, 0.1]. To have similar noise levels compared to the previous situation, the noise has been multiplied by 10 in agreement with the maximal amplitude displacement which is ten times higher than in the case of Westergaard boundary conditions. The R_{max} used in this case equals to 128 pixels. A hundred draws have been performed (see Figure 103) and the results from the optimization are presented in Table 35. The distance $d_{it1-it2}$ between the optimized values from iteration #1 and iteration #2 is inferior to 1 pixel. The procedure is stable.

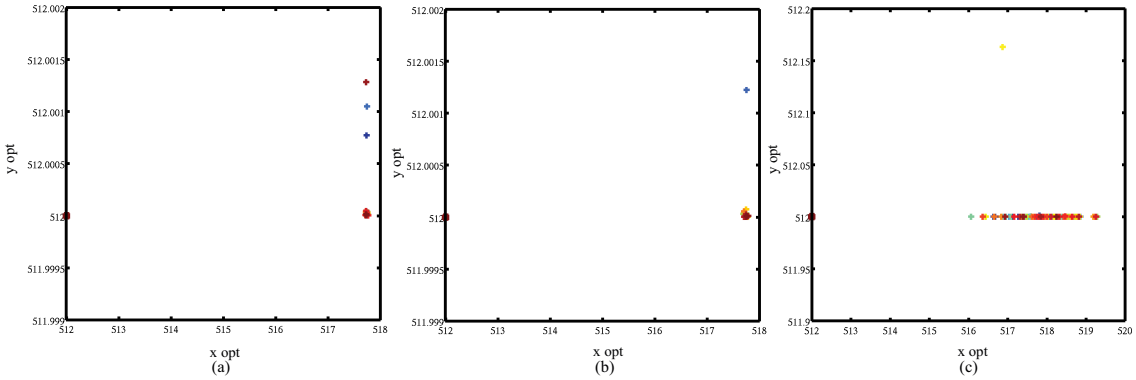

Figure 103: Results from optimization for hundred draws considering IE-ID (R_{max} = 128 pixels) with: b = 0.001 (a), b = 0.01 (b) and b = 0.1 (c). The square symbol is used for the estimated values and the cross symbol is used for the optimized values.

A statistic summary of the hundred draw results is given in Table 35.

In Figure 104, a comparison between the noisy displacement fields from the virtual experiments given as input data of the identification procedure u^{exp} and from LEFM projection u^{W} is proposed. There is a good reproduction of experimental displacement fields (see Figure 104 a) using Williams series (Figure 104 c).

This situation illustrates the influence of the mismatch between imposed boundary conditions and the ones associated with the LEFM shape functions used to describe the displacement fields when noise is present in the displacement fields. In this case IE-ID, the identification in which the value of R_{max} is equal to 512 pixels should be the most detrimental case since far from the crack (for large values of R_{max}), the computed displacement is far from the assumed Westergaard (solution due to boundary condition effects). When R_{max} decreases, the distance of the considered set of points from the boundaries increases leading to the diminution of the effects of mismatch between the chosen boundary conditions and the LEFM model, and thus to the decrease of the identification error. Moreover, the noise slightly influences the optimized crack parameters, with the chosen amplitudes.

b = 0.001, displacement amplitude = [-20,20]	$\bar{x}^{est}$	512	$\bar{x}^{opt}$	517.74
	$\bar{y}^{est}$	512	$\bar{y}^{opt}$	512.00
	$\bar{\Theta}^{est}$	0	$\bar{\Theta}^{opt}$	7.91×10^{-15}
	$\sigma_{x_0^{est}}$	0	$\sigma_{x_0^{opt}}$	0.0089
	$\sigma_{y_0^{est}}$	0	$\sigma_{y_0^{opt}}$	1.80×10^{-4}
	$\sigma_{\Theta_0^{est}}$	0	$\sigma_{\Theta_0^{opt}}$	3.49×10^{-14}
b = 0.01, displacement amplitude = [-20,20]	$\bar{x}^{est}$	512	$\bar{x}^{opt}$	517.74
	$\bar{y}^{est}$	512	$\bar{y}^{opt}$	512.00
	$\bar{\Theta}^{est}$	0	$\bar{\Theta}^{opt}$	4.06×10^{-14}
	$\sigma_{x_0^{est}}$	0	$\sigma_{x_0^{opt}}$	0.0169
	$\sigma_{y_0^{est}}$	0	$\sigma_{y_0^{opt}}$	1.22×10^{-4}
	$\sigma_{\Theta_0^{est}}$	0	$\sigma_{\Theta_0^{opt}}$	1.22×10^{-14}
b = 0.1, displacement amplitude = [-20,20]	$\bar{x}^{est}$	512	$\bar{x}^{opt}$	517.88
	$\bar{y}^{est}$	512	$\bar{y}^{opt}$	512.0017
	$\bar{\Theta}^{est}$	0	$\bar{\Theta}^{opt}$	2.95×10^{-14}
	$\sigma_{x_0^{est}}$	0	$\sigma_{x_0^{opt}}$	0.670
	$\sigma_{y_0^{est}}$	0	$\sigma_{y_0^{opt}}$	1.63×10^{-2}
	$\sigma_{\Theta_0^{est}}$	0	$\sigma_{\Theta_0^{opt}}$	1.09×10^{-14}

Table 35: Statistics for identification of the influence of noise (b = 0.001, 0.01, 0.1) on procedure (R_{max} = 128 pixels).

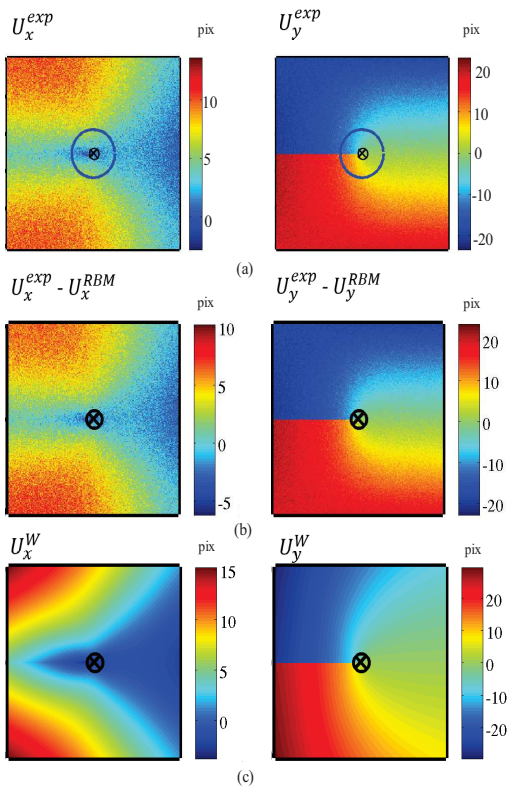

Figure 104: Comparison between the displacement fields for IE-ID (R_{max} = 128 pixels) and multiple sources of error: u_x^{exp}, u_y^{exp} (a), $u_x^{exp} - u_x^{RBM}$, $u_y^{exp} - u_y^{RBM}$ (b) u_x^W, u_y^W (c). Notations u_x^{RBM} and u_y^{RBM} stand for the displacement field associated to the rigid body motion (translation and rotation). The cross symbol is used for the estimated values whereas the circle symbol is used for the optimized values. The thick blue circle is used for R_{max}.

Conclusions:

In the case of an homogeneous elastic material under imposed displacement loading conditions:

- we have introduced a mismatch between the "experimental" displacement fields and the displacement shape functions used for the identification;
- The identification results show a limited sensitivity to the parameter initial guesses (with a systematic error of 5 pixels along the x-axis);
- When noisy displacement fields are used as input, there is a satisfactory reproduction of the kinematic fields and the procedure is still efficient;
- the procedure performance is increased when the considered set of points are far from the boundary conditions (decreasing R_{max}), where the mismatch between the analytic expressions of Williams and the imposed displacement boundary conditions is the highest;
- The noise also slightly affects the optimization procedure but satisfactory results are obtained even for high levels of noise.

4.5.3 Test Case I considering an isotropic plastic behaviour

It is expected that plasticity will develop ahead of the crack tip during creep tests. We propose to assess the robustness of the crack tip identification procedure considering an homogeneous macroscopic J_2 isotropic plastic behaviour associated with an imposed displacement on the four external boundaries given by the Williams expression for a given value of parameter a_I^1. The material parameters used in the FEM calculation are given in Table 26. The chosen calculation mode considered small loading increments and small rotations. Plane stress conditions have been considered, and the Kolossov constant introduced in the Williams series is computed with the actual Poison ratio. The Kolossov constant could be as a parameter to optimize. The results should be more accurate, especially when plasticity develops.

The displacement fields computed from FE analysis for a loading parameter $a_I^1 = 0.01$. To consider the critical situation, R_{max} is chosen equal to 512 pixels to study the influence of unconsistent material model with consistent boundary conditions on the crack tip identification.

Using the same procedure than the one used in the previous paragraphs, we propose to study the influence of R_{max}, the initial guessed values ($\sigma_{x_0^{est}}$, $\sigma_{y_0^{est}} = 50$ pixels and $\sigma_{\Theta^{est}} = 0.1$ radian) and the noise level b.

Sensitivity to the Region Of Interest R_{max}:

A comparison between the crack parameters for IP-WS for $R_{max} = 512$ pixels and $R_{max} = 128$ pixels is given in Table 36.

R_{max}	Θ^{est} (radian)	x^{opt}	y^{opt}	Θ^{opt} (radian)
512	0	561.57	512	-1.45 10^{-12}
128	0	525.96	512	1.55 10^{-13}

Table 36: Comparisons between guessed values and the optimized crack tip position for IP-WS(0.01) for $R_{max} = 512$ pixels and $R_{max} = 128$ pixels.

The procedure leads to a good crack tip position identification but the results are more accurately determined when R_{max} decreases due to a plasticity development in the calculation domain (see Figure 105). The procedure accuracy is increased by centering R_{max} around the crack tip without considering points close to the global boundaries.

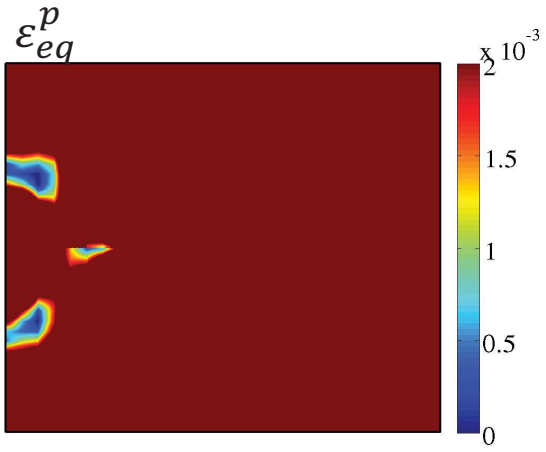

Figure 105: Equivalent plastic deformation field demonstrates that plasticity developped in the whole specimen.

Sensitivity to the initial guessed values:

As proposed in Paragraph 4.5.2.1, the sensitivity analysis with respect to noise has been performed considering a standard deviation of $\sigma_{x_0^{est}}$, $\sigma_{y_0^{est}}$ = 50 pixels on estimated crack tip coordinates. With R_{max} = 128 pixels, the optimized values are clustered close to (x^{opt} = 512 pixels, y^{opt} = 512 pixels, Θ = 0.0) (see Figure 106). The distance between the solutions from optimization #1 and optimization #2 is inferior to 20 pixels.

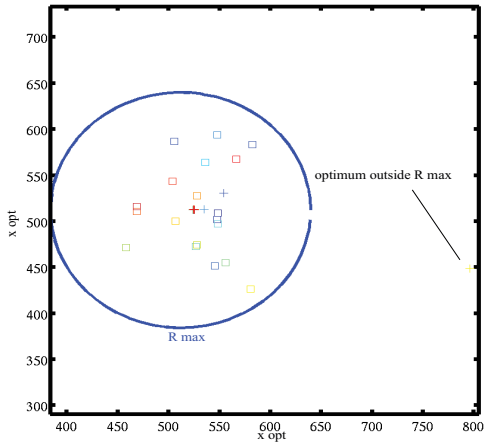

Figure 106: Results for x^{opt} and y^{opt} for IP-WS with R_{max} = 128 pixels and $\sigma_{x_0^{est}}$,$\sigma_{y_0^{est}}$ = 50 pixels. The square symbol is used for the estimated values whereas circle is used for optimized values.

The difference between the test case IP-WS and IE-WS relies on the choices of the material behaviour which are respectively isotropic plasticity and isotropic elasticity. In Table 36, the optimized value for R_{max} = 128 pixels is centered at (x^{opt}, y^{opt}) = (512,512). In the present case, (x^{opt}, y^{opt}) = (526,512) with R_{max} = 128 pixels. We assumed that the procedure is sensitive to the

initial guessed values due to the plasticity development which is not consistent with the chosen projection basis (see Table 37). Nevertheless, the results are satisfactory.

$\sigma_{x_0^{est}}$,$\sigma_{y_0^{est}}$	$\bar{x}^{est}$	512	$\bar{x}^{opt}$	539.97
	$\bar{y}^{est}$	512	$\bar{y}^{opt}$	510.07
	$\sigma_{x_0^{est}}$	50	$\sigma_{x_0^{opt}}$	59.12
	$\sigma_{y_0^{est}}$	50	$\sigma_{y_0^{opt}}$	14.66
	$\bar{\Theta}^{est}$	0	$\bar{\Theta}^{opt}$	4.95×10^{-12}
	$\sigma_{\Theta_0^{est}}$	0	$\sigma_{\Theta_0^{opt}}$	2.50×10^{-11}
$\sigma_{\Theta^{est}}$	$\bar{x}^{est}$	512	$\bar{x}^{opt}$	525.42
	$\bar{y}^{est}$	512	$\bar{y}^{opt}$	512.67
	$\bar{\Theta}^{est}$	0	$\bar{\Theta}^{opt}$	-0.0064
	$\sigma_{x_0^{est}}$	0	$\sigma_{x_0^{opt}}$	1.62
	$\sigma_{y_0^{est}}$	0	$\sigma_{y_0^{opt}}$	3.29
	$\sigma_{\Theta_0^{est}}$	0.1	$\sigma_{\Theta_0^{opt}}$	0.036

Table 37: Comparisons of statistics for estimated and optimized crack parameters in pixels for IP-WS with $\sigma_{x_0^{est}}$, $\sigma_{y_0^{est}}$ = 50 pixels and $\sigma_{\Theta^{est}}$ = 0.1 radian and R_{max} = 128 pixels.

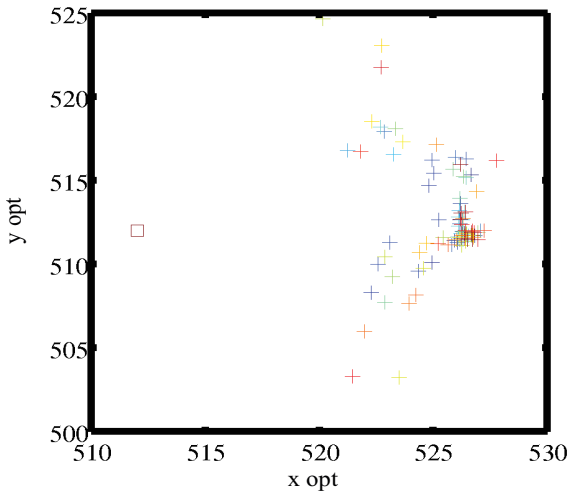

Figure 107: Results for x^{opt}, y^{opt} for IP-WS with $\sigma_{\Theta^{est}}$ = 0.1 radian. Square symbol is used for estimated values and cross symbol is used for optimized values.

The statistics for this case with $\sigma_{x_0^{est}}$, $\sigma_{y_0^{est}}$ = 50 pixels are less accurate because of one optimized value far from the known crack tip position.The sensibility of the procedure to the crack angle has been studied by generating a standard deviation error of $\sigma_{\Theta^{est}}$ = 0.1 radian on the estimated

value. The optimized values of crack tip coordinates are presented in Figure 107. The statistic characteristics for this case are given in Table 37. An influence is observed on the crack angle identification but there is no effet on crack tip coordinates. An error of 0.1 radian on the estimated crack angle slightly influences the optimization results (see Table 37).

Sensitivity to the noise:

We have studied the procedure robustness to noise in the displacement field by superimposing a noise of amplitude $b = 0.1$ to the virtual experiment displacement field. In Figure 108, a comparison between displacement fields from the virtual experiment u^{exp} and resulting from LEFM projection u^{W} is proposed. Notations u_x^{RBM} and u_y^{RBM} stand for the displacement field associated to the rigid body motion (translation and rotation).

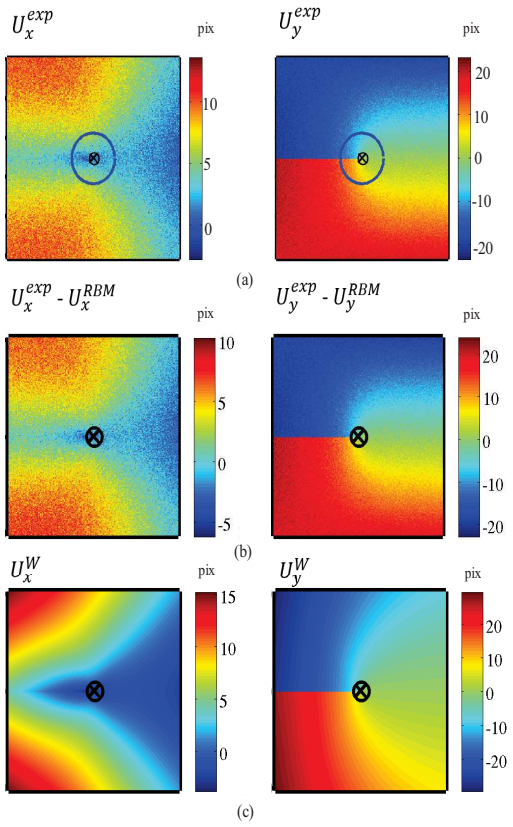

Figure 108: Comparison between the displacement fields for IP-WS (R_{max} = 128 pixels) and b = 0.1: u_x^{exp}, u_y^{exp} (a), $u_x^{exp} - u_x^{RBM}$, $u_y^{exp} - u_y^{RBM}$ (b) u_x^{W}, u_y^{W} (c). Notations u_x^{RBM} and u_y^{RBM} stand for the displacement field associated to the rigid body motion (translation and rotation). The cross symbol is used for the estimated values whereas the circle symbol is used for the optimized values.

Ten draws have been performed and the x^{opt} and y^{opt} are presented in Figure 109. The statistics from these draws are presented in Table 38. The noise slightly influences the optimization procedure compared to the effects of an error in the estimated crack tip coordinates.

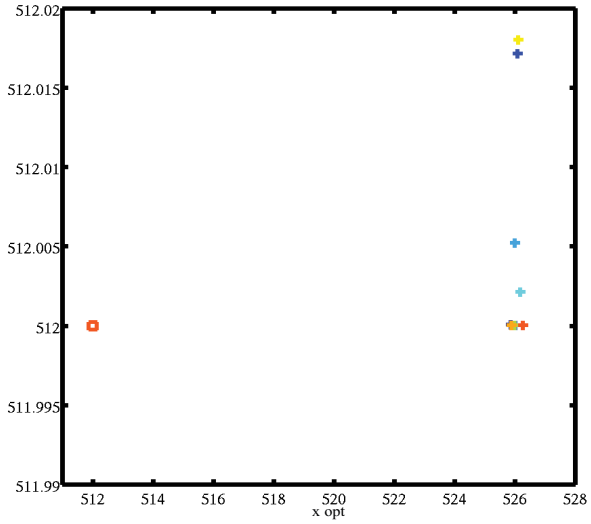

Figure 109: Results for x^{opt}, y^{opt} for IP-WS with $b = 0.1$. Square symbol is used for the estimated values and cross is used for the optimized values.

$\bar{x}^{est}$	512	$\bar{x}^{opt}$	526.05
$\bar{y}^{est}$	512	$\bar{y}^{opt}$	512.00
$\bar{\Theta}^{est}$	0	$\bar{\Theta}^{opt}$	4.33×10^{-13}
$\sigma_{x_0^{est}}$	0	$\sigma_{x_0^{opt}}$	0.127
$\sigma_{y_0^{est}}$	0	$\sigma_{y_0^{opt}}$	7.2×10^{-3}
$\sigma_{\Theta_0^{est}}$	0	$\sigma_{\Theta_0^{opt}}$	1.46×10^{-12}

Table 38: Comparisons of statistics for estimated and optimized crack parameters in pixels for IP-WS with $b = 0.1$ and $R_{max} = 128$ pixels.

In case of plastic material with Westergaard boundary conditions, here again decreasing the R_{max} parameter improves the accuracy of the identification. Generalized plasticity develops in the whole sample. Even if the ROI considered is within the plasticity zone, the procedure gives satisfactory results.

In the following part, we propose to study the errors generated by a crystal plasticity model with imposed displacement boundary conditions coupled with DIC. Considering a bicrystal, this model is source of anisotropy and dissymetry in the material reponse. The objective of this case is to assess the efficiency of the procedure when Linear Elastic Fracture Mechanics is the least adapted.

4.5.4 Test Case II considering a crystal plasticity model: CP-ID(0.002)

4.5.4.1 Deformation of image using G'MIC software

The G'MIC software [2] is commonly used for image transformations. It is an open source full-featured framework for image processing, providing several different user interfaces to convert/ manipulate/ filter/ visualize generic image datasets, from 1D scalar signals to 3D sequences of multi-spectral volumetric images [182]. The reference image is interpolated with the displacement field projected onto the image cartesian grid using the warp function (see Figure 110). For the sake of consistency, the reference image is also interpolated with a null displacement. Let us stress out that procedure is sensitive to interpolation errors.

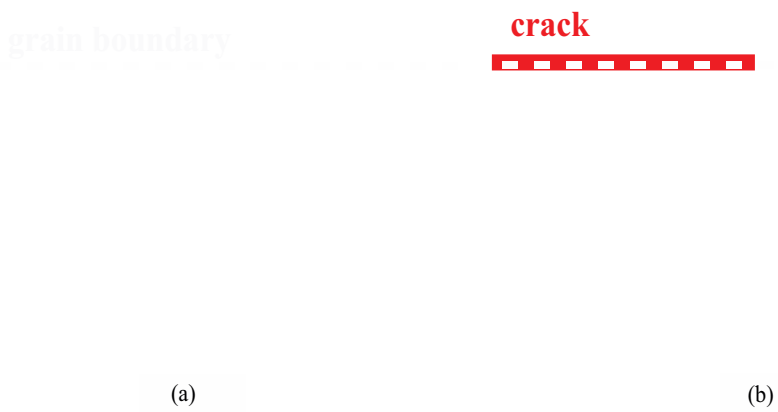

Figure 110: Gray level reference image (a) and deformed image (b) using displacement fields computed by FE analysis using Westergaard's boundary conditions ($a_I^1 = 0.001$). The image area is 100 x 100 pixels around the crack.

4.5.4.2 Kinematic fields with a crystal plasticity model

To generate the reference displacement fields, a bicrystal composed of a grain with the orientation [100] and a grain of orientation [111] has been loaded using imposed displacement boundary condition. The bicrystal is obtained considering the following orientations for Grain 1 and Grain 2 respectively: [100] corresponding to Euler angles (0 °, 90 °, 90 °) and [111] corresponding to Euler angles (0 °, 55 °, 45 °). A crystal plasticity law has been chosen to describe the plastic response (see Section 4.5).

[2] http://gmic.eu/

These displacement fields have been used to deformed a SEM image using G'MIC software (see paragraph 4.5.4.2). In this case, no numerical noise has been added.

A preliminary study has focused on the influence of DIC parameters (grid step (*GS*), subset size (*s*)) on the crack parameter identification procedure. As expected, the resolution of the discontinuity in the kinematic fields generated by the crack presence is essential to accurately identify the crack tip.

The gridstep *GS* and the subset size *s* must be chosen as small as possible to prevent the smoothing of the discontinuity and to have the most accurate and dense kinematic fields. The Kelkins routine has been used to obtain the displacement fields with *GS* = 1 pixel , *s* = 20 pixels. Then, they have been projected onto the LEFM base.

A comparison between the displacement fields from DIC and that from modelling is proposed in Figure 111. Figure 111 shows the dissymetry between the upper and lower grains due to heterogeneous and anisotropic crystal plasticity.

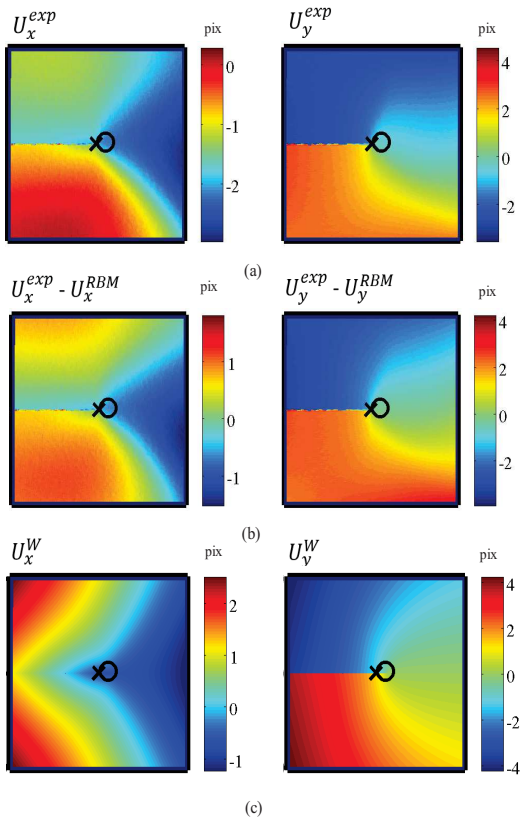

Figure 111: Comparison between the displacement fields for Case II CP-ID (R_{max} = 512 pixels): u_x^{exp}, u_y^{exp} (a), $u_x^{exp} - u_x^{RBM}$, $u_y^{exp} - u_y^{RBM}$ (b) u_x^W, u_y^W (c). Notations u_x^{RBM} and u_y^{RBM} stand for the displacement field associated to the rigid body motion (translation and rotation). The cross symbol is used for the estimated values whereas the circle symbol is used for the optimized values.

A comparison between the optimized values with R_{max} = 512 pixels and R_{max} = 128 pixels is proposed in Table 39. By reducing the ROI, the effects of the unconsistent boundary conditions and anisotropy development decreased. Hereafter, we propose to study the sensitivity to the crack angle, the initial guessed values and to the noise by considering R_{max} = 128 pixels.

R_{max}	Θ^{est} (radian)	x^{opt}	y^{opt}	Θ^{opt} (radian)
512	0	566.70	500	-3.95×10^{-14}
128	0	519.62	500	-1.63×10^{-14}

Table 39: Comparisons between guessed values and the optimized crack tip position for Case II CP-ID for R_{max} = 512 pixels and R_{max} = 128 pixels.

To study the sensitivity to the initial guessed values, a standard deviation error $\sigma_{x_0^{est}}$, $\sigma_{y_0^{est}}$ = 50 pixels is generated on the estimated crack tip coordinates. Twenty draws have been performed and the results are presented in Figure 112 and Table 40.

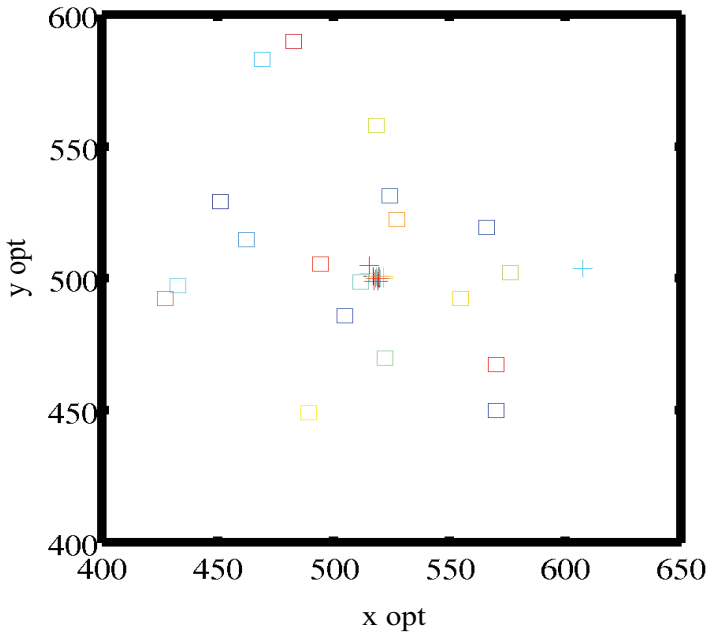

Figure 112: Results for x^{opt}, y^{opt} for case II CP-ID with $\sigma_{x_0^{est}}$, $\sigma_{y_0^{est}}$ = 50 pixels. The square symbol is used for the estimated values and the cross is used for the optimized values.

$\bar{x}^{est}$	512	$\bar{x}^{opt}$	523.39
$\bar{y}^{est}$	512	$\bar{y}^{opt}$	500.84
$\bar{\Theta}^{est}$	0	$\bar{\Theta}^{opt}$	-1.33×10^{-13}
$\sigma_{x_0^{est}}$	50	$\sigma_{x_0^{opt}}$	20.47
$\sigma_{y_0^{est}}$	50	$\sigma_{y_0^{opt}}$	1.50
$\sigma_{\Theta_0^{est}}$	0	$\sigma_{\Theta_0^{opt}}$	5.87×10^{-13}

Table 40: Comparisons of statistics for estimated and optimized crack parameters in pixels for Case II CP-ID with $\sigma_{x_0^{est}}$, $\sigma_{y_0^{est}}$ = 50 pixels and R_{max} = 128 pixels.

The value $\sigma_{x_0^{opt}}$ is particularly high due to one optimized value $x^{opt} > 600$ pixels.

A maximal error of 0.1 radian on the estimated crack angle has no influence on the optimized crack tip coordinates.

We propose to superimpose an amplitude noise b to the displacement fields (b = 1, 0.1). By addind this error, we are more representative of displacement fields obtained with unperfect imaging system. A comparison between optimized values for b = 1 and b = 0.1 are given in Table 41.

b = 0.1, displacement amplitude = [-5,5]	$\bar{x}^{est}$	512	$\bar{x}^{opt}$	520.20
	$\bar{y}^{est}$	512	$\bar{y}^{opt}$	500.3
	$\bar{\Theta}^{est}$	0	$\bar{\Theta}^{opt}$	1.43×10^{-14}
	$\sigma_{x_0^{est}}$	0	$\sigma_{x_0^{opt}}$	1.07
	$\sigma_{y_0^{est}}$	0	$\sigma_{y_0^{opt}}$	0.48
	$\sigma_{\Theta_0^{est}}$	0	$\sigma_{\Theta_0^{opt}}$	2.11×10^{-14}
b = 1, displacement amplitude = [-5,5]	$\bar{x}^{est}$	512	$\bar{x}^{opt}$	520.79
	$\bar{y}^{est}$	512	$\bar{y}^{opt}$	500.71
	$\bar{\Theta}^{est}$	0	$\bar{\Theta}^{opt}$	1.38×10^{-14}
	$\sigma_{x_0^{est}}$	0	$\sigma_{x_0^{opt}}$	1.73
	$\sigma_{y_0^{est}}$	0	$\sigma_{y_0^{opt}}$	0.68
	$\sigma_{\Theta_0^{est}}$	0	$\sigma_{\Theta_0^{opt}}$	1.01×10^{-14}

Table 41: Statistics for identification of the influence of noise (b = 0.1, 1) on Case II CP-ID (R_{max} = 128 pixels).

In Figure 113, a comparison between displacement fields from virtual experiment u^{exp} and LEFM projection u^W is proposed. The noise slightly influences the efficiency of the procedure identification.

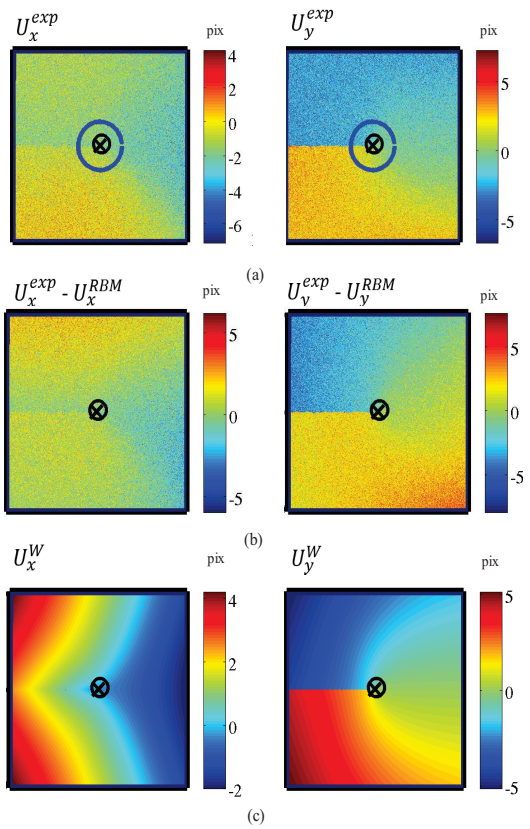

Figure 113: Comparison between the displacement fields for Case II CP-ID for $b = 1$ ($R_{max} = 128$ pixels): u_x^{exp}, u_y^{exp} (a), $u_x^{exp} - u_x^{RBM}$, $u_y^{exp} - u_y^{RBM}$ (b) u_x^W, u_y^W (c). Notations u_x^{RBM} and u_y^{RBM} stand for the displacement field associated to the rigid body motion (translation and rotation). The cross symbol is used for the estimated values whereas the circle symbol is used for the optimized values. The thick blue circle represents R_{max}.

To challenge the procedure efficiency, we propose to combine the sources of errors. We have combined the sources of errors presented above: errors on estimated crack tip coordinates $(\sigma_{x_0^{est}}, \sigma_{y_0^{est}})$, errors on crack angle $(\sigma_{\Theta^{est}})$ and noise level (b). The maximal amplitude errors have been chosen equal to $(\sigma_{x_0^{est}}, \sigma_{y_0^{est}}) = 50$ pixels and $\sigma_{\Theta^{est}} = 0.1$ radian and $b = 1$. The ROI equals to $R_{max} = 128$ pixels. Twenty draws have been performed. The crack parameter optimization results from these draws are given in Figure 114.

A statistic summary is proposed in Table 42. We propose to do not take into account optimized values outside a region containing the crack tip leading to the increase of the procedure accuracy.

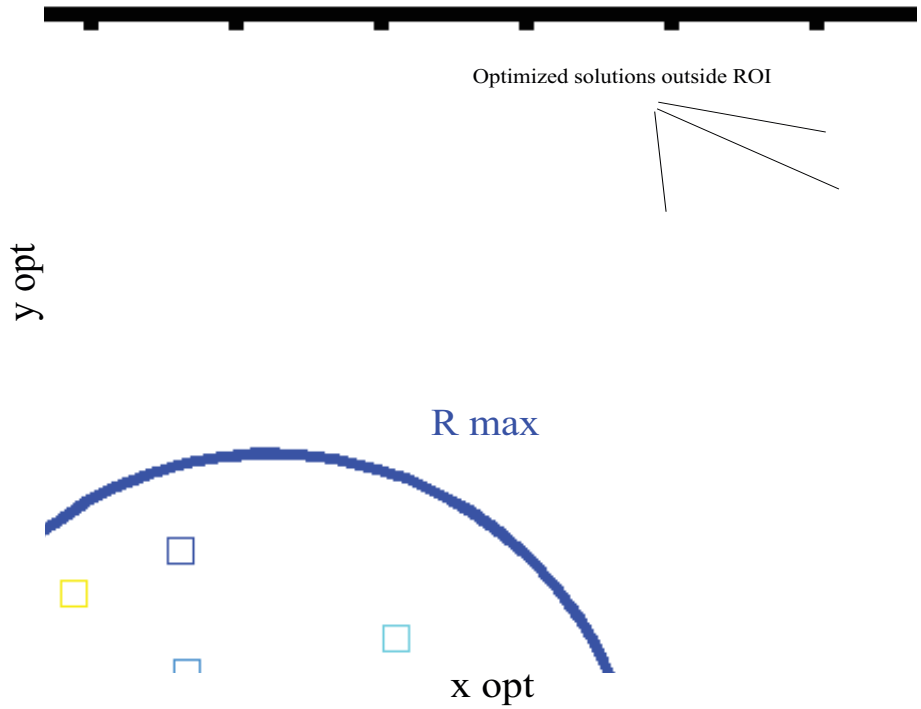

Figure 114: Representation of x^{opt}, y^{opt} for multiple error sources on the estimated crack parameters for Case II CP-ID R_{max} = 128 pixels. The square symbols is used for the estimated values and the cross is used for the optimized values.

			$R < R_{max}$	$R < R_{max}$ and $\sqrt{(x^{opt}-x^{est})^2+(y^{opt}-y^{est})^2} \leqslant R_{max}$
$\bar{x}^{est}$	512	$\bar{x}^{opt}$	572.22	521.29
$\bar{y}_{est}$	512	$\bar{y}^{opt}$	512.09	501.06
$\bar{\Theta}^{est}$	0	$\bar{\Theta}^{opt}$	1.13×10^{-2}	-3.7×10^{-3}
$\sigma_{x_0^{est}}$	50	$\sigma_{x_0^{opt}}$	127.13	5.02
$\sigma_{y_0^{est}}$	50	$\sigma_{y_0^{opt}}$	29.85	4.68
$\sigma_{\Theta_0^{est}}$	0.1	$\sigma_{\Theta_0^{opt}}$	6.75×10^{-2}	4.83×10^{-2}

Table 42: Comparisons of statistics for estimated and optimized crack parameters in pixels for Case II CP-ID with multiple error sources and R_{max} = 128 pixels.

Considering the crystal plasticity model with uniform imposed displacement boundary conditions is challenging the efficiency of the procedure. Even when multiple error sources (crack parameter or noisy displacement) are considered, the optimization procedure remains robust except for a few draws that lead to inappropriate optimized parameters (locating the crack tip outside

the R_{max} zone) and the crack position can be identified.

- The crystal plasticity model is source of anisotropy and heterogeneous response of the material. This case is not consistent with the LEFM analytic expressions.

- The mismatch generated an error of 10 pixels in the identification of the crack tip x-coordinate and the y-coordinate. This is the best achievable performance in this case. The choice of the ROI can decrease the effects of this mismatch between shape functions and material behaviour. Nevertheless, if an additional post-processing consisting in eliminating the optimized values far from the region containing the crack tip. These statistics are improved.

- We have shown that the procedure wasn't sensitive to error on crack angle and that noise slightly influences the efficiency of the procedure, with the chosen amplitude.

- Even when multiple source of errors are combined, the procedure has centered the optimized values close to the "achievable" limit.

- The efficiency of the procedure has been proved for displacement fields from DIC which could be considered as unperfect compared to the FEM kinematic fields.

4.6 Conclusion

By using advanced experimental techniques providing full field measurements, it is possible to detect mechanical fields singularities induced by cracks and other material discontinuities. In the context of creep crack growth, image analyses and Digital Image Correlation (DIC) are relevant techniques to monitor the crack advance and the plasticity and strain fields surrounding a propagating crack. Moreover, by performing acquisitions well sequenced in time, it is also possible to measure kinematic fields before and after crack initiation, and to precisely determine initiation time under a given load.

A specific procedure for the crack parameter identification has been set-up. The objective was focused on obtaining precise information on the crack location (crack tip position and orientation) and not on the stress intensity factor identification. Relying on LEFM theories, experimental displacement fields are projected onto chosen analytic expressions given by Williams'series. The efficiency of this method has been validated onto reference displacement fields computed using Finite Element Software Code_Aster. The reference displacement fields have been obtained for several behaviours: from homogeneous elastic material to heterogeneous crystal plasticity material. The main objective of this procedure is to be able to identify accurate crack parameters, in particular the crack tip positions. In Table 43, we summarize and compare the results from the identification when errors on estimated crack tip coordinates are made. The influence of the mismatch between the choice of projection basis and material behaviour or boundary conditions is adressed. Let us remind that the known crack tip positions is $(x_c, y_c) = (512.0, 512.0)$ and the standard deviation of errors made on estimated crack tip positions is $\sigma_{x^{est}} = \sigma_{y^{est}} = 50$ pixels. The mean values on estimated positions should be $\bar{x}^{est} = \bar{y}^{est} = 512$ pixels.

Material behaviour	Boundary conditions	$\bar{x}^{opt}$	$\sigma_{x^{opt}}$	$\bar{y}^{opt}$	$\sigma_{y^{opt}}$
Isotropic Elasticity	Westergaard solutions	512.29	0.94	512.86	2.74
	Imposed displacement	517.05	4.90	512.36	1.13
Isotropic plasticity	Westergaard solution	539.97	59.12	510.07	14.66
Anisotropic crystal plasticity	Imposed displacement	523.39	20.47	500.84	1.50

Table 43: Comparisons of statistics for the different behaviours and boundary conditions when an error is made on the estimated crack tip coordinates.

For this reference displacement fields, a sharp crack form has been modeled in the FEM method and as a perspective, it could be interesting to study the influence of the crack form on the procedure accuracy. Furthermore, the Kolossov constant should also be introduced in the optimization process in order to account for the evolution of the apparent elastic properties when plasticity has developped.

The results have shown that even if the material behaviour is heterogeneous and anisotropic (such as crystal plasticity model), the procedure is able to identify the crack parameters with an accuracy of 10 pixels for the crack tip location and inferior to $1°$ for the crack angle. Moreover, different sensitivity studies have led to the identification of parameters (R_{max}, s, GS) to perform this identification. In the light of these satisfactory results, the procedure can then be applied to real experiments. *In-situ* tensile tests have been carried out on SENT samples made of 316 at room temperature and 500 °C. The procedure has been also used and assessed in multicracking cases.

Chapter 5

Experimental validation on 316 *in-situ* tensile tests

The objective of the collaboration between EDF Energy, EDF R&D and the LMGC is to obtain relevant experimental data in view of proposing a creep crack initiation model that can be applied to AGR boilers, and more specifically to 316H tubes. Both experimental and computational approaches will be needed to achieve creep crack initiation predictions under operational conditions. Between each creep interruption, an in-situ tensile device will be used to apply elastic loadings to the SENT leading to crack opening and crack tip position identification. Combining SEM images acquisition and DIC techniques, the crack propagation will be monitored. This chapter aims at introducing the different in-situ tensile tests performed on SENT made of 316.

Contents

5.1 Introduction

The interrupted creep tests at 550 °C in air have been chosen to improve the understanding about creep cracking in 316H stainless steel. During creep interruptions, SEM images are acquired in view of monitoring the crack propagation at room temperature. This propagation is quantified using an *in-situ* tensile device in order to apply an elastic loading leading to the crack opening. This technique is efficient to identify the crack tip position identification without generating a crack propagation. A preliminary study has consisted in identifying the lower bound of the loading to be applied for generating a detrimental crack propagation on a 316L SENT specimen. Then, a similar study has been conducted on preconditioned 316H SENT specimen. The mechanical properties of the oxidised layer formed during the preconditioning treatment were also characterized during this test. Then, an example of DIC analysis to obtain the crack tip position during a creep stop is proposed. Finally, we have shown in the Chapter 2 that oxidation at high temperature in air may lead to pattern damages preventing DIC analysis during a long time period. An alternative solution has consisted in performing a tensile test at 500 °C using an *in-situ* tensile device in a SEM operated in high vacuum conditions.

5.2 *In-situ* tensile test on 316L SENT specimen at room temperature: identification of the microplasticty threshold

A SENT specimen made of 316LN has been set-up in the SEM *in-situ* tensile device (Figure 115). This apparatus is used for the crack monitoring during each creep stop. It makes crack detection possible using DIC by applying a small loading to the specimen.

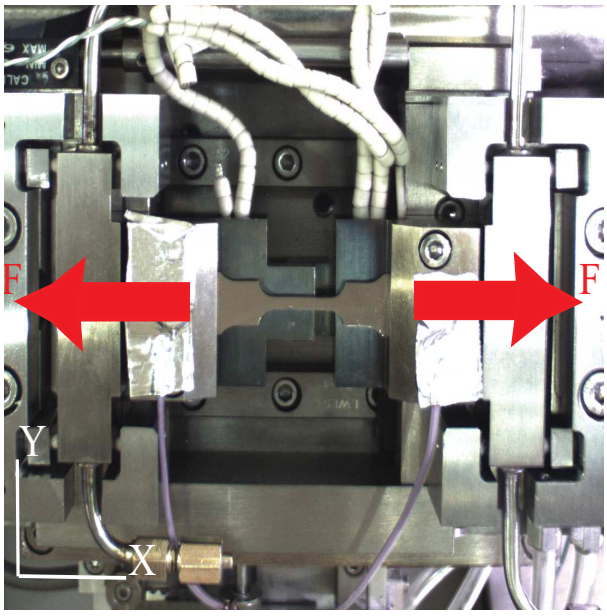

Figure 115: Photography of the *in-situ* tensile device.

At room temperature, cycles of loading and unloading at different load levels have been applied to the specimen (Figure 117). During each cycle, acquisitions of SEM images in BSE mode with

a chemical contrast have been performed: several images have been acquired during the loading step at chosen loading levels and only one image has been taken at the end of each unloading step, it corresponds to the lowest loading level (see Figure 116). Complementary to the BSE images, SEM images have been taken in the crack tip region using SE mode which is more sensitive to topology variations.

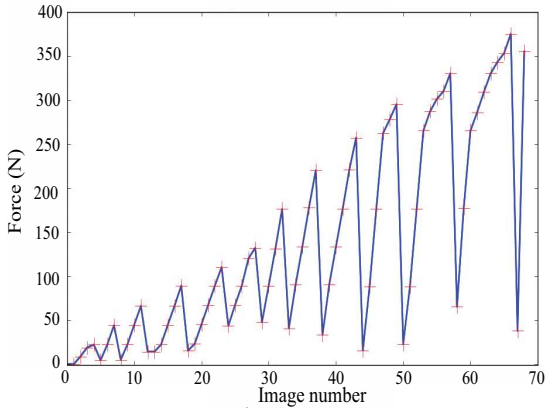

Figure 116: Sequence of load levels for each image acquisition.

These images will be used to perform DIC analysis and to detect the occurence of microplasticity in the crack tip region. Once the microplasticity onset is observed, the corresponding stress intensity factor K_I can be identified.

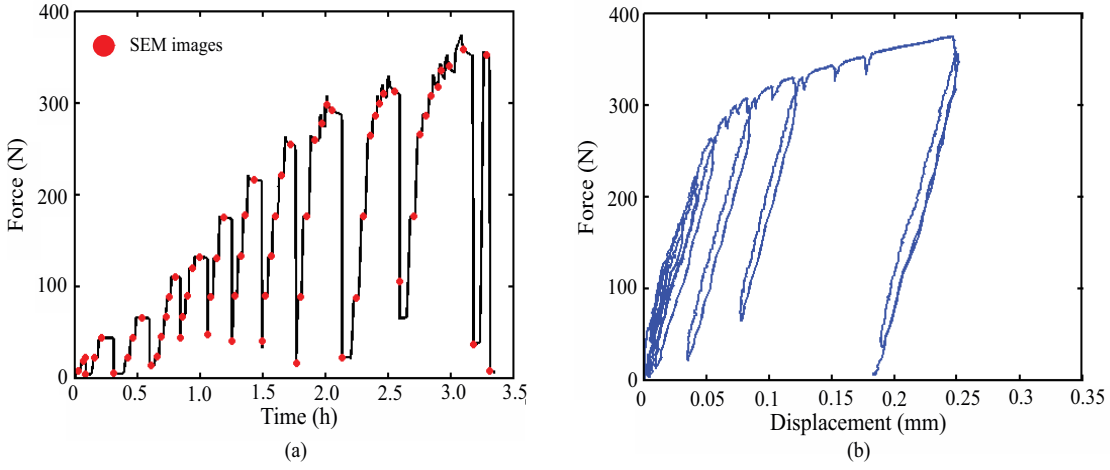

Figure 117: Force with respect to time (a) and (b) structure macroscopical response.

The first step has consisted in identifying the lower bound of the loading to apply to get crack propagation or plasticity development in the crack tip region. To achieve this objective, the kinematic fields have been measured during the test. A local kinematic method has been chosen to obtain the displacement fields during each "load-unload" cycle. The fourth cycle is represented on Figure 118: the beginning of this cycle is denoted A and its end is denoted B. The couple of

images corresponding to A and B are plotted in Figure 119.

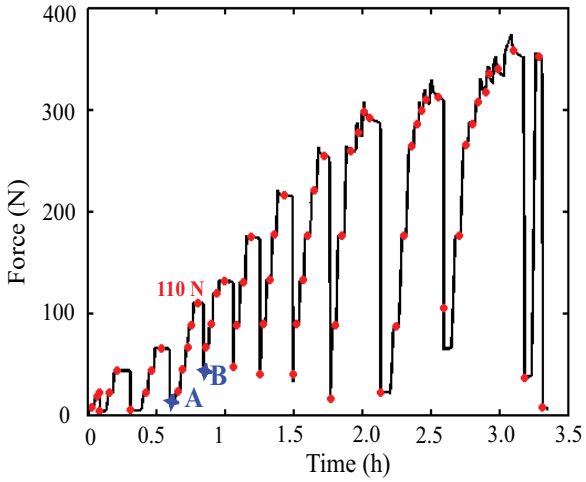

Figure 118: Tensile curve before (A) and after reaching 110 N (B).

Figure 119: SEM images in BSE mode of the ZOI before (A) and after reaching 110 N (B).

The residual displacement field is measured by a local DIC algorithm on each cycle and the Crack Mouth Opening Displacement (CMOD) is obtained by comparing the displacement value along the white profile represented in Figure 119 .

Before extracting the displacement jump, the kinematic fields have been corrected by the rigid body motion (translation and rotation) (see Figure 120 a). Figure 120 displays the profiles obtained on the different cycles. Each cycle is labeled by the maximum load. In this figure, an inflection point with a significant change in the slope of the curve displacement jump in function of the loading can be observed (Figure 120 b). It corresponds to a displacement jump of 0.5 µm and a

stress intensity factor K_I equals to 30 MPa.$\sqrt{m}$ (F = 257 N). The equation used to identify the stress intensity factor for SENT specimen is given as [112, 183]:

$$K_I = F_T(a/W)\sigma_\infty\sqrt{\pi a} \tag{5.1}$$

$$F_T(a/W) = \sqrt{\frac{1}{\tilde{r}}\tan(\tilde{r})}\left(\frac{0.752+2.02(a/W)+0.37\left(1-\sin(\tilde{r})\right)^3}{\cos(\tilde{r})}\right) \tag{5.2}$$

$$\tilde{r} = \frac{\pi a}{2W} \tag{5.3}$$

This stress intensity factor is estimated for the initial crack length. The displacement jump increases with the force. In Figure 120, the displacement jump corresponding to the first nine cycles has been drawn: F = [22, 44, 66, 89, 110, 132, 176, 220, 257, 295] in N.

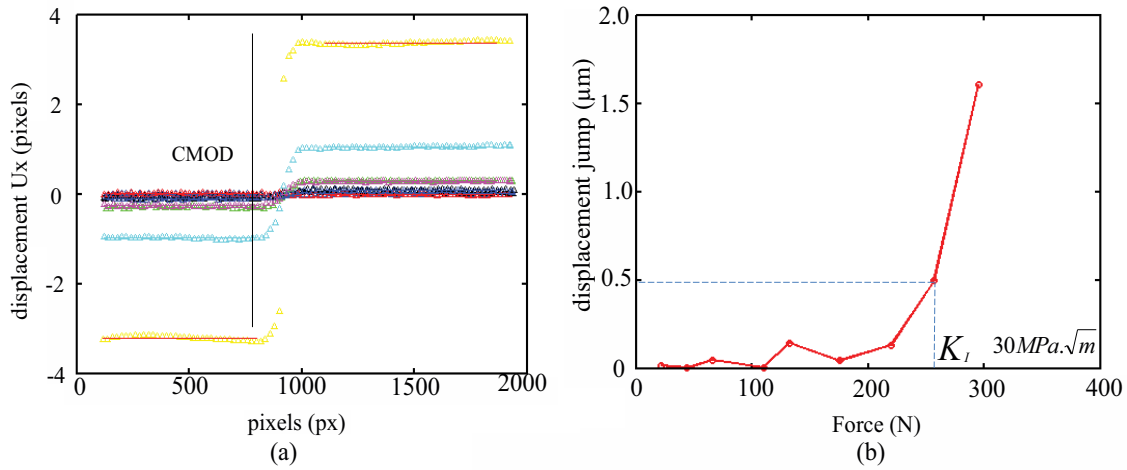

Figure 120: Displacement jumps along the profile (in pixels) (a) and displacement jump (µm) considering the loading levels (b) computed betwwen the unloaded and the loaded image for each cycle.

The first microplasticity onset is obtained for F = 257 N for this specimen (see Figure 120). The initial crack length is determined on the SEM image, which allows us to estimate the critical stress intensity factor for the crack propagation: $K_I = 30$ MPa.$\sqrt{m}$, using the method detailled in [112]. The microplasticity onset identification has been verified using the coefficient a_I^1 resulting from the Williams series projection. Let us underline that the geometry of the crack is not consistent with the underlying hypothesis of the Williams series expressions (sharp crack with a displacement discontinuity located for a given angle from the crack in the reference configuration). Here, the crack is well opened in the reference configuration. Nevertheless, it is proposed to use the projection on the Williams series to estimate the crack opening. The coefficient a_I^1 is referring to the Westergaard analytic solutions and is a function of the loading applied. A DIC analysis has been performed both on SEM images acquired for each peak load and on images acquired when the specimen was unloaded (see Figure 121 a). This displacement fields have been projected on the LEFM base function considering exclusively the mode I and orders 0, 1 and 2. The optimized Williams series coefficients a_I^1 resulting from the identification are shown in Figure 121 b. The

red cross is used for displacement fields at maximal loading and blue cross is used for displacement fields when the specimen is unloaded. Hereafter, the coefficients a_I^1 for maximal load will be denoted $(a_I^1)^h$. Conversely, the coefficients a_I^1 for unloaded image will be denoted $(a_I^1)^l$. To indicate the first microplasticity onset identified using the displacement jump ($K_I = 30$ MPa.$\sqrt{m}$), a black vertical line has been plotted. When the applied load is inferior to this previously identified threshold, a slight increase is observed on the a_I^1 coefficients. After reaching the threshold, a visible jump and increase in a_I^1 values is observed for both "loaded/unloaded"' SEM images. The increase of $(a_I^1)^l$ is consistent with the development of residual deformation and is attributed to a permanent opening of crack. The evolution of $(a_I^1)^h$ values is consistent with the increase of the applied load (see Figure 121 a).

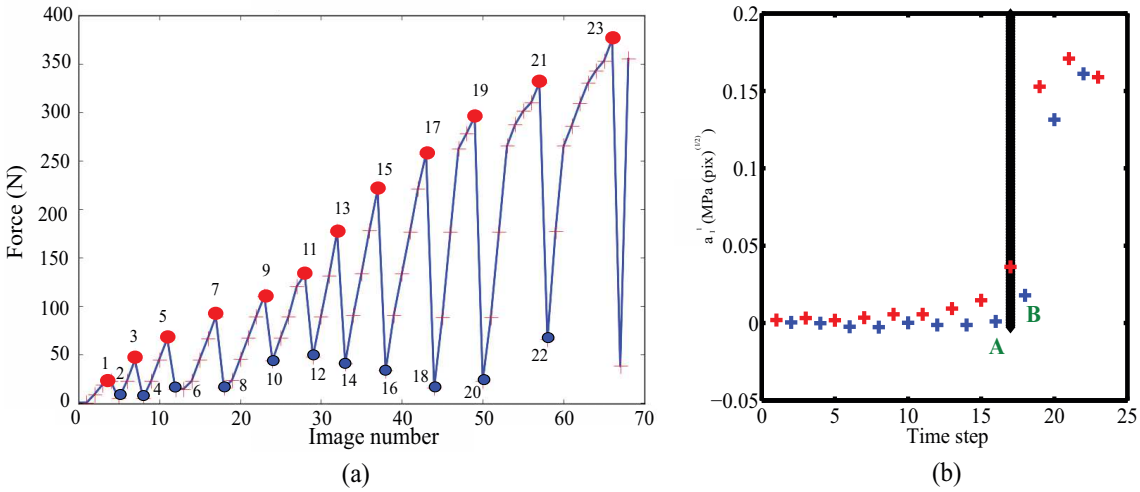

Figure 121: Force with respect to SEM image acquisition (a) and evolution of Williams coefficient a_I^1 during the test (b).

We propose to illustrate the development of residual deformation when the sample is unloaded before and after the first microplasticity onset, respectively denoted A and B in Figure 121. The residual deformation fields defined as the difference between the overall deformation and the deformation associated with the Williams series (the strain are computed using the Small Perturbations Hypothesis) in the loading direction for step #A and #B are presented respectively in Figure 122. The crack has been masked to annihilate the effects of the discontinuity presence in the strain fields. The residual strain level is higher in the crack tip region, where plasticity should develop.

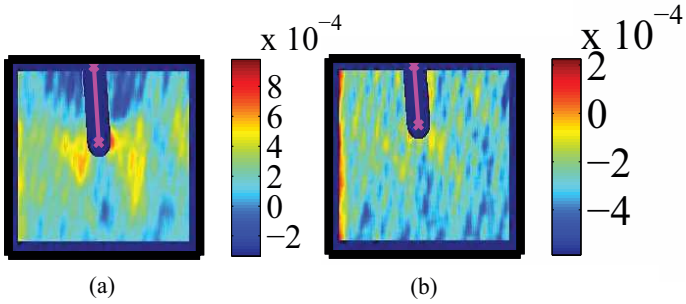

Figure 122: Residual deformation field in the loading direction (ε_{xx}) for step #A (a) and residual deformation field in the loading direction (ε_{xx}) for step #B (b). The dimensions is about 475.8 x 390.4 µm^2 (1950 x 1600 pixels^2).

A comparison of the microstructural observations of the crack tip region before and after the first microplasticity onset is proposed in Figure 123. After reaching the identified microplasticity threshold, numerous slip bands are observed. Moreover, the adhesive properties of tungsten pattern allow a precise representation of the kinematic fields in the crack tip region. It is confirmed by the perfect adhesion between the underlying 316 stainless steel and surface markers. Slip bands are intersecting some tungsten dots highlighting their good adhesion with the underlying 316 steels (Figure 123 d).

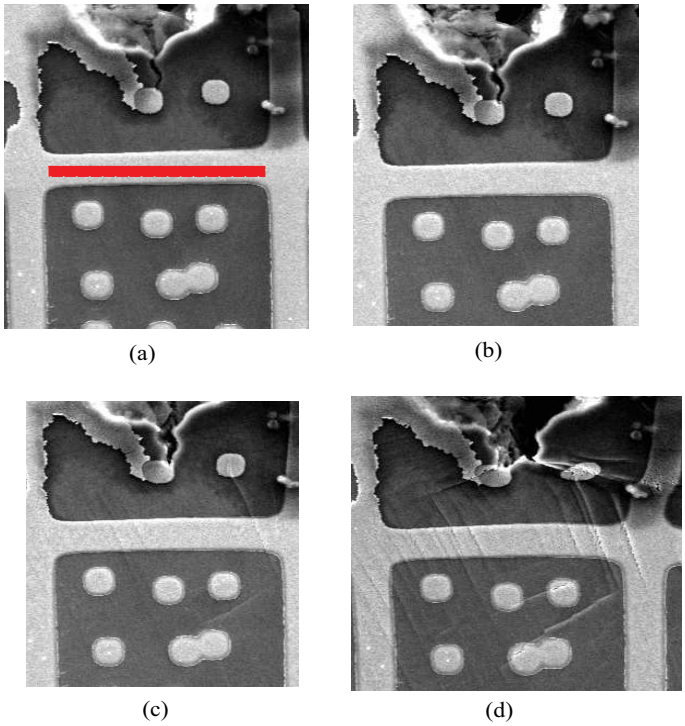

Figure 123: SEM images in SE mode in the crack tip region (a) 44 N, (b) 220 N, (c) 257 N (apparition of slip bands) and (d) 295 N. Magnitude: x1411. The red scale bar is 10 µm.

To verify the crack stationarity mentioned previously, we propose to apply the procedure in-

troduced in Chapter 4 on kinematic fields obtained by comparing SEM images acquired during the test (see Figure 121 a). A classical DIC approach has been used to obtain the kinematic fields. To avoid any side effects, the considered Region Of Interest (ROI) was 1750 x 2048 pixels. The grid step (*GS*) is 1 and the subset size (*s*) is 60 pixels for a working field of 500 µm. The physical size of the pixel is 0.244 µm.

A comparison with estimated crack positions and crack tip parameters identified by the procedure is proposed in Figure 124. Estimated crack tip positions are clustered around the crack tip identifed in the SEM images (see Figure 124 a,b). The optimized values are aligned along the crack lips (see Figure 124 c,d). The mismatch between the optimized position and the crack position in the SEM image is probably generated by the crack shape. As mentioned earlier, the discontinuity in the specimen is similar to a notch which is not consistent with the Williams series solutions expressed for a sharp crack.

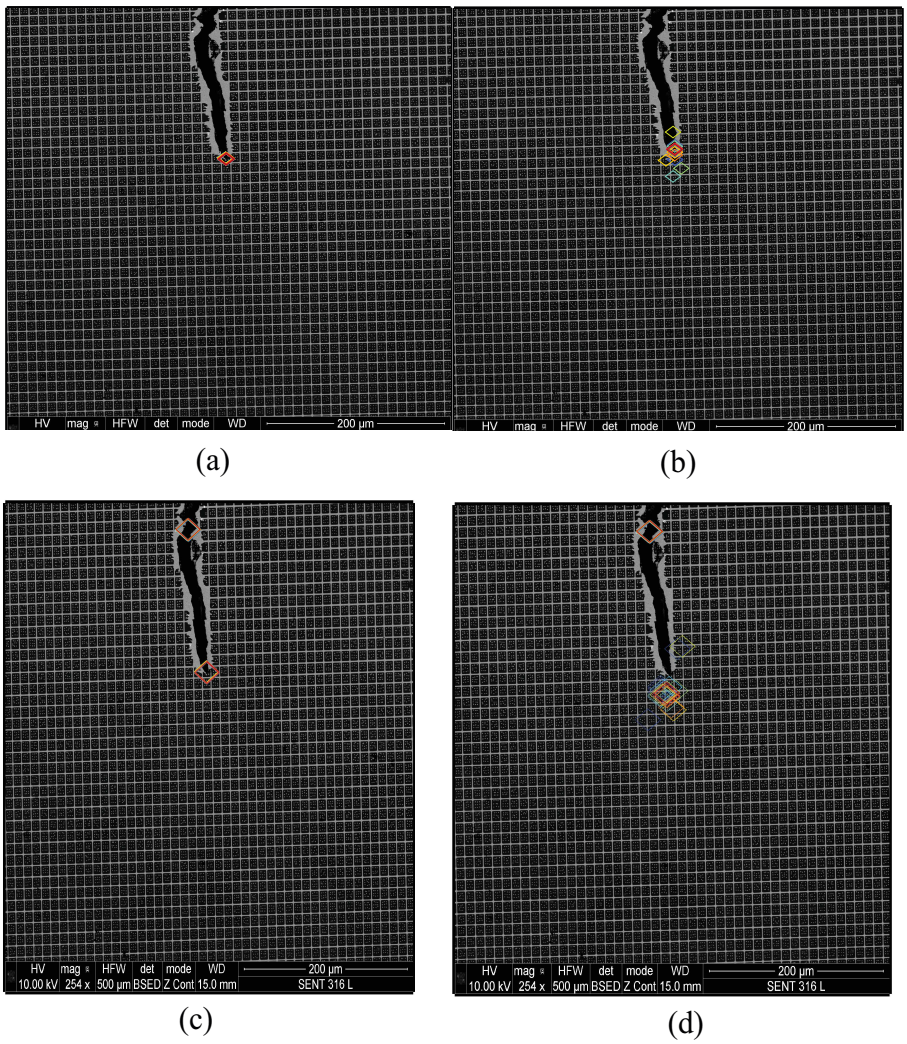

Figure 124: Estimated crack tip position during the *in-situ* tensile test (see Figure 121) (a) and optimized crack tip position using projection of displacement fields obtained by DIC (b). Magnified views of estimated crack tip coordinates (c) and optimized crack tip positions (d).

Contrary to the displacement jump, the optimized crack tip positions are not correctly identified. This could be explained by the mismatch between the "opened" crack form of SENT notch and the Williams series solutions expressed for a sharp crack and by the sensitivity of the identification functional which is higher for the displacement jump than for the crack position. Nevertheless, the optimized crack tips are clustered which is a potential evidence that the crack has not propagated during the test. This is confirmed by the SEM observations at small scales in the crack tip vicinity.

Conclusions:

The objective of the *in-situ* tensile test has consisted in identifying the lower bound of the loading to be applied for generating a detrimental crack propagation on a 316L SENT specimen. During the test, the crack has not propagated and plasticity development has been observed. The first microplasticity onset has been identified with two methods:

- The displacement jump has been extracted from SEM images acquired when the specimen was unloaded. These images have been used to measure the kinematic fields by performing DIC analysis. The increase of the displacement jump for $K_I = 30$ MPa.$\sqrt{m}$ has been attributed to a permanent deformation in the crack tip region possibly interpretable as plasticity development.

- The displacement fields have been projected on a basis of shape functions from LEFM. Exclusively mode I and orders 0, 1 and 2 have been considered for the Williams series. The order 1 referring to the Westergaard analytic expressions. The optimized values of a_I^1 have been plotted (see Figure 121). For $K_I = 30$ MPa.$\sqrt{m}$, an increase is observed for displacements fields measured for "unloaded" SEM images. It could be also interpreted as an indicator of plasticity development.

To verify the crack stationarity during the *in-situ* tensile test, the crack tip identification procedure has been applied on displacement fields obtained on the SEM images. The optimized crack tip positions are located in the crack lip. As the distance between the optimized crack tip positions is small, the procedure robustness is not at stake. The form of the SENT notch is not similar to a sharp crack and it has been identifed as a potential cause of the procedure accuracy decrease. The large space between the two lips may generate a disconinuity which is not consistent with the Williams series solutions. As a perspective, it could be relevant to study the influence of the crack shape on the validity choice of Williams series as displacement shape functions.

5.3 *In-situ* tensile test on carburized 316H SENT specimen at room temperature

An *in-situ* tensile test on carburized 316H SENT specimen has been performed at room temperature. This test aimed at both validating the microplasticity threshold identified considering a 316L specimen in Section 5.2. A second objective is to collect informations on the crack path and on the plasticity development in the carburized material. The test has been carried out in the SEM Quanta 600 following a procedure similar to that used previously on the 316L non carburized specimen.

The test has consisted in applying a sequence of loadings and unloadings, with increasing peak loads applied until reaching a significant crack propagation (see Figure 125). Hereafter, the step corresponding to crack observation will be denoted step #a.

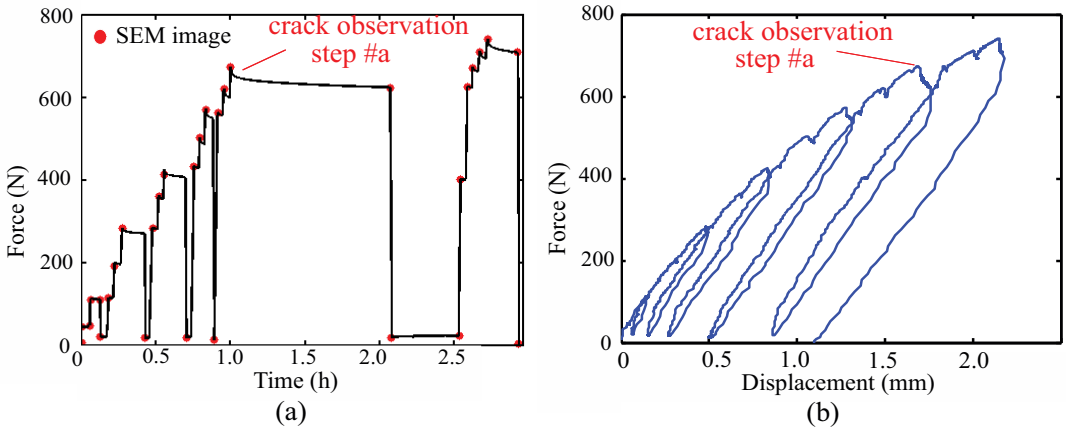

Figure 125: Force with respect to time (a) and specimen load-line displacement (b). The step corresponding to crack observation is denoted step #A.

In Chapter 2, we have introduced the preconditioning treatment giving rise to carburization and oxidation of the specimen surface. After 2,000 hours in CO_2 environment, an oxide has grown at the sample surface preventsfrom observing the crack. Figure 126 provides a SEM image of the oxide at the specimen location that corresponds to the fatigue crack initially developped in the specimen before carburization.

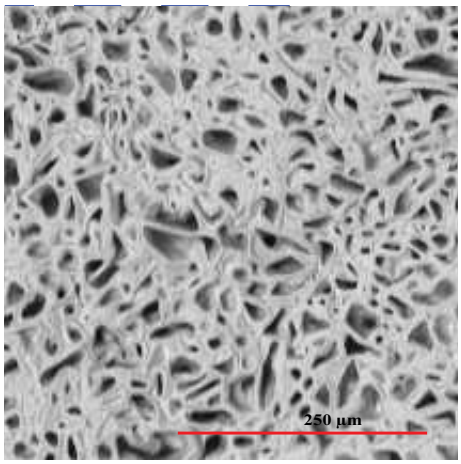

Figure 126: SEM image in BSE mode of oxidised region situated in the middle of the specimen gauge where the fatigue crack is expected. Magnitude: x254.

A drawback of the oxide development is to hide the crack. However, the oxide provides an ideal pattern for DIC at the scale relevant with the chosen micromechanical observation of the crack. Displacement fields between the unloaded oxidised sample and the loaded one can be in

turn monitored during the test.

The first crack propagation was observed for an overall loading of 670 N (σ_∞ = 305.9 MPa) (Figure 127). This corresponds to the loading point labelled "step #a" on the loading curve provided in Figure 125 a. After this load level, the oxide layer broke along the fatigue pre-crack. The crack is observed in a region located above the area shown in Figure 126 that corresponds to the reference configuration initially chosen before reaching step #a. Due to the lack of confidence in the initial fatigue crack tip location in the reference configuration, it is thus impossible to determine the total deformation field associated with this first propagation of the crack. At this stage, the crack length from the fatigue pre-crack is estimated to about 300 µm and the total length is measured to 600 µm (see Figure 127).

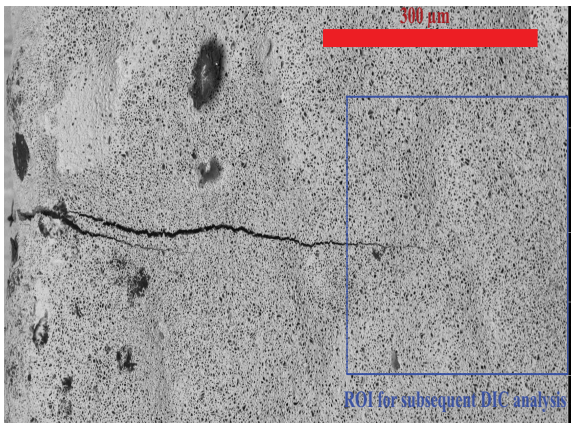

Figure 127: SEM image in BSE mode at the stage of crack onset (corresponding to step #a). The blue rectangle represents the chosen ROI for subsequent crack monitoring using DIC.

After the first crack observation at step #a, the specimen has been unloaded and the ROI has been chosen ahead of the previous crack tip position to monitor the crack propagation (see Figure 127). Then, the sample has been loaded until 750 N (σ_∞ = 342.4 MPa) which corresponds to the level of loading for crack to propagate outside the ROI.

As previously mentioned, an oxide layer has grown at the sample surface hiding the position of the fatigue pre-crack in the SENT. Nevertheless, the oxide is an ideal surface marker that can be used to perform DIC measurements. During the *in-situ* tensile test, some discontinuities have been observed on displacement fields and were attributed to the presence of cracks. In the following, the two consecutive tasks are presented:

1. After the first crack propagation, a new ROI region has been chosen to allow a crack monitoring using DIC. Then, the kinematic fields have been projected onto the LEFM basis introduced in Chapter 4 to identify the crack parameters;

2. After performing the kinematic approach, we propose to study the crack propagation in the sample volume using fractography at microscopical scale.

5.3.1 Crack monitoring using full-field measurements

Figure 128 represents the load levels that have been considered for the displacement measurements: 400 N (σ_∞ = 182.6 MPa), 620 N (σ_∞ = 283.1 MPa), 670 N (σ_∞ = 305.9 MPa) and 710 N (σ_∞ = 319.6 MPa). At 750 N, the crack tip moves out of the SEM image. Even if the kinematic fields can be obtained, it is not possible to apply the identification procedure for this last load level. The grid step *GS* is equal to 10 pixels and the subset size *s* is 12 pixels.

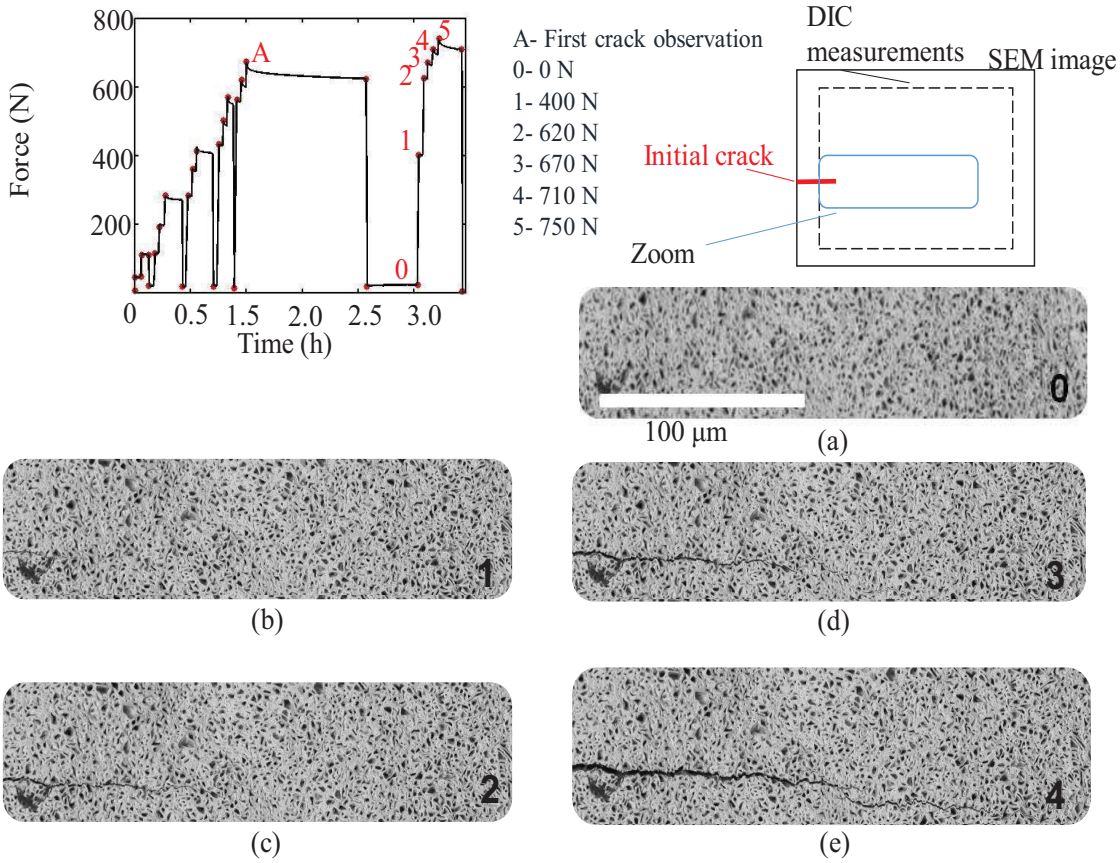

Figure 128: Zoomed view of the SEM images which have been used to obtain the kinematic fields and to monitor the crack at 0 N (a), 400 N (b), 620 N (c), 670 N (d) and 710 N (e).

After the first crack propagation, the specimen has been unloaded and the next propagation has been obtained for a load inferior to 670 N. At 400 N, the crack started to propagate again. This illustrates the low toughness of the oxidised layer.

These local kinematic fields obtained by DIC (Figure 129 a-d) have been projected onto the LEFM base made of Williams series considering exclusively the mode *I* and the orders 0, 1, 2 (Figure 129 f-i). As mentioned earlier, the kinematic fields obtained for F = 750 N have not been processed because the crack tip position is located outside the SEM image. One can notice that the propagation is straight.

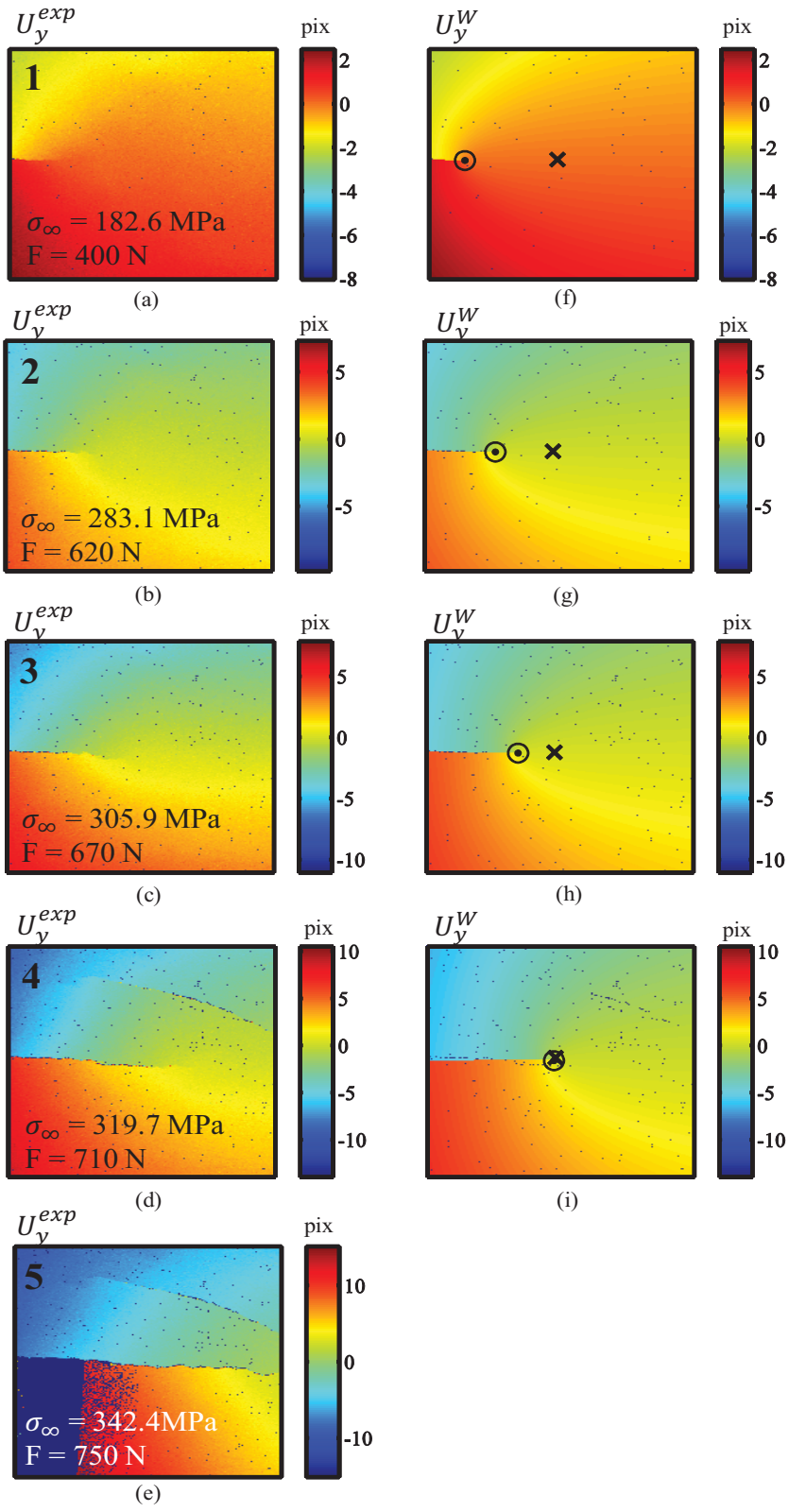

Figure 129: Comparisons between the kinematic fields in the loading direction obtained with a local DIC method (a), (b), (c) and the displacements fields reconstructed from LEFM projection (d), (e), (f). The image resolution is 2048 x 1760. R_{max} = 512 pixels = 125 µm.

The optimized values are given in the Table 44 for R_{max} = 512 pixels. For the first three load levels (σ_∞ = 182.6 MPa, 283.1 MPa, 305.9 MPa), there is a good agreement between the measured displacement fields and the LEFM projected ones because there is only one crack propagating. For the last load step, it is proposed to reduce the set of points considered for the optimization of crack tip position, with R_{max} = 300 pixels in order to limitate the influence of the second crack on the optimization. By reducing R_{max}, the accuracy of the optimization is increased (see Figure 130).

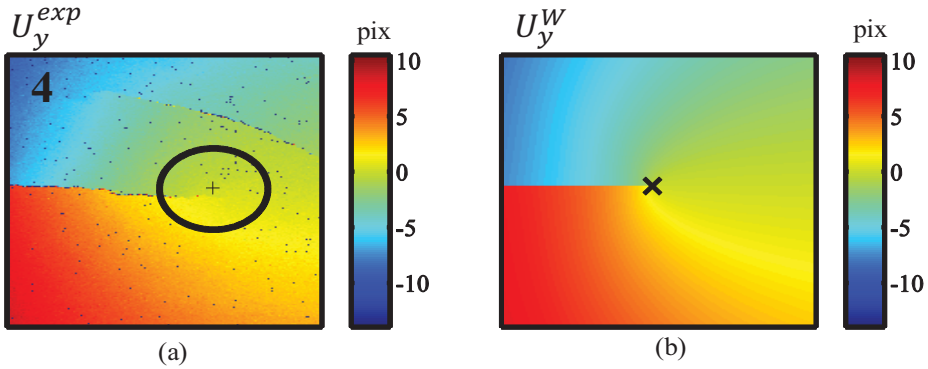

Figure 130: Comparisons between the kinematic fields in the loading direction obtained with a local DIC method (a) and the displacements fields reconstructed from LEFM projection (b). The image resolution is 2048 x 1760. R_{max} = 300 pixels = 73 µm.

For the fourth load (σ_∞ = 319.6 MPa), two cracks can be observed and the LEFM base is not sufficient to capture the whole field: the crack identification procedure is launched twice for two different initial guessed (x_1^{est}, y_1^{est}) and (x_2^{est}, y_2^{est}) chosen manually in the vicinity of the two cracks ends. This manual operation allows to determine the two cracks positions. Hereafter, the cracks will be denoted respectively crack #1 and crack #2 (see Figure 131).

After a manual selection of the two cracks ends in the SEM image (see Figure 131 a), the optimization procedure is performed. For this case, R_{max} is chosen equal to 190 pixels. The optimized crack tip positions are indicated using diamond markers and are consistent with the estimated crack tip positions for crack #1 (see Figure 131 c) and for crack #2 (see Figure 131 b).

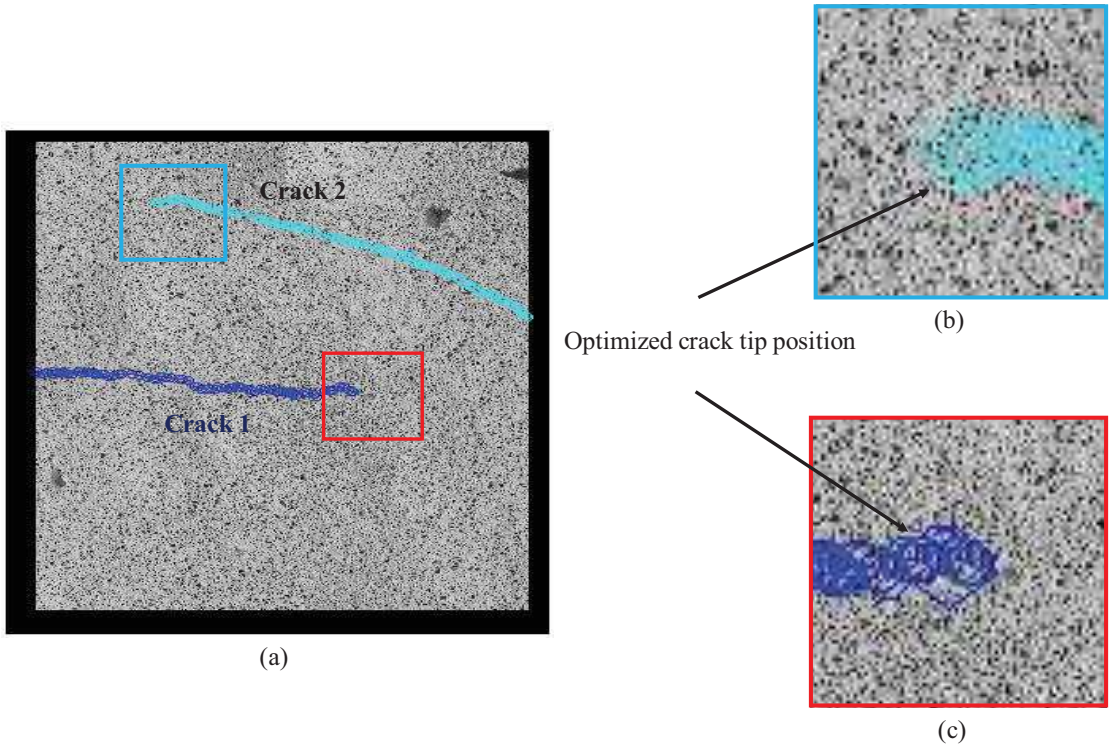

Figure 131: A manual selection of cracks in the SEM image allows to identify the two cracks ends (a). After projection on LEFM base, the optimized values are represent with diamond markers for crack #2 (b) and crack #1 (c).

A summary of the identified crack tip postions for F = [400, 620, 670] N is proposed in Table 44 . Due to the presence of two cracks for F = 710, the results will be presented in Table 45.

x^{est}	y^{est}	Θ^{est} (radian)	x^{opt}	y^{opt}	Θ^{opt} (radian)	Force (N)	σ_∞ (MPa)
835	975	0.00	233.1	983.8	1.88×10^{-2}	400	182.6
835	975	0.00	459.38	980.8	1.48×10^{-8}	620	283.1
835	975	0.00	596.2	981.2	2.27×10^{-3}	670	305.9

Table 44: Comparisons between estimated values and the optimized crack tip position for F = 400, 620 and 670 N. R_{max} = 512 pixels.

Crack	x^{est}	y^{est}	Θ^{est} (radian)	x^{opt}	y^{opt}	Θ^{opt} (radian)	R_{max} (pixels)
Crack #1	835	975	0.00	821.5	1000.1	-7.39×10^{-5}	512
Crack #1	835	975	0.00	1076	1042.4	-4.9×10^{-3}	300
Crack #1	1130.9	986.1	0.00	1098.5	970.9	-4.17×10^{-4}	190
Crack #2	490.2	1760.0	0.00	491.0	1759.1	-1.07×10^{-4}	190

Table 45: Comparisons between estimated values and the optimized crack tip position for F = 710 N.

Each optimized position from Table 44 has been plotted in the "deformed" images in Figure 132. The identified position is accurate compared to the position determined by SEM observation. The red square represents the subset size, the green cross the position identified by SEM observation and the red one is used to indicate the optimized crack tip position.

Table 44 shows that the crack orientation remains constant, and that the propagation is mainly in the **x** direction. In Table 45, a comparison between:

- the optimized crack tip position (crack #1) with estimated coordinates at the center of the image and R_{max} = 512 pixels,
- the optimized crack tip position (crack #1) with estimated coordinates at the center of the image and R_{max} = 300 pixels,
- the optimized crack tip position (crack #2) with estimated coordinates observed on the SEM image and R_{max} = 190 pixels.

As mentioned before R_{max} influences the accuracy of the optimization procedure, expecially when two cracks tips have to be identified. An arbiratrory choice slightly influence the results from the procedure if the R_{max} is adapted. The second crack tip position has been identified and it is consistent with the SEM observations.

The difference between the optimized position and the crack tip position identified in the SEM image relies on the resolution of the kinematic field measurement, on the SEM image magnification but also to the intrinsic limitations of the procedure identification presented in Chapter 4 (associated with unconsistant boundary conditions or material behaviour). The distance (d) between the crack tip position observed on the SEM image (x_{SEM}, y_{SEM}) and the optimized one for each loading level is presented in Table 46. The physical size of a pixel equals to 0.2441 µm. The mean value of the distance ($\bar{d}$) between (x_{SEM},y_{SEM}) and the optimized values can be estimated $\bar{d}$ = 29 µm, with consistent R_{max}.

x_{SEM} (pixels)	y_{SEM} (pixels)	distance d (pixels)	distance d (µm)	Force (N)
282.0	1058.7	49.2	12.01	400
571.1	1013.0	116.2	28.35	620
804.7	1053.8	220.7	53.85	670
1164.1	1076.0	348.9	85.13	710
1164.1	1076.0	91.47	22.31	710, R_{max} = 300 pixels

Table 46: Distances between estimated values and the optimized crack tip position for F = 400, 620, 670 N and 710 N.

It is proposed to select the estimated crack tip position for each discontinuity appearing in the displacement fields to get the best accurate results. In the last section, a detailed methodology to handle multiple cracks is presented. From several fields resulting from DIC analysis, a crack mask can be created and be used as a robust estimated crack tip positions.

Conclusions:

Contrary to the first test on SENT 316L specimen, this sample has been submitted to preconditioning treatment responsible for oxide growth at the surface. Due to the oxide layer presence, the material should be considered as a ”composite” material made of bi-materials (oxide layers and 316H base metal). It appears that for this case, the identification of K_I using the expression given for SENT specimen is not so relevant.

This oxide can be used as a pattern for the DIC analysis and displacement fields are obtained during the *in-situ* tensile test. It is require to make the assumption that the pattern moves in agreement with the underlying material. In this precise case, it seems that the mechanical properties of the oxide are different compared to the 316H steel. Particularly, a lower toughness could generate crack propagation at the surface in the oxide and not in the underlying austenitic stainless steel. It could explain the difference between the optimized crack tip positions and the estimated ones, especially when the crack length increases. Considering the presence of this supplementary layer, the results from the identification procedure are considered as satisfactory.

After unloading the specimen, some observations have been made using SEM to get information about crack path and microstructure evolution. Moreover, the effects of preconditioning treatment on cracking behaviour have been observed. They are presented in the next paragraph.

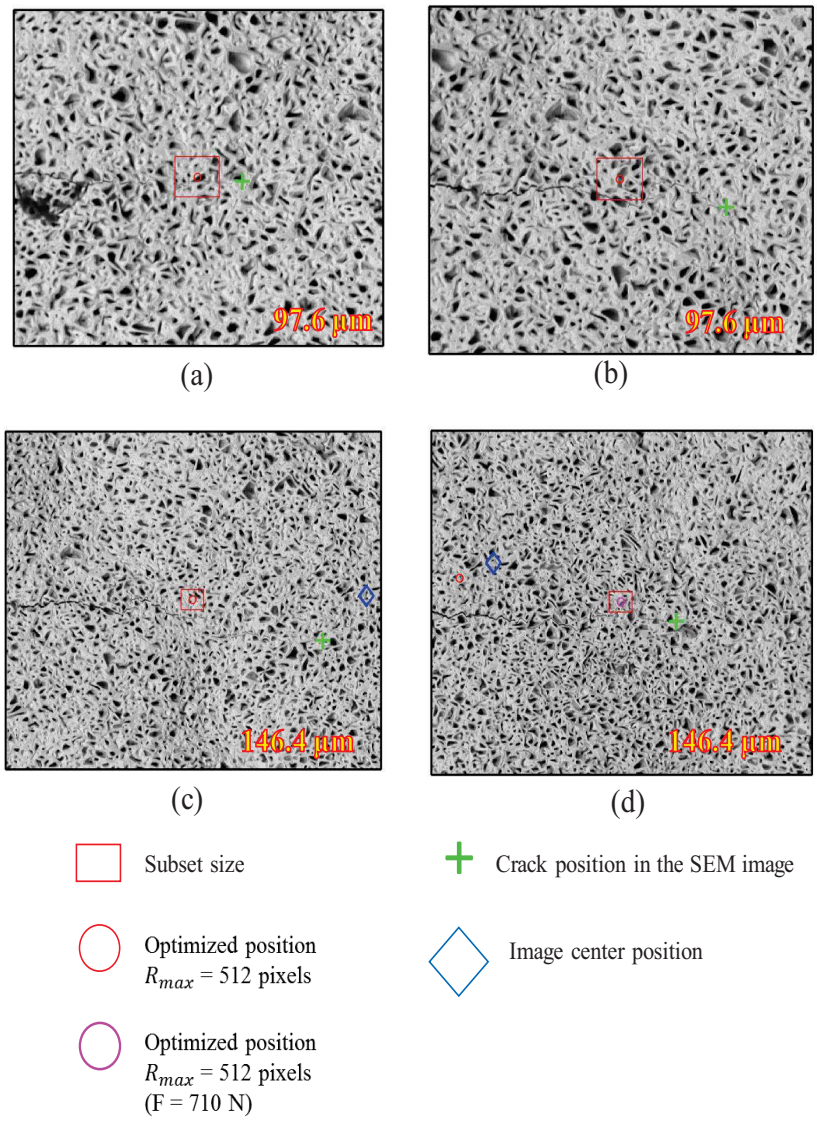

Figure 132: Optimized crack tip position in the corresponding deformed SEM image for F = 400 N (a),620 N (b), 670 N (c) and 710 N (d). For F = 710 N, two optimized positions have been plotted: red circle symbol is used for R_{max} = 300 pixels and magenta circle is used for R_{max} = 512 pixels.

5.3.2 SEM observations and fractography

SEM observations have allowed to obtain measures about the cracking behaviour of the superficial layers such as kinematics, morphology, extent, propagation as well as in the thickness of the specimen. By measuring the crack dimensions in SEM images, the final main crack length is close to 1 mm and a secondary crack due to oxide failure is observed (see Figure 133 a). At the surface, the crack has propagated along the oxide structure (see Figure 133 b).

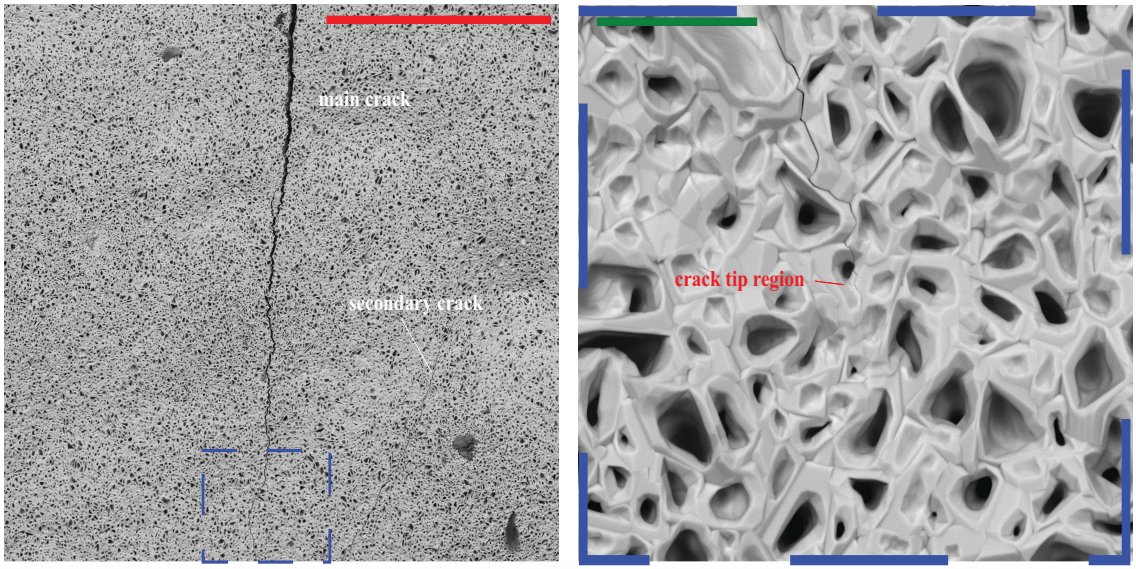

Figure 133: SEM images in BSE mode at the end of the test: The red scale bar is 300 µm (a), the crack tip region at higher magnification (b). The green scale bar is 10 µm.

After unloading the specimen, SEM imaging allows to observe that the crack has slightly closed and the final visible crack length is about 800 µm. The sample has been removed from the *in-situ* tensile machine to perform observations of the uncarburized face. The crack length on this side is shorter than the one in the carburized face and measures about 500 µm (see Figure 134). The difference between the two crack lengths is interpreted as the consequence of differences in mechanical properties of the preconditioned face: the fracture toughness of the carburized material is weaker than the uncarburized one. On the uncarburized face, several cracks are observed at the surface and they are aligned with the principal shear directions at about $\pm$ 45° of the crack plane (see Figure 135). A SEM image taken in the crack tip region indicates that the crack path is inter or transgranular (see Figure 135). Moreover, numerous vertical short cracks are present but they seem to be confined near the surface.

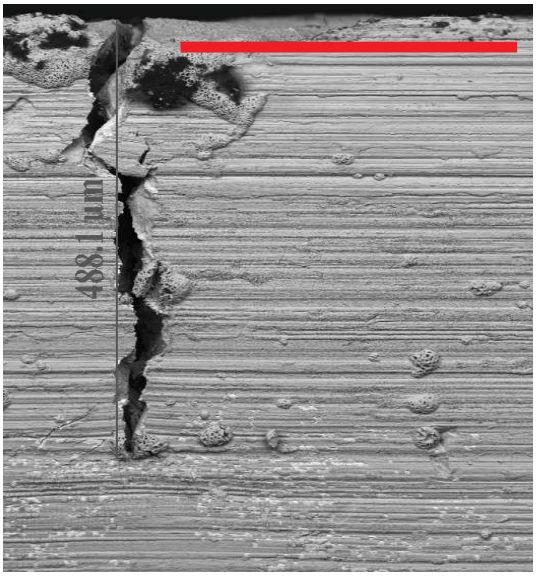

Figure 134: SEM images in BSE mode at the end of the test after unloading in the uncarburized face. The red scale bar is 300 µm.

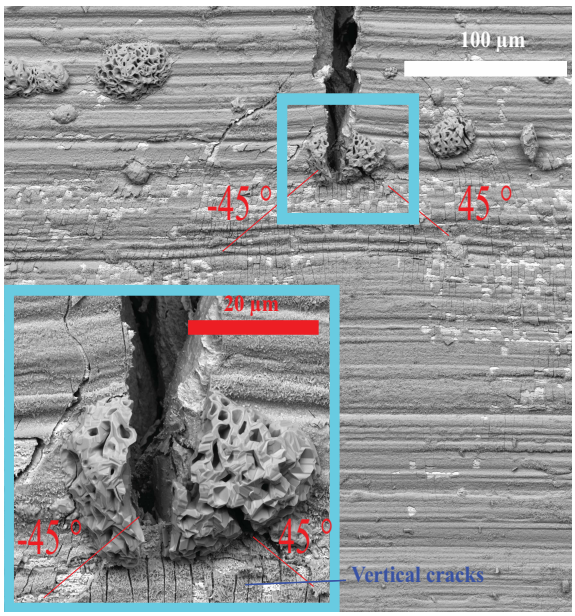

Figure 135: SEM images in BSE mode at the end of the test after unloading of the crack tip region in the uncarburized face.

To investigate the intergranular or transgranular nature of the crack, a fine polishing treatment up to OPS finish has been applied to the carburized face. The LEICA EM TXP polishing device has been used. An EBSD map has been performed using the OIM TSL software of the SEM MIRA. The dimensions of the ROI is 2 mm x 1 mm. The austenite phase has been used as the reference crystallographic phase (see Figure 136). In this figure, the crack path is revealed by the

non-indexed pixels. The areas embedded by the red squares highlight the microhardness marks used to monitor the thickness removed during the etching process. They are not related to the crack. The crack has propagated with a inter/transgranular path.

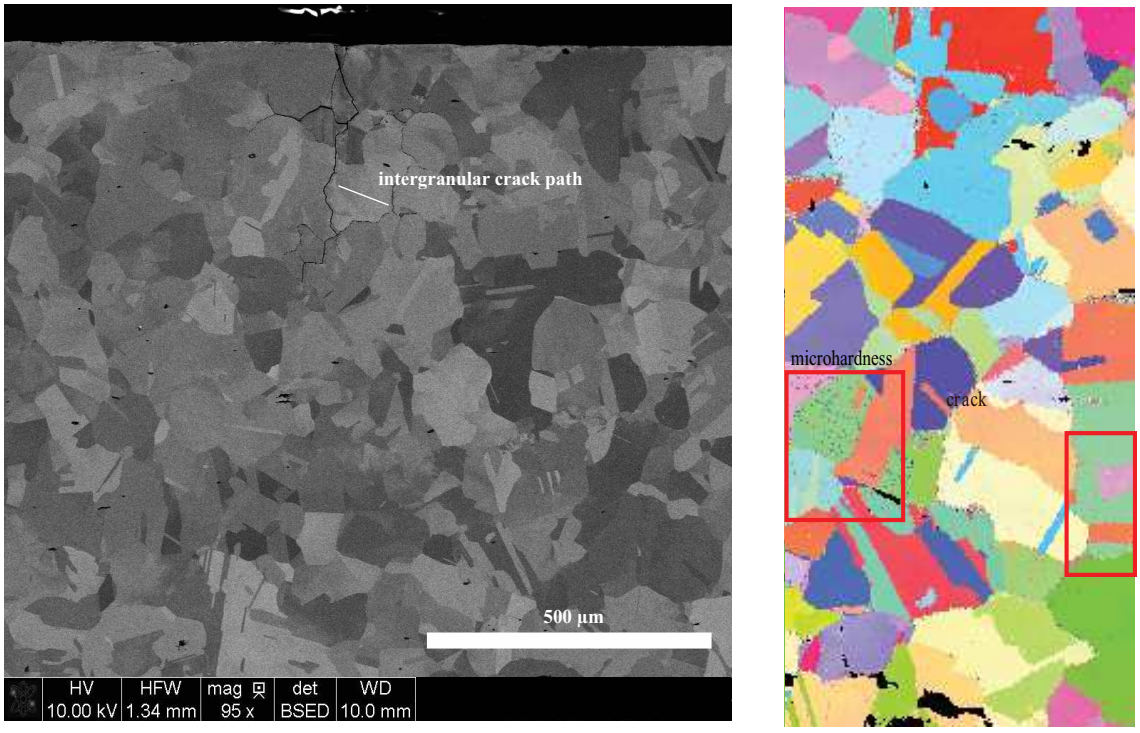

(a) (b)

Figure 136: An example of intergranular path observed on a SENT 316H sample before preconditioning (a) and EBSD cartography from OIM TSL software after OPS finish of the carburized face of the SENT 316H (b): the crack final crack path seems to be inter/transgranular.

To characterize a possible grain boundary embrittlement, we propose to observe and monitor the crack propagation path along the thickness of the SENT sample using a campaign of successive erosions by polishing from a surface normal to the crack propagation direction. A reference coordinate system is provided on Figure 137 and the polishing has been performed in the (X, Z) plane (see Figure 60).

Three successive erosions have been performed. First, 100 µm have been removed (see Figure 137 a), then 100 µm have been removed again to reach 200 µm (see Figure 137 b). The fatigue pre-crack measured approximately 300 µm. At this stage, the crack path is transgranular and corresponds to the fatigue pre-crack. During the last erosion, 200 µm were removed to reach 400 µm (see Figure 137 c). The crack shown in Figure 137 c has resulted from the crack propagation during the *in-situ* tensile test. The crack path is not uniform along the sample depth and it seems that the main crack is transgranular with a few intergranular bifurcations. The crack has more propagated in the carburized face than in the non carburized one. As the SEM image observation has been done only for a few polishing treatment and considering that the crack length is different from one face to an other, the crack morphology is only partially characterized.

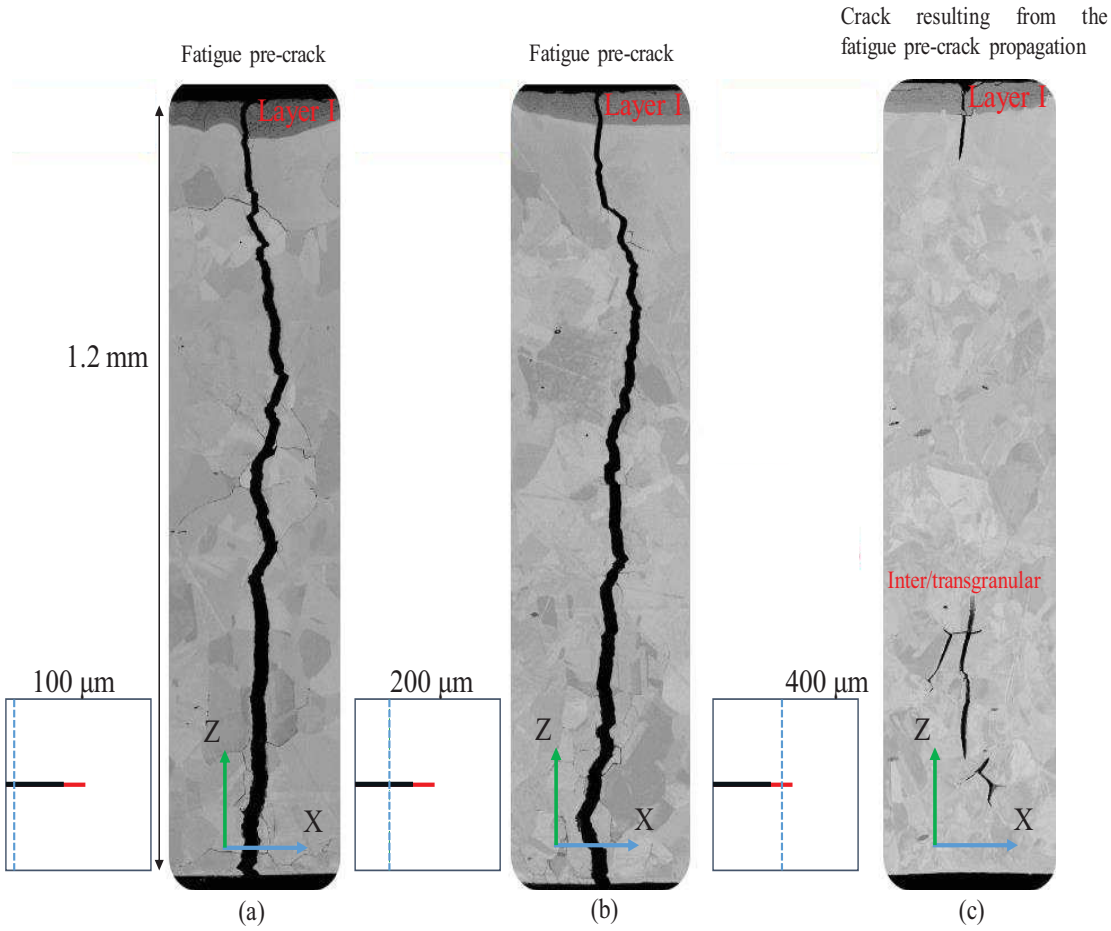

Figure 137: Description of the three successive erosions to study the evolution of the crack path: 100 µm (a), 200 µm (b) and 400 µm (c).

5.4 DIC crack monitoring between three creep test periods

An interrupted creep test has been performed in air at 550 °C on 316H SENT specimen to perform a crack monitoring at the microstructural scale. Prior to creep testing, the specimen has been polished to remove the magnetite layer. At the beginning of each creep stop, the furnace is turned off and the specimen is unloaded. Then, the specimen has been placed in the SEM chamber of the FEI Quanta 600. An *in-situ* tensile device has been used to apply elastic loadings and to slightly open the crack. This procedure is used to make the crack position observable on the SEM images. The DIC analysis then allows the crack tip position identification highlighting the possible crack propagation. The crack tip position identification is obtained by projecting the kinematic fields onto the LEFM base. The methodology of this experiment is presented in Figure 186.

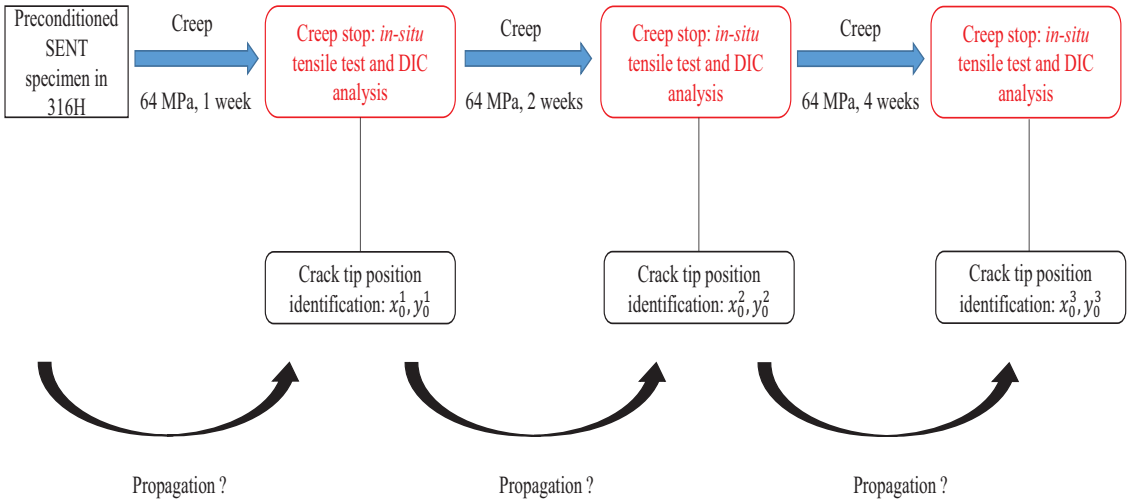

Figure 138: Methodolgy of the interrupted creep test at 550 °C in air.

The chosen loading for the creep test is 64 MPa, it corresponds to a $K_I = 2.5$ MPa.$\sqrt{m}$ [112]. It is well below the threshold value of 30 MPa.$\sqrt{m}$ associated with the crack propagation. The value of K_I for creep crack growth test on CT specimen is usually chosen equal to $K_I = 10$ MPa.$\sqrt{m}$ [184] and post-processed using the parameter C^* ($C^* = \frac{da}{dt}$). The total creep curve is presented in Figure 139.

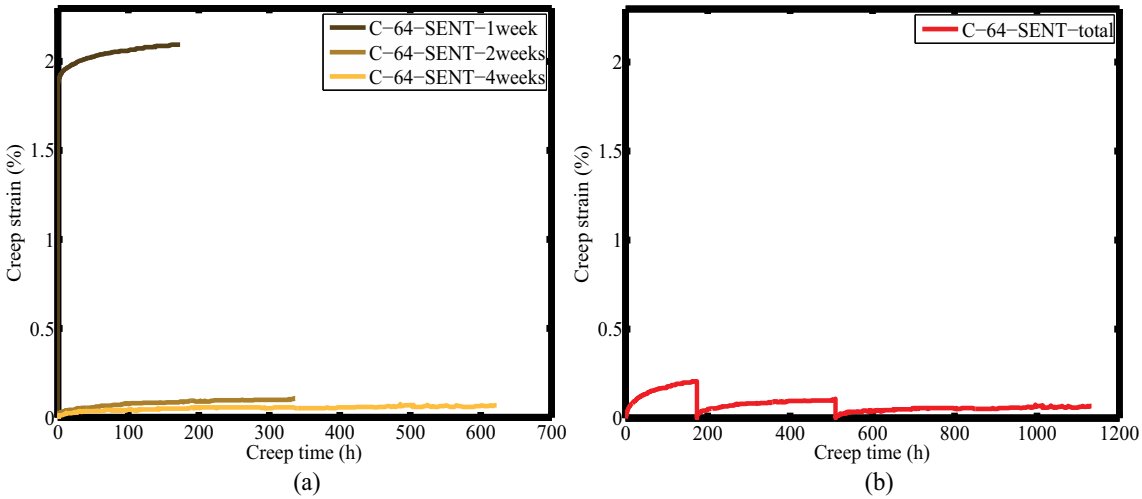

Figure 139: Creep curves for the C-64-SENT test at 550 °C in air. The total creep curve has been plotted to respect the creep test chronology.

Homogeneous deformations have been observed for the second and the third periods (see Appendix D). No discontinuities have been observed in the displacement fields, thus the identification procedure will not be applied. In the following, we will exclusively consider the first creep period. We propose to use the kinematic fields to identify the crack parameters during the first creep interruption.

5.4.1 *In-situ* tensile test after an one week creep period

After one week at 550 °C in air under a loading of 64 MPa, the sample has been removed from the creep rigs and placed in the *in-situ* tensile device. Then, a sequence of loadings has been applied with the objective of observing a crack at the sample surface (see Figure 140).

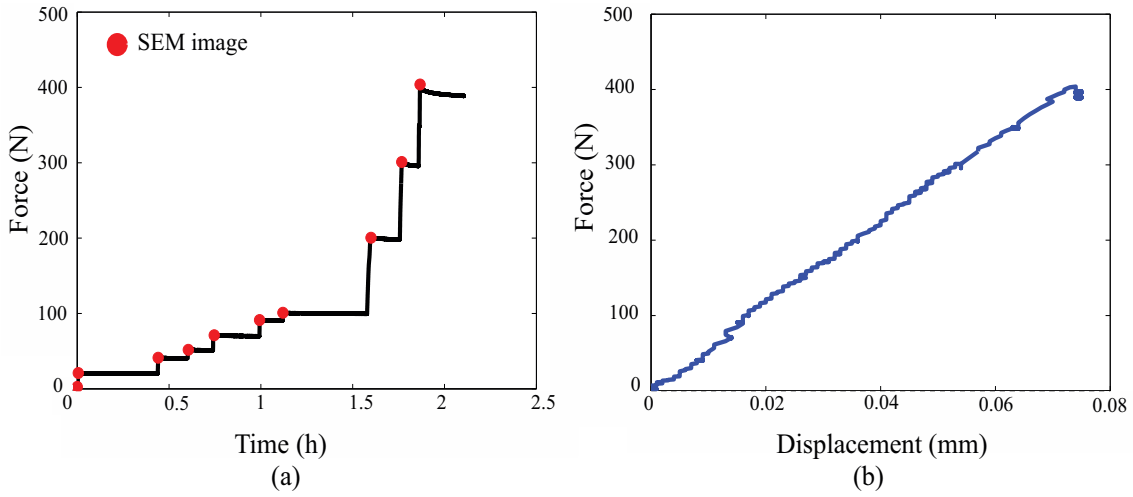

Figure 140: Force with respect to time (a) and specimen load-displacement response (b).

Some SEM images have been taken and DIC analysis has been performed to monitor the crack observation and its propagation. The image resolution is 2048 x 1887 pixels. After one week at 550 °C in air, oxidation is visible at the specimen surface (see Figure 141). At 400 N (σ_∞ = 182.6 MPa), no crack is visible on the SEM image (see Figure 141) as well as on the kinematic fields (see Figure 142). In fact, no discontinuity has been observed in the loading direction.

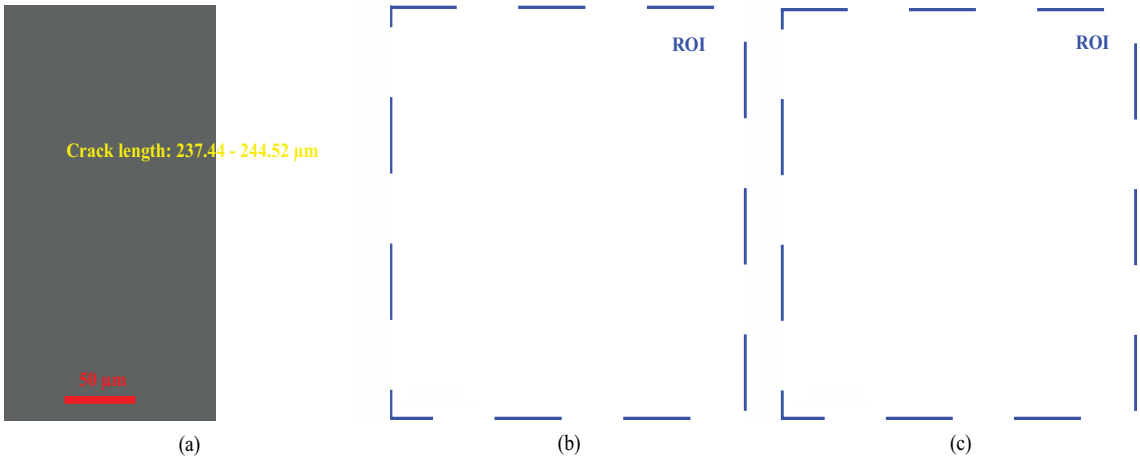

Figure 141: SEM images after the OPS finish of the crack tip region (a), after one week creep at 64 MPa and 550 °C and in the unloaded state at 0 N (reference image)) (b), at 400 N (deformed image) (c).

The effect of oxydation is clearly visible between Figure 141 a and Figure 141 b: the oxyde

growth has modified the surface aspect and filled the fatigue pre-crack.

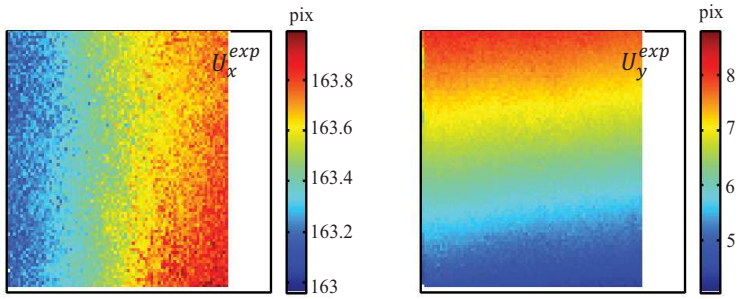

Figure 142: Displacement fields measured between unloaded state and 400 N, obtained by correlating images shown in Figure 141 b and Figure 141 c.

As no discontinuity has been observed in the kinematic fields, the test is continued until reaching $F = 700$ N ($\sigma = 319.6$ MPa) which is consistent with $K_I = 30$ MPa$\sqrt{m}$ (see Figure 143). At this load level, two cracks are observed (see Figure 144). They have been found in the region where the fatigue pre-crack propagation was expected. They are denoted crack #1 and crack #2.

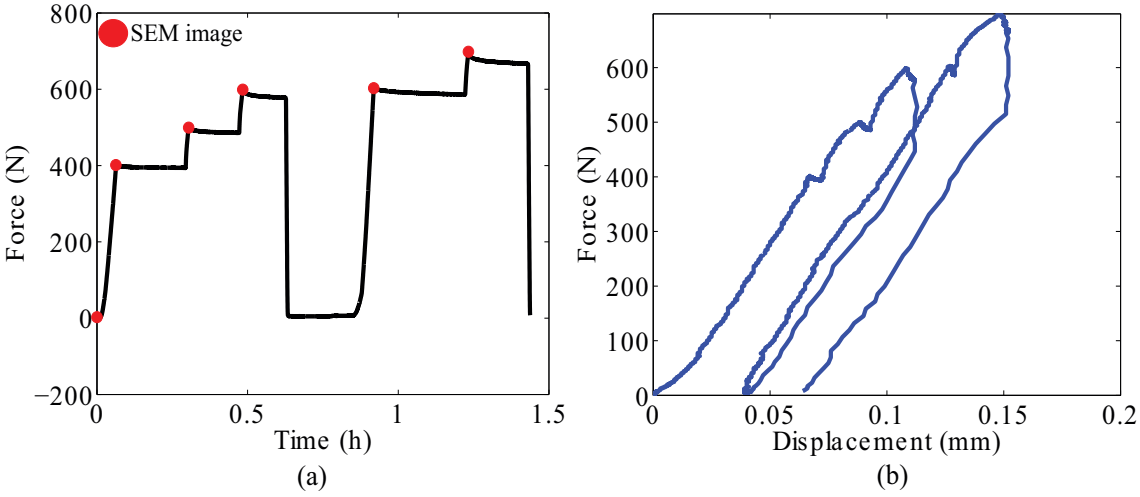

Figure 143: Force with respect of time (a) and specimen load-displacement response (b).

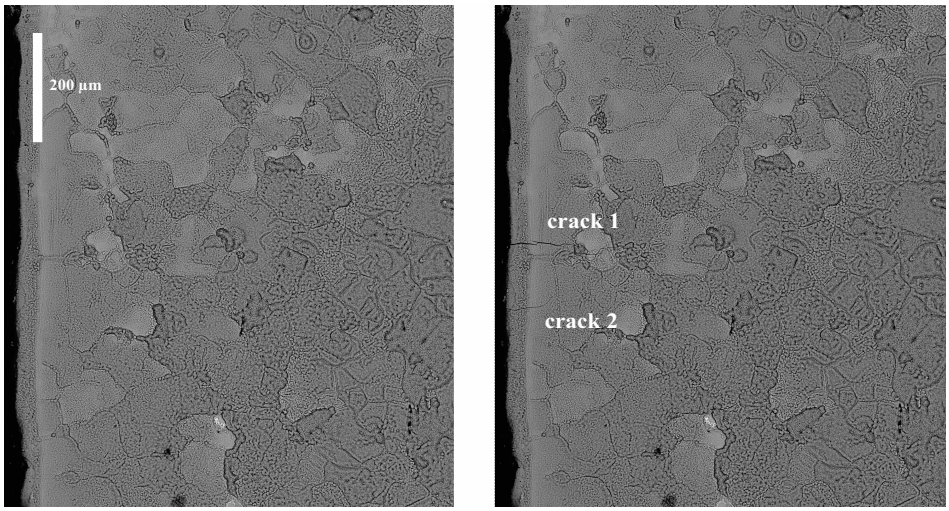

Figure 144: Reference SEM image at 0 N (a), deformed image at 700 N (b). The white scale bar is 200 µm long.

DIC analysis has been performed between Figure 144 a and Figure 144 b with a grid step *GS* of 50 pixels and a subset size *s* of 100 pixels. Two discontinuities appear on the kinematic fields due to the two surfacic cracks (see Figure 145).

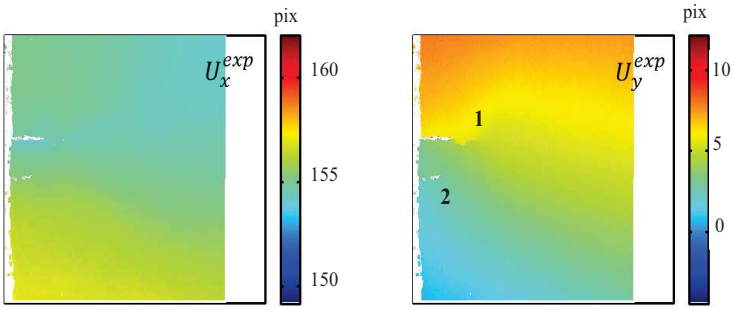

Figure 145: Kinematic fields between Figure 144 a and Figure 144 b. Two discontinuities are visible and are labelled 1, 2.

The same strategy that one used for SENT 316H specimen testing at room temperature, the estimated crack tip position has been identified respectively for crack #1 and crack #2. This procedure allows to get estimated crack tip coordinates which are not arbitrarily chosen and to make a relevant choice of R_{max} in order to distinguish the two crack ends.

In Figure 146, a comparison of the estimated crack positions and the optimized ones is proposed.

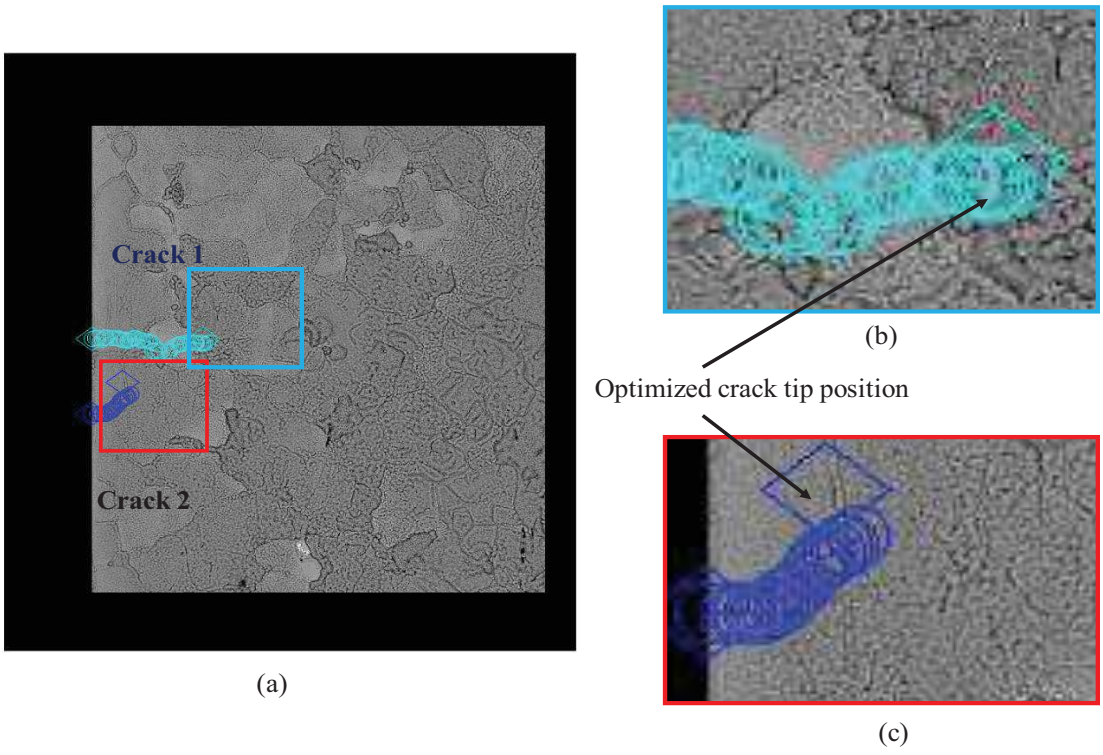

Figure 146: Crack positions in the SEM image after the first creep stop (a). Optimized crack tip positions have been respectively identified and plotted: crack#1 (b) and crack#2. Diamond symbol is used for the optimized positions.

Crack denomination	x^{est}	y^{est}	Θ^{est} (radian)	x^{opt}	y^{opt}	d (pixels)	d (µm)
Crack#1	1216.0	1057.1	0.00	1229.1	1067.8	16.91	7.57
Crack#2	1469.0	877.5392	0.00	1498.3	919.97	51.16	24.97

Table 47: Comparisons between estimated values and the optimized crack tip position for the two cracks appeared after the first creep stop. The physical size of one pixel is 0.488 µm.

The crack tip position optimization procedure has been applied to displacement fields introduced in Figure 145. The short length of the crack and the small displacement jump generated by the crack during the test have not allowed to get an accurate results for crack#2.

To confirm that the observed cracks are formed during creep and not during the initial plastic loading, a new creep dwell is planned. The sample has been replaced in the microcreep rigs for a longer period. It has also been decided to increase the loading from 64 MPa to 96 MPa. As the creep test is still ongoing when writing this manuscript, no results will be presented here.

5.4.2 Conclusions

An interrupted creep test at 550 °C in air has been performed. The creep stops have allowed to make SEM observations of the SENT sample surface. Due to oxide growth at the specimen

surface due to environmental interactions, a direct monitoring of crack evolution is not possible. An *in-situ* tensile device has been used to apply some elastic loadings allowing crack detection. After one week under creep loading of 64 MPa, two cracks appeared during the *in-situ* tensile test. As expected, two discontinuities have been found in the kinematic fields. The crack tip position has been identified using the procedure introduced in Chapter 4. The identified crack parameters are consistent with the SEM observations. Then, the sample has been submitted again to a creep period: six additional weeks have not lead to a crack evolution and the two previous cracks have not opened again. The corresponding SEM images and the kinematic fields are introduced in Appendix D. It is assumed that these cracks were resulting from oxide crack due to poor mechanical properties compared to the underlying 316H. It has been proposed to increase the creep load but the results are still being collected.

We have seen that the crack tip identification procedure efficiency could be impacted by the presence of several cracks. An enhancement of the initial procedure has been proposed allowing the monitoring of multiple cracks. In this protocol, DIC is used to locate individually each crack tip position against time. A projection of displacement fields on a reduced area around the estimated crack tip position onto LEFM base functions is performed. Then, identification steps are performed until reaching the optimized crack parameters. In the next section, we propose to introduce the multiple crack method and results of experimental validations are presented.

5.5 Multiple creep crack monitoring using Digital Image Correlation

5.5.1 Introduction of the multiple crack monitoring procedure

In the previous experimental cases, we have seen that several cracks can be generated during *in-situ* tensile test caused by the mechanical property difference between 316H base metal and carburized material.

The methodology to monitor the appeared cracks is introduced in Figure 147. The first step consists in DIC analysis with a classical local approach [185]. The step 2 relies on specific post-treatments of kinematic fields and it is expected to obtain the crack parameters against time during step 3.

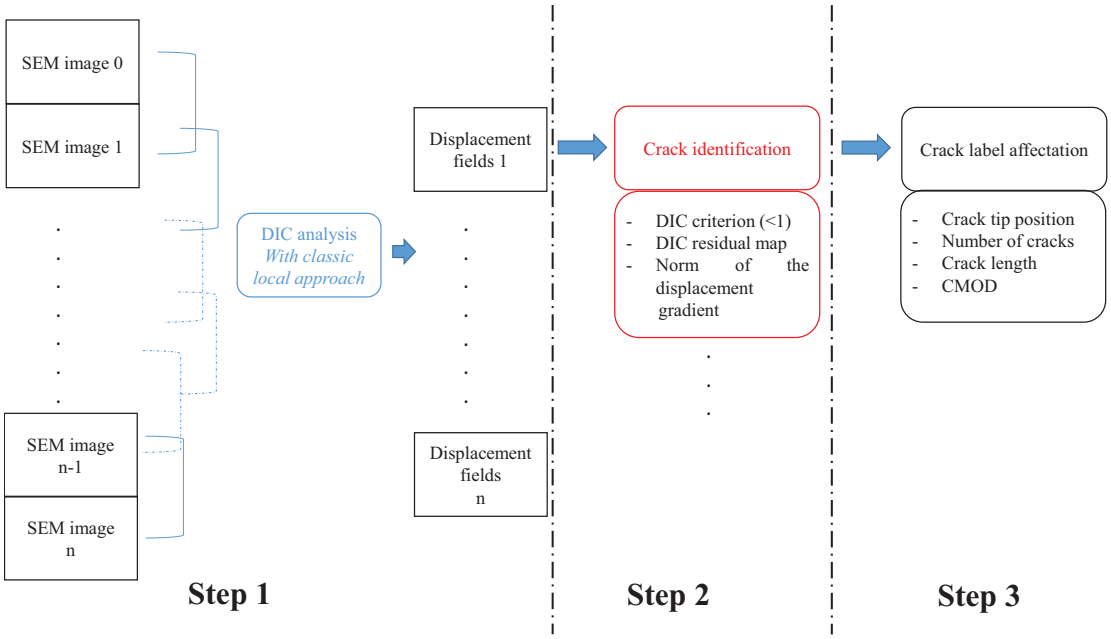

Figure 147: Methodology for the crack monitoring in case of multiple cracks: local DIC computation (step 1), crack identification (step 2), crack parameters identification (step 3).

A classical local DIC approach was applied during step 1 of the study. This technique is already well known and has been introduced in Part 4.2.1. The novelty of this work is related with crack identification presented here after.

After DIC analysis, the kinematic fields are available as well as some indicators of the DIC performance. One of the indicator of DIC performance relies on the DIC criterion. As we use a Normalized Cross Correlation (NCC) criterion, a value of 1 means perfect matching and lower values indicate less accurate matching. Let us remind that the NCC criterion writes as follows:

$$C_{NCC} = \frac{\sum_{x,y} I_0(x,y)\, I_1(x+u,y+v)}{\sqrt{\sum_{x,y} I_0(x,y)^2 \, \sum_{x,y} I_1(x+u,y+v)^2}} \tag{5.4}$$

with I_0 and I_1 respectively the intensity in the reference image and in the deformed image. u and v refer to the displacement components aiming at finding the best correlation between $I_0(x,y)$ and $I_1(x+u,y+v)$.

The cracks generate discontinuities in the displacement fields that are “smoothed“ by the local DIC approach because the shape functions used for the DIC are continuous. When a crack propagates, the gray level conservation hypothesis fails (see Figure 148 b) and the correlation residual increases while the NCC criterion decreases.

Consequently, a crack apparition between two correlated subsets leads to a low DIC criterion. The DIC criterion for a couple of image during the *in-situ* tensile test is presented in Figure 149. The zones in blue correspond to subsets where correlation procedure failed. These zones are attributed to both crack position and areas with poor gray level gradients.

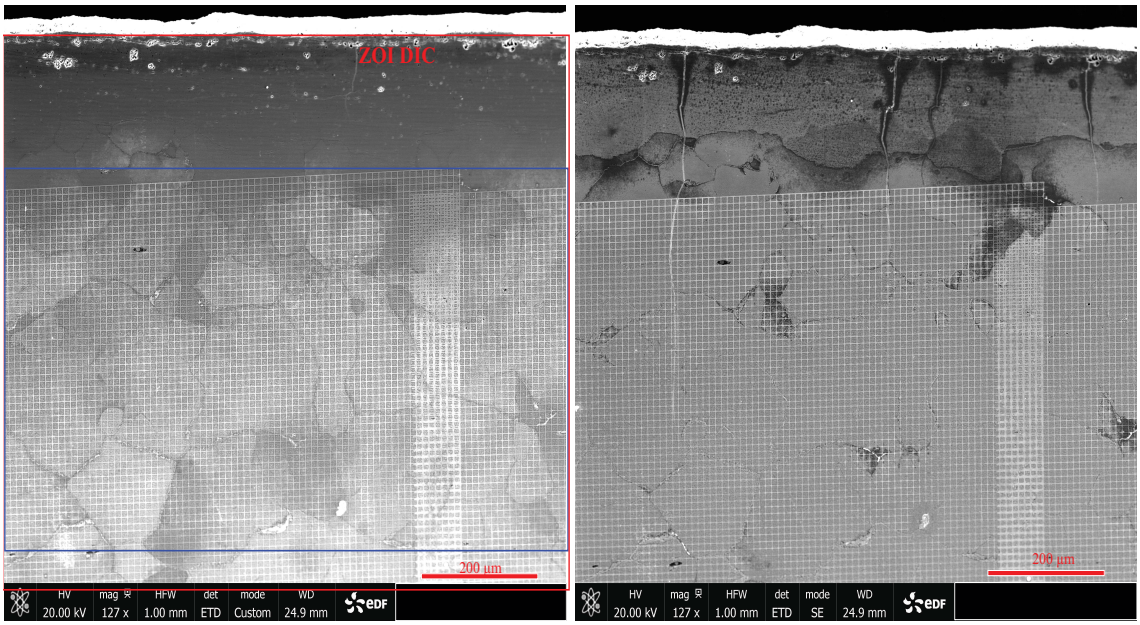

(a) (b)

Figure 148: SEM images used to perform DIC analysis: initial (a) and deformed (b). The blue rectangle represents the ROI that will be used in the local gray level equalization method presented in Appendix E.

Some SEM images resulting from *in-situ* tensile test at 500 °C are presented in the following to introduce the methodology of the enhanced crack tip position identification procedure.

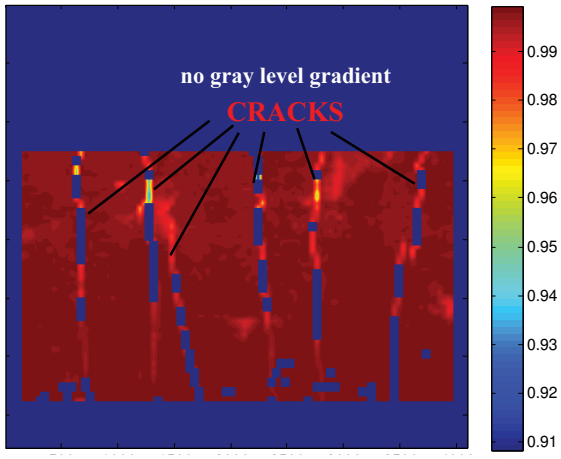

Figure 149: Example of a representation of DIC criterion in the presence of multiple cracks.

A complementary representation of the DIC performance relies on gray levels residuals. The residuals results from the difference in gray level between the reference image and the deformed

image corrected with the identified transformation using the DIC procedure. These residuals are directly minimized when using a Sum of Square Difference (SSD) criterion. Here, we use a Normalized Cross Correlation (NCC) criterion. Consequently, the residuals are computed by linearly interpolating the displacement field computed by DIC providing a displacement value for each pixel in the reference image. The deformed image gray levels are then linearly interpolated (in accordance with the DIC computation), to compute the residuals.

Here, the couple of images considered for the DIC is often separated by long time periods of more than one hour leading to change in SEM image contrast and brightness (see Figure 148). It is proposed to correct the histogram of deformed image in order to have it similar to the initial one and thus giving more reliable residuals. We propose to make the gray level of the initial image locally correspond to the deformed one. Hereafter, the method will referred to as "local gray level equalization". This method is detailed in Appendix E.

In Figure 194 of , a comparison between residual maps before and after equalization is proposed. Before equalization, the pattern is visible due to tremendeous contrast change between image 0 and image 1. After equalization, the grids are less visible and two discontinuities attributed to crack can be seen at the top of the residual map.

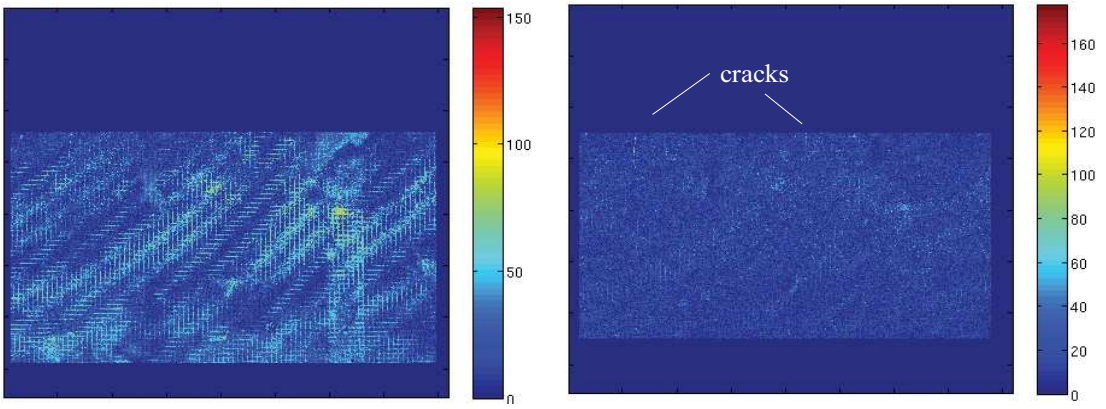

(a) (b)

Figure 150: The residual maps before equalization (a) and after equalization (b).

An other field resulting from correlation and sensitive to the crack presence is the norm of the displacement gradient ||∇U||. It is expressed as:

$$||\nabla U|| = \sqrt{U_{x,x}^2 + U_{x,y}^2 + U_{y,x}^2 + U_{y,y}^2} \tag{5.5}$$

The crack presence generates a displacement jump associated with large deformation when they are computed with symetrical local differentiation schemes (finite differences, least square approximation). The displacement gradient field computed by a centered finite difference scheme is presented in Figure 151 c.

In view of identifying the crack position during the *in-situ* tensile test using DIC, the informations obtained during the step 2 can be crossed or combined. As presented in Figure 151, the

cracks are visible on the three fields resulting from DIC measurements: DIC criterion C^{DIC}, optimized residual map R^{opt} and displacement gradient norm $||\nabla U||$. The fields C^{DIC} and $||\nabla U||$ are only computed on the DIC grid. They are linearly interpolated in order to be sampled on every pixel of the reference image. These three fields are thus spatially consistent.

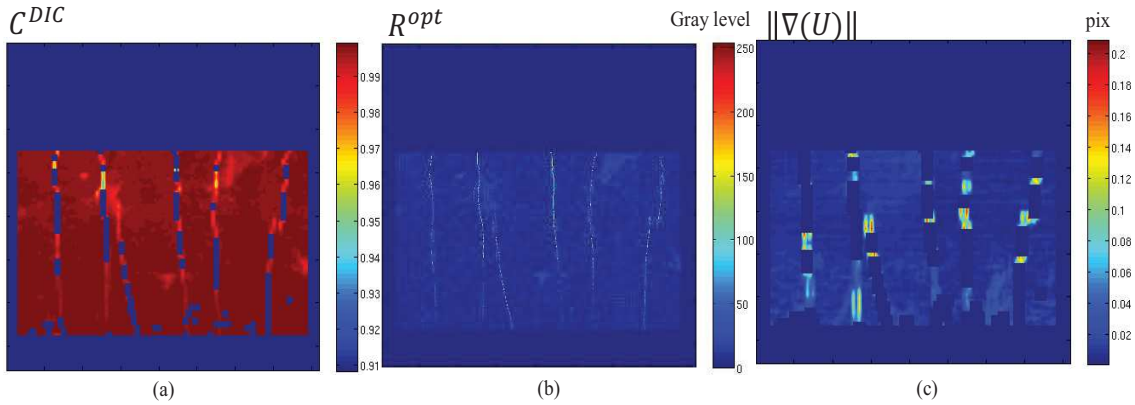

Figure 151: After DIC analysis, threee fields can be extracted: DIC criterion C^{DIC} (a), the optimized residual map (R^{opt}) (b) and the displacement gradient norm $||\nabla U||$ (c).

Due to the different resolutions of each data field, it could be relevant to combine these fields in order to identify the presence of cracks, with the maximum number of informations. One mask is determined for each data field (C^{DIC}, $||\nabla U||$ and R^{opt}). Each mask is obtained by binarizing the corresponding data.The introduced threshold values are defined for all the images of a given test.

$$P_{C^{DIC}} = 0.985 \tag{5.6}$$
$$P_{R^{DIC}_{opt}} = 0.9995 \tag{5.7}$$
$$P_{||\nabla U||} = 0.985 \tag{5.8}$$

They allow determining the threshold values used for the binarization of the three fields C^{DIC}, $||\nabla U||$ and R^{opt} for each image denoted $\varepsilon_{C^{DIC}}$, $\varepsilon_{R^{opt}}$ and $\varepsilon_{||\nabla U||}$. The threshold values introduced in the binarization are determined using the cumulated probability function of each data field.

$$C^{DIC} < \varepsilon_{C^{DIC}} \tag{5.9}$$
$$R^{DIC}_{opt} > \varepsilon_{R^{opt}} \tag{5.10}$$
$$||\nabla U|| > \varepsilon_{||\nabla U||} \tag{5.11}$$

For the fields presented in Figure 151, the threshold values are worth:

$$\varepsilon_{C^{DIC}} = 0.9849 \tag{5.12}$$
$$\varepsilon_{R^{opt}} = 83.50 \tag{5.13}$$
$$\varepsilon_{||\nabla U||} = 1.0525 \tag{5.14}$$

The cumulated probabilities for each field are presented in Figure 152. The vertical lines represents

the threshold values allowing to select the convenient points to locate the cracks. These latter values change for every displacement field.

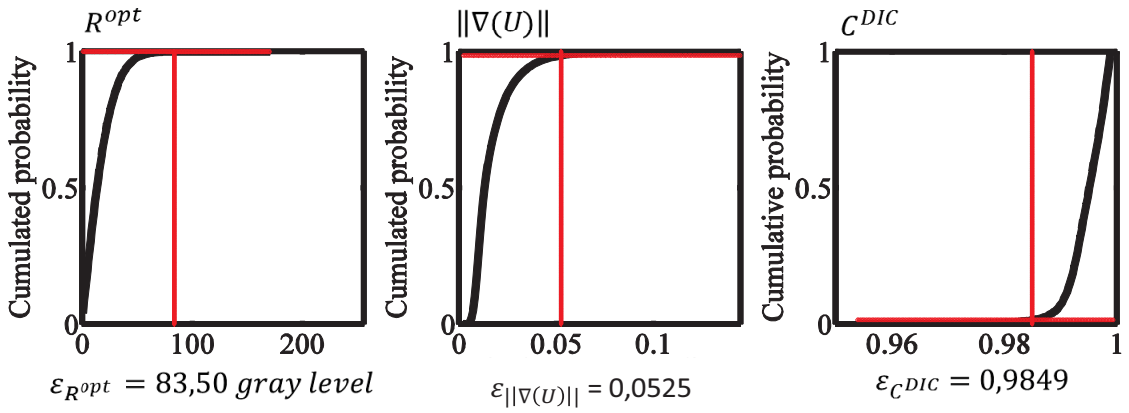

Figure 152: Cumulated probability for optimized residuals (a), for the displacement gradient (b) and for the DIC criterion (c). The horizontal lines correspond to the values of $P_{C^{DIC}}$, $P_{R^{DIC}_{opt}}$ and $P_{||\nabla U||}$. The vertical lines represents the threshold values allowing to select the convenient points to locate the cracks ($\varepsilon_{C^{DIC}}$, $\varepsilon_{R^{opt}}$ and $\varepsilon_{||\nabla U||}$). These latter values change for every displacement field.

The procedure of the multiple crack monitoring using DIC is presented in Figure 153. A validation is needed to select the relevant point belonging to each crack for each time step.

After the manual selection of points belonging to cracks, the consistency of crack labels between successive timesteps is verified, in view of following cracks with respect to time. A distance criterion between cracks allows the decorrelation of two close cracks and the improved method allows to obtain the respective crack tip position with accuracy.

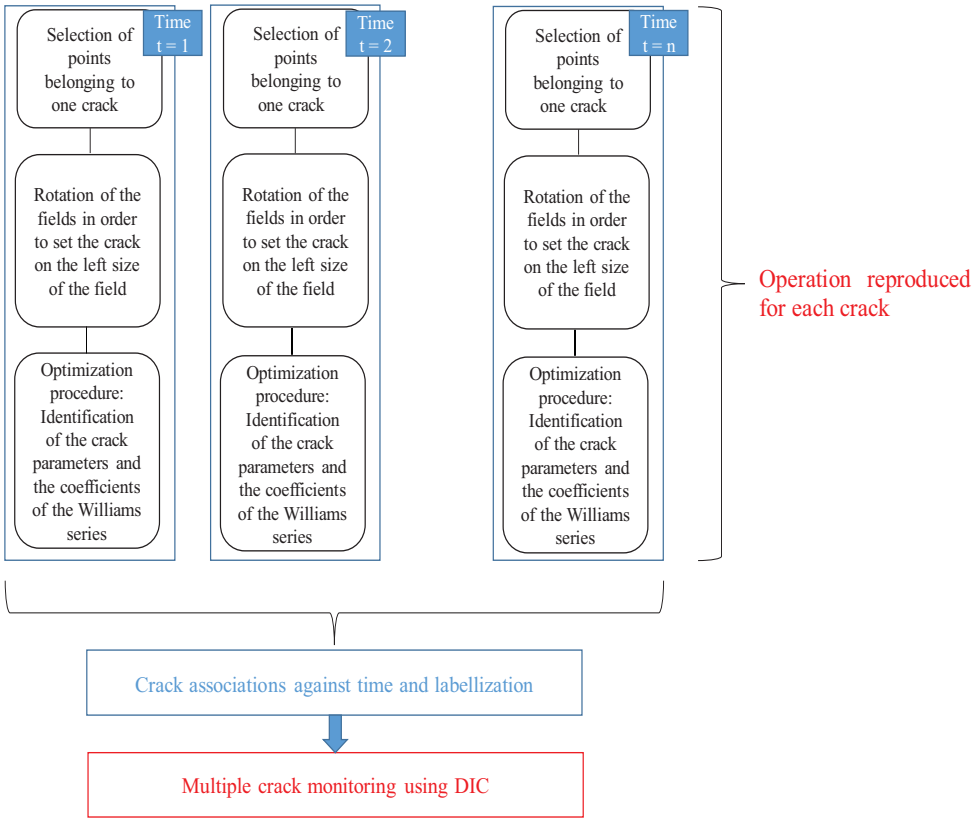

Figure 153: Introduction of the multiple crack monitoring procedure: 1-Selection of points belonging to crack, 2- Rotation of the fields in order to set the crack ”roughly“ horizontal in the left size of the fields, 3- Identification of the crack properties.

5.5.2 *In-situ* tensile test on carburized 316H SENT at 500 °C

5.5.2.1 Description of the SENT preparation and the test

In Chapter 2, we have shown that 316H stainless steel in air at 550 °C is subjected to oxidation. This oxidation leads to surface changes during the test preventing crack monitoring using DIC. The alternative solution proposed consists in performing *in-situ* creep test in a Quanta 600 SEM. The high vacuum environment may largely decrease the surface reactivity preserving the tungsten pattern. The cooling system of this SEM uses water to control the temperature in the chamber and in the tensile device. The operator presence is required to avoid any water leakage that may damage the apparatus. The duration of the test cannot exceed a day. Consequently, it is rather difficult to conduct a real creep test that would require a continuous operator presence for several days. The stage has been used to perform exclusively tensile test. The SENT specimen has been preconditioned and polished until OPS finish (W = 2.1 mm and thickness e = 1.1 mm). Prior to the tungsten patterning, a layer of Niobium with a thickness of 10 nm has been deposited. Let us remind that the preconditioning treatment has hidden the fatigue pre-crack. It has been proposed to deposit six patterns using microlithography allowing the fatigue pre-crack or creep crack monitoring (see Figure 154). The patterns are made of a combination of grids and dots with a thickness of 15 nm. The grids are spaced by 10 µm and the square length is 0.8 µm. To improve our understanding of crack initiation and propagation at high temperature, these cracks have to be monitored.

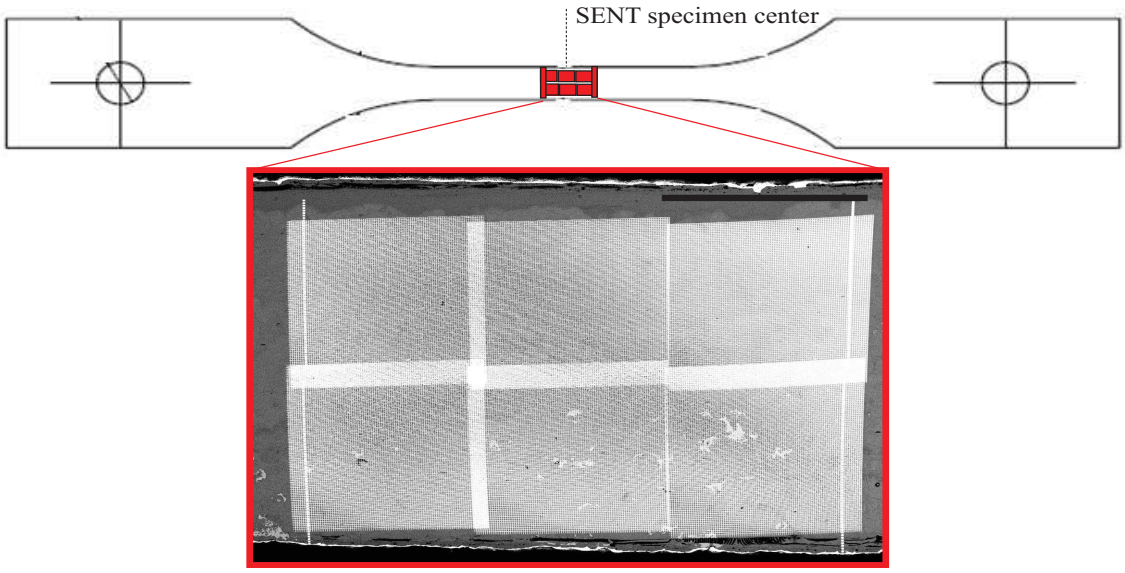

Figure 154: Presentation of the microlithography tungsten deposition onto the SENT specimen. The black scale bar is 1 mm.

The temperature chosen to perform this test is 500 °C. It is known yet as the maximal temperature admissible for the different devices and detectors inside the SEM chamber. The *in-situ* tensile device has been used to apply cycles of loadings and unloadings before reaching the sample failure. An example of the loading curve is presented in Figure 155. It can be separated in three

phases: the heating period (A), the loading (B) and the decrease of the temperature (C).

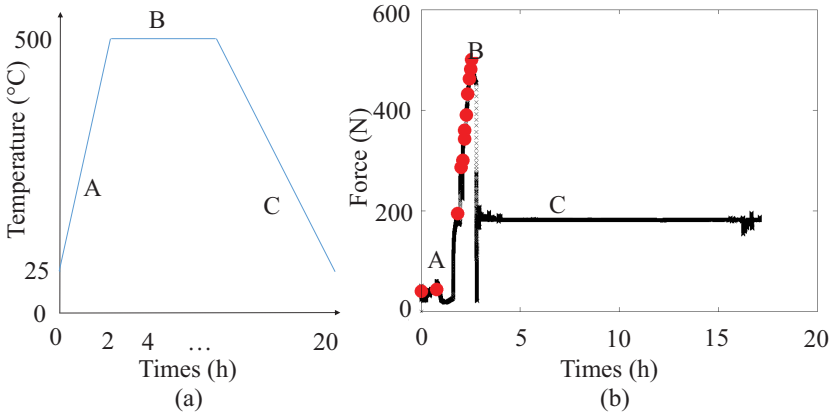

Figure 155: Temperature evolution with respect of time (a) and example of an *in-situ* tensile curve with the three distinct periods: (A) heating, (B) loading and (C) cooling (b). Heating period lasts 2 hours and cooling period lasts several hours. During the night break, the temperature in the SEM chamber is 20 °C.

During this procedure, SEM images are taken to allow surface monitoring. The aim of the first loading cycles was to identify a loading threshold relevant for the crack evolution. Few surface changes have been observed until σ_∞ = 271 MPa (F = 650 N). It was expected to observe only one crack propagation from the fatigue pre-crack but rapidly, several cracks appeared. Each crack has been studied using SEM. To discriminate superficial cracks from the notch, the loading has been increased. A summary of the load sequence applied to the specimen is given in Table 48.

σ_∞ (MPa)	F^M (N)	Observations
271	650	A few number of cracks (nb = 4)
283	680	Development of several cracks (nb » 10)
437.5	1050	Significant crack propagation from the notch
483.6	1160	**Sample final failure**

Table 48: Summary of loadings applied to the SENT specimen prior to reach the failure.

At σ_∞ = 437.5 MPa, the fatigue pre-crack propagation is observable (see Figure 156).

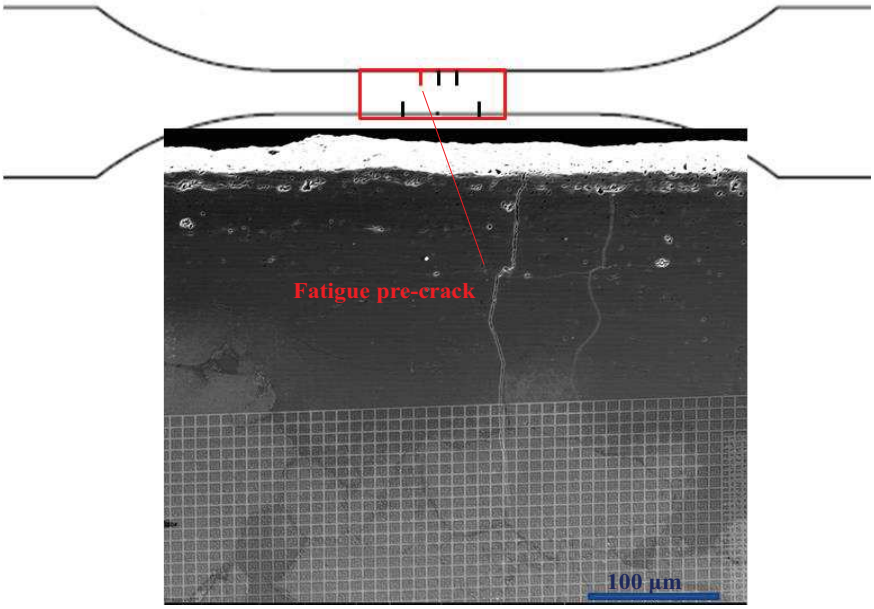

Figure 156: SEM image in SE mode of fatigue pre-crack propagation (F^M = 1050 N).

Others opened cracks are also present (see Figure 157).

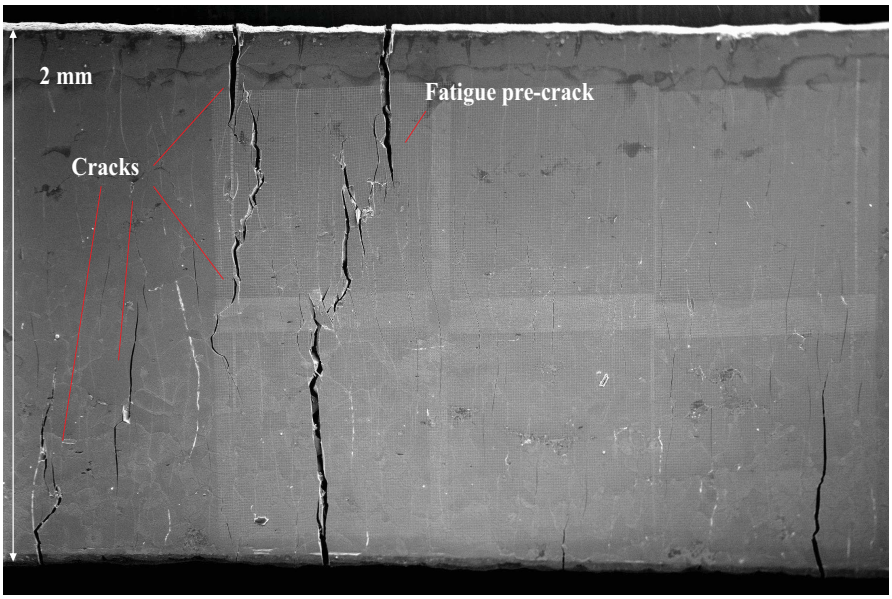

Figure 157: SEM image in SE mode of the overall view of the SENT gauge part: several cracks have appeared during the test (F^M = 1060 N).

Contrary to what was expected, several cracks perpendicular to the loading direction have appeared during the test. Nevertheless, the specimen has been submitted to a loading of σ_∞ = 483 MPa to reach the failure. Even if numerous cracks are well opened, a significant load was still applied to the specimen. To perform a quantitative and mechanical assessment of crack develop-

ment at high temperature, it is proposed to monitor each appeared crack during the *in-situ* tensile test. The expected quantities of interest are the macroscopic strain, the Crack Mouth Opening Displacement (CMOD), the number of cracks and their lengths. To obtain these informations, an identification of each crack position during the test is required.

The operator has to select the points belonging to crack at each time step. After this step, the position of the crack extremity are optimized since these positions are needed to use LEFM displacement fields.

The experimental conditions of SEM acquired during the tests are given in Figure 158. At step #C, a short crack propagation is observed on the SEM image. Nevertheless, the contrast in the region is not sufficient to perform DIC analysis due to the lack of information (see Figure 159).

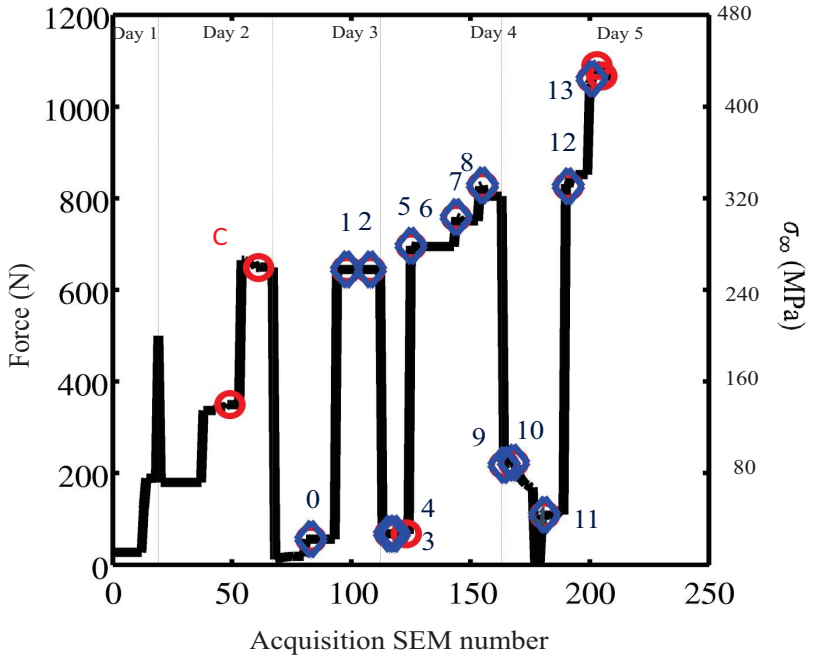

Figure 158: Evolution of the force during the *in-situ* tensile test. Red circles are used to indicate SEM acquisitions and blue diamond symbols are used to label (fortheen steps) particularly interesting SEM images for crack monitoring. The step #C indicates a crack propagation non convenient for DIC due to poor gray level surrounding the crack tip.

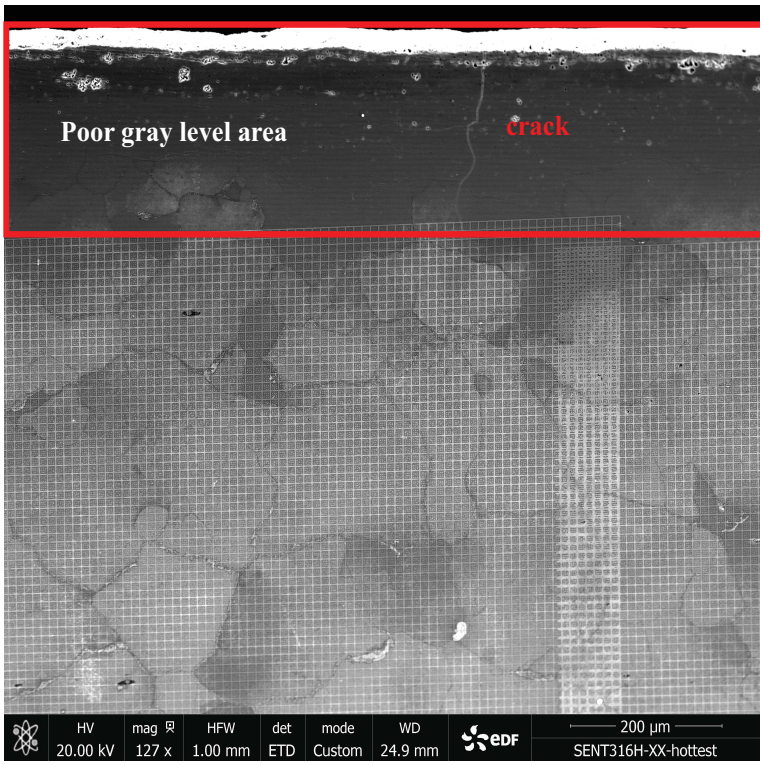

Figure 159: SEM image acquired in BSE mode at step #C (F = 660 N) indicates a crack propagation non convenient for DIC due to poor gray level surrounding the crack tip.

The results for the optimization of crack parameters at time step #1 and #13 are given in Figure 160 a and Figure 160 b. In these figures, the circles represent the extremities of the segments constituting each crack. The diamond marker corresponds to the optimized crack tips. At the first time, two cracks have been observed and at the last time step, seven supplementary cracks have formed. The main crack which has led to the sample failure can be found at the image center.

Once, the crack tip positions of each crack are identified the total crack length evolution can be monitored. The evolution of crack lengths during the *in-situ* tensile test is proposed in Figure 161. An important increase is observed for the last step due to the development of several new cracks.

The cumulated crack lengths with respect to time step are presented in Table 49.

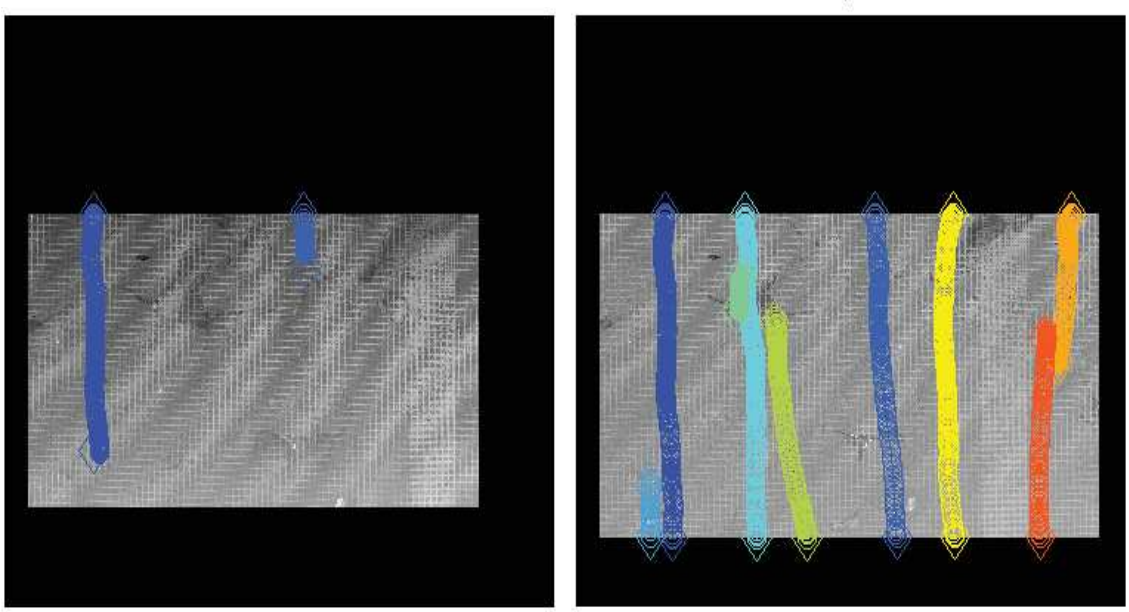

Figure 160: Results from the operator selection of points belonging to cracks at time step #1 (a) and at the last time step #13 (b).

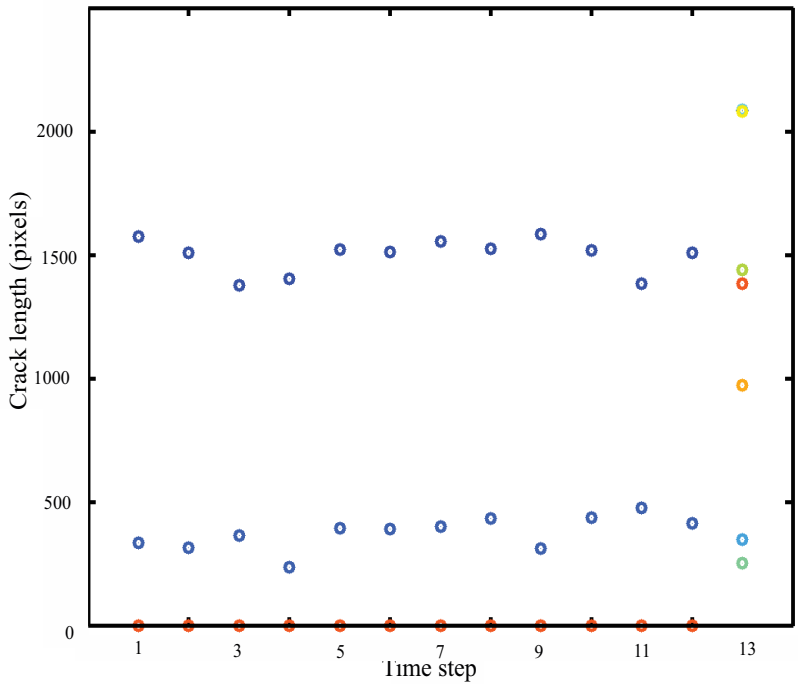

Figure 161: Evolution of crack lengths from time step #1 to the last time step #13. A color is attributed to a crack to highlight the respective crack growth with respect to time.

σ_∞ (MPa)	Time step number	Number of crack	Total crack length (pix)	Total crack length (µm)
22	#0	0	0.00	0.0
254	#1	2	1.908×10^3	465.5
254	#2	2	1.820×10^3	444.20
27	#3	2	1.740×10^3	424.4
27	#4	2	1.638×10^3	399.6
274	#5	2	1.915×10^3	467.1
274	#6	2	1.904×10^3	474.5
299	#7	2	1.954×10^3	476.8
326	#8	2	1.959×10^3	478.0
86	#9	2	1.895×10^3	462.3
88	#10	2	1.951×10^3	476.1
43	#11	2	1.858×10^3	453.4
325	#12	2	1.922×10^3	468.9
418	#13	9	1.2729×10^4	3.106×10^3

Table 49: Evolution of crack length during *in-situ* tensile test. The pixel physical size is 0.244 µm.

Time step number	Crack length by surface unit (μm^{-1})
#1	1.00×10^{-3}
#2	9.27×10^{-4}
#3	9.22×10^{-4}
#4	8.68×10^{-4}
#5	1.00×10^{-3}
#6	1.00×10^{-3}
#7	1.00×10^{-3}
#8	1.00×10^{-3}
#9	1.00×10^{-3}
#10	1.00×10^{-3}
#11	9.85×10^{-4}
#12	1.00×10^{-3}
#13	6.7×10^{-3}

Table 50: Evolution of crack length by surface unit during *in-situ* tensile test. The pixel physical size is 0.244 µm.

In Table 50, the crack length by surface unit during the different time steps is given. The dimensions of the ROI used for DIC and for crack monitoring is 908.9 x 506.3 μm^2. At the end of the DIC crack monitoring and prior to final failure of the sample, the total crack length was 3.106

$\times 10^3$ µm. The crack length by surface unit (µm) is then 0.0067 μm^{-1}.

5.6 Conclusion

The objective of the collaboration between EDF Energy, EDF R&D and the LMGC is to obtain a creep crack initiation information representation of the phenomenon occuring in AGR boilers, and more specifically to 316H tubes and their welds in critical regions of these components. Both experimental and computational approaches are needed to achieve creep crack initiation predictions under operational conditions.

A campaign of interrupted creep tests at 550 °C in air on SENT 316H specimen has been performed. Due to combined effects of preconditioning treatment and experimental conditions, an oxide layer has grown at the sample surface avoiding a straightforward crack monitoring. It has been proposed to use an *in-situ* tensile device to apply elastic loadings to obtain a crack opening and make crack tip position identification possible using DIC. This procedure should not lead to damage, plasticity development or crack propagation between two interrupted creep stops. Two assessment tests on SENT 316 specimens have been proposed.

- A preliminary test using pre-cracked microspecimen 316L SENT has been carried out at room temperature. Using *in-situ* tensile device, it has consisted in applying cycles of loading/unloadings coupled with SEM observations both at microscale and in the crack tip region. The objectives were to identify the first microplasticity onset threshold and the corresponding stress intensity factor K_I. E-beam microlithography has been used to make a tungsten surface marker around the crack. During the test, the crack opening has been monitored using DIC. The development of microplasticity has been assessed by performing SEM observations, using an imaging mode sensitive to specimen topology (SE mode), at high magnitude in the crack tip region. At K_I = 30 MPa.$\sqrt{m}$ (F = 257 N), slid bands appeared and no crack propagation was observed.This strategy has been then applied to preconditioned SENT 316H sample;

- This experiment has been reproduced using preconditioned SENT 316H to compare the cracking behaviour with that observed for 316H SENT test. Contrary to the test with SENT 316L, no tungsten pattern has beeen used. The preconditioning treatment of 2000 hours at 600 °C in CO_2 environment has lead to the growth of an oxide layer at the specimen surface. This oxide is a good pattern for the DIC at small scale. After the first crack observation, SEM images have been taken ahead of the first crack tip position in order to perform a crack monitoring using DIC. To quantify the crack propagation, the procedure introduced in Chapter 4 and developped to identify crack parameters has been used. The displacement fields obtained using a classical local DIC approach have been projected onto a LEFM base constructed using Williams' series. A robust crack monitoring can be performed if even if several discontinuities can be observed in the kinematic fields.

- After performing these two preliminary tests, it has been proposed to study the creep crack propagation by performing test stops and SEM observations. After several weeks at 64 MPa,

the fatigue pre-crack does not propagate. Two cracks are observed but they were resulting from oxide layer crack. The presence of two discontinuities in the displacement field is challenging for the procedure identification. Precaution must be taken with R_{max} to get an accurate estimation of the main crack tip position. Then, it has been proposed to increase the loading applied to this specimen to 96 MPa and it is expected to collect these results in a near future.

- Two strategies for protecting the tungsten pattern from oxidation damage have been presented in Appendix A. It has not been possible to keep a convenient DIC pattern for a long period in the creep experimental conditions: 550 °C in air. As an alternative solution, a high temperature *in-situ* testing has been proposed at 500 °C. The vacuum environment leading to a limited oxidation of the sample surface. Due to technical constraints imposed by the SEM water cooling system, the experiment has been stopped every day. Cycles of loading/unloadings with increasing levels have been applied to the specimen. Rapidly, several cracks perpendicular to the loading direction were observed at the sample surface each 100 nm making difficult the identification of the crack propagating from the notch. Series of SEM images in SE mode have been taken to monitor each crack evolution. An improvement of the initial procedure identification has been proposed. Relying on several fields resulting from specific post-treatments of DIC, the multicrack approach is able to identify each crack position and to make an individual crack monitoring possible. A choice of the method used to accurately identify the crack parameters can be done: the analytical expressions from Williams' series can be used as a projection base after classical local DIC or the Williams' series can be directly used as shape function for the DIC analysis. Due to an accurate identification of the crack extremities positions, the linear density of crack during the *in-situ* has been measured. These experiments have highlighted that performing creep crack monitoring using DIC at 550 °C has been challenging and it has required to use *in-situ* tensile device to make crack tip position identification using SEM.

The experiment on SENT 316H specimens at room temperature has highlighted that the crack in the carburized face has propagated along a transgranular path. The difference between the crack length in the carburized face and in the non carburized face suggests that the mechanical properties of layers formed during the preconditioning treatment are lower than that of the underlying 316H material. This assumption has been corroborated during the *in-situ* tensile test at 500 °C. After a few cycles of loading/unloading (σ_∞ = 271 MPa), multiple cracks appeared at the sample surface. Nevertheless, the final sample failure happened at σ_∞ of 483.6 MPa suggesting that the cracks observed were shallowed and that the oxidised and the carburized layers resulting from chemical interactions between austenitic stainless steel and the surrounding CO_2 environment have degraded mechanical properties compared to as-received material. The sensitization phenomenon responsible for carbide prescipitation and oxide formation plays a key role in the cracking behaviour of 316H material.

General conclusion and perspectives

In the coming years, the life of existing nuclear plants in the UK has to be extended in order to achieve the company's vision of generating 65 TWh over 9 years. The long term operation of Advanced Gas cooled Reactors (AGR) is a current research area at the core of EDF Energy industrial strategy, due to the number of installed AGR plants, due to the power demand in UK and due to the planned end of operation of these reactors.

The austenitic stainless steel AISI 316H has been commonly used in AGR boilers. Its good corrosion resistance and its particular creep properties make this material suitable to manufacture the components operating in the conditions of the reactor. In view of safe operation engineering, the creep crack initiation and growth needs to be well predicted for 316H components operating in CO_2 environment. This objective was challenging since the creep fracture is potentially affected by a number of parameters:

- material heterogeneities such as carbide-induced stress heterogeneities,
- microstructure and grain boundary properties,
- effect of carbides at grain boundaries on the grain boundary toughness,
- environmental effects and diffusion of elements from the surrounding environment in the material,
- temperature effects,
- stress effects:
  - normal stress to the grain boundaries,
  - stress triaxiality,

To improve the knowledge of creep crack mechanisms in this context, it has been proposed to conduct experiments allowing to collect data on crack initiation and growth, with the objective of identifying a creep crack law for an environmentally aged material.

The 316H material was provided by EDF Energy Generation Ltd. It has been obtained from an ex-service AGR superheater header. Despite its long service time (> 93 000h), the material was not exposed to the AGR gas environment; therefore the service exposure should only lead to thermal ageing as the service stresses were too low for any significant creep deformation or damage [2]. The microstructure of the as-received material has been characterized using both optical microscope and EBSD analysis: heterogeneity in the grain size and numerous twin boundaries can be observed, resulting propably from process manufacturing.

To reproduce the in-service material ageing, a preconditioning treatment has been set-up by EDF Energy. A fine polishing treatment until OPS finish is performed to increase the surface reactivity. Then, the specimen is subjected to a thermal ageing at 600 °C in an autoclave filled with CO_2 gas during 2,000 hours. In these conditions, both carburized and oxidised layers formed, similar to that observed after real service.

To study crack initiation and propagation at the microscopical scale, we have proposed to follow the propagation of a "natural" fatigue crack in creep at the scale of few grains using SEM technique coupled with DIC methods on millimetric fields of view. A specific methodology has been set-up to machine pre-cracked specimen. The "natural" crack is obtained by propagating the initial notch in a macroscopic CT specimen using a cyclic loading. These specimens are then cut in a stack of thin slices and the crack location is determined for each slice. Single Edge Notched Tensile (SENT) specimen are then machined in order to precisely locate the crack in the middle of the specimen.

In parallel, conventional round bar samples (RBT) have been machined. These samples were used to characterize the creep macroscopical response of the as-received material. By performing creep tests at two different stress levels of 270 and 290 MPa, it was possible to identify Norton law parameters and to complete the creep experimental programme proposed by EDF, Areva, CEA and the PhD thesis partners. To complete the study and to quantify the effects of geometry and carburization on the creep response, some uncracked microsize specimens (FT) have been machined in as-received and preconditioned material. The preconditioning treatment does not seem to significantly modify the RBT creep response. At microscopical scale, both preconditioned and uncarburized samples have been tested. The oxidising treatment has reduced the ductility of the material. To reach the critical strain associated with oxide cracking (0.5 %), it took about 25h to C-270-FT and 50h to N-270-FT. The effect of geometry has been quantified using the as-received material. The microsized specimen deformation happened faster than with the RBT. To reach 2% of creep strain, it took about 3,000h to N-270-FT and more than 10,000h to N-270-RBT. Nevertheless, the slope of the three curves are similar. The minimum creep rate is not reached yet. By comparing the fracture surface of two microsized specimens (C-128-SENT and C-270-FT) with SEM, a change in the failure mechanism is highlighted. At low stresses, numerous cavities are observed which are characteristic of creep diffusion. Long creep time lead to cavities and growth. At higher stresses, the crack seems to have followed mainly an inter/transgranular path. An interrupted creep test on a preconditioned SENT has been performed in order to get a crack monitoring at the microscopical scale. Between each creep period, some SEM images of the ZOI have been taken and used to obtain the kinematic full-field measurements. After six weeks under a loading of 64 MPa, no crack propagation is observable. The loading applied has been increased until 96 MPa but the results are not yet available.

The creep response of the preconditioned material has to be weighed against the environmental effects of preconditioning treatment on the 316H microstructure. Different techniques with specific resolutions up to the nanoscale have been used to characterize the changes. EDX and Castaing microprobe were particularly convenient to reveal the presence of a magnetite (Fe_3O_4) and a duplex oxide layer. The small size of carbide precipitates was too challenging for the SEM. TEM sample preparation has been performed and numerous chromium carbides have been found in a region under the duplex oxide layer. The influence of crystallographic parameters and the role

of grain boundaries as preferential path for the oxygen and carbon elements is corroborated by the unconstant thickness of both duplex oxide layer and carburized area. The complex structure of the layers resulting from preconditioning treatment highlighted by TEM observations may suggest that their mechanical performance is reduced compared to as-received 316H material.

By using advanced experimental techniques providing full field measurements, it was expected to detect mechanical fields singularities induced by cracks and other material discontinuities. In the context of creep crack growth, image analyses and Digital Image Correlation (DIC) were relevant techniques to monitor the crack advance and the plasticity and strain fields surrounding a propagating crack. Complementary finite element simulations of intergranular cracks in bicrystals have been performed and used as reference fields to develop an identification procedure of the crack tip position. It relies on kinematic measurements using a local DIC approach and on projections using Linear Elastic Fracture Mechanic (LEFM) expressions. Reference displacement fields have been obtained for several behaviours: from homogeneous elastic material to heterogeneous crystal plasticity. A quantification of bias due to the model errors when plasticity is taken into account is possible as well as the robustness of the procedure. The results have shown that if the material behaviour is uniform enough, the procedure is able to identify the crack parameters. We have considered these results as satisfactory and the procedure has been applied on real experiments.

A campaign of interrupted creep tests at 550 °C in air on SENT 316H specimen has been performed. Due to combined effects of preconditioning treatment and experimental conditions, an oxide layer has grown at the sample surface preventing a straightforward crack monitoring. It has been proposed to use an *in-situ* tensile device to apply elastic loadings to obtain a crack opening and make crack tip position identification possible using DIC. It is expected that this procedure does not lead to damage, plasticity development or crack propagation between two interrupted creep stops. Two assessment tests on SENT 316 specimens have been proposed.

- A preliminary test using pre-cracked microspecimen 316L SENT has been carried out at room temperature. Using *in-situ* tensile device, it has consisted in applying cycles of loading/unloadings coupled with SEM observations both at microscale and in the crack tip region. The objectives were to identify the first microplasticity onset threshold and the corresponding stress intensity factor K_I. E-beam microlithography has been used to make a tungsten surface marker around the crack. During the test, the crack opening has been monitored using DIC. The development of microplasticity has been assessed by performing SEM observations, using an imaging mode sensitive to specimen topology (SE mode), at high magnification in the crack tip region. This strategy has been then applied to preconditioned SENT 316H sample;

- This experiment has been reproduced using preconditioned SENT 316H to compare the cracking behaviour with that observed for 316H SENT test. Contrary to the test with SENT 316L, no tungsten pattern has beeen used. The preconditioning treatment of 2000 hours at 600 °C in CO_2 environment has lead to the growth of an oxide layer at the specimen surface. This oxide is a good pattern for the DIC at small scale. After the first crack observation, SEM images have been taken ahead of the first crack tip position in order to perform a crack monitoring using DIC. To quantify the crack propagation, the procedure introduced in Chapter 4 and developped to identify crack parameters has been used. The displacement

fields obtained using a classical local DIC approach have been projected onto a LEFM base constructed using Williams' series. A robust crack monitoring can be performed even in presence of several discontinuities observed in the kinematic fields.

- After performing these two preliminary tests, it has been proposed to study the creep crack propagation by performing test stops and SEM observations. After several weeks at 64 MPa, the fatigue pre-crack does not propagate. Two cracks are observed but they were resulting from oxide layer crack. The presence of two discontinuities in the displacement field is challenging for the procedure identification. Precaution must be taken with R_{max} to get an accurate estimation of the main crack tip position. Then, it has been proposed to increase the loading applied to this specimen to 96 MPa and it is expected to collect these results in a near future.

- Two strategies for protecting the tungsten pattern from oxidation damage have been presented in Appendix A. Despite a long experimental program, it has not been possible to keep a convenient DIC pattern for a long period in the creep experimental conditions at 550 °C in air. As an alternative solution, a high temperature *in-situ* testing has been proposed at 500 °C. The vacuum environment leading to a limited oxidation of the sample surface. Due to technical constraints imposed by the SEM water cooling system, the experiment has been stopped every night. Cycles of loading/unloadings with increasing peak load levels have been applied to the specimen. Rapidly, several cracks perpendicular to the loading direction were observed at the sample surface at every 100 nm making it difficult to identify the crack propagating from the notch. A serie of SEM images in SE mode have been taken to monitor each crack evolution. An improvement of the initial procedure identification has been proposed. Relying on several fields resulting from specific post-treatments of DIC, the multicrack approach is able to identify each crack position and to make an individual crack monitoring possible. A choice of the method used to accurately identify the crack parameters can be done: the analytical expressions from Williams' series can be used as a projection base after classical local DIC or the Williams' series can be directly used as shape function for the DIC analysis.

Microplasticity development in the crack tip region in SENT 316L at room temperature has been observed. For K_I = 30 MPa.$\sqrt{m}$, slip bands appeared and no crack propagation was observed. Experiment on SENT 316H specimens at room temperature has highlighted that the crack in the carburized face has propagated along a transgranular path. The difference between the crack length in the carburized face and in the non carburized face suggests that the mechanical properties of layers formed during the preconditioning treatment are lower than that of the underlying 316H material. This assumption has been corroborated during the *in-situ* tensile test at 500 °C. After a few cycles of loading/unloading (σ_∞ = 271 MPa), multiple cracks appeared at the sample surface. Nevertheless, the final sample fracture happened at σ_∞ of 483.6 MPa suggesting that the observed cracks were not deep and that the oxidised and the carburized layers resulting from chemical interactions between austenitic stainless steel and the surrounding harsh environment of AGR reactor have reduced fracture toughness, creep ductility and strength compared to as-received material. The sensitization phenomenon responsible for carbide prescipitation and oxide formation plays a key roles in the cracking behaviour of 316H material.

As the creep facilites available at EDF Lab Les Renardieres can not be used in controlled atmosphere, it is proposed in the future to perform creep tests in:

- an environment free from oxygen elements to limit oxide growth at the sample surface. Within a very short time, this oxide generates detrimental pattern damage avoiding the use of DIC technique.

- Intergranular creep cracks have been observed at elevated temperature in CO_2 environment. The influence of carbon rich gas inside the crack should be taken into account. The presence of the crack can lead to the diffusion of oxygen and carbon elements deep in the bulk. When interacting with oxidation and carburization, the creep cracking mechanism can be accelerated compared to preconditioned specimens not exposed to CO_2.

In this PhD thesis work, some conventional RBT samples have been polished to get a surface reactive for preconditioning treatment. It is suggested to submit these specimens to CO_2 environment in order to obtain preconditioned 316H material. As proposed for SENT samples, a campaign of interrupted creep tests at 550 °C in air could be also performed. By performing SEM acquisitions well sequenced in time, it will be possible to precisely determine crack initiation time under a given load. The objective will be to identify creep cracking law and to be able to predict first the probability of crack occurences and secondly, the creep behaviour of cracked specimen in service.

During the PhD thesis period, some developments have been initiated to perform *in-situ* test at high temperature (500 °C) in the MIRA FEI SEM. Contrary to Quanta 600 SEM, this apparatus is cooled by liquid hydrogen system allowing longer testing period. Creep experiments could be performed on this apparatus. Equiped with High Resolution camera and a stage which can be tilted at 70 °C, EBSD analysis could be performed ahead of the crack tip position to measure misorientation evolution during the test. Moreover, a specific software, developped following EDF instructions, will allow to automate image acquisitions with SEM detector or EBSD technique.

The DIC analysis has been performed only at the specimen surface. Due to heterogeneous microstructure in the material, it could be interesting to perform study of the crack propagation in the sample volume using Dual Beam microscope. This facility allows automatic precise cuts and material volume reconstruction. Intergranular cracking could be proved for carburized layer and favorite grain misorientations for intergranular crack growth could be explored.

Permanent deformation can potentially be extracted from kinematic fields and can be used as an indicator of plasticity development in the region surrounding the crack tip. It can be expressed as follows:

$$\varepsilon^{residual} = \varepsilon^{exp} - \varepsilon^{W} \tag{5.15}$$

where ε^{exp} and εW represent respectively the total experimental deformation and the deformation associated with the projection of the displacement on the Williams series. This kind of information has not be interpreted in this work.

Concerning the crack tip identification, the procedure accuracy can be affected if the crack is straight or not. During the multiple crack tip identification procedure, the operator has to select manually the crack path formed with adjacent segments generated between each point selection.

This identification results could be improved by restricting the set of points located in the vicinity of the crack tip (see Figure 162).

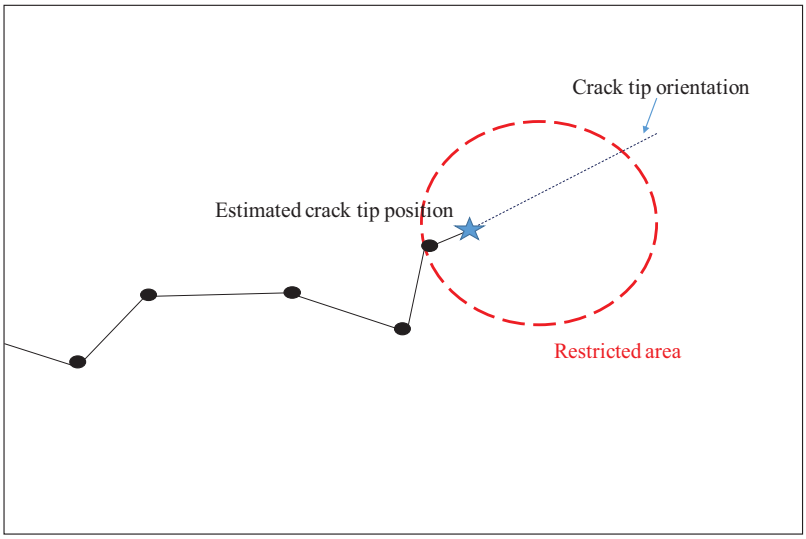

Figure 162: Proposal to get an accurate identification of crack angle in case of curved cracks.

Furthermore, the identification of cracks could be automated by performing mathematical morphology operations such as successive closure and dilatation operations for example.

The Williams series have been used as the projection basis for the identification of the crack parameters using kinematic measurements. A restriction of the displacement shape functions at mode *I* and orders 0, 1 and 2 has been performed. This basis could be enriched with Williams series for supersingular terms such as order -1 or to subsingular orders such as order 3.

Concerning the numerical study, this experimental PhD thesis work will be used as a basis for a numerical PhD thesis at the University of Manchester. A model with a cohesize zone model will be developped to describe the intergranular creep crack behaviour.

Bibliography

[1] E. Nonbol. Description of the advanced gas cooled type of reactor (agr). Technical report, Nordic nuclear safety Research- Riso National Laboratory, 1996.

[2] M.J. Chevalier. Carburisation of type 316 stainless steel in an agr environment: status of current understanding.

[3] A.J. Baker, O'Donnell M.P., and D. Dean. Use of the r5 volume 4/5 procedures to assess creep-fatigue crack growth in a 316l(n) cracked plate at 650 °c. *International Journal of Pressure Vessels and Piping*, 80:481–488, 2003.

[4] R.A. Ainsworth, P.J. Budden, D. Dean, Fox. M.J.H., and O'Donnell M.P. Assessment of creep and creep fatigue crack growth following the r5 procedures. *ASME*, 2003.

[5] J. X.Y. Tao and G. Rayner. Creep fatigue crack initiation assessment for weldment joint using the latest r5 assessment procedure. *Procedia Engineering*, 130:879–892, 2015.

[6] D.W. Dean, R.A. Ainsworth, and S. Booth. Development and use of the r5 procedures for the assessment of defects in high temperature plant. *International Journal of Pressure Vessels and Piping*, 78:963–976, 2001.

[7] J.M.H. Dean, I.W. Goodall, D.G. Hooton, R.A. Ainsworth, P.J. Budden, D. Dean, M.J.H. Fox, and M.P. O'Donnell. Assessment of creep and creep-fatigue crack growth following the r5 procedures. 2003.

[8] D.W. Dean and D.N. Gladwin. Creep crack growth behaviour of type 316h steels and proposed modifications to standard testing and analysis methods. *International Journal of Pressure Vessels and Piping*, 84(6):378–395, June 2007.

[9] R.K. Desu, H.N. Krishnamurthy, A. Balu, A.K. Gupta, and S.K. Singh. Mechanical properties of austenitic sainless steel 304l and 316l at elevated temperatures. *Journal of Materials Research and Technology*, 2015.

[10] M.F. Ashby and M. Smidman. Materials for nuclear power systems. In *Nuclear Power*, 2010.

[11] ASTM international. Standard specification for chromium and chromium- nickel stainless steel plate, sheet, and strip for pressure vessels and for general applications. 2016.

[12] C.M. Davies, D.W. Dean, M. Yatomi, and K.M. Nikbin. The influence of test duration and geometry on the creep crack initiation and growth behaviour of 316h steel. *Materials Science and Engineering: A*, 510?511(0):202–206, June 2009.

[13] R. Beneke and R.F. Sandenbergh. The influence of nitrogen and molybenum on the sensitization properties of low-carbon austenitic stainless steels. *Corrosion Science*, 29:543–555, 1989.

[14] E.A. Kenik, T. Inazumi, and G.E.C. Bell. Radiation-induced grain boundary segregation and sensitization of a neutron-irradiated austenitic stainless steel. *Journal of Nuclear Materials*, 183:145–153, 1991.

[15] H. Hanninen, I. Aho-Mantila, and K. Torronen. Environment sensitive cracking in pressure boundary materials of light water reactors. *International Journal of Pressure Vessels and Piping*, 30:253–291, 1987.

[16] L. Murr, A. Advani, V. Shankar, and D.G. Atteridge. Effects of deformation (strain) and heat treatment on grain boundary sensitization and precipitation in austenitic stainless steels. *Materials Characterization*, 24:135–158, 1990.

[17] M. Grujicic and S. Tangrila. Thermodynamic and kinetic analyses of time-temperature-sensitization diagrams in austenitic stainless steels. *Materials Science and Engineering: A*, 142:255–259, 1991.

[18] P.M. Scott. Environt-assisted cracking in austenitic components. *Fracture in Austenitic Components*, 65:255–264, 1996.

[19] S. Lozano-Perez, T. Yamada, T. Terachi, M. Schroder, C.A. English, G.D.W. Smith, C.R.M. Grovenor, and B.L. Eyre. Multi-scale characterization of stress corrosion cracking of cold-worked stainless steels and the influence of cr content. *Acta Materialia*, 57:5361–5381, 2009.

[20] D. Noel. Etude du risque de corrosion intercristalline des composants en acier inoxydable. HT-40/99/015/A, 1999.

[21] M.J. Deleury. *Fluage et évolution structurale des aciers inoxydables austénitiques*. PhD thesis, Ecole des Mines de Paris, 1980.

[22] P. Bouchard, P. Withers, S.A. McDonald, and R.K. Heenan. Quantification of creep cavitation damage around a crack in a stainless steel pressure vessel. *Acta Materialia*, 52:23–34, 2004.

[23] H. Pommier, E.P. Busso, T.F. Morgeneyer, and A. Pineau. Intergranular damage during stress relaxation in aisi 316l-type austenitic stainless steels: Effect of carbon, nitrogen and phosphorus contents. *Acta Materialia*, 103:893–908, 2016.

[24] A.D. Warren, I.J. Griffiths, R.L. Harniman, P. Flewitt, and T.B. Scott. The role of ferrite in type 316h austenitic stainless steels on the susceptibility to creep cavitation. *Materials Science & Engineering A*, 635:59–69, 2015.

[25] W. Niu, R.S. Lillard, Z. Li, and F. Ernst. Properties of the passive film formed on interstially hardened aisi 316l stainless steel. *Electrochimica Acta*, 176:410–419, 2015.

[26] R.K. Wild. High temperature oxidation of austenitic stainless steel in low oxygen pressure. *Corrosion Science*, 17:93–104, 1977.

[27] J.C. Langevoort, L.J. Hanekamp, and P.J. Gellings. On the kinetics of oxidation of austenitic stainless steels aisi 304 and incoloy 800h. *Applied Surface Science*, 28:189–203, 1987.

[28] P. Kofstad. *High temperature corrosion*. 1988.

[29] M. Kostelitz. Atmosphères industrielles. *Techniques de l'ingénieur*, 1988.

[30] A. Tasovac, R. Markovic, and Z. Strbacki. Comparative investigatiob of some austenitic chromium-nickel steels in hot air. *Materials Science and Engineering: A*, 120-121:229–234, 1989.

[31] P. Sarrazin, A. Galerie, and J. Fouletier. *Les mécanismes de la corrosion sèche. Une approche cinétique*. EDP Sciences, 2000.

[32] M.F. Ball. Intergranular oxidation of two austenitic stainless steel components operating at intermediate temperatures. *Fracture and Fracture Mechanics*, pages 255–263, 1985.

[33] J. Gilman, R. Rungta, P. Hinds, and H. Mindlin. Corrosion-fatigue crack-growth rates in austenitic stainless steels in light water reactor environments. *International Journal of Pressure Vessels and Piping*, 31:55–68, 1988.

[34] H.P. Seifert, S. Ritter, and H.J. Leber. Corrosion fatigue initiation and short crack growth behaviour of austenitic stainless steels under light water reactor conditions. *Corrosion Science*, 59:20–34, 2012.

[35] H.C. Wu, B. Yang, S.L. Wang, and M.X. Zhang. Effect of oxidation behavior on the corrosion fatigue crack initiation and propagation of 316ln austenitic stainless steel in high temperature water. *Materials Science and Engineering: A*, 633:176–183, 2015.

[36] I.J. O'Donnell, H. Huthmann, and A.A. Tavassoli. The fracture toughness behaviour of austenitic stainless steels and weld metal including the effects of thermal ageing and irradiation. *International Journal of Pressure Vessels and Piping*, 65:209–220, 1996.

[37] K.G. Budinski. Effect of hardness differential on metal-to-metal fretting damage. *Wear*, 301:501–507, 2013.

[38] J.F. Peng, C. Song, M.X. Shen, J.F. Zheng, Z.R. Zhou, and M.H. Zhu. An experimental study on bending fretting fatigue characteristics of 316l austenitic stainless steel. *Tribology International*, 44:1417–1426, 2011.

[39] M. Kubota, K. Kuwada, Y. Kondo, and J. Furtado. Effect of oxygen addition on fretting fatigue strength in hydrogen of jis sus304 stainless steel. *Tribology International*, 2014:92–99, 2011.

[40] R. Komoda, M. Kubota, and J. Furtado. Effect of addition of oxygen and water vapor on fretting fatigue properties of an austenitic stainless steel in hydrogen. *International Journal of Hydrogen Energy*, 40:16868–16877, 2015.

[41] M. Esteves, A.. Ramalho, and F. Ramos. Fretting behavior of the aisi 304 stainless steel under different atmosphere environments. *Tribology International*, 88:56–65, 2015.

[42] P. Sarrazin, A. Galerie, and J. Fouletier. Mechanisms of high temperature corrosion: a kinetic approach. *Trans Tech Publications*, 36-37, 2008.

[43] H.E. Evans. Stress effects in high temperature oxidation of metals. *International Materials Reviews*, 40:1–40, 1995.

[44] M.J. Deleury, J.L. Strudel, and J.R. Donati. Creep behaviour and structural changes of 316 type stainless steels. *Annales de Chimie Science des Matériaux*, 6:59–72, 1981.

[45] G. Murry. Aciers résistant au fluage. *Techniques de l'Ingenieur*, 1999.

[46] W.Z. Abuzaid, M. D. Sangid, J.D. Caroll, H. Sehitoglu, and J. Lambrosc. Slip transfer and plastic strain accumulation across grain boundaries in hastelloy x. *Journal of the Mechanics and Physics of Solids*, 60:1201–1220, 2012.

[47] J. Caroll, W. Abuzaid, J. Lambrosc, and H. Sehitoglu. High resolution digital image correlation measurements of strain accumulation in fatigue grack growth. *International Journal of Fatigue*, 57:140–150, 2013.

[48] L. Balogh, S.R. Niezgoda, A.K. Kanjarla, D.W. Brown, B. Clausen, W. Liu, and C.N. Tomé. Spatially resolved in situ strain measurements from an interior twinned grain in bulk polycrystalline az231 alloy. *Acta Materialia*, 61:3612–3620, 2013.

[49] J.L.W. Carter, M.W. Kuper, M.D. Uchic, and M.J. Mills. Characterization of localized deformation near grain boundaries of superalloy rené-104 at elevated temperature. *Materials Science and Engineering: A*, 605:127–136, 2014.

[50] K.L. Murty. *Materials ageing and degradation in Light Water Reactors*. Woodhead Publishing, 2013.

[51] R.L. Coble. Sintering crystalline solids: I- intermediate and final state diffusion models. *Journal of Applied Physics*, 32, 1961.

[52] I.G. Crossland and B. D. Clay. Diffusion creep and its inhibition in a stainless steel. *Acta Metallurgica*, 25:929–937, 1977.

[53] J. Schneibel, R. Coble, and R.M. Cannon. The role of grain size distributions in diffusional creep. *Acta Metallurgica*, 29:1285–1290, 1981.

[54] P.M. Hazzledine and J.H. Schneibel. Theory of coble creep for irregular grain structures. *Acta Metallurgica et Materialia*, 41:1253–1262, 1993.

[55] P.J. Henderson and E.D. Hondros. Effect of impurities on coble creep. *Scripta Metallurgica*, 16:1247–1248, 1982.

[56] Aurélie Soula. *Etude de la déformation intergranulaire au cours du fluage à haure température d'un superalliage à base de nickel polycristallin*. PhD thesis, 2008.

[57] F. Dobes. The internal stress in nabarro-herring creep. *Scripta Metallurgica*, 12:63–64, 1978.

[58] A. C. F. Cocks. Variational principles, numerical schemes and bounding theorems for deformation by nabarro-herring creep. *Journal of the Mechanics and Physics of Solids*, 44:1429–1452, 1996.

[59] F. A. Mohamed. Harper-dorn creep: Controversery, requirements and origin. *Materials Science and Engineering: A*, 463:177–184, 2007.

[60] P. Yavari and T. Langdon. The transition from nabarro-herring to harper-dorm creep at low stress levels. *Scripta Metallurgica*, 11:863–866, 1977.

[61] O.A. Ruano, J. Wadsworth, J. Wolfenstine, and O.D. Sherby. Evidence of nabarro-herring creep in metals: fiction or reality ? *Materials Science and Engineering: A*, 165:133–141, 1993.

[62] D.M. Owen and T.G. Langdon. Low stress creep behaviour: An examination of nabarro-herring and harper-dorn creep. *Materials Science and Engineering: A*, 216:20–29, 1996.

[63] E.H. Wong, W.D. Van Driel, A. Dasgupta, and M. Pecht. Creep fatigue models of solder joints: A critical review. *Microelectronics Reliability*, 59:1–12, 2016.

[64] D.J. Breton, I. Baker, and D.M. Cole. Microstructural evolution of polycristalline ice during confined creep testing. *Cold Regions Science and Technology*, 2016.

[65] F.R. Larson and J. Miller. A time-temperature relationship for rupture and creep stresses. *Transaction of ASME*, 74:765–775, 1952.

[66] D. Hayhurst. Creep rupture under multi-axial states of stress. *Journal of the Mechanics and Physics of Solids*, 20:381–382, 1972.

[67] D.R. Hayhurst. The effects of test variables on scatter in high temperature tensile creep rupture data. *International Journal of Mechanical Sciences*, 16:829–840, 1974.

[68] Mathieu Touboul. *Étude du comportement mécanique à chaud de l'acier P91 : vers la compréhension du rôle des mécanismes intra/intergranulaires sur la tenue en fluage. Application aux structures soudées*. PhD thesis, 2012.

[69] V. Gaffard. *Experimental study and modelling of high temperature creep flow and damage behaviour of 9Cr1MoNbV*. PhD thesis, Ecole Normale Superieure des Mines de Paris, 2004.

[70] V. Gaffard, A.F. Gourgues-Lorenzon, and J. Besson. High temperature creep flow and damage properties of 9cr1monbv steels: Base metal and weldment. *Nuclear Engineering and Design*, 235(24):2547–2562, December 2005.

[71] E. Contesti and G. Cailletaud. Description of creep plasticity interaction with non unified constitutive equations: Application to an austenitic stainless steel. *Nuclear Engineering and Design*, 116:265–280, 1989.

[72] C.E. Pugh. On establishing constitutive equations for use in design of high temperature fast reactor structure. *Nuclear Engineering and Design*, 51:23–27, 1978.

[73] L. Kloc and V. Sklenicka. Transition from power law to viscous creep behaviour of p91 type heat treated steel. *Materials Science and Engineering: A*, 234-236:962–965, 1997.

[74] J. Besson, S. Leclercq, V. Gaffard, and A.-F. Gourgues-Lorenzon. Analysis of creep lifetime of a asme grade 91 welded pipe. *Engineering Fracture Mechanics*, 76(10):1460–1473, July 2009.

[75] A. Kanni Raj. On high-temperature materials: A case on creep and oxidation of a fully austenitic heat-resistant superalloy stainless steel sheet. *Journal of Materials*, 2013, 2013.

[76] F.C. Monkman and NJ. Grant. An empirical relationship between rupture life and minimum creep rate in creep-rupture tests. *Proceedings of ASTM*, 56:593–620, 1956.

[77] J.S. Zhang. *High temperature deformation and fracture of materials*. Woodhead Publishing, 2010.

[78] European Creep Collaborative Committee. Creep and fracture in high temperature components: design and life assessments issues. 2014.

[79] I.A. Shibli. Overview of the hida project. *International Journal of Pressure Vessels and Piping*, 78:729–735, 2001.

[80] H. Riedel. Creep deformation at crack tips in viscoelastic solids. *Journal of Mechanical Physics Solids*, 29:35–49, 1979.

[81] H. Riedel and J. Rice. Tensile cracks in creeping solids. *ASTM*, pages 112–130, 1980.

[82] J.R.R. Rice. A path independant integral and the approximate analysis of strain concentration by notches and cracks. *Journal of Applied Mechanics*, 35:379–386, 1968.

[83] R.A. Ainsworth. R5: An assessment procedure for the high temperature response of structures. 2003.

[84] M. Yatomi and M. Tabuchi. Issues relating to numerical modelling of creep crack growth. *Engineering Fracture Mechanics*, 77(15):3043–3052, October 2010.

[85] S. Foletti, A. Lo Conte, S. Salgarollo, and F. Bassi. Creep crack initiation and growth in 12 pages 340–348, 2013.

[86] M. Yatomi, C M. Davies, and K. M. Nikbin. Creep crack growth simulations in 316h stainless steel. *Engineering Fracture Mechanics*, 75(18):5140–5150, December 2008.

[87] G.A. Webster, C.M. Davies, and K.M. Nikbin. Assessment of creep crack growth due to stress relief. *International Journal of Solids and Structures*, 47(7?8):881–886, April 2010.

[88] A. Mehmanparast, C.M. Davies, D.W. Dean, and K.M. Nikbin. The influence of pre-compression on the creep deformation and failure behaviour of type 316h stainless steel. *Engineering Fracture Mechanics*, 110(0):52–67, September 2013.

[89] ASTM international, editor. *ASTM-E1457-07: Measurement of creep crack growth rates in metals*, pages 1012–1035. Annual book of ASTM standards, 2007.

[90] C.M. Davies, N.P. O?Dowd, K.M. Nikbin, and G.A. Webster. An analytical and computational study of crack initiation under transient creep conditions. *International Journal of Solids and Structures*, 44(6):1823–1843, March 2007.

[91] E. Molinie. *Mécanique et mécanismes de l'endommagement et de la fissuration en viscoplasticité des aciers ferritiques faiblement alliés : éléments d'estimation de la durée de vie résiduelle de composants fissurés*. PhD thesis, Ecole des Mines de Paris, 1991.

[92] J.A. Begley and J.D. Landes. The j integral as a fracture criterion. *ASTM STP 514*, 1972.

[93] E.G. Ellison and M.P Harper. Creep bahaviour of components containing cracks: a critical review. *Journal of Strain Analysis*, 35, 1979.

[94] E.M. Christian, D. Smith, G. Webster, and E. Ellison. Critical examination of parameters for predicting creep crack growth. In *Fifith International Conference on Fracture*, 1981.

[95] K. Nikbin, D. Smith, and G. Webster. Prediction of creep crack growth from uniaxial creep data. *Proc R Soc*, A 396:183–197, 1984.

[96] C. Tan, NJC Célard, K. Nikbin, and G. Webster. Comparison of creep crack initiation and growth in four steels tested in hida. *International Journal of Pressure Vessels and Piping*, 78:737–747, 2001.

[97] C-S. Oh, N-Y. Kim, Y-J. Kim, C M. Davies, K. Nikbin, and D. Dean. Creep failure simulations of 316h at 550 °c: Part i - a mthod and validation. *Engineering Fracture Mechanics*, 78:2966–2977, 2011.

[98] A. Mehmanparast, C.M. Davies, D. Dean, and K. Nikbin. Effects of plastic pre-straining level on the creep deformation, crack initiation and growth behaviour of 316h stainless steel. *International Journal of Pressure Vessels and Piping*, 141:1–10, 2016.

[99] A. Mehmanparast, C M. Davies, and K. Nikbin. Creep-fatigue crack growth testing and analysis of pre-strained 316h stainless steel. *Procedia Structural Integrity*, 2:785–792, 2016.

[100] M. Chevalier. Metallography of carburised sample : 316 pre- conditioned during 2 khours at 600 celsius degree.

[101] B. Chen, J.N. Hu, P. Flewitt, A. Cocks, Ainsworth R.A., D.J. Smith, D. Dean, and F. Scenini. Effect of thermal ageing on creep and oxidation behaviour of type 316h stainless steel. *Materials at High Temperatures*, 32:592–606, 2015.

[102] J.C. Danko, R.E. Smith, and D.W. Gandy. Effect of surface preparation on crack initiation in welded stainless steel piping. *INIS*, 26:372–377, 1992.

[103] S. Cisse, L. Laffont, B. Tanguy, M-C. Lafont, and E. Andrieu. Effect of surface preparation on the corrosion of austenitic stainless steel 304l in high temperature steam and simulated pwr primary water. *Corrosion Science*, 56:209–216, 2012.

[104] D. Lloyd. The dependence of oxidation and carburisation in boiler stainless steels on gas chemistry. Technical report, Atkins, 2013.

[105] D. Chicot, J. Mendoza, A. Zaoui, G. Louis, F. Lepingle, V. Roudet, and J. Lesage. Mechanical properties of magnetite (fe3o4), hematite (alpha-fe2o3) and goethite (alpha-feo oh) by instrumented indentation and molecular dynamic analysis. *Materials Chemistry and Physics*, 129:862–870, 2011.

[106] D. Gomez-Briceno, F. Blazquez, and A. Saez-Maderuelo. Oxidation of austenitic and ferritic/martensitic alloys in supercritical water. *The Journal of Supercritical Fluids*, 78:103–113, 2013.

[107] S. Pentilla, A. Toivonen, J. Li, W. Zheng, and R. Novotny. Effect of surface modification on the corrosion resistance of austenitic stainless steel 316l in supercritical water conditions. *The Journal of Supercritical Fluids*, 81:157–163, 2013.

[108] W.H. Yeo, A.T. Fry, S. Ramesh, R. Mohan, H.L. Liew, J.I. Inayat-Hussain, and J. Purbolaksono. Simulating the implications of oxide scale formations in austenitic steels of ultra-supercritical fossil power plants. *Engineering Failure Analysis*, 42:390–401, 2014.

[109] C. Mansour and S. Trevin. Corrosion-erosion des aciers ferritiques dans les centrales nucléaires. *Techniques de l'Ingenieur*, 2014.

[110] M. Wehbi. *Modélisation de l'amorçage de la Corrosion Sous Contrainte dans les alliages base nickel 182 et 82 en milieu primaire des Réacteurs à Eau sous Pression*. PhD thesis, Ecole normale supérieure des Mines de Paris, 2014.

[111] J. Caballero, C. Duhamel, T. Couvant, and J. Crepin. Intergranular oxidation of alloy 600 exposed to simulated pwr primary water. In *17th international conference on environmental degradation of material in nuclear power systems - water reactors*, 2015.

[112] M.A. Mattoni and F.W. Zok. A method for determininig the stress intensity factor of a single edge-notched tensile specimen. *International Journal of Fracture*, 119, 2003.

[113] C Lee, WH Peters, YJ Chao, and MA Sutton. Improved digital image processing technique to investigate plastic zone formation in steel. *Image and Vision Computing*, 4(4):203–207, November 1986.

[114] C. Lee, W.H. Peters, M.A. Sutton, and Y.J. Chao. A study of plastic zone formation by digital image processing. *International Journal of Plasticity*, 3(2):129–142, 1987.

[115] M. Brunet and F. Morestin. Experimental and analytical necking studies of anisotropic sheet metals. *Journal of Materials Processing Technology*, 112:214–226, 2001.

[116] A.F. Ashour and C.T. Morley. Three-dimensional nonlinear finite element modelling of reinforced concrete structures. *Finite Elements in Analysis and Design*, 15:43–55, 1993.

[117] M. Bornert, F. Bremand, P. Doumalin, J-C Dupre, M. Fazzini, M. Grediac, F. Hild, S. Mistou, J. Molimard, J-J Orteu, L. Robert, Y. Surrel, P. Vacher, and B. Wattrisse. Assessment of digital image correlation measurement errors: methodology and results. *Experimental Mechanics*, 49:353–370, 2009.

[118] G. Catalanotti, P.P. Camanho, J. Xavier, C.G. Davila, and A.T. Marques. Measurement of resistance curves in the longitudinal failure of composites using digital image correlation. *Composites Science and Technology*, 70:1986–1993, 2010.

[119] M. Grediac and F. Hild. *Full-field measurements and identification in solid mechanics*. ISTE Ltd and John Wiley and sons, 2013.

[120] R. Caborgan. *Contribution à l'analyse expérimentale du comportement thermomécanique du caoutchouc naturel*. PhD thesis, Université de Montpellier 2, 2011.

[121] A. Guery, F. Latourte, F. Hild, and S. Roux. Characterization of sem speckle pattern marking and imaging distorsion by digital image correlation. *Measurement Science and Technology*, 25, 2014.

[122] L. Li. *Caractérisation et identification du comportement thermomécanique de multicristaux d'aluminium*. PhD thesis, Université de Montpellier, 2014.

[123] E. Plancher. *Mesures de champs de déformations élastique et totale pour la détermination du comportement mécanique local de matériaux cristallins*. PhD thesis, Ecole des Mines de Saint-Etienne, 2015.

[124] T. Madani. *Identification expérimentale de comportements élastoplastiques de matériaux hétérogènes pour des sollicitations complexes*. PhD thesis, Université de Montpellier, 2015.

[125] Julien Réthoré, Nathalie Limodin, Jean-Yves Buffière, Stéphane Roux, and François Hild. Three-dimensional analysis of fatigue crack propagation using x-ray tomography, digital volume correlation and extended finite element simulations. *Procedia IUTAM*, 4(0):151–158, 2012.

[126] B. Koohbor, S. Mallon, A. Kidane, and M.A. Sutton. A dic-based study of in-plane mechanical response and fracture of orthotropic carbon fiber reinforced composite. *Composites Part B: Engineering*, 66:388–399, 2014.

[127] J. Rethore. Automatic crack tip detection and stress intensity factors estimation of curved cracks from digital images. *International Journal for Numerical Methods in Engineering*, 103:516–534, 2015.

[128] M. Mokhtarishirazabad, P. Lopez-Crespo, B. Moreno, A. Lopez-Moreno, and M. Zanganeh. Evaluation of crack-tip fields from dic data: A parametric study. *International Journal of Fatigue*, 89:11–19, 2016.

[129] E. Salvati, S. O'Connor, T. Sui, D. Nowell, and A.M. Korsunsky. A study of overload effect on fatigue crack propagation using ebsd, fib-dic and fem methods. *Engineering Fracture Mechanics*, 2016.

[130] A. Guery, F. Hild, F. Latourte, and S. Roux. Identification of crystal plasticity parameters using dic measurements and weighted femu. *Mechanics of Materials*, 100:55–71, 2016.

[131] François Hild and Stéphane Roux. Measuring stress intensity factors with a camera: Integrated digital image correlation (i-dic). *Comptes Rendus Mécanique*, 334(1):8–12, January 2006.

[132] C. Roux-Langlois, A. Gravouil, Rethore J. Baietto, M-C., F. Mathieu, F. Hild, and S. Roux. Dic identification and x-fem simulation of fatigue crack growth based on the williams' series. *International Journal of Solids and Structures*, 53:38–47, 2015.

[133] S. Roux and F. Hild. Stress intensity factor measurements from digital image correlation : post-processing and integrated approaches. 2005.

[134] Garrett J. Pataky, Michael D. Sangid, Huseyin Sehitoglu, Reginald F. Hamilton, Hans J. Maier, and Petros Sofronis. Full field measurements of anisotropic stress intensity factor ranges in fatigue. *Engineering Fracture Mechanics*, 94(0):13–28, November 2012.

[135] MA Sutton, WJ Wolters, WH Peters, WF Ranson, and SR McNeill. Determination of displacements using an improved digital correlation method. *Image and Vision Computing*, 1(3):133–139, August 1983.

[136] B. Bay, D. Smith, D. Fyhrie, and M. Saad. Digital volume correlation: three dimensional strain mapping using x-ray tomography. *Experimental Mechanics*, 39:217–226, 1999.

[137] M. Rossi and F. Pierron. Identification of plastic constitutive parameters at large deformations from three dimensional displacement fields. *Computational Mechanics*, 49:53–71, 2011.

[138] K. Denys, S. Coppieters, M. Seefeldt, and D. Debruyne. Multi-dic setup for the identification of a 3d anisotropic yield surface of thick high strength steel using a double perforated specimen. *Mechanics of Materials*, 100:96–108, 2016.

[139] J.-E. Dufour, S. Leclercq, J. Schneider, S. Roux, and F. Hild. 3d surface measurements with isogeometric stereocorrelation. application to complex shapes. *Optics and Lasers in Engineering*, 2016.

[140] F. Latourte, T. Salez, A. Guery, N. Rupin, and M. Mahe. Deformation studies from in situ sem experiments of a reactor pressure vessel at room and low temperatures. *Journal of Nuclear Materials*, 454:373–380, 2014.

[141] E. Bosso. *Comportement du Zircaloy-4 recristallise : identification du comportement anisotrope pour application à la situation d'accident de réactivité*. PhD thesis, Ecole Nationale des Mines de Paris, 2015.

[142] P. Doumalin. *Microextensométrie locale par Corrélation d'Images Numériques*. PhD thesis, Ecole Polytechnique, 2000.

[143] D. Garcia. *Mesure de formes et de champs de déplacements tridimensionnels par stéréo-corrélation d'images*. PhD thesis, INP de Toulouse, 2001.

[144] A. Sutton, N. Li, D. Garcia, N. Cornille, J-J Orteu, S. McNeill, H. Schreier, and X. Li. Metrology in scanning electron microscope: theoretical developments and experimental validation. *Measurement Science and Technology*, 17:2613–2622, 2006.

[145] A. Sutton, N. Li, D. Garcia, N. Cornille, J-J Orteu, S. McNeill, H. Schreier, X. Li, and A.P. Reynolds. Scanning electron microscopy for quantitative small and large deformation measurements part ii: Experimental validation for magnifications from 200 to 10000. *Experimental Mechanics*, 47:789–804, 2007.

[146] A. Sutton, N. Li, D.C. Joy, A. Reynolds, and X. Li. Scanning electron microscopy for quantitative small and large deformation measurements part i: Sem imaging at magnifications from 200 to 10000. *Experimental mechanics*, 47:775–787, 2007.

[147] M. Grédiac and F. Hild. *Mesures de champ et identification en mécanique des solides*. Série Mécanique et Ingénierie des matériaux, 2011.

[148] G. Nolze. Image distorsions in sem and their influences on ebsd measurements. *Ultramicroscopy*, 107:172–183, 2007.

[149] S. Wen. *Identification experimentale de modeles de zones cohesives à partir de techniques d'imagerie thermomécanique*. PhD thesis, Universite de Montpellier, 2012.

[150] A. Guery. *Development of a digital image correlation procedure for displacement field measurements in polycristals, for identification of crystalline plasticity law parameters.* PhD thesis, ENS Cachan, 2014.

[151] B. Wattrisse. *Etude cinématique des phénomènes de localisation dans des aciers par intercorrélation d'image*. PhD thesis, Universite de Montpellier 2, 1999.

[152] F. Latourte, C. Toulemonde, J-F. Rit, J. Sanahuja, N. Rupin, J. Ferrari, H. Perron, E. Bosso, A. Guery, J-M. Proix, and B. Wattrisse. The materials ageing plateform: towards a toolbox to perform a wide range of research studies on the behaviour of industrial materials. In *Conference Photomechanics*, 2013.

[153] B. Wattrisse, A. Chrysochoos, J.-M. Muracciole, and M. Némoz-Gaillard. Analysis of strain localisation during tensile test by digital image correlation. *Journal of Experimental Mechanics*, 41:29–38, 2011.

[154] A. Griffith. The phenomena of rupture and flow in solids. *Philosophical Transactions of the Royal society of London*, 221, 1921.

[155] G.R. Irwin and J.A. Kies. Critical energy rate analysis of fracture strength. *Welding Research Supplement*, pages 193–198, 1954.

[156] G.R. Irwin. Analysis of stresses and strains near the end of cracking traversing a plate. *Journal of Applied Mechanics*, 24:361–364, 1957.

[157] G.R. Irwin, H. Liebowitz, and P.C. Paris. A mystery of fracture mechanics. *Engineering Fracture Mechanics*, 1(1):235–236, June 1968.

[158] G.R. Irwin. Linear fracture mechanics, fracture transition, and fracture control. *Engineering Fracture Mechanics*, 1(2):241–257, August 1968.

[159] G.R. Irwin. Fracture strength of relatively brittle structures and materials. *Journal of the Franklin Institute*, 290(6):513–521, December 1970.

[160] G.R. Irwin and P.C. Paris. Elastic-plastic crack tip characterization in relation to r-curves. In D.M.R. TAPLIN, editor, *Advances in Research on the Strength and Fracture of Materials*, pages 93–100. Pergamon, 1978.

[161] H. Westergaard. Bearing pressure and cracks. *Journal of Applied Mechanics*, 6:49–553, 1939.

[162] J.L. Bassani and J. Qu. On elasticity solutions for cracks on bimaterial and bicrystal interfaces. *Materials Science and Engineering: A*, 107(0):177–184, January 1989.

[163] J.L. Bassani and J. Qu. Finite crack on bimaterial and bicrystal interfaces. *Journal of the Mechanics and Physics of Solids*, 37(4):435–453, 1989.

[164] J. Bassani, D.E. Hawk, and F.-H. Wu. Crack growth in small-scale creep. *ASTM STP 995*, I:68–95, 1989.

[165] J. Qu and J.L. Bassani. Cracks on bimaterial and bicrystal interfaces. *Journal of the Mechanics and Physics of Solids*, 37(4):417–433, 1989.

[166] J.L. Bassani and J. Qu. Interfacial discontinuities and average bimaterial properties. In M. RÜHLE, A.G. EVANS, M.F. ASHBY, and J.P. HIRTH, editors, *Metal–Ceramic Interfaces*, pages 401–406. Pergamon, Oxford, 1990.

[167] J. Qu and J.L. Bassani. Interface cracks between anisotropic elastic solids. In M. RÜHLE, A.G. EVANS, M.F. ASHBY, and J.P. HIRTH, editors, *Metal–Ceramic Interfaces*, pages 407–412. Pergamon, Oxford, 1990.

[168] J. Hutchinson. Singular behavior at the end of a tensile crack tip in a hardening material. *Journal of the Mechanics and Physics of Solids*, 16:13–31, 1968.

[169] J. Rice and G.F. Rosengren. Plane strain deformation near a crack tip in a power-law hardening material. *Journal of the Mechanics and Physics of Solids*, 1968:1–12, 16.

[170] M.S. Dadkhah and A. Kobayashi. Hrr field of a moving crack, an experimental analysis. *Engineering Fracture Mechanics*, 34:253–262, 1989.

[171] G.B. May and A.S. Kobayashi. Plane stress stable crack growth and j-intergral/hrr field. *International Journal of Solids and Structures*, 32:857–881, 1995.

[172] C.E. Inglis. Stresses in a plate due to the presence of cracks and sharp corners. *Journal of Applied Mechanics*, 24:316–364, 1957.

[173] M.L. Willliams, Pasadena, and Calif. On the stress distribution at the base of a stationary crack. *Journal of Applied Mechanics*, 24:109–114, 1957.

[174] Y. Barranger, P. Doumalin, J-C Dupre, A. Germaneau, S. Hedan, and V. Valle. Analyse à coeur des champs de déplacement obtenus sur une éprouvette fissurée. In *19 ème Congrès Français de Mécanique*, 2009.

[175] J. Rethore, S. Roux, and F. Hild. Optimal and noise-robust extraction of fracture mechanics parameters from kinematic measurements. *Engineering Fracture Mechanics*, 78:1827–1845, 2011.

[176] Paul Leplay. *Identification de comportements mécaniques et à rupture par corrélation d'images 2D et 3D : Application aux filtres à particules Diesel à base de titanate d'aluminium*. PhD thesis, INSA Lyon, 2011. Directeur de thèse : Marie-Christine Baietto.

[177] L. Meric, P. Poubanne, and G. Cailletaud. Single crystal modeling for structural calculations : I model presentation. *Journal of engineering materials and technology transaction of the ASME*, 113:162–170, 1991.

[178] Y. Guilhem. Identification du modèle de comportement monocristal de méric-cailletaud pour l'acier 316ln sous chargement cyclique. Technical report, EDF R&D, 2010.

[179] M.K. Samal and S. Ghosh. Evaluation of creep deformation and mechanical properties of nickel-based superalloys through fe analysis based on crystal plasticity models. *Procedia Engineering*, 55:342–347, 2013.

[180] V. Hasija, S. Gosh, M.J. Mills, and D.S. Joseph. Deformation and creep modeling in polycrystalline ta6al alloys. *Acta Materialia*, 51:4533–4549, 2003.

[181] Yoann Guilhem. *Étude numérique des champs mécaniques locaux dans les agréagts polycristallins d'acier 316 L sous chargement de fatigue*. PhD thesis, Ecole nationale supérieure des mines de Paris, 2011.

[182] D. Tschumperlé. *GMIC - The Handbook*. 2016.

[183] H. Tada, P. Paris, and G. Irwin. *The stress analysis of cracks handbook*. Del research Corporation, 1985.

[184] C.M. Davies, D.W. Dean, K.M. Nikbin, and N.P. O'Dowd. Interpretation of creep crack initiation and growth data for weldments. *Engineering Fracture Mechanics*, 74(6):882–897, April 2007.

[185] B. Wattrisse, A. Chrysochoos, J.-M. Muracciole, and M. Némoz-Gaillard. Kinematic manifestations of localisation phenomena in steels by digital image correlation. *European Journal of Mechanics - A/Solids*, 20(2):189–211, March 2001.

[186] R. Syre. Niobium. *Techniques de l'ingénieur*, 1976.

[187] D. Charquet. Propriétés du zirconium et du hafnium. *Techniques de l'iingénieur*, 1985.

Appendix A

Solutions to prevent oxide growth at the surface

In Chapter 2, the surface evolution due to the oxidant atmoshpere at 550 °C has been shown. Inspired by [68], two strategies have been explored to insure the pattern integrity with respect of time. The two methodologies are presented in Figure 163.

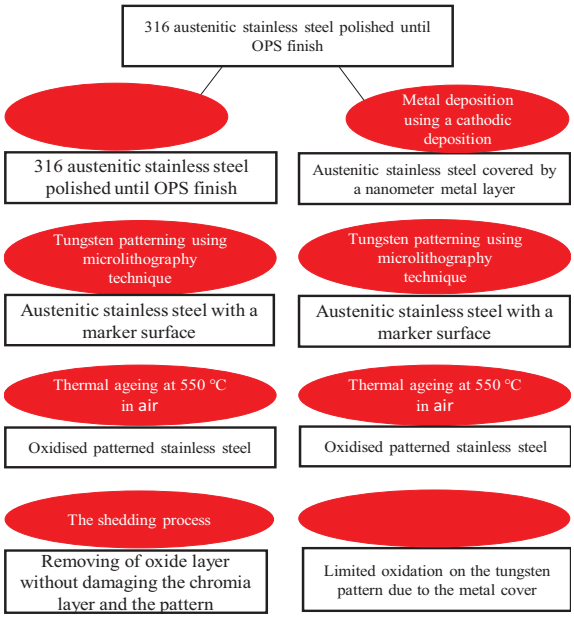

Figure 163: Presentation of explored strategies to insure the pattern integrity against oxidation at high temperature.

1. *The first technique relies on a combination of thermal ageing and chemical treatment and will be named hereafeter the spalliation process.*

2. *The second technique relies on a nanometer metal layer deposition prior to microlithography step. This cover must act as a barrier to the oxidation and allows the pattern protection. This strategy will name hereafter the metal cover process.*

The results are adressed in the following sections.

Results for the spalliation process

After five weeks at 550 °C, two samples (9 and 11) made of 304L and B3-3 have been immersed successively in two chemical solutions. These solutions interact with the oxide layer and must permit the oxide removing without damaging the tungsten pattern and the chromia film. Being rich in chromium, it acts as a barrier to oxidation and must stay intact. The choice of the chemical solutions has been made in agreement with the norm NF ISO8407:2010-01. The solutions have been used at room temperature using ultrasounds:

- $HCl + H_2O$ has been obtained by melting 500 mL of muriatic acid, 5 g of hexamethylenetetramine and distilled water during ten minutes at 20-25 °C. This solution is particularly efficient for the steel;

- $HNO_3 + H_2O$ has been obtained by melting 200 mL of nitric acid and distilled water at 20-25 °C. This one is specific to stainless steels.

After 1 minute in HCl solution, some areas of the 316LN B3-3 sample are free of oxide layer (see Figure 164). The oxide is removed piece by piece following the underlying microstructure.

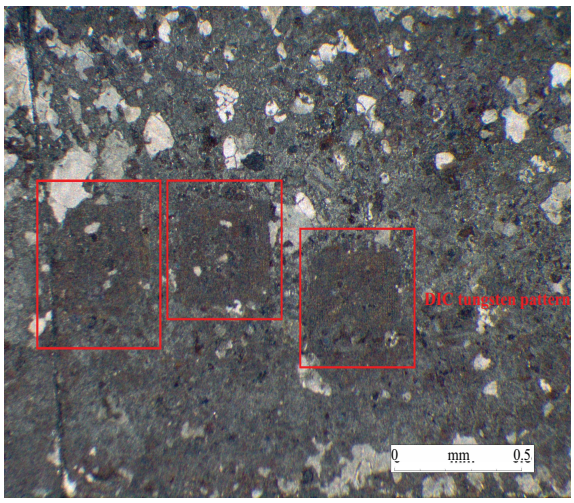

Figure 164: Optical imaging of pattern onto B3-3 sample after **1 minute in HCl solution**. Tungsten patterns are still present given by the red squares.

After 1 minute in HCl solution and 8 minutes 30 seconds in HNO_3, most of the oxide layer in the pattern region has been removed (see Figure 165). At some places, grids and dots seem to be missing.

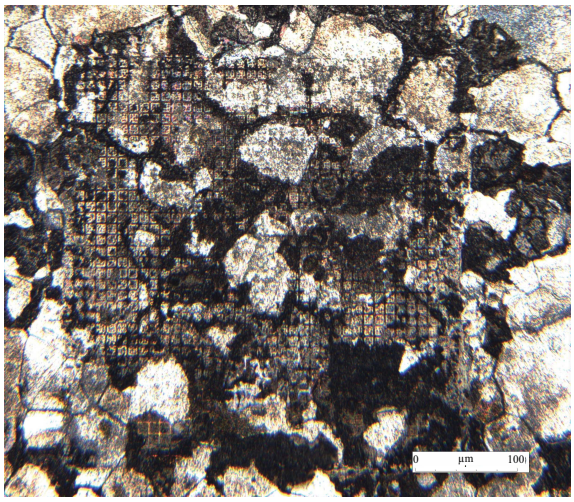

Figure 165: Optical imaging of pattern onto B3-3 sample after **1 minute in HCl solution and 8 minutes 30 seconds in HNO_3**.

After 11 minutes, there are few changes on the sample surface (see Figure 166).

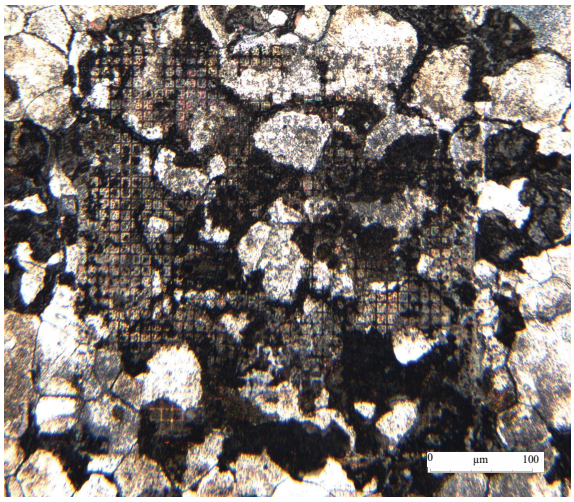

Figure 166: Optical imaging of pattern onto B3-3 sample after **1 minute in HCl solution and 11 minutes in HNO_3**.

The observation of a reduced area in the pattern has confirmed that the pattern seems to be also removed by the chemical treatment (see Figure 167).

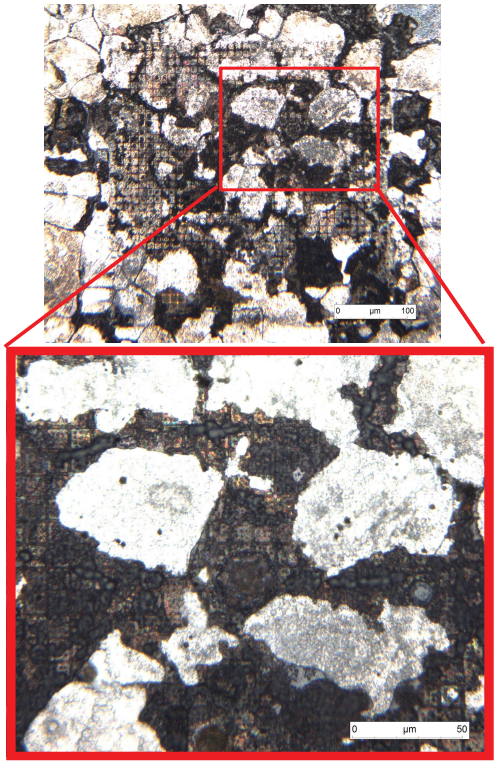

Figure 167: Optical imagings of pattern onto B3-3 sample after **1 minute in HCl solution and 16 minutes in HNO_3**.

At the end of the entire process (see Figure 168), most of the oxide layer has been removed but unfortunately, the solutions have been detrimental for the tungsten pattern. The SEM imagings have shown the impact of the chemical solutions on the pattern grids and dots (see Figure 168 a and Figure 168 c). The SE mode reveals that the oxide has disappeared piece by piece damaging the tungsten pattern. The BSE mode with chemical contrast couldn't allow distinguishing the tungsten.

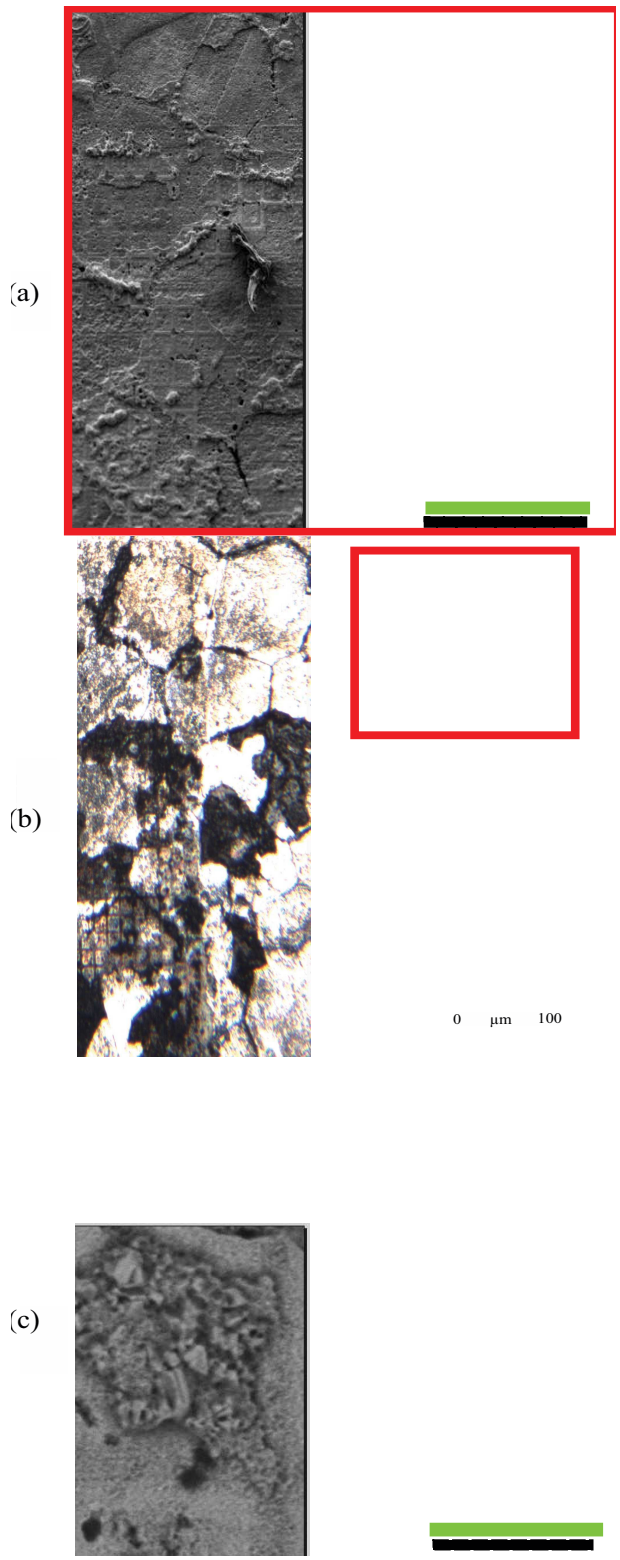

Figure 168: B3-3 sample after **1 minute in HCl solution and 31 minutes in HNO_3**. (a) SEM image in SE mode of a small area: the grids and the dots are not visible anymore, (b) optical imaging of a pattern onto B3-3 sample, (c) zoom onto a microsquare in BSED mode: the contrast is low between the pattern and the sample. The green scale bar is 100 µm.

To explain this, two presumed reasons are proposed:

- The tungsten is oxidised (WO_3,W_2O_3 or WO_2) leading to a contrast evolution. As there is no contrast at all, the tungsten is covered by the oxide;

- The tungsten or the tungsten oxide has been (partially) removed from the sample by the chemical solutions and the ultrasounds use.

To corroborate the oxide removing, some cuts have been done using the SEM FEI dual-beam Helios (see Figure 169).The chemical solutions combined with ultrasounds have led to surface changes (see Figure 169 a) and to oxide layer removing (see Figure 169 d).

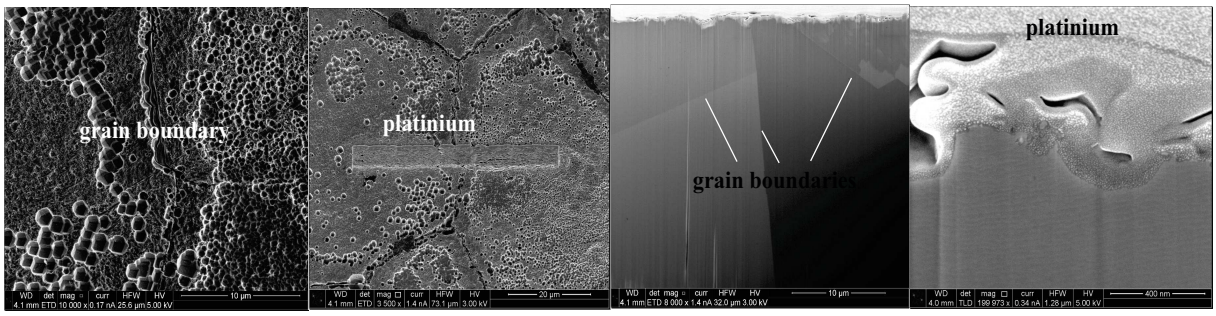

(a) (b) (c) (d)

Figure 169: SEM imaging of 316 LN sample surface after the spalliation process (a) the topography of the surface is quite heterogeneous with circular structures, (b) after platinium deposition to protect the surface, (c) after the cut, all the grain boundaries are visible, (d) at high level of magnification, no oxide layer is found (x199973).

The same study has been performed onto OPS polished 316H as-received sample, named ACFM (see Figure 170). The changes in the surface color relies on the oxide removing (see Figure 170 a and Figure 170 b). After 10 minutes in HCl solution and 19 minutes in HNO_3, most of the oxide has been removed (see Figure 170 e).

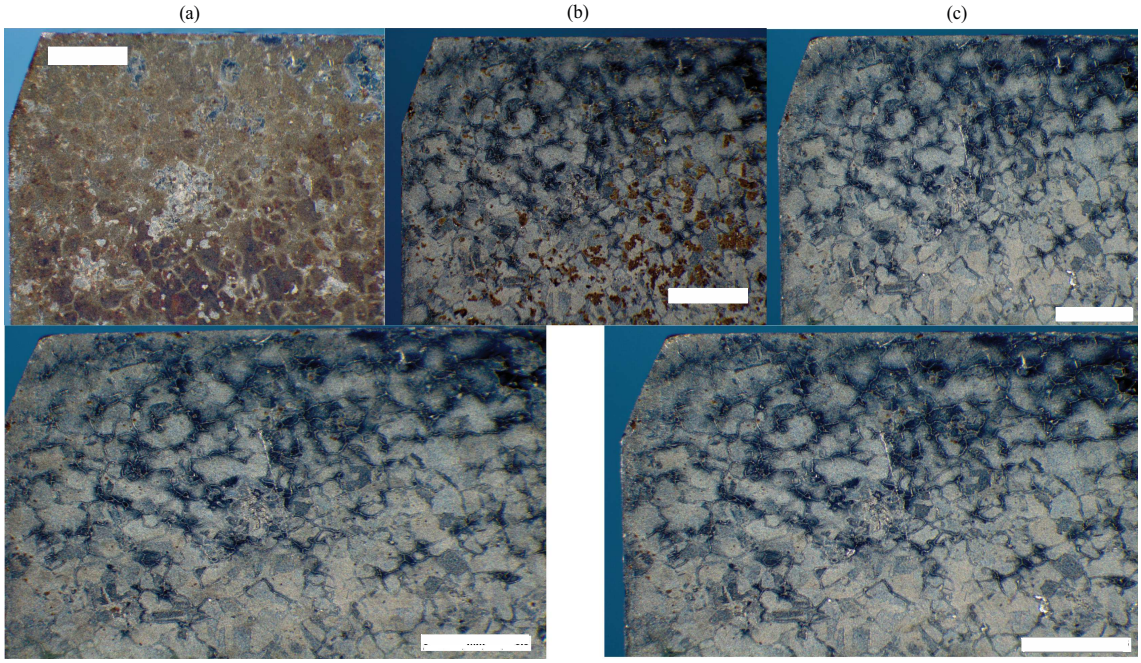

Figure 170: Optical imagings of ACFM sample **during the spalliation process**: (a) 10 minutes in HCl solution, (b) 10 minutes in HCl solution and 2 minutes 30 seconds in HNO_3, (c) 10 minutes in HCl solution and 9 minutes in HNO_3, (d) 10 min in HCl solution and 14 minutes in HNO_3, (e) 10 minutes in HCl solution and 19 minutes in HNO_3, few changes occured between 9 and 19 min. The white scale represents 0.5 mm.

SEM observations have highlighted that the used chemical solutions led to grain loss (see Figure 171 b) and that the attack affected the microstructure (see Figure 171 c). The grain boundaries seem to be particularly attacked by the solution. Their shapes have evolved with the spalliation process (see Figure 172 b and Figure 172 c). The efficiency of the spalliation process to remove oxide has been proved.

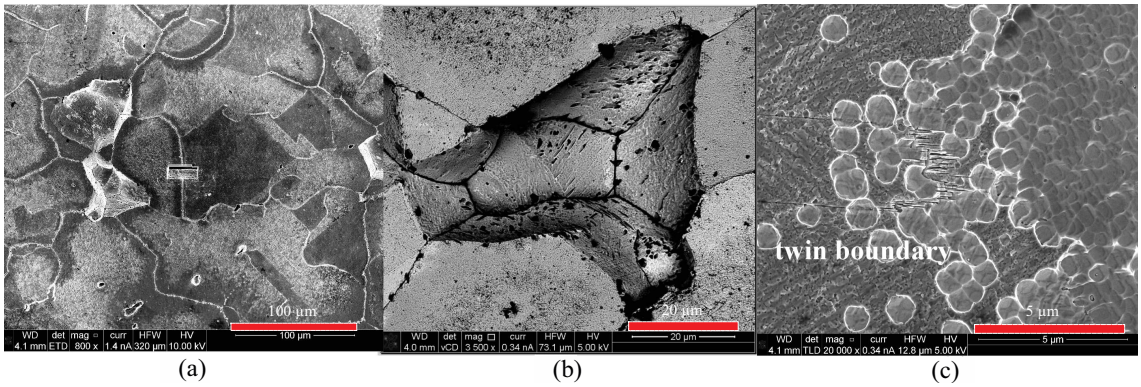

Figure 171: SEM imagings in SE mode of ACFM sample **after** the spalliation process: (a) a FEI dual-beam cut has been done at a grain boundary interface, (b) the chemical solutions have led to some grains pullout, (c) some attack sites are visible as well as the microstructure.

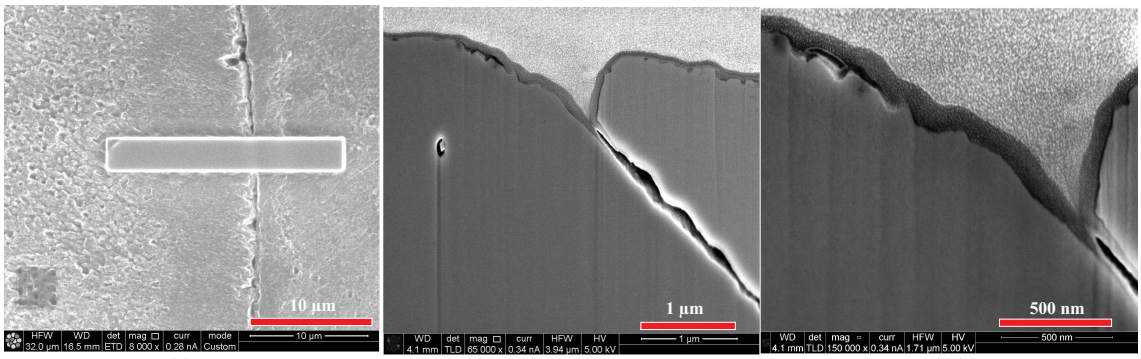

(a) (b) (c)

Figure 172: SEM imagings in SE mode of ACFM sample **after** the spalliation process: (a) a platinium deposition has been performed prior to the cut, (b) the grain boundary seems to be affected by the chemical solutions (c) the oxide layer has been removed from the sample surface.

Conclusions

The efficiency of the spalliation process using a combination of HCl and HNO_3 solutions with ultrasounds has been proved. Unfortunately, the muriatic acid contained in the HCl solution is too agressive for the 316H stainless steel and some grains pullouts are observed. The only use of HNO_3 solution could be sufficient but there is no guarantee that the protective layer won't be attacked. Moreover, we saw that the grain boundaries were particularly affected by the chemical solutions which is detrimental for the intergranular creep crack monitoring. Then, the microlithography can't be carried out before the spalliation process because the chemical solutions combined with the ultrasounds are responsible for pattern damaging. To conclude, the spalliation process can not be used to prepare and stabilize the sample surface from oxidation.

The metal cover process

Touboul has tried to cover this sample during this test at 625 °C but without full success [68]. Inspired by this strategy, we have performed some metal cover deposition using a cathodic system prior to the microlithography process. Several samples made of 316LN, 316H as-received and 316H preconditioned have been used to try different metal coatings as protective cover: Nickel, Chromium, Hafnium, Niobium. Prior to the deposition, the Type 316 samples have been polished until OPS finish. This treatment insures the best adhesive properties between the Type 316 and the filler metal.

The nickel and chromium coatings

Nickel and chromium have been deposited onto the ACFM sample made of 316H as-received. To make a comparison of the metal coating effect on the oxidation, this specimen has been separated into three areas. One of them has been covered by a 5-nm thickness of nickel (see Figure 173 c), the second one with 5-nm thick layer of chromium (see Figure 173 b) whereas the third one has been kept to be used as a reference (see Figure 173 a). The sample has been submitted to a thermal ageing at 550 °C in air during two weeks (see Figure 173 d, Figure 173 e and Figure 173 f). The SEM images have been taken using BSE detector in Z contrast configuration with an acceleration

voltage of 10kV or 30kV and a working distance of 10 mm.

A DIC analysis between the SEM images of Figure 173 a and Figure 173 d has been performed. The kinematic fields are in agreement with the movement made of translation and rotation observed due to the unperfect repositioning of the sample in the SEM chamber between the two acquisitions (see Figure 174). Nevertheless, the damaged pattern onto nickel and chromium can't be used to perform DIC.

In parallel, two tensile samples named B1-1 and B3-4 made of 316LN have been covered with a thickness ranging between 0.5 nm and 5 nm with a 0.5 nm step of nickel and chromium respectively to study the influence of the thickness on the oxidation protection. Then, tungsten patterns have been deposited at different places in the gage part to follow the deformation of the oxide during a tensile test. The aim of this test was to study the adhesive properties of the coating layers. The tests have consisted in an uniform tensile test at room temperature using a SEM tensile device (see Figure 175). Some stops have been made to make SEM image acquisitions.

During the two tensile tests, it appears that the layers deposited were relatively brittle. Rapidly, after a few loadings, some cracks are observed (see Figure 176 a and Figure 177 a). Sometimes, the oxide has left piece by piece (see Figure 176 b and Figure 177 b). Then, after cracking, the oxide layer followed the underlying material (see Figure 176 c and Figure 177 c).

Moreover, it was planned to perform EBSD analysis after the microlithography process to correlate the mechanical fields with the microstructure. Using the Quality Indice (QI), a match can be done between the EBSD coordinates and the kinematic fields. It could be useful to identify a grain misorientation which is in favor of intergranular crack propagation. We tried to obtain EBSD map of B1-1 and B3-4. The OIM TSL software isn't able to get an accurate value of the grain misorientations because the index quality is too bad. The metal coating is too thick to get enough signal to index. The threshold values identified are 1.0 nm for the chromium and 0.5 nm for the nickel. To conclude, the nickel and the chromium are not efficient to protect the tungsten pattern from oxidation and to be used as cover at high temperature because their mechanical properties are not adapted for DIC monitoring.

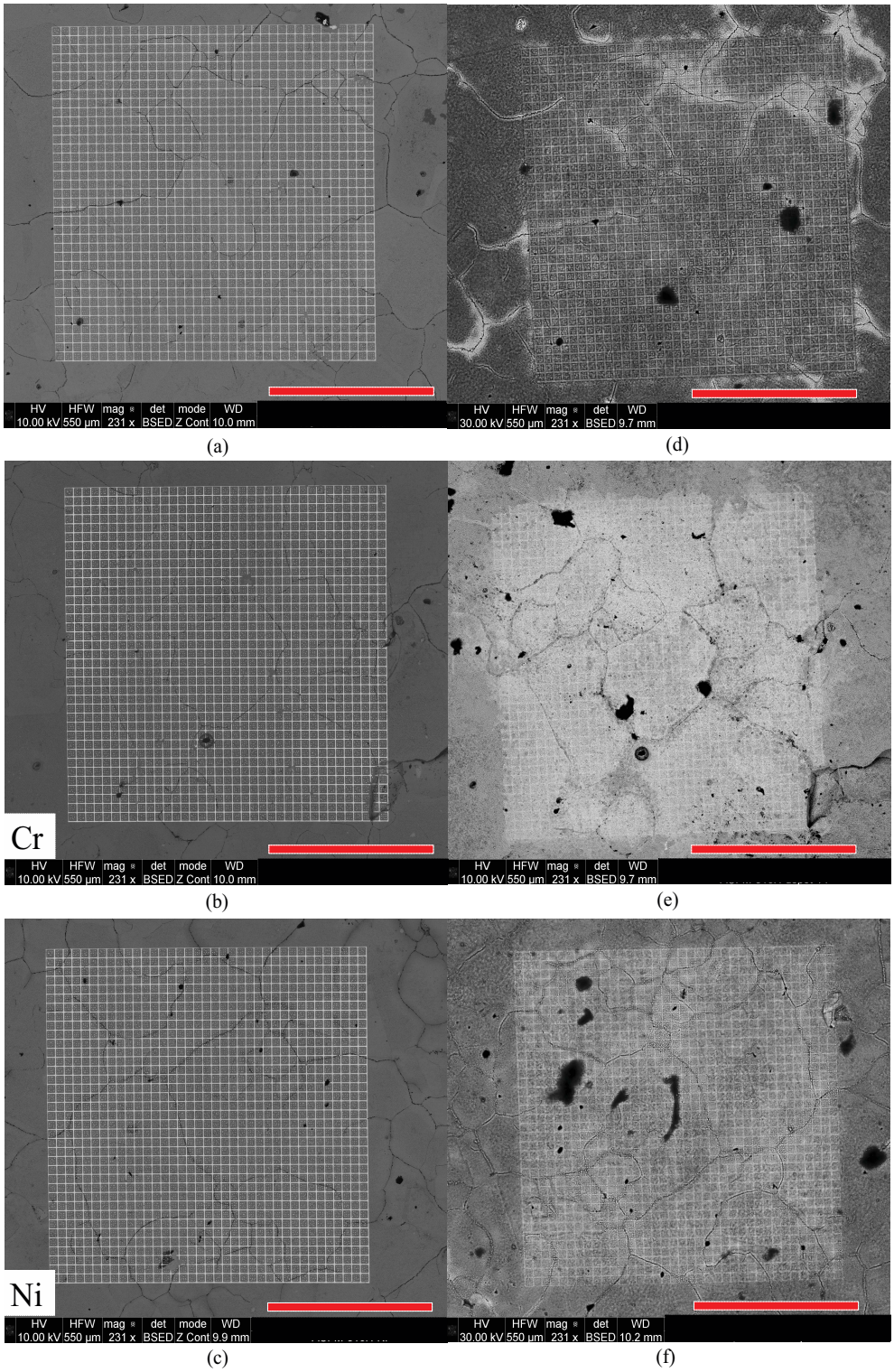

Figure 173: SEM images of pattern onto the ACFM sample in BSED mode **before** and **after** after two weeks in air at 550 °C: (a,d) uncoated area, (b,e) chromium coating, (c,f) nickel coating. The red scale bar is 200 µm (magnification: x231).

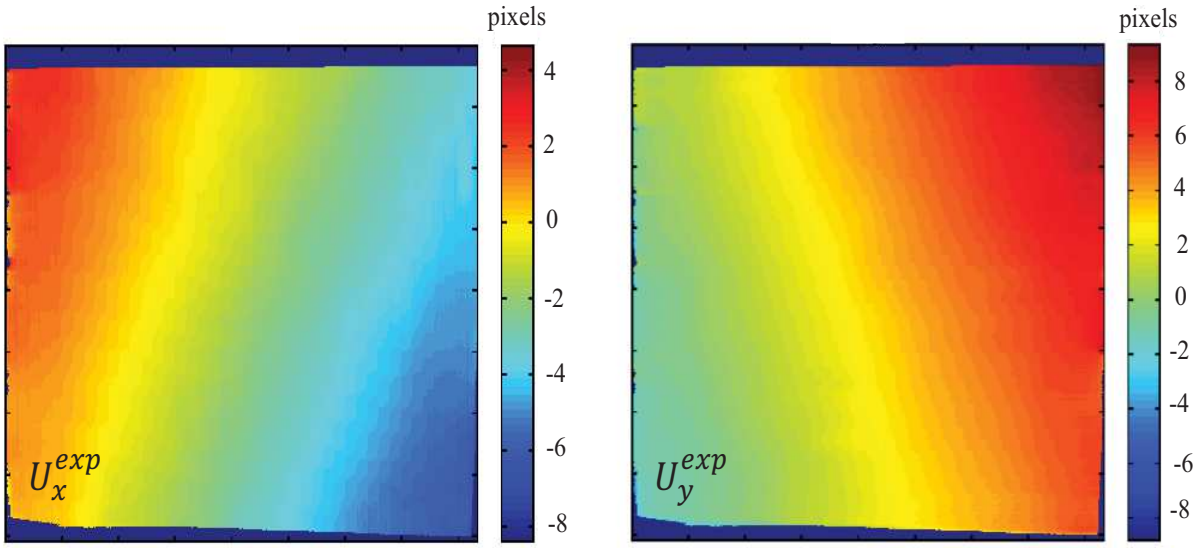

Figure 174: Kinematic fields with a local approach between the SEM images of Figure 173 a, Figure 173 d: (a) U_x , (b) U_y.

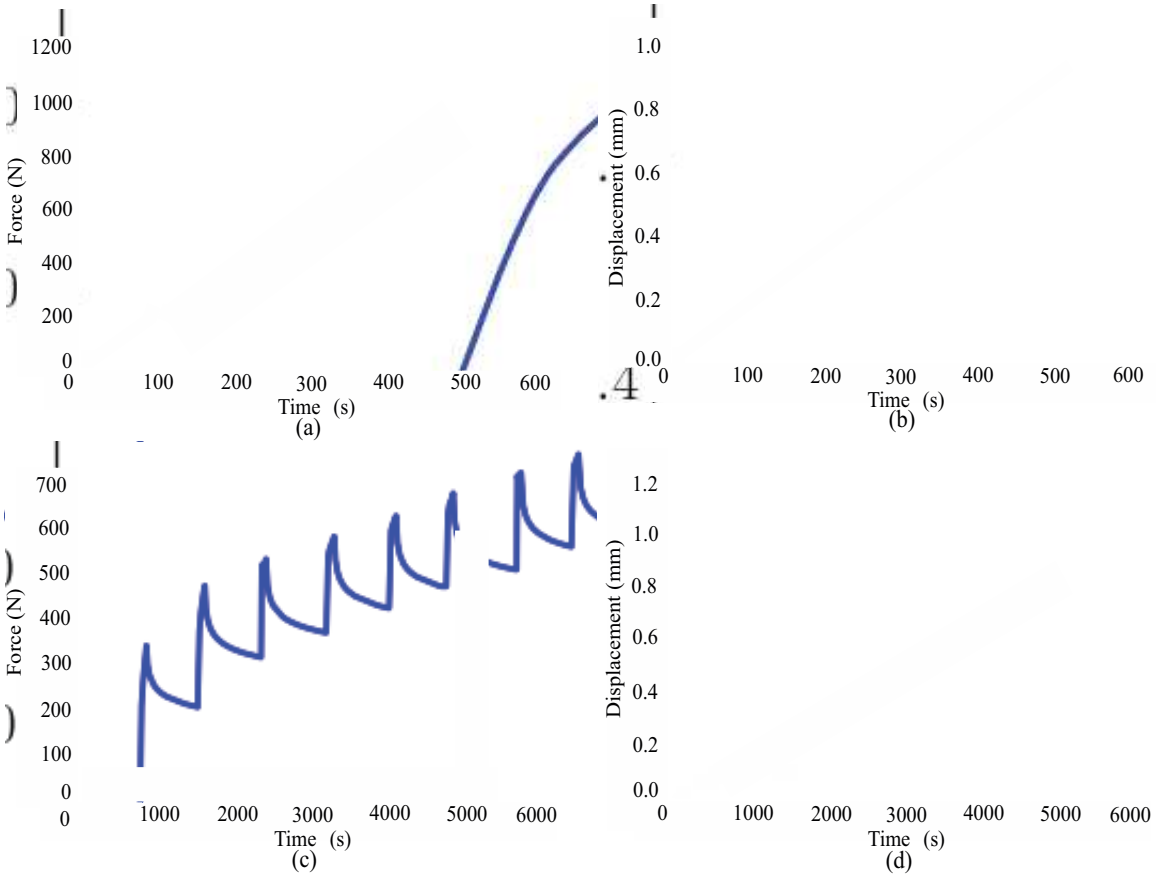

Figure 175: (a) Tensile curve for B1-1 sample, (b) displacement curve for B1-1 sample, (c) Tensile curve for B3-4 sample, (d) displacement curve for B3-4 sample.

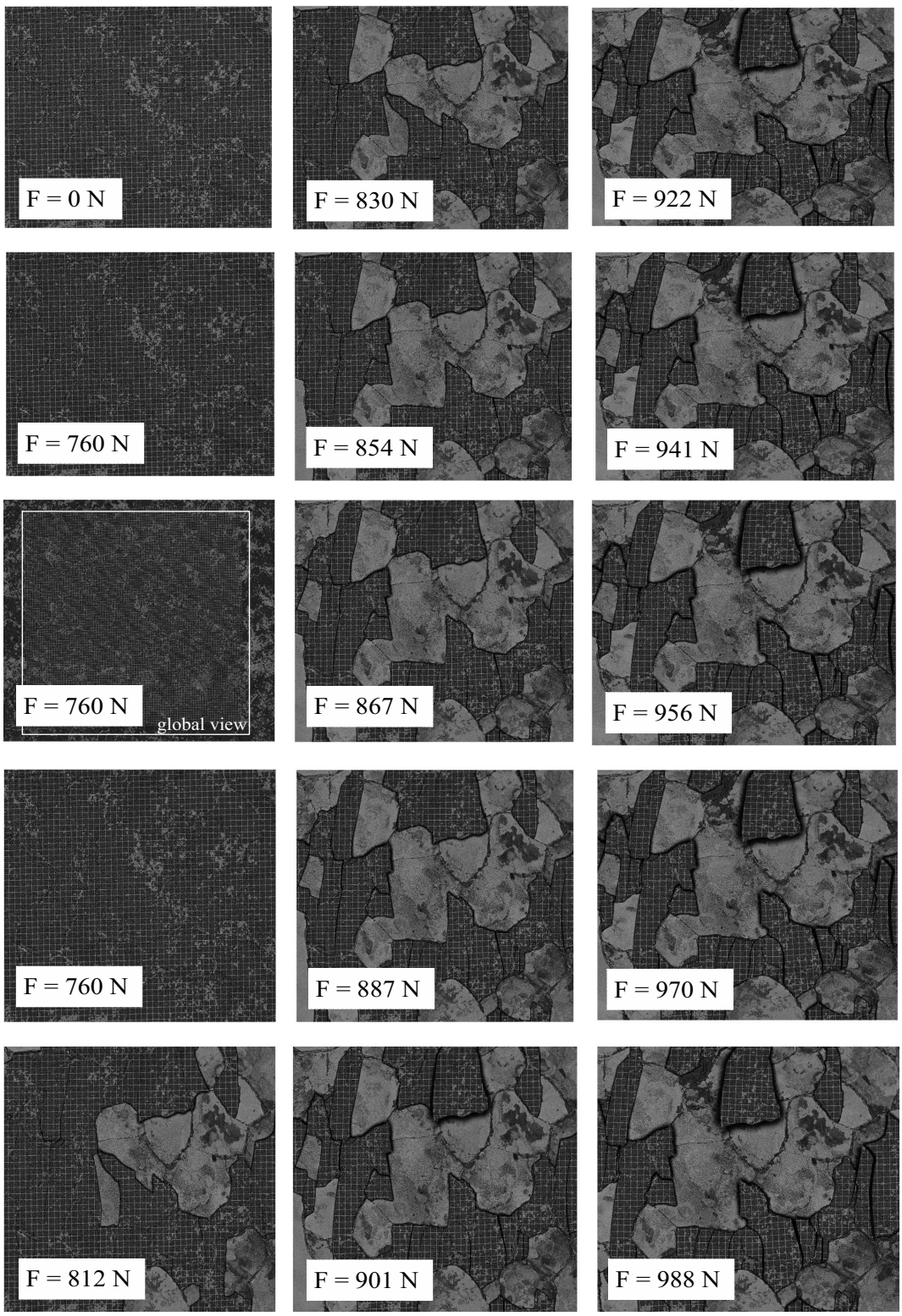

Figure 176: Tungsten pattern evolution during tensile test of B1-1 sample: decohesion of the oxide layer (812 N) and loss of pattern integrity, deformation of material under the coating (887 N).

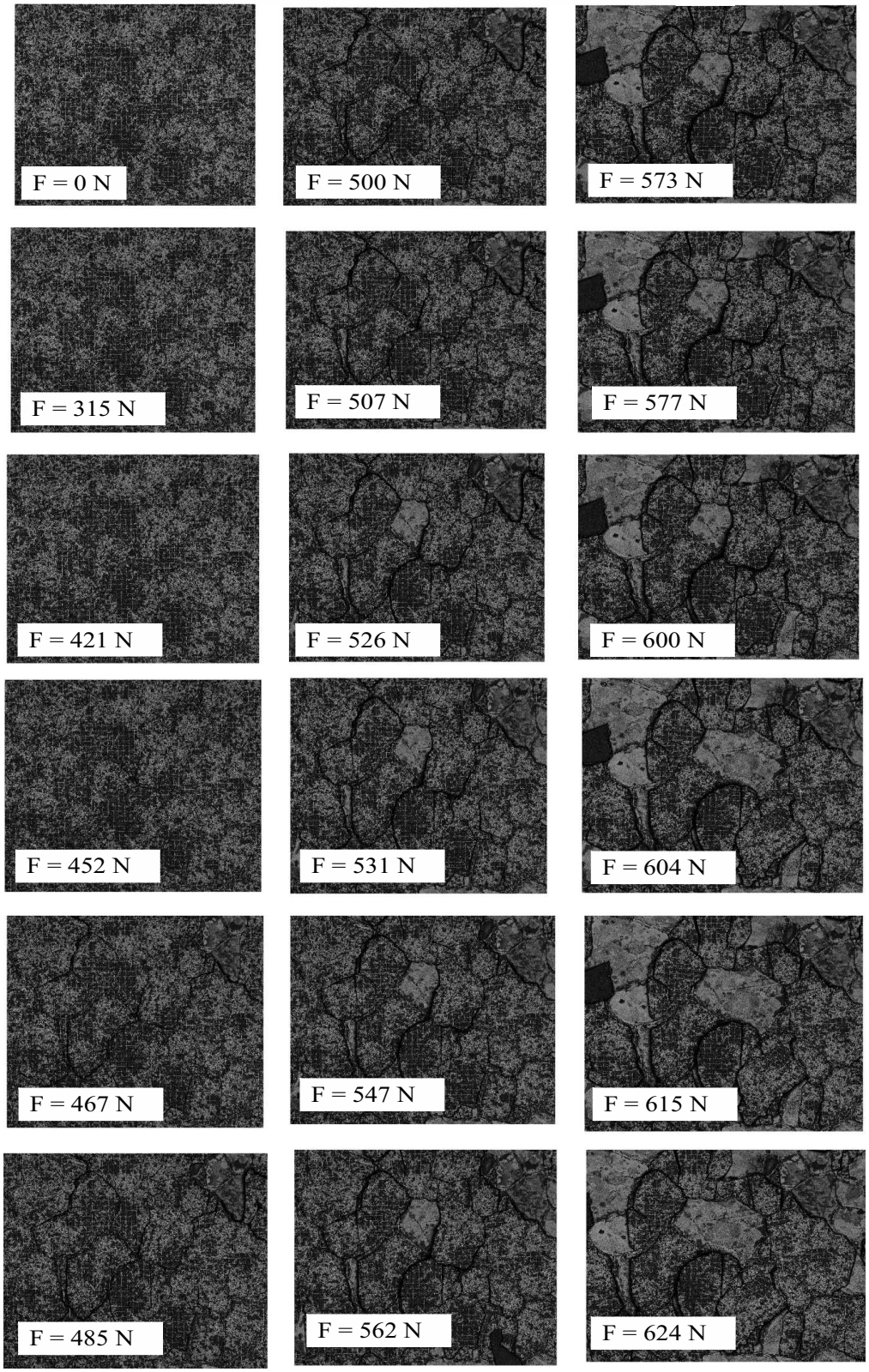

Figure 177: Tungsten pattern evolution during tensile test of B3-4 sample: decohesion of the oxide layer (421 N), loss of pattern integrity (467 N), deformation of material under the coating (507 N).

The Niobium and Hafnium coatings

The properties of niobium have been described by Syre [186]. Its Young's modulus is 107.8 GPa. It has a good mechanical resistance until 1000 °C. Theses properties rely on the metal purety (see Table 51).

Temperature (°C)	Vickers hardness for F = 196 N	$R_e^{0.2}$ (MPa)	R_m (MPa)	Elongation (%)
500	60	150	350	30

Table 51: Properties of pure niobium [186].

Up to 100 °C, the niobium is oxidised in Nb_2O_5 with an important volume expansion. This oxide layer is porous, brittle and does not protect from oxygen diffusion. Nevertheless, some mechanical tests have been performed using niobium as surface marker for DIC monitoring so it was interesting to compare the results obtained with this metal and with the oxidised sample coated by chromium and niobium.

Charquet has described the properties of hafnium [187]. At 20 °C, the Young's modulus of hafnium is 140 GPa which is higher than the niobium one. Table 52 adressed the main mechanical properties of hafnium with respect to oxygen content. The oxygen acts as an addition elements and increases the mechanical properties of the hafnium as well as Vickers' hardness due to crystal lattice expansion. The metal deposition is performed using a cathodic deposition system which relies on a gas plasma creation. The current configuration of this apparatus doesn't allow the control of oxygen content in the chamber during the process. Moreover, the metal target is cleaned before each coating so it is expected that the coated metal should be made of the pure metal. After thermal ageing, the oxides can't be removed using chemical solutions but rather by using some mechanical polishing letting expect some good adhesive properties.

Oxygen content (ppm)	R_m (MPa)	$R_e^{0.2}$ (MPa)	Elongation (%)	Vickers' hardness on the surface (HV)
100	360	150	33	140
300	460	300	20.5	175
600	570	350	18	215

Table 52: Properties of hafnium with respect to oxygen content [187].

Two specimens made of 316L have been polished until OPS finish. Then, the first one has been covered by a 10nm-thick niobium coating and the second one has been covered by a 10nm-thick hafnium coating. Then, the samples have been placed in a furnace at 550 °C in air. After ten weeks, the thermal ageing was stopped and some SEM observations of the sample surfaces have been performed (see Figure 178). Both niobium and hafnium have affected the oxydation behaviour of the sample surface. In Figure 178 a, the oxide has grown following the underlying microstructure whereas the oxidation on the coated samples is more homogeneous (see Figure 178 e and Figure 178 f).

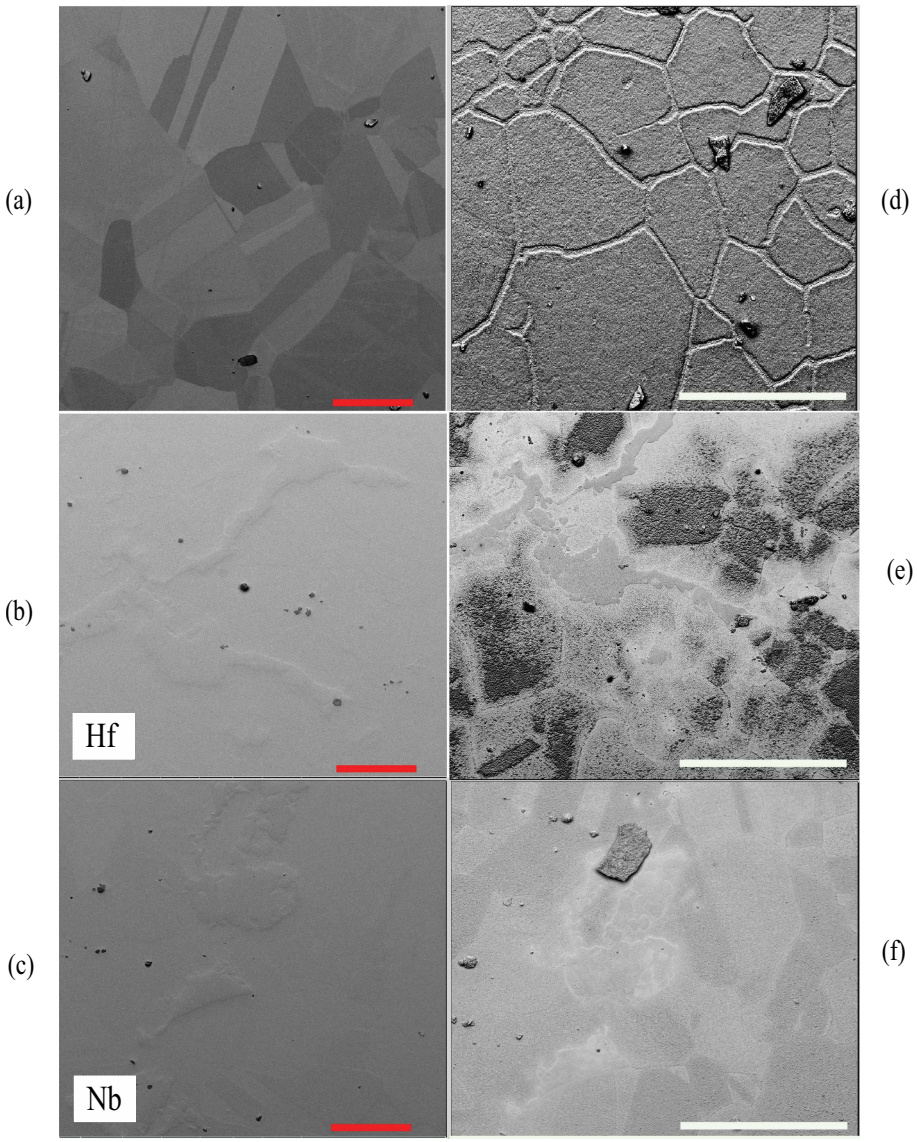

Figure 178: SEM images of 316L sample before and after ten weeks at 550 °C in air oxidation (a, d) after etching with OPS (b, e) covered by hafnium and (c, f) niobium. The red scale bar is 50 µm and the white scale bar is 100 µm.

After the thermal ageing, tungsten patterns have been deposited with a thickness of 10 nm onto the sample coated by hafnium oxide (see Figure 179) and by niobium oxide (see Figure 180). Even if the sample surface is irregular due to the oxide growth, the quality of the pattern is satisfying.

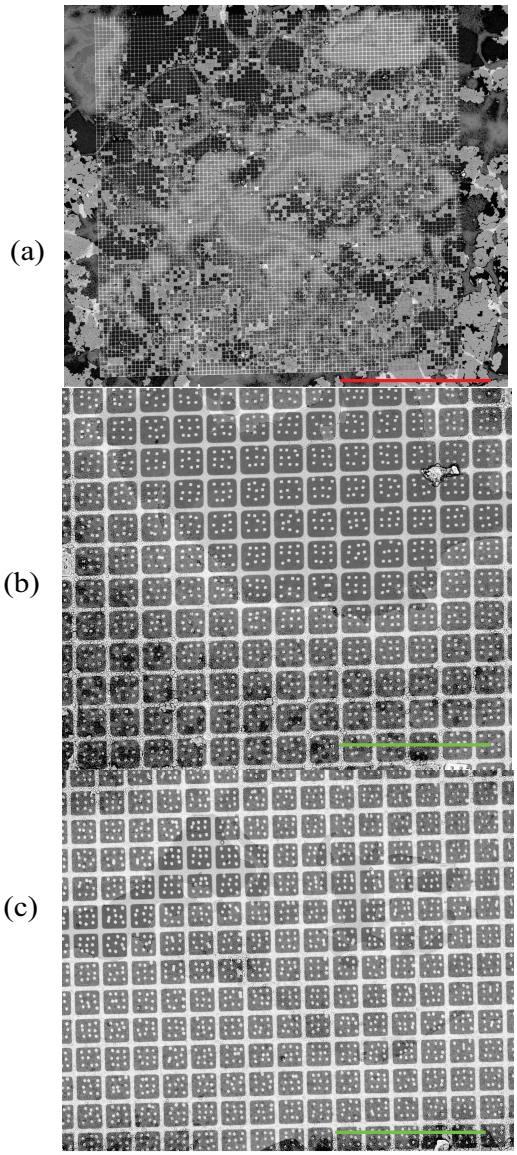

Figure 179: SEM images of tungsten pattern deposition onto 316L covered by Hafnium in (a) SE mode and (b),(c) in BSE with Z contrast mode. The red scale bar is 500 µm and the green one is 50 µm.

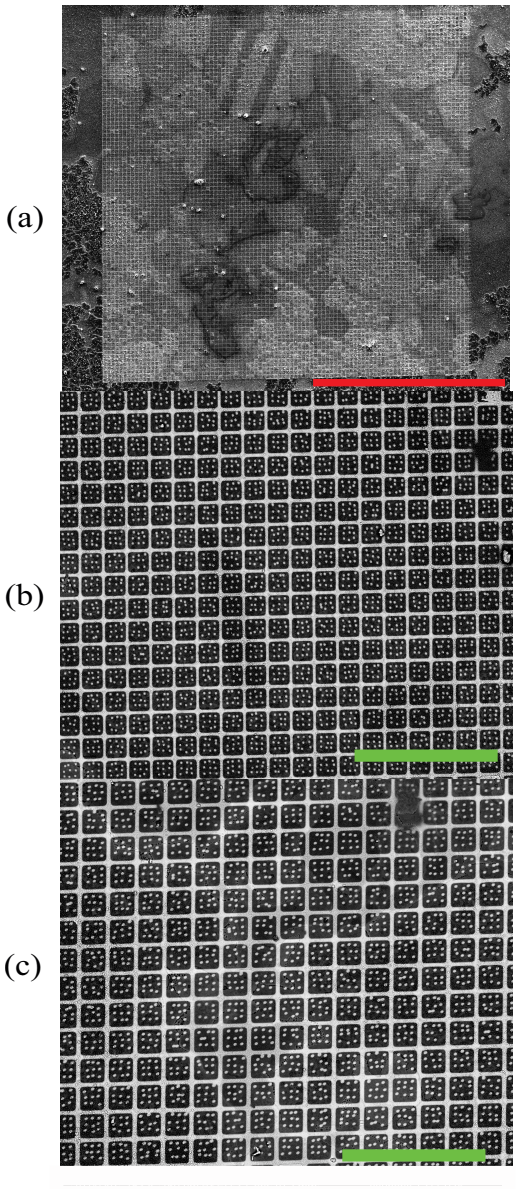

Figure 180: SEM images of tungsten pattern deposition onto 316L covered by niobium in (a) SE mode and (b),(c) in BSE with Z contrast mode. The red scale bar is 500 µm and the green one is 50 µm.

After two weeks at 550 °C, the pattern has been damaged by the interaction with the gas environment (see Figure 181). It is not possible to expect performing DIC anymore.

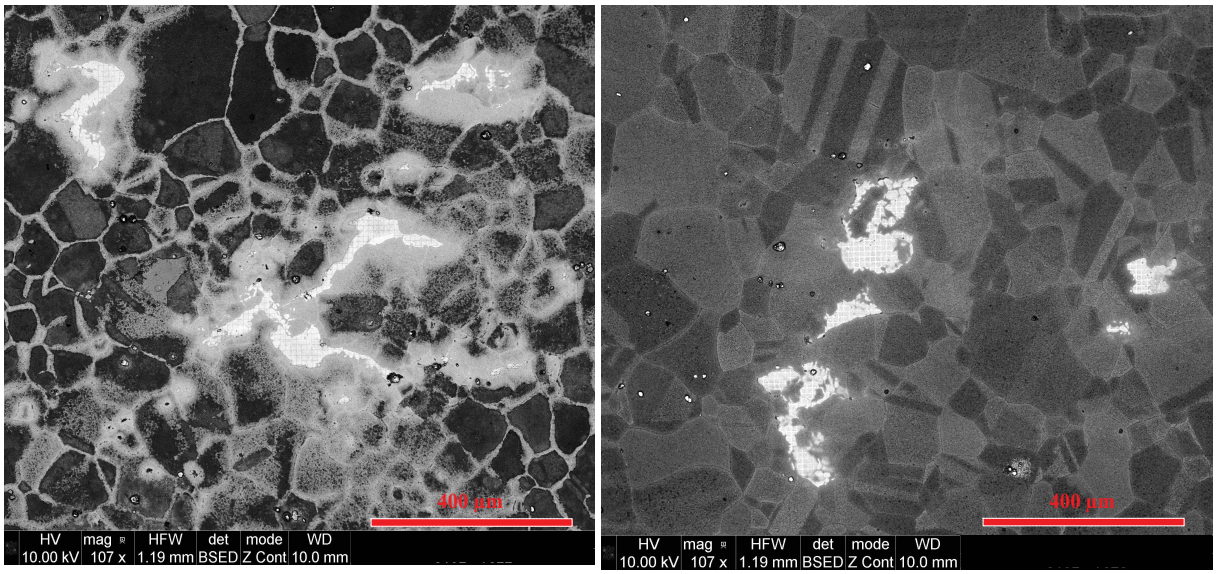

(a) (b)

Figure 181: SEM images of tungsten pattern deposition onto 316L covered by hafnium (a) and by niobium (b) in BSE mode with Z contrast after two weeks in air at 550 °C.

After carburization, a sample of 316H has been polished until OPS finish to remove the magnetite at its surface and get a convenient surface for the microlithography process. Then, the surface has been covered by a tungsten marker and the sample has been submitted to thermal ageing at 550 °C during two days (see Figure 182).

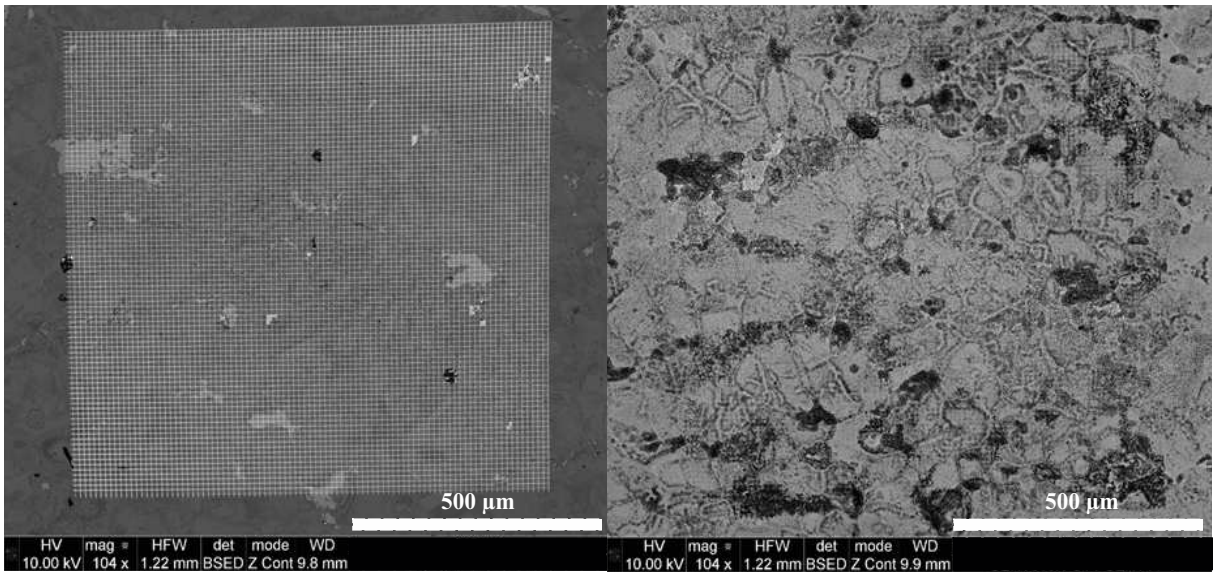

(a) (b)

Figure 182: SEM images in BSE mode with Z contrast of tungsten pattern deposition onto 316H polished until OPS finish (a) before (b) after two days at 550 °C in air.

After two days, the changing in the contrast and the pattern evolution are too detrimental for the DIC procedure. A crack monitoring using DIC can't be performed.

Conclusions

None of the metal cover tried has permited to reduce the oxidation at the sample surface. Rapidly, at 550 °C in air, the tungsten pattern is damaged by the oxide growth. These changes are so detrimental that it is not possible to expect performing DIC analysis during a long period. In fact, after 48h, the gray level conservation hypothesis is not satisfied and the kinematic fields are inaccurate and incomplete.

Appendix B

Instruments and technical details of e-beam microlithography

In Chapter 4, the e-beam microlithography has been presented. The five steps of this technique require to use some specific apparatus and chemical solutions devoted to the pattern deposition. As mentioned, the use of tungsten has led to an improvement of the method using two kinds of polymer resins. Technical details are given in this section.

The coating process is performed using a spin-coater in protected atmosphere (see Figure 75 a). The centrifugal force spreads the resin insuring the obtention of an homogeneous layer with a constant thickness, typically a few hundred nanometers, depending on the resin and the spin-coater speed.

To irradiate the resin (see Figure 75 b), a FEI Quanta FEG 600 SEM was used. The SEM properties for the microlithography are given in Table 53.

Energy	Beam current	Spot size	Diaphragm	Area dose, Line dose, Dot dose
25 keV	0.25 nA	3.59	6	187.5-190 µC/cm^2, 560 µC/cm, 0.2 C

Table 53: SEM characteristics used for the e-beam microlithography process.

This apparatus is synchronized with a Raith Elphy Quantum commercial system which controls the SEM beam. This software use is requested to expose the specific areas with the accurate precision and the optimized time process.

Once the sample surface has been exposed, the pattern has to be revealed (see Figure 75 c). The developper used is Methyl Isobutyl Ketone dissolved in propan-2-ol, known as MIBK. The sample is then washed with water and dried with compressed air before the metal coating. The metal coating is performed using a sputtering system. The method relies on a plasma creation leading to particles ejection from a chosen metal target. These particles will then be deposited onto the "developped" specimen surface (see Figure 75 c).

Finally, to achieve the pattern deposition, the unexposed resin must be removed. The product used, called "remover", is the 1-Methyl-2-Pyrrolidon. The removing process can be quite long and an ultrasound bath can be used to speed up the process. At the end of the process, the sample is washed using successively acetone and water.

Appendix C

Multiscale approach using a double scale pattern

In Chapter 4, the DIC method has been introduced as well as the technique to get surface markers when the material is not convenient for the kinematic measurements. The influence pattern choice on DIC performance has been studied by [142]. To improve our understanding of creep cracking, we need to get quantities of interest at several material scales: considering a few grains and at the scale of an aggregate. To achieve this multiscale vision, an improvement of the pattern is proposed. The methodology to obtain a pattern made of grids and dots with random characteristics at several scales is introduced.

The creep cack problem requires to get quantities of interest at several material scales: the scale of a few grains and at the scale of an aggregate. To achieve this multiscale vision, an improvement of the pattern is proposed. It is based on the microgrids/dots pattern with double-scale random characteristics: a double scale pattern of 1 mm field with random characteristics at both macroscopic scale (considering the full pattern) and at the microscopical scale (20 microns). The aim of this double-scale use is to get kinematic field in a millimetric field and fine measurements in the region surrounding the crack tip.

The double-scale pattern has been created using a numerical pattern made of random dots (see Figure 183).

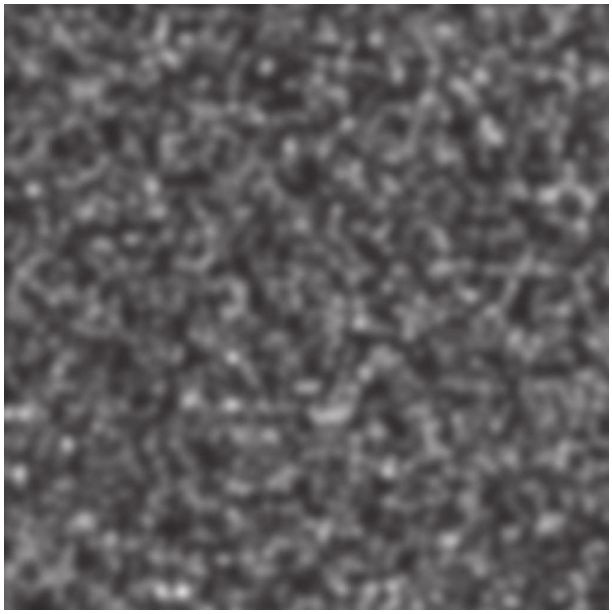

Figure 183: Random numerical pattern used to create the double scale pattern [122].

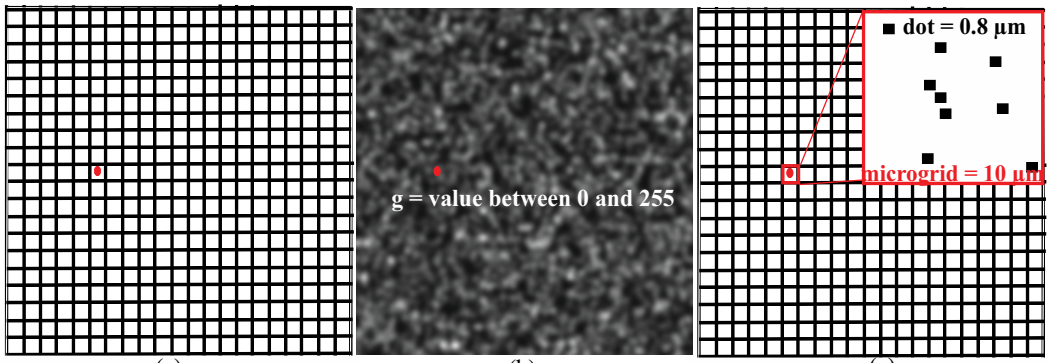

Figure 184: Methodology to obtain the double scale pattern with the desired properties using Figure 183.

The methodology to obtain the double-scale pattern is described in Figure 184.

- All the positions of the center of microgrid in the double scale pattern are known (see Figure 184 a);
- The numerical pattern and the double scale pattern have the same dimensions (1024 x 1024 pixels). The center positions in Figure 184 a correspond to a grey level value in the numerical pattern (g) Figure 184 b;
- A maximal number of dots by microgrid is chosen $nbmax$. The number of dots d for the corresponding microgrid in the double scale pattern is given by:

$$d = g \cdot nbmax \tag{C.1}$$

- Once d has been identified, the dots are randomly placed in the corresponding microgrid (see Figure 184 c). The operation is performed for each center of microgrid.

Several combinations were tried to obtain the best trade-off between size and density of dots resulting in the highest contrast in mode BSE with Z contrast image (see Figure 185).

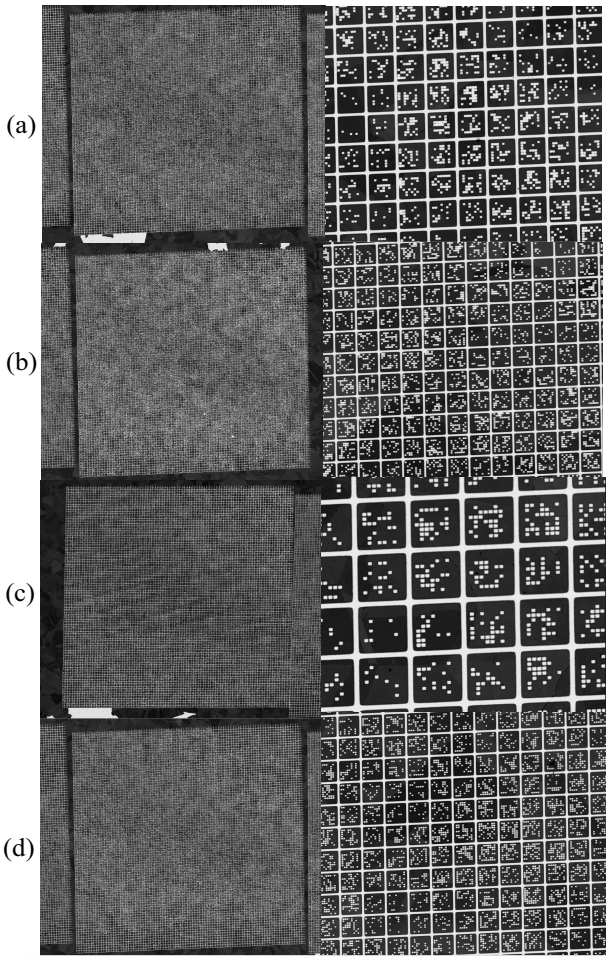

Figure 185: SEM images of double scale patterning (a) 0.6 µm 49 dots, (b) 0.6 µm 64 dots, (c) 0.7 µm 49 dots and (d) 0.7 µm 64 dots.

Appendix D

DIC crack monitoring between three creep test periods

In Chapter 5, an interrupted creep test performed in air at 550 °C on 316H SENT specimen has been presented. The objective of this experiment was to perform a crack monitoring at the microstructural scale. After creep period, an in-situ tensile device has been used to apply elastic loadings and to slightly open the fatigue pre-crack in the SENT specimen. This procedure is used to make the crack position observable on the SEM images. The DIC analysis then allows the crack tip position identification highlighting the possible crack propagation. Three in-situ tensile tests have been performed (see Figure 186):

- *During the first in-situ tensile test, two cracks have been observed on the SEM images for F = 700 N. These images have been used to perform DIC analysis. In the kinematic fields, two discontinuities relevant with the observed crack positions have been captured. The displacement fields have been used to precisely identify the respective crack tip position.*
- *Then, the sample have been subjected to another creep periods. During the second and the third in-situ tensile tests, the specimen has been loaded until reaching F = 700 N without observing cracks or capturing discontinuities in the displacement fields. The kinematic fields are presented in this Appendix.*

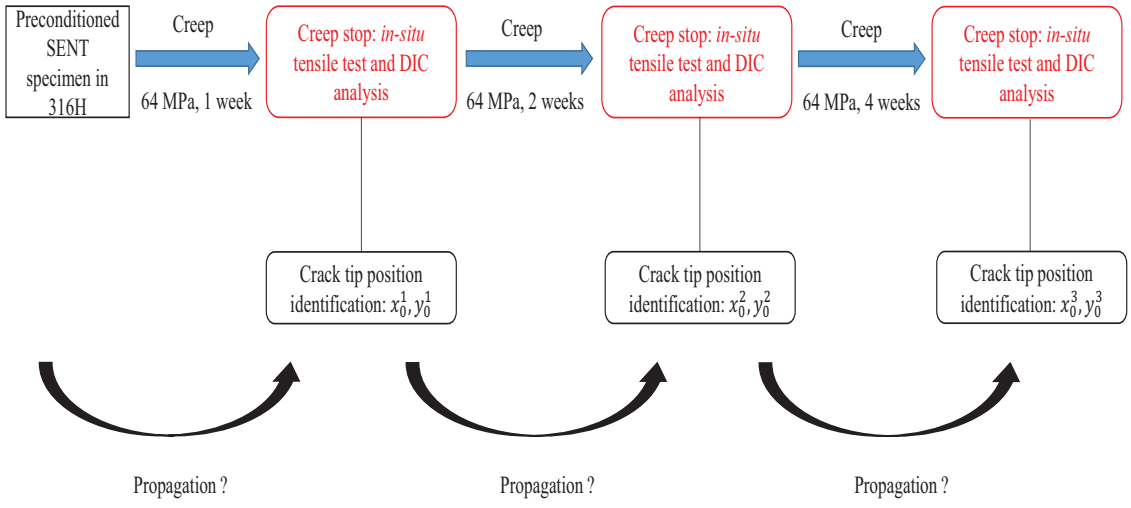

Figure 186: Methodolgy of the interrupted creep test at 550 °C in air.

During the *in-situ* tensile tests, the applied load has been increased until reaching F = 700 N corresponding to the load threshold of crack occurences for the first test. The kinematic fields proposed in Figure 187 correspond to the displacement fields obtained by comparing the first SEM image acquired for the current creep stop when the specimen is unloaded with the SEM image at F = 700 N. After the second creep period (*i.e.* 3 weeks of creep), no crack has been observed both by comparing the SEM images or by analysing displacement fields (see Figure 187 a,b). For the third period, a very small discontinuity can be observed in the upper region of the displacement field (see Figure 187 d). This discontinuity has been attributed to a short crack by observing the specimen at high scale. The location of this appearing crack was not consistent with the two cracks observed previously. It has been concluded that this crack was generated due to the weak mechanical properties of the oxide layers. Moreover, a start of discontinuity can be observed in the middle of the specimen. SEM observations have not highlighted the presence of a visible crack. Consequently, it has been decided to slightly increase the load applied during the creep test to σ_∞ = 96 MPa.

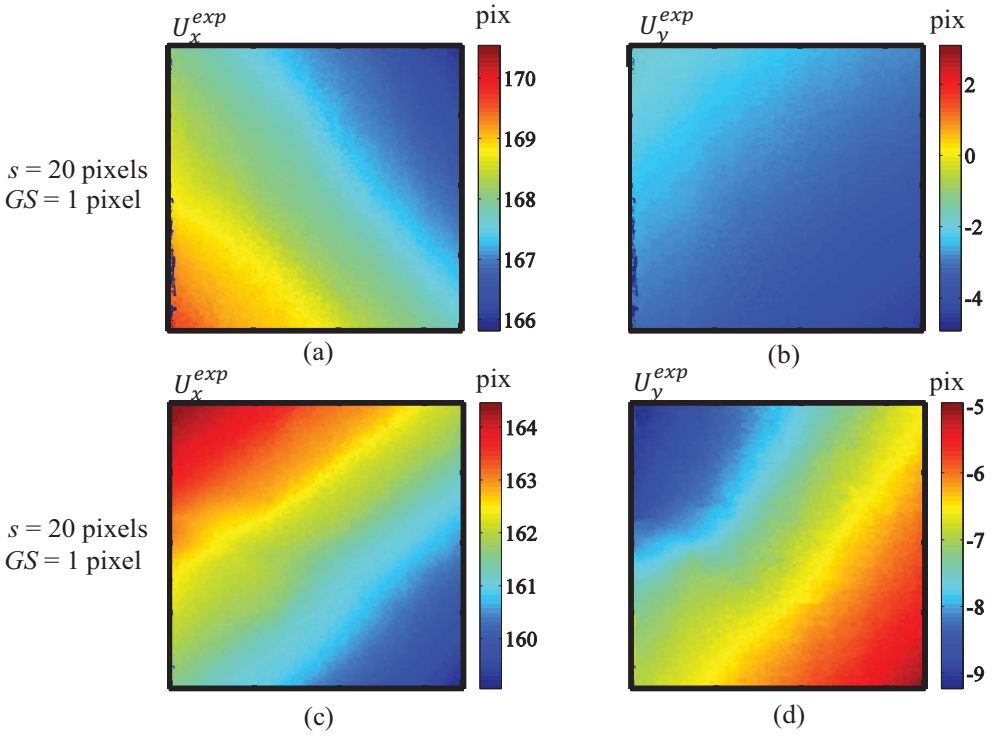

Figure 187: Kinematic fields measured with Kelkins routine u_x^{exp} and u_y^{exp} for the second interruption creep stop respectively (a,b) and for the third interruption creep stop respectively (c), (d).

Figure 188 shows the reference image before creep test (Figure 188 a). SEM images are referring to reference image and SEM image at maximal loading after the first creep test period (Figure 188 b,c). As mentioned earlier, two cracks have been observed. In Figure 188 d,e, we present respectively the reference image and the deformed image for the second creep test period. And finally, the images used to perform DIC after the third creep test period are given in Figure 188 f,g.

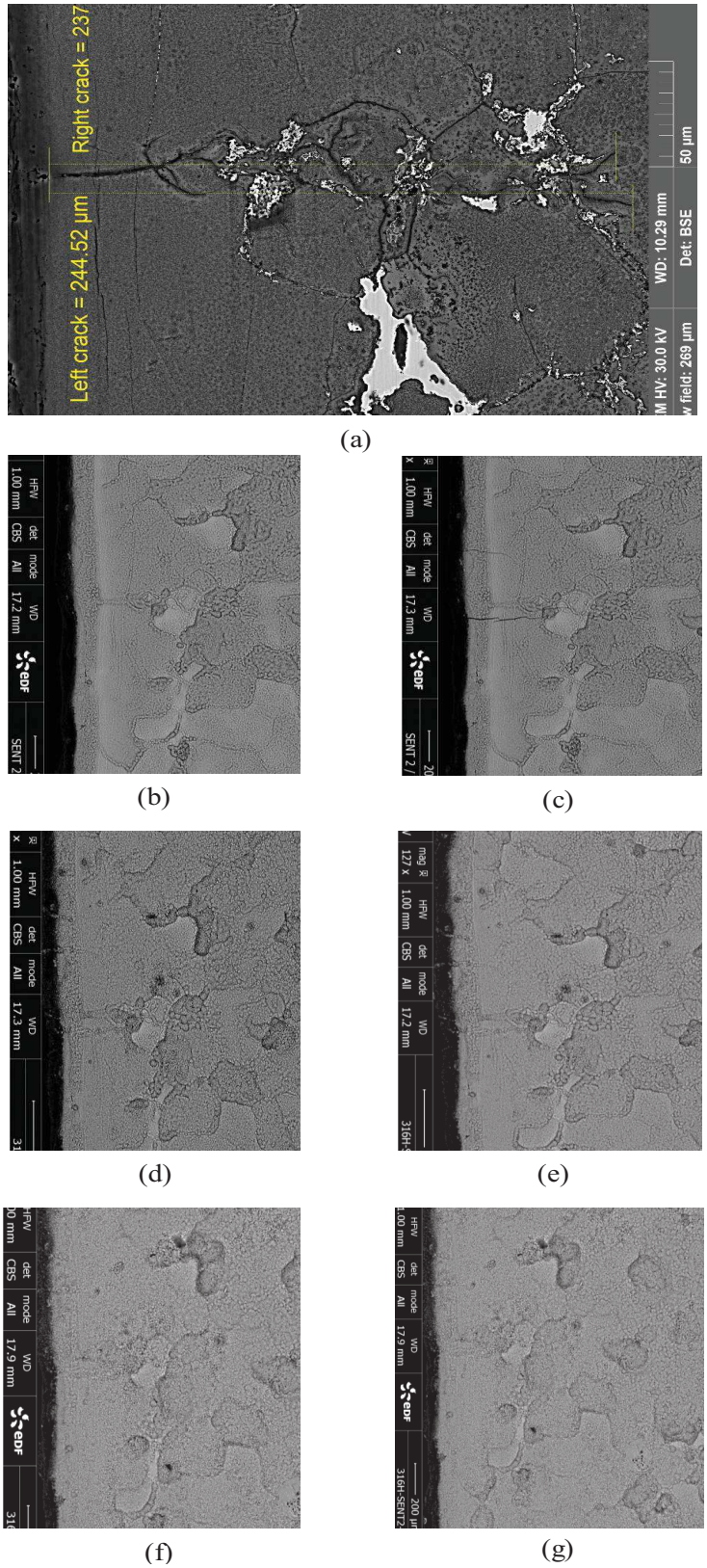

Figure 188: SEM images of the expected crack location before creep (a), after the first creep test period (b,c), after the second creep test period (d,e) and finally, after the third creep test period (f,g).

Appendix E

Principle of the local gray level equalization method

In Chapter 5, an in-situ tensile test performed in SEM Quanta 600 at 500 °C on 316H SENT specimen has been presented. The objective of this experiment was to perform a crack monitoring at the microstructural scale at high temperature. DIC analysis has been chosen to obtain information about crack propagation and plasticity development. The couple of images considered for the DIC can be separated by long time periods (> 1 h) leading to change in SEM image contrast and brightness (see Figure 148). It is proposed to correct the histogram of deformed image in order to have it similar to the initial one and thus giving more reliable residuals. We propose to make the gray levels of the initial image locally correspond to the ones of deformed image.

Firstly, the area of interest in the initial image is identified: it corresponds to the zone where the pattern has been deposited and where the displacements are accurately measured (see Figure 148 a). Considering exclusively DIC measurements in this area, the residual maps for the initial and deformed image in gray level presented in Figure 189 can be obtained. Using a Normalized cross correlation criterion, the displacement computations are insensitive to contrast variations.

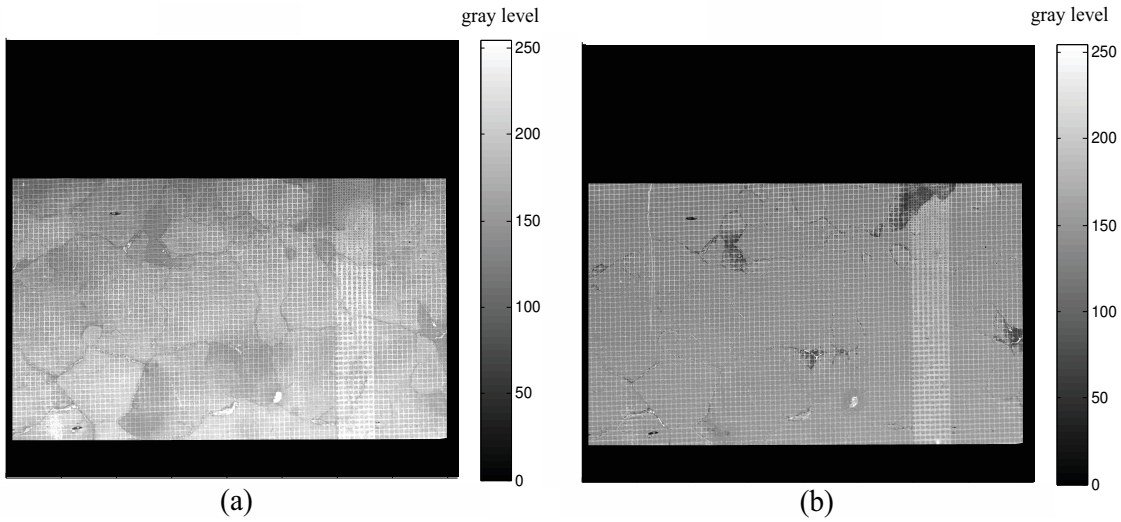

Figure 189: SEM image in gray levels in the identified area of initial image (a) and deformed image interpolated on the deformed configuration (b).

The histograms for the initial SEM image and the final one in the deformed configuration are respectively denoted h_0 and h_1 (see Figure 190). The objective is to make h_1 correspond as well as possible with h_0 using the equalization method in order to estimate relevant gray level residuals. Figure 190 shows that the initial image saturates while the final one is not saturated. The aim of the equalization method is to apply an affine transformation (characterized by a gain and an offset) to the deformed image in order to minimize the gap between the histograms of the initial and the final transformed image.

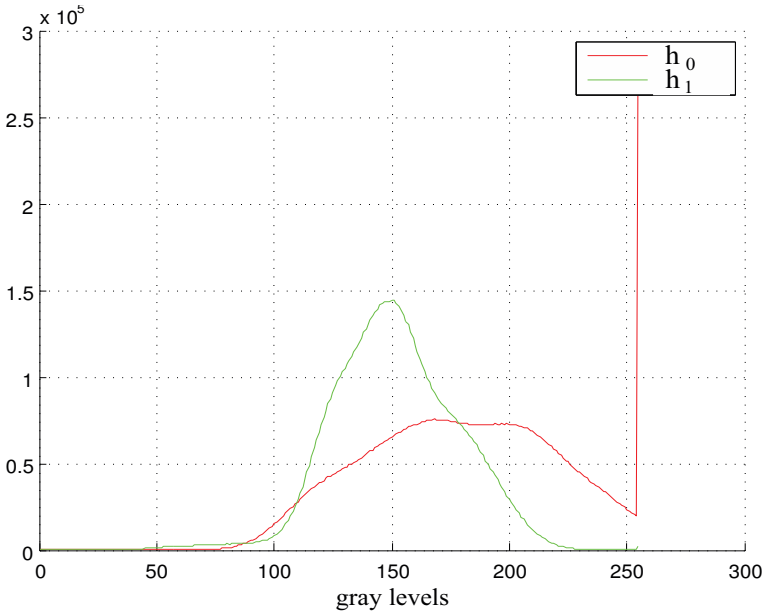

Figure 190: Histograms for respectively image initial (h_0) and deformed image (h_1).

This method relies on the resolution of a linear system with two sets of variables: the gains (corresponding to the contrast) and the offset (corresponding to the brightness). The area identified previously is sampled in quadrangular elements in order to apply a heterogeneous transformation. A set of bilinear basis function in gain and in offset is attributed to each element:

$$f_1(\chi,\psi) = (1-\chi)(1-\psi) \quad \text{(E.1)}$$
$$f_2(\chi,\psi) = \chi(1-\psi) \quad \text{(E.2)}$$
$$f_3(\chi,\psi) = \chi\,\psi \quad \text{(E.3)}$$
$$f_4(\chi,\psi) = (1-\chi)\psi \quad \text{(E.4)}$$

with (χ, ψ) the reduced coordinates in the chosen elements. In the case of rectangular elements they are expressed as:

$$\chi = \frac{(x-\min_e(x))}{(\max_e(x)-\min_e(x))} \quad \text{(E.5)}$$
$$\psi = \frac{(y-\min_e(y))}{(\max_e(y)-\min_e(y))} \quad \text{(E.6)}$$

where $\min_e()$ and $\max_e()$ represent respectively the minimal and maximal value of the variable on element e. The gain (α^e) or the offset (β^e) are expressed in element (e):

$$\alpha^e(x,y) = \sum_{k=1}^{4} \alpha_k^e f_k(\chi,\psi) \quad \text{(E.7)}$$
$$\beta^e(x,y) = \sum_{k=1}^{4} \beta_k^e f_k(\chi,\psi) \quad \text{(E.8)}$$

with k is the node number and e the element number. Then a cost function (F) can be constructed to represent the gap betwwen the initial image gray level at pixel i and the one of the modified final image:

$$F = \sum_{e}^{nb\,elem} \sum_{i}^{nb\,pix} [I_i^0 - (\alpha^e(\chi_i,\psi_i)I_i^1 + \beta^e(\chi_i,\psi_i))]^2 \quad \text{(E.9)}$$
$$F = \sum_{e}^{nb\,elem} \sum_{k=1}^{4} [I_i^0 - (\alpha_k^e f_k(\chi,\psi)I_i^1 + \beta_k^e f_k(\chi,\psi))]^2 \quad \text{(E.10)}$$

To identify the values of gain (α^e) and offset (β^e) for each element e, the cost function is minimized for each variable α_k^e and β_k^e. Figure 191 shows gain α (a) and offset (β) (b) calculated for a mesh of 10 x 10 elements e. The elements appear in black.

Once the optimal values of gain and offset have been obtained, the histogram of the modified image $\tilde{h}_1$ can be plotted. The results of the histogram equalization method on residual maps are presented in Figure 193.

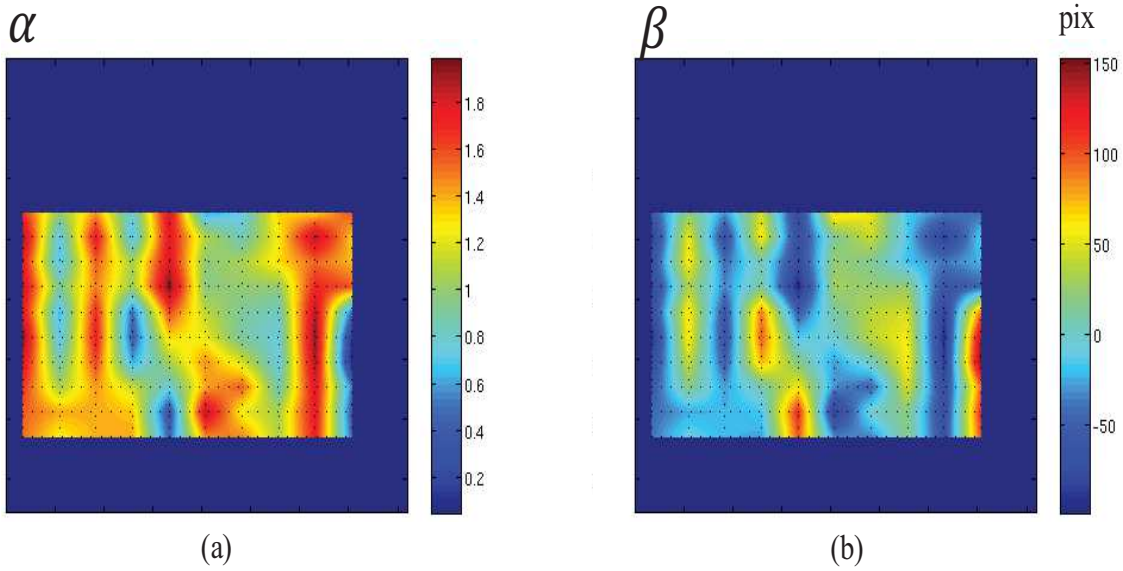

Figure 191: Representation of gain α^e (a) and offset β^e (b) for each element e. Mesh of 10 x 10 elements appears using black dashed-lines.

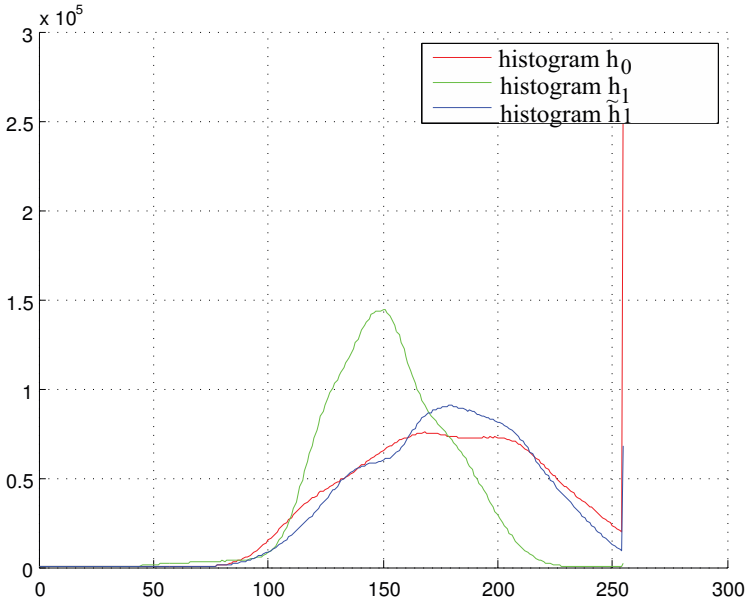

Figure 192: Representation of histograms h_0, h_1 and the modified version of h_1, $\tilde{h}_1$.

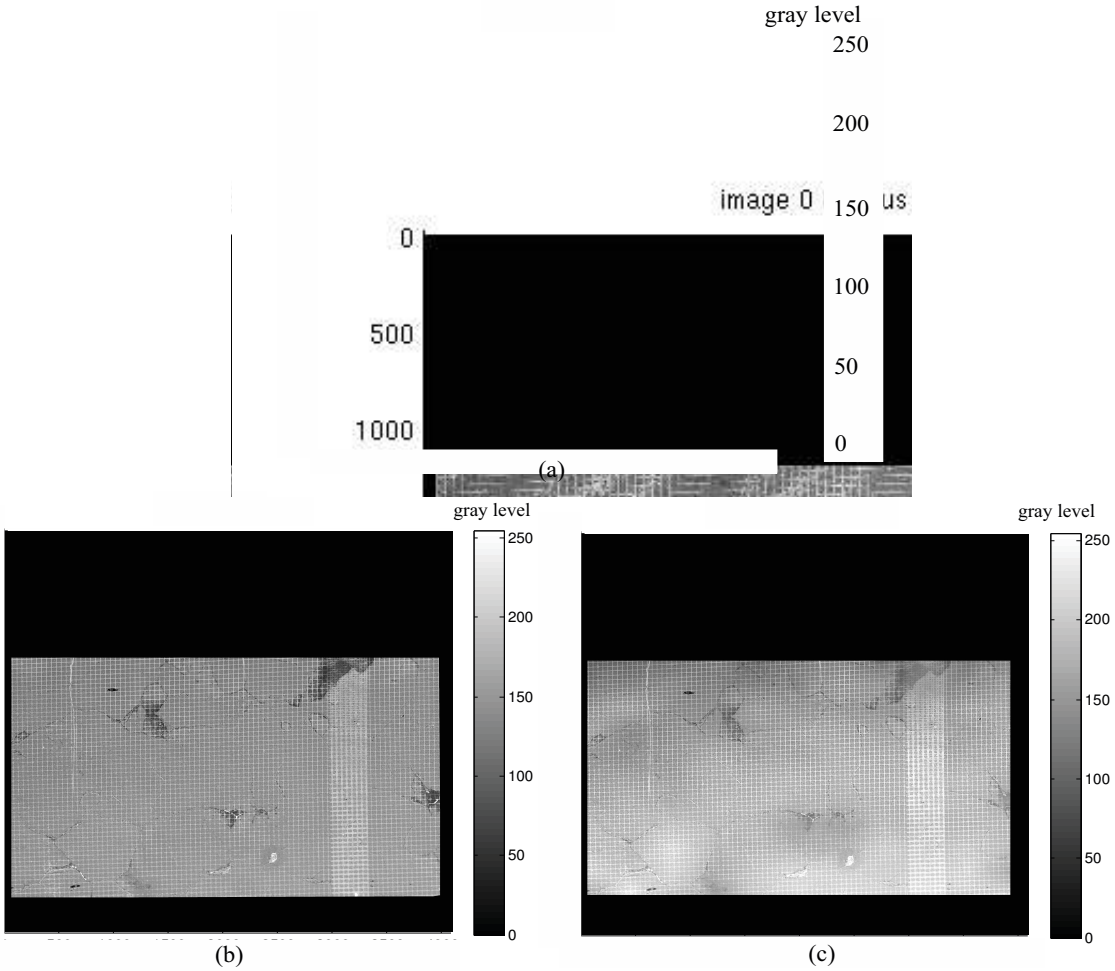

Figure 193: SEM image in the identified area of the initial image (a) and deformed image before equalization (b) and after equalization (c).

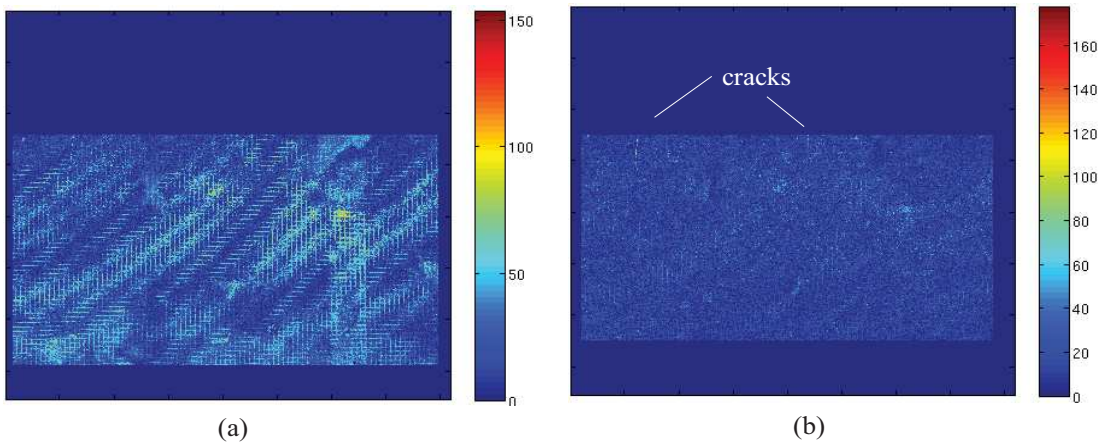

Figure 194: The residual maps before equalization (a) and after equalization (b).

Etude expérimentale de la fissuration en fluage de l'acier 316H vieilli sous environnement CO2

Résumé: Des fissures intergranulaires ont été observées sur des composants évoluant dans un environnement CO_2 à haute température (550 °C). Le matériau, un acier austénitique inoxydable de nuance 316H, est soumis à des sollicitations en fluage. L'objectif de la thèse est de permettre une meilleure compréhension du mécanisme d'endommagement par fluage et des effets de l'environnement sur l'apparition et la propagation de ces fissures. Une synergie entre la simulation par éléments finis et la mesure de champs cinématiques au moyen de la Corrélation d'Images Numériques (CIN) a été créée pour aborder ce problème avec une approche locale, à l'échelle de la microstructure. Une méthode de CIN adaptée au suivi de la fissuration basée sur l'utilisation des expressions de la Mécanique Linéaire Elastique de la Rupture a été développée. Une validation expérimentale sur essais de traction *in-situ* sur microéprouvette pré-fissurée de matériau 316H est proposée.

Mots-clés: fissuration intergranulaire, fluage, acier austénitique 316H, plasticité cristalline, Corrélation d'Images Numériques

Environmentally assisted creep crack growth in 316H stainless steel

Abstract: At elevated temperature (550 °C) in CO_2 environment, intergranular creep cracks have been observed in thermally and environmentally aged 316H. The ojective of this PhD work is to enhance the understanding of the creep crack mechanism and the effects of environment on crack initiation and growth. Some microtests on Single Edge Notched Tensile specimen (SENT) have been performed to better describe the interaction between chemistry and mechanics at the microstructural scale. Acreep crack monitoring procedure using Digital Image Correlation (DIC) have been developped and assessed using Finite Element Modelling (FEM) of cracked bicrystal. Based on a projection on Linear Elastic Fracture Mechanics expressions, the crack parameters (crack tip position, orientation) can be determined and the growth can be measured. A validation on *in-situ* tensile test at room temperature on SENT 316H is proposed.

Key words: creep crack growth, intergranular fracture, 316H stainless steel, Digital Image Correlation, crystal plasticity

Discipline : Mécanique et Génie Civil

Laboratoire de Mécanique et Génie Civil - UMR 5508
Université de Montpellier
CC 048 Place Eugène Bataillon
34095 MONTPELLIER cedex 5